Modelling nano-oxide materials with technological and environmental relevance : silica, titania and titanosilicates

Andi Cuko

DOCTORAL THESIS IN COTUTELLE

Modelling Nano-Oxide Materials with Technological and Environmental Relevance: Silica, Titania and Titanosilicates

Andi Cuko

Supervised by:
Prof. Stefan Bromley
(Universitat de Barcelona)
&
Prof. Monica Calatayud
(Sorbonne Université)

UNIVERSITAT DE BARCELONA

SORBONNE UNIVERSITÉ

UNIVERSITAT DE BARCELONA
FACULTAT DE QUÍMICA
Departament de Ciencia de Materials i Química Física
Institut De Química Teòrica I Computacional
Programa de doctorat de Química Teòrica i Computacional
&
SORBONNE UNIVERSITÉ
FACULTÉ DES SCIENCES ET INGÉNIERIE
Laboratoire de Chimie Théorique
ED:388 Chimie physique et chimie analytique de Paris Centre

Andi Cuko
2018

Difended on 24 September 2018
Jury:
Dr. Jacek Goniakowski (Sorbonne Université)
Dr. Konstantin Neyman (Universitat de Barcelona)
Dr. Silvia Casassa (Universià di Torino)
Dr. Celine Chizallet (IFP Energies Nouvelles)
Dr. Scott Woodley University College London (UCL)
Dr. Stefan Bromley (Universitat de Barcelona)
Dr. Monica Calatayud (Sorbonne Université)

UNIVERSITAT DE BARCELONA

SORBONNE UNIVERSITÉ

This doctorate program is part of the Initiative Training Networks - European Joint Doctorate (ITN-EJD) in Theoretical Chemistry and Computational Modelling (TCCM). The work presented in this thesis has been carried out in co-tutelle between the University of Barcelona and the Sorbonne University. First 16 months took place at the Materials Science and Physical Chemistry Department of the Chemistry Faculty of the University of Barcelona and within the Institute of Theoretical and Computational Chemistry (IQTC). Two months were spent at SIMUNE, the industrial partner for the doctorate Secondment program. The remaining 18 months, have taken place in the Laboratory of Theoretical Chemistry (LCT) of the Faculty of Science & Engineering of the Sorbonne University. This project has received funding from the European Union's Horizon 2020 research and innovation program under the Marie Skłodowska-Curie ITN-EJD-TCCM grant agreement No. 642294. Computational resources where provided from Red Española de Supercomputación (RES) and from Centre Informatique National de l'Enseignement Supérieur (CINES).

"There's plenty of room at the bottom"

Richard P. Feynman, 1959

Acknowledgments

These three years of the PhD program have been really great and intense in many aspects. I want therefore to express my acknowledgments to several people that shared with me some of the nicest moments during this journey.
I will start thanking my supervisors, Stefan and Monica which guided and motivated me meanwhile being patient during the several errors that I made. I think what motivated me the most was our friendship relation rather than the usual hierarchical and distant student-supervisor relationship.
Vorrei ringraziare i miei genitori, Marjeta e Franco che durante questi anni si sono fatti carico delle mie preoccupazioni sostenendomi sempre e il loro orgoglio per me è sempre stato la mia fonte di carica. Un ringraziamento va anche ai mio zio Kosta e a mia zia Lela per essermi stati vicini in questi anni e per aver creduto in me. Vorrei anche ringraziare Anna e Carmelo, Salvo e Mariarita, Ary, Alberto e Sara per aver reso le mie estati indimenticabili.
I would like to thank friends from the TCCM doctoral program specially Jelle, Stefano, Martina, Carles, Ewa, Dima, Neus, Vani and Max with whom the joint doctoral activities were really funny.
I would like to thank Monica and Federico from SIMUNE that helped and supported me during my secondment. From Barcelona I acknowledge my former flatmates, Panta and Franz for our nice and funny joint activities. I also thank my colleges and friends form the University specially Isaac, Toni, Fransis, Alberto, Sergi, Oriol, Angel, Tommy, Sergey, Helena and KC. Our Bowling nights will remain unforgettable.
I am also thankful to colleges and friends in Paris, specially to Salem, Sehr, Frédéric, Olivier, Maya, Cairedine, Ariel, Felix, Özge, Manuel, Anthony, Daniele, Veronica, Flavio and Daria. We had a great time together during this last year.
I would like to thank also Fede and Jaz, Mosca, Nadir and Ila whith which I shared several funny moments. Last but not least, I am really thankful to Cate, my girlfriend and flatmate in Paris. These last months would have been much harder without your smiles, your pumiddis and your support.

Abstract

Properties of nanomaterials are known to be size dependent and generally are very different from those of the corresponding bulk. Such behaviour, which is strongly system and structure dependent, allows one to tune material's properties by varying their dimensions. This tunability opens up many possibilities in nanotechnology for manufacturing materials with tailored properties for specific applications. Thus, understanding size-dependent properties of nanoparticles and mechanisms taking place at the nanoscale is fundamental for the improvement of existing materials and for the designing of more efficient and optimized ones. However, the synthesis of nanomaterials and their experimental characterization is difficult, especially for very small sizes. Here, theoretical modelling plays a fundamental role in the characterization of small nanoparticles for both helping experimental interpretation and predicting novel and potentially synthesizable materials with new properties.

In this thesis we focus on modelling of titania, silica and titanosilicate based materials because of their technological and environmental importance as they are employed in heterogeneous (photo-)catalysis, electronics and gas sensing to cite a few. For such systems, we firstly performed global optimization studies in gas-phase and water containing environments in order to identify the structures of nanoparticles. Secondly, we studied structural, energetic and electronic size-dependent properties of such nanoparticles as well as their reducibility, extrapolating up to the bulk macroscopic level in some cases. For such characterization we used accurate quantum mechanical methods based on Density Functional Theory (DFT).

Our results point to a series of important predictions, such as for instance: (i) the crystallinity of titania nanoparticles, which is the key property for the photoactivity of such material, is predicted to emerge when nanoparticles become larger than 2.0-2.5 nm; (ii) the mixing of titania and silica to form titanosilicates, which are an important class of materials used in industry as catalyst, is found be thermodynamically favorable at the nanoscale, contrarily to the bulk; (iii) the hydration of silica and titania nanoclusters, which plays an important role in the aggregation and nucleation process

during the synthesis of larger nanoparticles, is controlled by the environmental factors such as temperature and water vapor pressure as predicted from calculated phase diagrams; iv) the oxygen vacancy formation, which is an indicator of the system reducibility, is found to be less energetically costly in small nanosilica clusters rather than in nanotitania which is the opposite of what happen at the corresponding bulk level. We hope to inspire experimental studies to address the synthesis of novel titanosilicates materials with potentially enhanced properties by using as building blocks nanoparticles predicted here.

Contents

Chapter 1

Introduction

Materials have shaped the development of civilizations for the whole human history. Having better materials meant for instance manufacturing more powerful weapons and in turn conquer more land or defend better from conquerors. Historians have labeled the human history according to the material central to the civilization development. For example, in the Stone Age during large part of the prehistory, a wide variety of stone tools were used by modern humans and by their predecessor species. Bronze Age occurred between 3300 and 1200 years BC where first bronze artifacts (copper and tin alloy) start to appears. Finally in the Iron Age where tools and weaponry based on iron with improved mechanical properties appeared. If our future descendants would label our present history according to a material that characterized our civilization and was central to our technological advancements, how this era would be called? Could it be the era of silicon which is the main material for manufacturing computers that so greatly are revolutionizing out present society or such material has yet to be discovered? This question is undoubtedly difficult to answer, however, it is clear the role of materials across the history to present days. In our days, we want to be able to design the most appropriate material according to the desired function. To do so, a deep understanding of the whole range of materials properties are needed during both their synthesis and application process. Here, we will focus on oxides materials because of their technological and environmental importance. Rather than describing in detail the

several vast areas of applicability of oxides we focus specificity at nanoscale properties because of the strong challenges faced in experimental structural characterization and for which theoretical studies can provide fundamental insights.

1.1. Nano-oxide materials

Oxygen forms bonds with almost all elements in the periodic table forming a vast variety of molecules and materials. In the lithosphere, oxygen is one of the most abundant elements followed by silicon. To a large extent, our planet is an oxygen-rich environment which further hosts vast oxygen-dependent biological systems. In our society, oxide materials have a great technological impact in diverse fields such as catalysis[1], optoelectronic devices[2–5], environmental remediation[6,7] etc. Such success has been driven, not only by their particular chemical and physical properties, but also by their typical intrinsic stability. In recent years, it has been also discovered that properties of oxides, and also more generally of many materials, can be enhanced by reducing their size down to the nanoscale. The

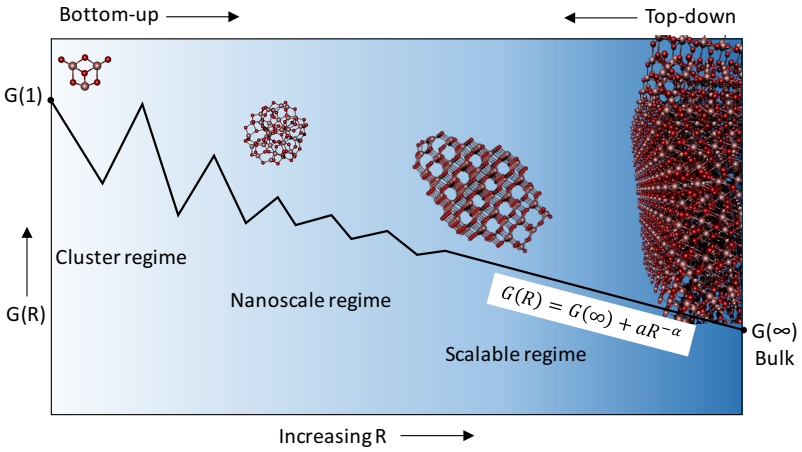

Figure 1.1: Schematic representation of the different size regimes.

nanoscale can be defined as the size range between 1 and 100 nm of particle dimension and typically, at these sizes, materials begins to display specific non-bulk-like properties. More specifically, it is possible to define three

size regimes possessed by materials[8,9] as also shown in Figure 1.1 in a schematic representation:

- Scalable regime: generally, particles in this size range display bulk-like structural and electronic properties which scale linearly towards those of the corresponding bulk materials as the size increases. The stability of particles in this size regime can be expressed and justified in terms of their surface-to-bulk ratio.
- Nanoscale regime: although particles may retain the bulk structure, due to the high surface-to-bulk ratio their properties may display significant changes with the system size and, for instance, structural phase transitions may occur. Moreover, semiconductor and metal nanoparticles begin to display peculiar electronic properties due to not only to the high surface-to-volume ratio but also to quantum confinement effects originating from when the wavelength of electrons is comparable to the system size. These effects allows to tune the band gap of by the semiconductor nanoparticle by changing its size and thus opens many applications for optoelectronic devices, fuel cells etc.
- Cluster regime: this is the regime where nanoparticles exhibit unique properties which are distinct from those of the corresponding bulk material. Moreover, these properties dramatically change with the system size. This size regime is also called the regime where every atom counts due to the sensitivity with the system dimension.

The transition between one size regime to another is not precisely defined and generally is strongly system dependent.

1.2. Synthesis and characterization of nanomaterials

In 1996, Harold Kroto, James R. Heath and Richard Smalley were awarded of the Nobel Prize in Chemistry for their contribution to the discovery of C_{60}[10] in 1985. Nanoscience and nanotechnology has grown exponentially since then and, to date, several cluster-assembled and nanostructured materials with tailored properties have been produced[11–16]. Such

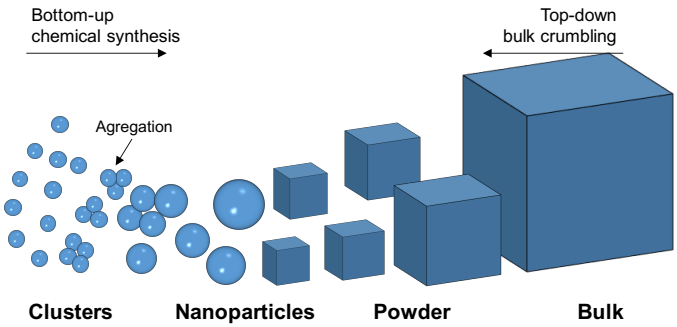

Figure 1.2: Schematic illustration of nanoparticles preparation techniques: bottom-up chemical methods against top-down physical methods.

materials are created using nanoclusters or small nanoparticles as building blocks which maintain their identity and properties in the final product.

Experimentally there are several ways to synthesize small nanoparticles which are fundamentally divided into two categories. The top-down bulk crumbling[17] approach is considered to be a physical method and consists in mechanically reducing the system size starting from the bulk. However, with such techniques, the control of nanoparticle size and the size distribution is rather problematic. Much better control can be achieved with bottom-up techniques such as in gas-phase cluster beams and via solution-phase colloidal methods[18]. From one side, cluster beam methods relies on ablating a material with a plasma or laser beam and dispersing the resulting cluster droplets on an inert support after selecting and filtering clusters with specific size. From the other side, colloidal methods relies on the solution chemistry of molecular precursors that undergo nucleation, aggregation and self assembly in a dynamical equilibrium environment. Such methods allows one to obtain uniform nanoparticles with controllable size. There are several variants of these techniques and going into detail of the synthetic procedures is out of the scope of this thesis. Nevertheless, such techniques are crucial in order to obtain nanostructured materials, however, their structure determination from experiments is typically very difficult.

X-ray diffraction spectroscopy which is one of the most important techniques for atomic scale structure determination in the bulk, is of little value in small nanoparticles due to the lack of long range structural order, even in bulk like nanostructures. However, some X-ray adsorption spectroscopy

techniques such as XANES (X-ray Adsorption Near Edge Structure) and EXAFS (Extended X-ray Adsorption Fine Structure) can provide useful information about the local environment around specific atoms (i.e. the average coordination number). Both transmission and scanning electron microscopy (TEM and SEM) can provide direct visual images of nanoparticles helping therefore to determine their size and shape. However, these two techniques are limited by their low resolution, depending on the material type, for small nanoparticles with sizes in the cluster regime. Photoelectron spectroscopy can provide useful informations relative to the binding energy of electrons into the substrate and therefore to the electronic structure, especially for small nanoclusters. Finally, vibrational spectroscopy which is one the most important techniques for determining structural information, can be used in order to determine vibrational fingerprints related to the atomic structure of gas-phase nanoclusters. All these techniques are found to be particularly useful when coupled with size selecting instruments such as mass spectrometers, in order to characterize size dependent system properties. Although such techniques allow the determination of several properties of nanosized systems, the structure determination and assignment with atomic resolution remains very challenging. Here is where theory and modelling can play a crucial role.

1.3. The role of modelling nanomaterials

The role of modelling for understanding nanomaterials is wide-ranging. When experimental observations are available, theory can provide a comprehensive, accurate and reliable microscopic picture of the system and properties of interest. Specifically, when studying systems in the nanoscale regime, typically thorough atomistic simulations and accurate first principle quantum mechanics calculations, it is possible to predict the atomic structure and properties of clusters and nanoparticles. Thus, through the comparison between experimentally observed properties and calculated ones, modelling can provide fundamental atomistically detailed insights.

The role of theory and modelling can go beyond of the simple support and interpretation of experimental observations. Thanks to advances made

in recent years such as the improve of computational methods, increase of hardware and software efficiency, and the large amount of collated structure-property relationship data in several repositories, it is possible to explore and predict new materials with novel properties by means of theoretical modelling. Such studies are not limited to bulk materials but also can be used for nanosystems. For instance it is possible to study materials size dependent properties from nanoclusters and extrapolated all the way through to the bulk. This allows to better understand unknown size-dependent nanoparticle behaviors such as phase transitions, aggregation and nucleation etc. In some cases, via high-throughput screening it is possible to theoretically characterize a large number of materials or molecules in order to guide experimental studies, therefore avoiding the high cost of random trial and error approaches.

Nevertheless, theoretical approaches also face some limitations that restrict their applicability. In structure prediction, the number of possible geometrical configurations increases exponentially with the system size, and quickly reaches an unfeasibly high number of structures to be sampled. This is an intrinsic limit of structure prediction approaches arising from the high dimensional space of structural parameters. This restriction forces us to make assumptions with respect to the structural shape and morphology when modelling relatively large nanoparticles. An other strong restriction arise from the high computational cost of the most accurate quantum mechanical methods. Such methods can certainly be used to describe relatively small clusters and molecular systems (e.g. containing 20-30 atoms). However, for larger systems the computational cost rapidly and inherently become unfeasibly large. More approximate quantum mechanical based methods such as those based on Density Functional Theory (DFT) have been introduced in the last 30-years providing a good compromise between accuracy and computational cost. Moreover, even with such approximate methods, simulating a typical experimental sample which is highly heterogeneous systems and has nanoparticles with at least tens or hundred of thousands of atoms, is still computationally prohibitive.

1.4. Aims of this thesis

As it has been outlined in this Introduction, nanosized materials can possess very specific and unique properties which can be different to those of the corresponding bulk. Such properties, specially for small nanoparticles or nanoclusters, are typically strongly system size dependent. Several experimental techniques allows one to characterize the different nanoparticle properties such as vibrational frequencies, electron binding energy, the local coordination of atoms, etc, but, the structural assignment cannot typically be achieved exclusively by experiments. Structural information of such nanoparticles can be determined theoretically through global optimization methods and their properties can be characterized with accurate first principle quantum mechanical methods. The aim of this thesis is to predict nanoscale structural and size dependent properties of silica and titania based oxides materials. These two oxides have been chosen because of their great technological and environmental relevance which will be presented in the introduction of each dedicated chapter. We mainly focus on their mixing and of their interaction with water-containing environments. To do so, we use a series of computational tools such as global optimization and first principle calculations in order to predict the most stable atom structure of nanoclusters for a range of sizes and characterize the structure-property relations. Several systems studied in this thesis have not been yet synthesized, thus, our study can provide helpful atomistic level insight for their future experimental characterization. With this work we hope to draw the attention of the experimental scientific community in order to address the synthesis of novel cluster assembled materials.

1.5. Thesis organization

This thesis it is organized in 6 chapters. The present chapter was about an introduction to the thesis content. In chapter 2, I report on the theoretical aspects of methods and approaches used during this thesis. Chapters 3 is related to the mixing between titania and silica materials systems and their relative chemical reactivity at the nanoscale. Chapter 4 relates to the predic-

tion of the amorphous-to-crystalline phase transition in titania nanoparticles. Chapter 5 is dedicated to methodological developments for improving structural searches: (i) for hydrated nanocluster systems and (i) for extending the size limit of the global optimization method used in this thesis. In chapter 6 I present a study on size dependent properties of globally optimized hydrated silica and titania nanoclusters. Finally, the thesis conclusions are reported summarizing and highlighting the main achievements and contributions to the field. An appendix with supplementary relevant data of each chapter is also included.

Chapters 3, 4, 6 and first part of chapter 5 are summaries of the four scientific articles reported at the end of thesis. Three of the such articles have been already published in peer-reviewed journals and are freely available in the scientific repositories of the Sorbonne Université (`https://hal.sorbonne-universite.fr/`) and of the University of Barcelona, while the last article has been submitted.

Chapter 2

Theoretical Methodology

In this chapter we will focus on the theoretical aspects of simulations employed during this thesis. We will start with the main characteristics of atomistic simulations by means of classical and quantum mechanics. Afterwards, structural optimization procedures will be discussed as large part of this thesis is related with the global optimization problem. Some concepts of statistical thermodynamics and the connection between microscopic and macroscopic regimes will be also presented. All information reported in this chapter considered to be standard knowledge (such as quantum mechanics, classical mechanics, DFT, etc.) has been taken from books in ref[19–21] while more specific informations will be cited separately as appropriate.

2.1. Atomistic simulations

Macroscopic properties of materials are directly determined by the interaction of the building block constituents, the atoms and molecules. Atomistic simulations try to elucidate the interactions and relations occurring between atoms to find insights into experimentally observed behaviours. Such methodologies became increasingly frequent since the advent of computers just few decades ago, mirroring the increasing power of CPUs during this time. Nowadays, atomistic simulations are standardly and widely employed in the scientific community.

2.1.1. The Potential Energy Surface

One of the central problems in atomistic simulations is to calculate the energy of systems that obey to quantum mechanical laws. In order to calculate the system energy we must solve the Schrödinger equation, which is impossible to solve exactly for multi-electron systems. As such, there is no other choice than to introduce approximations. If we are interested in the electronic ground state energy and properties of a specific system, the Born-Oppenheimer approximation is the first step towards the Schrödinger equation solution. In this approximation the motion of nuclei is assumed to be independent from the motion of electrons due to their difference in mass of about three orders of magnitude. In this picture, electrons move extremely fast as compared to the nuclei and they adapt instantaneously to the nuclei positions. Therefore, the energy of the system becomes a parametric function of the nuclear positions giving rise to a so called potential energy surface (PES). We note that The Born-Oppenheimer approximation is not valid in conditions where the system wave function is not stationary such as in electronic excited state phenomena.

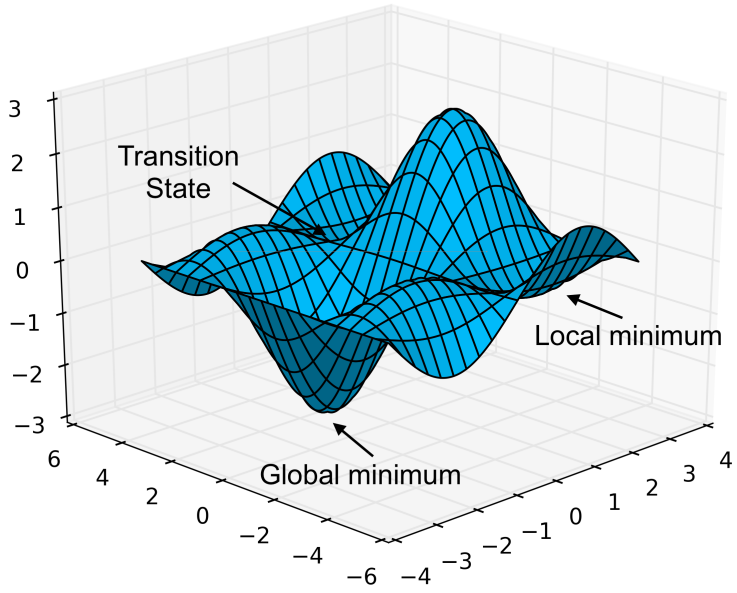

Figure 2.1: Representation of 3-dimensional Potential Energy Surface (PES).

Only the PES critical points have physical meaning, such as minima and first order saddle points which represent (meta-)stable nuclei configurations and transition states respectively (Fig. 2.1). The energy of the system can be calculated either quantum mechanically by solving the Schrödinger equation by approximated methods, or classically. In the following three sections (2.2, 2.3, 2.4) we will focus on how to determine the energy of a given system fist classically and then quantum mechanically.

2.2. Classical Interatomic Potentials

In the classical world, the quantum mechanical interaction between atoms is approximated by parametric functions. These parametric functions are called Interatomic Potentials (IPs). We can also refer to a set of IPs as a force field (FF). Parameters are fitted to experimental or high level computational data. Electrons are completely neglected in this picture and atoms are considered as point particles with charges whose values are also fitted. The accuracy and the applicability of the IP will strongly depend on the fitting dataset. Usually IPs are very system specific and they should not be applied outside the range of materials/conditions fitted for. There are repositories with many IP fitted for specific purposes[22,23]

Nevertheless, over the last few years, much effort has been made to create transferable IPs[24]. For covalently bonded systems, such as organic molecules, the bonding information has to be included *a priori* instead of being the result of a quantum mechanical calculation. Here, the system is modeled as balls (atoms) and springs (bonds) and all degrees of freedom (i.e. stretching, bending, torsion, etc.) are described by the FF. Several FFs have been developed for a wide variety of systems such as the MM2[25] suited from describing small organic molecules, AMBER[26] fitted for relatively big macromelocules such as DNA and proteins etc.

In this thesis, the focus is mainly on inorganic nanoparticle materials and only the IPs used will be described in detail. For inorganic materials, there is a less clear definition of a bond between two atoms with respect to organic molecules and such systems are typically described by distribution

of atomic distances according to specific conditions (i.e. crystalline and amorphous phases, pressure etc.). Inorganic materials can be well described by suitable IPs.

Generally, the total energy of a system can be defined as the expansion of a multi-body interaction between atoms (eq 2.1).

$$E_{tot} = \sum_{i,j}^{N_{atoms}} V_{ij}^{II} + \sum_{i,j,k}^{N_{atoms}} V_{ijk}^{III} + ... \tag{2.1}$$

where V_{ij}^{II} and V_{ij}^{III} are the two and three-body energetic terms contributing to the total energy E_{tot}. The one-body term has been omitted since it is meaningful only if the system is immersed in an external field. For our purposes this expansion is truncated to the two-body or three-body terms. A simple model to show the difference between IPs is the He-He interaction at different interatomic separation. He-He interaction according to Lennard-Jones, Buckingham and Morse potentials in which the multi-body expansion is truncated at the second order, are plotted in Figure 2.2 where each of them is fitted to highly accurate *ab initio* data.

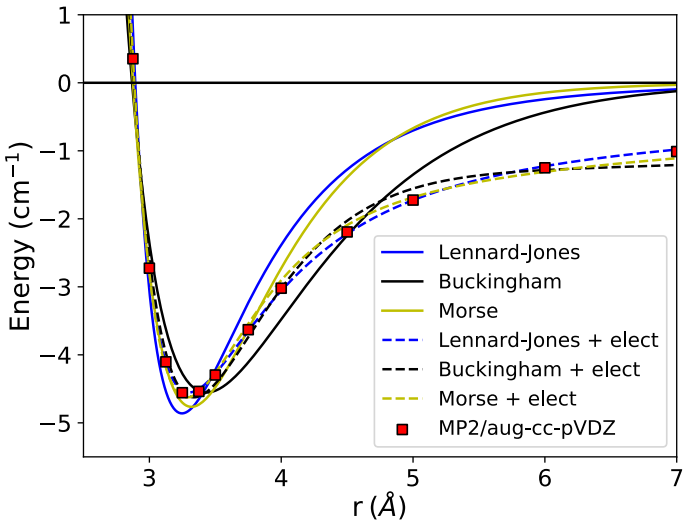

Figure 2.2: He-He Morse, Buckingham and Lennard-Jones potentials fitted to highly accurate *ab initio* calculations. Solid lines represent purely interatomic potentials while in dashed lines electrostatic interactions are added (with fitted charges $q_i, q_j = \pm 0.83$).

2.2.1. Coulomb electrostatic potential

$$V_{ij}^{elect} = \frac{1}{4\pi\varepsilon_0}\frac{q_i q_j}{r_{ij}} \tag{2.2}$$

The performance of fitted IPs can improve specially in the long-range interaction, by including the Coulomb electrostatic potential as we can notice from Figure 2.2.

This is the interaction between two charged particles as shown in eq. 2.2. q_i and q_j are charges of i-th and j-th atoms to be fitted, r_{ij} is their interatomic distance and ε_0 is the dielectric constant. Notice that in Figure 2.2 He atoms are neutral but their dimer interaction can be described better with models including charged atoms. It is common to introduce a cutoff function for any type of classical interaction and commonly it is a constant value indicating a distance above which the interaction is turned off. A typical cutoff radius for each atom pair of 12 Å is enough to capture the major electrostatic interactions. It is moreover possible to provide flexibility to the model including electronic polarizability effect by considering the core-shell ion model. With this model, anions can be represented with a positively charged core connected by a spring to a massless and negatively charged shell. The spring is represented by an harmonic potential ($V_{ij}^{harm} = -\frac{1}{2}kx^2$ where k is the force constant and x is the core-shell separation). This procedure introduces two more parameters to be fitted, the core charge and the harmonic force constant. Such models can be used to represent the polarizability of O atoms, especially important when involved in hydrogen bond interactions.

2.2.2. Lennard Jones interatomic potential

$$V_{ij}^{LJ} = 4\varepsilon\left[\left(\frac{r_e}{r_{ij}}\right)^{12} - 2\left(\frac{r_e}{r_{ij}}\right)^{6}\right] \tag{2.3}$$

Lennard-Jones is a very common potential and usually is used to model weakly bonded neutral systems such as noble gases. The mathematical form

this IP (eq 2.3) is the result of a repulsive term that decays as r^{-12} and an attractive term which decays with r^{-6}. The repulsion term dominates at the very short-range while the attraction term prevail at more longer distances. ε and r_e control respectively the deep and the equilibrium distance. Lennard-Jones, where exponents are 12 and 6, is a particular case of Mie potential in which exponents can have different values. One of the problems of Lennard-Jones potential is the short distance repulsion term which is overestimated with respect to accurate quantum mechanical methods. Moreover, the attractive part decays quicker than it should. To better resemble the quantum mechanical wave function behavior, the exponentially decay function is more appropriate. This feature is improved in the Buckingham IP. In Figure 2.2 it is shown the He-He Lennard-Jones interaction as a function of interatomic distance fitted to high level *ab initio* data.

2.2.3. Buckingham interatomic potential

$$V_{ij}^{Buck} = A_{ij}\ \exp\left(-\frac{r_{ij}}{B_{ij}}\right) - \frac{C_{ij}}{r_{ij}^6} \tag{2.4}$$

The Buckingham potential was introduced by Sir Buckingham in 1945 and its mathematical form is described in equation 2.4. Here A, B and C are parameters for each pair interaction type to be fitted. In principle, the Buckingham potential introduces improvements with respect to the Lennard-Jones IP also thanks to one more fitting parameter. Usually, the problem of the Buckingham potential is the divergence to $-\infty$ at the limit of zero interatomic distance. This is a well known short-range effect of this potential in which if two atoms get accidentally too close the attractive part dominates with respect to the repulsion part. This effect has to be taken into account, especially when building IPs for performing global optimization with methods in which atoms are randomly displaced as we will see in section 2.5.

2.2.4. Morse potential

$$V_{ij}^{Morse} = D_e \left[\left(1 - e^{(-a(r_{ij} - r_e)} \right)^2 - 1 \right] \tag{2.5}$$

The Morse potential (eq 2.5) is another analytic function to model pair interactions between atoms. This is the natural extension of the harmonic potential in which anharmonicity is taken into account. Here D_e is the well depth with respect to not-interacting systems, r_e is the equilibrium distance between atoms, and a is related to the force constant at the equilibrium point k_e as $a = \sqrt{k_e/2D_e}$. In principle, the Morse potential performs equally well or slightly better than the Buckingham potential. Since its natural description of anharmonicity it is employed to describe pair interaction affected by anharmonic contributions such as OH bonds.

2.3. Machine learning force fields

Within the last few decades, thanks to the increase of both the amount of data produced world-wide and increases in computer power, machine learning (ML) models have introduced new ways to predict, improve and better solve problems for a wide range of technological applications. Huge international efforts and investments have been made from private and public research institutes in order to develop algorithms able to learn to perform tasks from ”looking” into big databases. An example of such a success is Google DeepMind’s AlphsGo algorithm which mastered the game of Go. In such game, the number of possible strategic moves that a player can do is higher than the estimated number of atoms in the universe. It is therefore impossible for an algorithm to actuate strategies based on all possible opponent’s moves. It was thus believed that no algorithm could compete with human intuition, but surprisingly, in 2016, AlphaGo won 4-1 in a competition against the world n^{o} 1 ranked player. The performance of ML goes far beyond gaming applications. There are several applications in health care, computer vision, speech recognition, self driving cars etc.[27,28] Although the topic is very interesting, we will not discuss deeply the details

behind the broad range of ML techniques. Just as matter of classification, there are three different classes of ML depending on how the "learning" task takes place: supervised, unsupervised and reinforced learning. In the first case, the learning takes place by looking into "labeled" output set of data. Labeled data are nothing but data opportunely described as linked to a known output such as a picture with the relative description, atomic geometric configuration with its relative energy etc. By experience the algorithm should understand the underling rules that characterize data-label or input-output relation and it should apply those rules to describe new and unknown data. In the second case, to the learning algorithm is given a set of inputs and it has to figure out rules and relations occurring between the different data. Clustering a data set into sub-classes of similar objects is a typical example of such learning task. Finally, reinforced learning, represents a sort of intermediate learning between supervised and unsupervised.

As well as fundamental applications in quantum physics and quantum chemistry, ML has attracted the attention of several scientists for predicting material's properties[29], discovering new molecules or crystals[30,31], finding new reactions[32] etc. Our interest is using ML for fitting clusters PES by means of supervised models. For doing so, we consider an artificial neural network model (ANN) which acts as a ML force field able to calculate the energy given the molecular geometry. Similar approaches have been successfully applied for several materials[33]. In the next subsections we will see a bit more in detail what an ANN is and how we can train and use it as a force field.

2.3.1. Artificial Neural Network

The ANN is inspired by the biological structure of the brain, as the name suggests. The brain is composed of neurons and each neuron is connected to other neurons to form a complex network. Unlike a classic IP where the mathematical form is chosen in order to emulate a physical process or property such as the variation of energy with pair interatomic distances, an ANN model approach has different philosophy. From practical point of view, ANNs are models having usually a relatively high number

of parameters that are fitted to a set of data to statistically emulate their behaviors. The first ANN models appeared in the early 40s but no practical use was possible due to the lack of sufficiently powerful computers and difficulties in the training. Things changed in the 80s where an efficient training algorithm called *backpropagation* which was successfully applied to train ANNs for the first time. Since then, many advances have been made and this is still a "hot topic" research field in computational science and applied mathematics. In atomistic simulations, for the first time in 1995 an ANN was used to fit the DFT potential energy surface by Doren and coworkers[34]. To date many different types of ANN have been used for different purposes and generally it has been proven that they can represent multidimensional non-linear functions (i.e. such as the PES) with arbitrary precision. Two of the most critical steps in developing an ANN are the building of an appropriate training set and the choice of the input. Global optimization is a very convenient tool to generate highly heterogeneous database with a large number of different isomers. In Figure 2.3 there is a

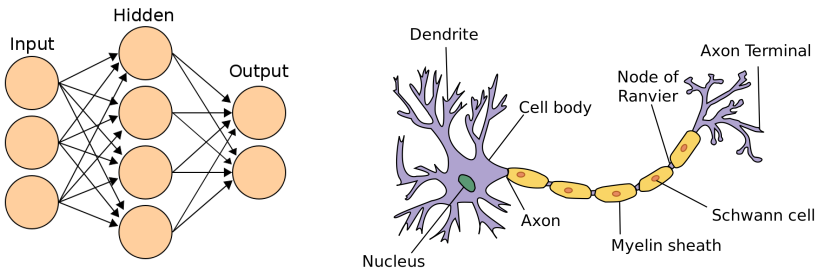

Figure 2.3: Simple artificial neural network model (on the left) as inspired by the biological neuron (on the right). Pictures are taken from wikipedia.

simple representation of an artificial neural network (ANN) and a biological neuron. The ANN can be seen as a graph network where nodes are neurons connected between them by edges. To each node is associated a function called an activation function while edges represent weights which determine how strong any two nodes are connected. Each node outcome is determined from the weighted outcomes of all the nodes of the previous layer through the activation function. The information flows, or is mapped, from the input to the output layer modulated by the weights and activation functions. These types of ANNs are also called *Feed-Forward Neural Networks*. More specifically, in Figure 2.4 we show an example of how ANN can be used

to determine the energy of a molecular system. Here, the input is the

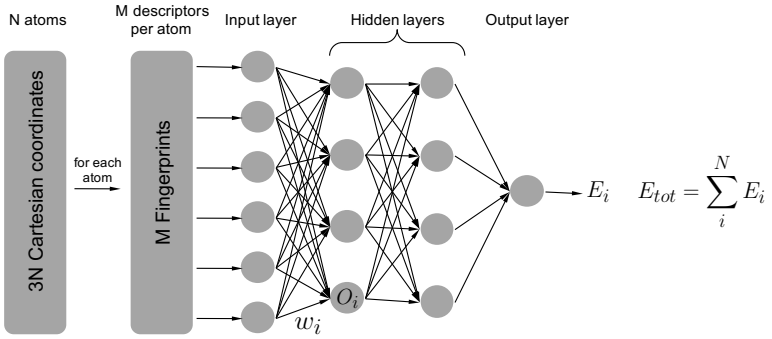

Figure 2.4: Schematic representation of the artificial neural network (ANN) used to calculate the energy of a system.

representation of the molecular geometry and the output is the energy. The Cartesian coordinates of the molecular geometry can not be used as input and must be transformed in an equivalent representation usually called descriptor or fingerprint. We will dedicated the next section on this topic because the choice of the descriptor can affect the performance of the ANN. In Figure 2.4, the outcome of each node can be defined as $O = f(x)$ where the argument $x = \sum_i \omega_i X_i$ where the ω_i are weights, X_i are the inputs to the node and $f(x)$ is the activation function. Weights are obtained during the "training" procedure in which the ANN "learns" to associate the energy to each of the input molecular geometries in the training database. Activation functions are characteristic to the neural network and are chosen according to the task the ANN is meant for. One of the simple activation functions is the binary step function where the outcome of the node will be 0 or 1 according to a threshold. In this case the neuron is called a *perceptron*. This type of activation function allows only a binary output. However, this type of activation function is not able to describe the smooth variation of the energy upon a geometrical change. Sigmoid functions $f(x) = \frac{1}{1+e^{-x}}$ or hyperbolic tangent functions $f(x) = tanh(x) = \frac{e^x - e^{-x}}{e^x + e^{-x}}$ are more suitable activation functions for our purposes since their outcome can smoothly vary upon a small geometry change.

2.3.2. Atomic coordinates representations

The ANN input is a very important choice since strongly affects the quality of the learning process. An appropriate input for atomic coordinates should be a rotationally and translationally invariant representation. The idea is to express the total energy of the system as a sum over all atomic contributions. The input representation should therefore take in account the local chemical environment of each atom. Note that in this case, the ANN cannot be trained to predict properties which depend on non-local interactions such as the materials band-gap. One of the commonly used representations in atomistic simulations is the *Behler-Parrinello* descriptor[35]. This representation captures the atomic local environment by using atom-centered symmetry functions. It is composed by two parts as shown in equations 2.6 and 2.7. The first part captures the radial interactions between atoms by using atom-centered gaussian functions with different width. For each atom there is a feature vector composed by a set of $\{G_i^I\}$ which acts as an unique signature of the interatomic distances with respect to all neighbors.

$$G_i^I = \sum_{j \neq i}^{N_{atoms}} e^{-\eta(R_{ij}-R_a)^2} f_c(R_{ij}) \tag{2.6}$$

Each of G_i^I is a sum of gaussian functions with width controlled by the η parameter. The sum runs over all neighbor atoms determines by the cutoff function f_c. This cutoff function ensures a smooth decay to zero of the pair interaction until reaching a cutoff radius R_c which typically is between 6 and 10 Å. R_a is the atomic center and R_{ij} is the interatomic distance between i-th and j-th atoms.

The second part, similarly to the fist one, capture the angular interaction of each atom with its neighbors. Here again, depending on the number of symmetry functions used, is possible to obtain a feature vector, $\{G_i^{II}\}$ that represents a fingerprint of angular interaction of each atom and all its neighbors.

$$G_i^{II} = 2^{1-\zeta} \sum_{j,k\neq i}^{all} (1 + \lambda cos\theta_{ijk})^{\zeta} e^{-\eta(R_{ij}^2+R_{ik}^2+R_{kj}^2)} f_c(R_{ij}) f_c(R_{ik}) f_c(R_{kj}) \quad (2.7)$$

G_i^{II} is a sum over cosine values of all possible angles and with η, ζ and $\lambda = \pm 1$ as parameters. Typically, a set of 20 symmetry functions (of the G^I and G^{II} type) per atomic species with different parameters are used in order to have a good description of the local chemical environment. These descriptors, jointly employed, account for many-body interactions and provide a fingerprint specific to the system geometry which is rotationally and translationally invariant.

2.3.3. The learning problem

Learning, or training, is the process by which an ANN is trained to associate to each of the molecular geometries in the training dataset the proper energy. In other words, we need to find the optimum set of ANN ω_i parameters that minimizes the error in determining the energy. In doing so, we need to have a dataset of several different geometrical configurations with known energy of the systems that we want to study. Afterwards it is important to split the entire available dataset in two parts in which one, will be dedicated to the actual training and the other, to the testing. The training and testing sets should be chosen randomly to avoid introducing bias in the training procedure. The training procedure consists in minimizing the loss function (eq. 2.8) which can be done either though local optimization (see 2.5.1) or global optimization methods (see 2.5.2), thanks to the backpropagation algorithm which is able to efficiently calculate gradients with respect to errors.

$$L = \sum_{i}^{n} \left(\frac{E_i^{target} - E_i^{ANN}}{i_{\,atoms}} \right)^2 \quad (2.8)$$

where E_i^{target} and E_i^{ANN} are respectively the target total energy (e.g.

DFT) and the ANN predicted total energy. The sum runs over all n isomers (sometimes also called images) of the training set. Backpropagation is a way to compute the derivatives of the loss functions with respect to the ANN weights. As in an IP fitting procedure we can have overfitting which strongly bias the ANN answer to the training set. Nevertheless, there are procedures to avoid overfitting such as the cross-validation method [36]. After the training, the ANN can be used to predict the energy of an unknown configuration.

2.4. Quantum mechanical methods

Quantum Mechanics (QM) theory was born in the late nineteenth century to firstly explain the interaction between atoms and molecules with light which was poorly described by the classical physics at that time. Since then, in the twentieth century, human society has seen one of its greatest scientific revolutions made by a gifted generation of scientists. To date, QM is essential to understand the behavior of atomic scale phenomena.

2.4.1. Wave function Theory

The wave function is a mathematical object, central in QM, that completely describes and characterizes a given system. It is a complex function of all particles with spatial and spin coordinates and time. Its square is real and is associated with the probability for a certain measurement result to be observed. The Schrödinger equation (eq. 2.9), in turn, is the fundamental equation in QM. It is a differential equation that describes the evolution over time of a specific wave function.

$$i\hbar\frac{\partial\Psi(\mathbf{r},t)}{\partial t} = \hat{H}\Psi(\mathbf{r},t), \tag{2.9}$$

$\hat{H}$ is the Hamiltonian operator associated with the total energy of the system. Ground state system properties can usually be described by a time-independent wave function (also called *stationary state wave functions*), there-

fore the Schrödinger equation can be written in the time-independent form (eq. 2.10).

$$\hat{H}\Psi(\mathbf{r}) = E\Psi(\mathbf{r}) \tag{2.10}$$

The non relativistic Hamiltonian which contains kinetic and potential energy terms can be written as follow:

$$\begin{aligned}\hat{H} &= \hat{T}_e + \hat{T}_N + \hat{V}_{eN} + \hat{V}_{ee} + \hat{V}_{NN} \\ &= -\sum_{i=1}^{N_e} \frac{\hbar}{2m_e}\nabla_i^2 - \sum_{i=1}^{N_N} \frac{\hbar}{2M_i}\nabla_i^2 - \sum_{i=1}^{N_e}\sum_{j=1}^{N_N} \frac{Z_j e^2}{4\pi\varepsilon_0} \frac{1}{\mid \mathbf{r}_i - \mathbf{R}_j \mid} \\ &+ \frac{1}{2}\sum_{i=1}^{N_e}\sum_{j\neq i} \frac{e^2}{4\pi\varepsilon_0} \frac{1}{\mid \mathbf{r}_i - \mathbf{r}_j \mid} + \frac{1}{2}\sum_{i=1}^{N_N}\sum_{j\neq i} \frac{Z_i Z_j e^2}{4\pi\varepsilon_0} \frac{1}{\mid \mathbf{R}_i - \mathbf{R}_j \mid}\end{aligned} \tag{2.11}$$

where $\hat{T}_e$ is the electronic kinetic energy operator, $\hat{T}_N$ is the nuclear kinetic energy operator, $\hat{V}_{eN}$ is the electron-nucleon electrostatic potential operator, $\hat{V}_{ee}$ is the electron-electron electrostatic potential operator and $\hat{V}_{NN}$ is the nucleus-nucleus electrostatic potential operator. Moreover, m_e and M are electron and nucleus mass, e and Z are electron and nucleus charge, ∇_i^2 is the Lagrangian operator, **r** and **R** are electron and nucleus position vectors. In the frame of the Born-Oppenheimer approximation, the nuclear kinetic energy term $\hat{T}_N$ can be neglected and $\hat{V}_{NN}$ becomes an external potential which depends only on the positions of nuclei (**R**). As result of doing this, the Schrödinger equation can be written as follows:

$$\hat{H}_{el}(\mathbf{r};\mathbf{R})\Psi(\mathbf{r};\mathbf{R}) = E_{el}(\mathbf{r};\mathbf{R})\Psi(\mathbf{r};\mathbf{R}) \tag{2.12}$$

The system energy becomes the electronic energy, E_{el}, and will depend in parametric way on the position of nuclei. E_{el}, as being a function of nuclear positions **R**, represents the PES.

There are several methods that solves the Schrödinger equation with different approximations. Describing such methods in detail is out of the scope of this thesis. Here we will limit ourselves to briefly introducing the Hartree-Fock method, its limitations and how such limitations are overcome with more accurate methods. Hartree-Fock is an historically important method that dates back to the late twenties. In this method the multi-body character of the wave function is simplified by a single Slater determinant of χ spin

orbitals. Such spin orbitals are normalized and orthogonal (*orthonormal*) spin orbitals being $\langle\chi_i|\chi_j\rangle = \delta_{ij}$ the orthogonality constrain and a prefactor being the normalization constraint that scales the electron density calculated from the Slater determinant to have N_e electrons. The total electronic Hartree-Fock energy can be determined according to the following equation:

$$E_{HF}^{SD} = \langle\Phi_{SD}|\hat{H}_{el}|\Phi_{SD}\rangle \tag{2.13}$$

where the *bra-ket* notation has been introduced. From practical point of view, this notation, introduced by Dirac in 1939, represents the scalar product between the terms inside the brackets. Since we are dealing with functions (i.e. orbitals, wave functions etc.) their scalar product is the integral over all variables space of their product. The explicit form of equation 2.13) can be written as:

$$E_{HF}^{SD} = \sum_{i}^{N_e} \langle\chi_i|\hat{h}|\chi_i\rangle + \frac{1}{2}\sum_{ij}^{N_e}\Big(\langle\chi_i\chi_i|\,\hat{g}\,|\chi_j\chi_j\rangle - \langle\chi_i\chi_j|\,\hat{g}\,|\chi_j\chi_i\rangle\Big) + V_{NN} \tag{2.14}$$

where $\hat{h}$ is the one-electron operator describing the i-th electron kinetic energy and its interaction with all the nuclei, and $\hat{g}$ is the two-electron operator defined as $\hat{g} = 1/|\mathbf{r}_i - \mathbf{r}_j|$ which describes the electronic repulsion. This energy depends on the molecular spin-orbital chosen which are still unknown. The choice of the molecular mathematical functions describing the spin-orbitals is crucial for the accuracy of the energy and properties. Usually molecular spin-orbitals are expanded by a set of functions called basis set or basis functions. Moreover, several computational quantum packages are specialized in different type of basis functions, therefore, we will describe these in more detail in section 2.4.3. Finding the appropriate spin orbitals relies on the *variational principle* which states that the energy of a trial and approximated wave function is always an upper bound of the true energy. Therefore, the χ_i that minimizes the E_{HF}^{SD} in equation 2.14 are obtained in the following way:

$$\hat{F}_i\chi_i = \epsilon_i\chi_i \tag{2.15}$$

where $\hat{F}$ is the Fock one-electron operator and ϵ_i is the energy associated with the χ_i molecular spin-orbital. Notice that in equation 2.15 the solution

will depend on the molecular spin-orbital χ, therefore this equation must be solved in an iterative way, also called *self consistence field* (SCF), and an initial guess for the spin-orbitals is needed. The Fock operator is, in turn, defined in terms of one and two electronic operators:

$$\hat{F}_i = \hat{h}_i + \sum_{j}^{N_e} (\hat{J}_j - \hat{K}_j) \tag{2.16}$$

Jj and Kj are respectively the Coulomb and exchange operator describing the interaction between i-th electron and the mean field of all the other electrons. J is equivalent to the classical repulsion of two negatively charged particles while K is purely a quantum mechanical effect and has no equivalent classical analogy. When the SCF convergence criteria are met, the total energy corresponds to the Hartree-Fock energy. In the Hartree-Fock method, because of the nature of the Slater determinant, each electron interacts with the mean field generated by all the other particles. In this picture, the instant correlation between each of the electron is neglected. We can therefore refer to the exact energy of the system as:

$$E_{exact} = E_{HF} + E_{correlation} \tag{2.17}$$

Although the correlation energy represents only 1% of the exact energy, it plays a very important role in describing chemically important phenomena. In order to recover the electron correlation there are more advanced methods, referred to as post Hartree-Fock methods. The general strategy is to represent the wave function as linear combination of Slater determinants relative to ground state and exited states electronic configurations. Methods that can be employed are either variational (i.e. Correlation Iteration methods such as CI, CISD, Coupled Cluster methods such as CCSD, etc.) or perturbative (i.e. Moller-Plesset methods such as MP2, MP4 etc.). The problem of such methods is that the more electron correlation is included the more the computational price will dramatically increases with the system size. Moreover, some of such advanced methods suffer of *size-consistency* problem which leads to a not correct dimer dissociation curves.

2.4.2. Density Functional Theory

Density Functional Theory (DFT) provides an alternative solution to a quantum mechanics problems. DFT is based on the idea that the system energy is a functional of its electron density and this is written as $E_{[\rho]}$. In this sense, the information included in such a complicated object as the wave function is redundant and all information needed to correctly describe the system is included in the its electron density. The electron density (ρ) can be observed experimentally (with X-ray experiments for instance), is always positive, is a 3-dimensional function, by integration gives the total number of electrons N_e, and has maxima which indicate the location and and type of nuclei present. The origins of DFT date back to 1927 with the Thomas-Fermi model in which authors were the first to express the total kinetic energy of a multi-electron system as a functional of the electron density. The DFT mathematical foundations and the Thomas-Fermi model generalization came only in the 50s with the two Hohenberg-Kohn theorems. The first theorem states that *the external potential V_{ext} is determined, to within an additive constant, uniquely by the electron density $\rho(\boldsymbol{r})$*. Since from electron density we can recover the number of electrons, nuclei types and positions, in principle the electron density determines the ground state wave function, and therefore all ground state system properties. We can thus express the total energy as:

$$E[\rho] = T[\rho] + V_{ee}[\rho] + \int V_{ext}(\mathbf{r})\rho(\mathbf{r})d\mathbf{r} \tag{2.18}$$

where $T[\rho]$ is the electron kinetic energy, $V_{ee}[\rho]$ the electron-electron interaction which in turn is determined from the classical Coulomb electrostatic repulsion plus non-classical terms and, finally, V_{ext} is the external potential. The second Hohenberg-Kohn theorem is analog to the variational theorem in the Wave Function Theory and states that *for a trial density $\tilde{\rho}(\boldsymbol{r})$, such as $\int \tilde{\rho}(\boldsymbol{r})d\boldsymbol{r} = N$ and $\tilde{\rho}(\boldsymbol{r}) \geq 0$ the energy functional evaluated at $\tilde{\rho}$, $E_{[\tilde{\rho}]}$, is never smaller than the ground state energy*. Originally, the main problem in DFT was to assign an explicit expression to the kinetic energy term. In this regard, several initial attempts were made but all of them gave poor results in chemistry. The breakthrough came with Kohn and Sham who suggested

to express the kinetic energy as the contribution of two terms, the first one which can be calculated exactly and the second as a correction to the first term. Although this solves the problem of the mathematical form of the kinetic energy functional, it loses the original DFT simplicity by including molecular spin-orbitals as in wave function theory. The Kohn-Sham DFT total energy is shown in equation 2.19.

$$E[\rho] = T_s[\rho] + E_H[\rho] + E_{xc}[\rho] + \int V_{ext}(\mathbf{r})\rho(\mathbf{r})d\mathbf{r} \tag{2.19}$$

where $T_s[\rho]$ is the kinetic calculated exactly from a Slater determinant, $E_H[\rho]$ is the Hartree energy and represent the classical Coulombic repulsion between electron densities which is defined as:

$$E_H[\rho] = \frac{1}{2}\int\int \frac{\rho(\mathbf{r})\rho(\mathbf{r}')}{\mid \mathbf{r} - \mathbf{r}' \mid} dr dr' \tag{2.20}$$

$E_{xc}[\rho]$ is called the exchange-correlation functional and contains the remaining of the exact kinetic energy and all the non-classical electron-electron interactions:

$$E_{xc}[\rho] = (T[\rho] - T_s[\rho]) + (E_{ee}[\rho] - E_H[\rho]) \tag{2.21}$$

Notice that no approximations have been made in equation 2.19, therefore we can consider it exact. Unfortunately, $E_{xc}[\rho]$ is not known and must be approximated. All the difficulty in DFT methods consists in defining the appropriate exchange-correlation functional. To date, many exchange-correlation functionals have been created and their accuracy depend on the type of approximation made. Different methods are categorized in *Jacob's ladder* which consists in families of approximations with increasing accuracy. Here, we will briefly describe a few classes of the most common approximation with their limitations.

The *Local Density Approximation* (LDA) is a method in which the $E_{xc}[\rho]$ is a functional of an uniform electron density. This approximation purely describe chemically interesting systems since an uniform electron density is far from the real one. Indeed, in an atomic and molecular system the electron density rapidly increases as getting closer to nuclei and vanishes far

from them. A natural improvement to the LDA is including the dependency on the gradient of electron density into the functional. These methods are called *Generalized Gradient Approximation* (GGA) and are widely used both in chemistry and material science community. One of the most used GGA functional, employed as well in this thesis, is the one developed by Perdew-Burke-Ernzerhof (PBE). Notoriously, both LDA and GGA methods fail to correctly predict band gaps of materials. Moreover, they lack of the self-interaction which is a spurious effect describing the interaction of each electron with it self. This effect has strong implications on the accuracy of such DFT methods affecting properties such as ionization potentials, electron affinity, etc. The self-interaction is propertly described in Hartree-Fock theory due to the exchange operator $\hat{K}_j$. A way to further improve GGA methods is therefore to include a fraction of exact Hartree-Fock exchange as proposed by Becke in 1993. This gives rise to a new class of methods called *Hybrid Functionals* and they can be expressed as:

$$E_{xc}^{Hyb}[\rho] = \alpha E_x^{HF} + (1-\alpha)E_x^{DFT}[\rho] + E_c^{DFT}[\rho] \tag{2.22}$$

where α is between 0 and 1 and controls the percentage of the exact Hartree-Fock exchange. $E_x^{DFT}[\rho]$ and $E_c^{DFT}[\rho]$ are respectively GGA or LDA exchange and correlation functional. Hybrid functionals greatly improve the accuracy of DFT methods but with a considerable additional computational price over GGA and LDA methods. Moreover, the optimum fraction of the exact exchange to be included depends on the specific property.

One of the most used hybrid functional is PBE0 which includes 25% of the Hartree-Fock exchange, whereas the exchange-correlation part is taken from PBE. An other very popular hybrid functional is the B3LYP (Becke, three-parameter, Lee-Yang-Parr) and it is defined as:

$$E_{xc}^{B3LYP}[\rho] = (1-a_0)E_x^{LDA} + a_0 E_x^{HF} + a_x E_x^{B88_x} + a_c E_c^{LYP88_c} + (1-a_c)E_c^{VWN80_c} \tag{2.23}$$

where the three parameters $a_0 = 0.2, a_x = 0.72, a_c = 0.81$ are obtained by fitting to experimental data. The three parameters control the percentage of the exact exchange and DFT exchange (B88 and LDA) and correlation (LYP88 and VWN80) functionals.

Nowadays, hybrid functionals are considered as standard methods and are widely used. Although improvements over GGA methods, hybrid functionals, as with the pure Hartree-Fock method, lack the correct description of dispersive interactions. Such dispersive interactions can be included by either using (semi)empirical formulas[37,38] which require little or any additional computational cost, or by including finer corrections through perturbation post Hartree-Fock methods which are computationally more expensive but also more accurate.

2.4.3. The basis set problem

In this section we will discuss how to represent molecular spin-orbitals introduced in previous sections. Molecular spin-orbitals are usually represented as the product of a spin function which can be α or β and an spatial part $\psi(\mathbf{r})$ which we will refer simply to orbital from now on. There are two different choices to explicitly express molecular orbitals: one through atomic orbitals in the frame of *Linear Combination of Atomic Orbitals* (LCAO) approximation and the other one using plane waves. The choice of the basis set is very important, can strongly affects the accuracy of the simulation and it is always specified together with the method used for each simulation. Under the LCAO approximation, each molecular orbital is expanded in terms of atom-centered basis functions as shown in equation 2.24

$$\psi_i = \sum_{\alpha}^{M_{basis}} c_{\alpha i}\phi_\alpha \tag{2.24}$$

where $c_{\alpha i}$ are coefficient of each atomic orbital ϕ_α. Notice that if the expansion is made with an infinite number of atomic orbitals the resulting molecular orbital would be exact. Atomic orbital functions can be expressed in terms of *Gaussian Type Orbitals* (GTOs), *Slater Type Orbitals* (STOs) or *Numeric Atomic Orbitals* (NAOs). STOs are derived from the resolution of the Schrödinger equation for the hydrogen atom which can be solved analytically. Such functions are sometimes called hydrogen-type and have the

following form:

$$\phi^{STO}_{\zeta,n,l,m}(r,\theta,\varphi) = NY_{l,m}(\theta,\varphi)r^{-1}e^{-\zeta r} \tag{2.25}$$

where N is a normalization prefactor, $Y_{l,m}$ are spherical harmonics functions and n, l, m, are, respectively, principal, azimuthal and magnetic quantum numbers. These functions represent very accurately the natural behavior of the wave function in close to and far from nuclear regions and relatively few of them are necessary in order to correctly describe each molecular orbital. Despite STO accuracy, the two-electron integrals can not be computed analytically. Thus, especially in previous years where the computational power was limited, STOs were not widely used except for semi-empirical methods where two-electron integrals were neglected. Contrarily to STOs, GTOs functions became more commonly used because two-electron integrals can be solved analytically. They have a gaussian mathematical form as suggested by the name and are shown in equation 2.26.

$$\phi^{GTO}_{\zeta,n,l,m}(r,\theta,\varphi) = NY_{l,m}(\theta,\varphi)r^{2n-2-l}e^{-\zeta r^2} \tag{2.26}$$

However, GTOs are less accurate than STOs in representing the wave function therefore a higher number of them is usually required for each molecular orbital. NAOs instead have the following form:

$$\phi^{NAO}_{n,l,m}(r,\theta,\varphi) = \frac{u(r)}{r}Y_{l,m}(\theta,\varphi) \tag{2.27}$$

where $u(r)$ represents the radial function. The advantage of NAO is that $u(r)$ is flexible to be any function and in practice is chosen to be a numeric and highly accurate solution of Schrödinger-like radial functions such as a free atom radial function confined by a cutoff potential. Moreover, in recent years, efficient numerical integration schemes have been developed such that two-electron integrals are relatively easy to evaluate. The accuracy of NAO is comparable to that of STO functions therefore also the number of basis functions per atom needed for a relatively good accuracy is similar.

In all cases the minimal basis set which is minimum number of atomic orbitals to host all electrons of neutral atoms, is not enough to assure good results. Such basis sets have to be expanded by increasing the number of

atomic orbitals. A common approach is to increase the number of valence orbitals in the so-called *split valence basis*. For instance, by doubling the valence orbitals we would have a *Double-ζ split valence* basis set, by tripling them, *Triple-ζ split valence* etc. It is possible to increase the flexibility of the basis functions by including atomic orbitals with higher angular momentum. In the case of NAO, since they are projected onto a grid, a further improvement can be also obtained by increasing the density of grid points representing each atomic orbital.

The second class of basis functions that can be employed are plane waves (PW). They consist of complex periodic functions with the general form is shown in equation 2.28. Because of the periodic nature of PWs, they are particularly suitable for describing solid state systems. Indeed, infinitely extended solid materials are modeled by using a unit cell with periodic boundary conditions (PBC). Gas-phase molecular systems can also be described but only if they are introduced in a sufficiently large 3-dimensional unit cell.

$$\begin{aligned} \phi^{PW}(x) &= Ae^{ikx} + Be^{-ikx} = A\cos(kx) + B\sin(kx) \\ E^{PW} &= \frac{1}{2}k^2 \end{aligned} \tag{2.28}$$

k is the wave vector and plays a similar role as the the exponent ζ in GTO functions. Notice that the higher k, the higher the degree of function oscillation, thus, it can also be considered as a frequency factor. The number of basis functions are determined only by the size of the box and the cutoff PW energy as shown in equation 2.28. In simulations with such basis functions, the core electrons are described by pseudopotentials while the valence electrons are described with PWs. The pseudopotential modifies the effective Coulomb potential and is constructed such that core states are eliminated and the valence electrons are described by pseudo-wave functions. The use of pseudopotentials it is justified from the fact that most of the chemistry phenomena involve the valence electrons. Moreover, core electrons are usually very complicated to describe with PWs since the system wave function has a high number of nodes. Consequently, a very large number of PWs is needed to describe such wave function regions.

2.5. Optimization methods

Optimization methods are techniques employed in many diverse fields such as mathematics, engineering, (bio)physics, (bio)chemistry etc. Generally speaking, optimization entails minimization or maximization of a cost or a fit function. In other words, optimization means finding stationary points (i.e. minima, maxima and/or saddle points) of a given function. When dealing with convex functions (such as $f(x) = x^2$), which have only one minimum, the optimization problem of finding its minimum can be solved in a *Polynomial* time (a P problem in computer science). When dealing with non-convex functions which may have more than one minimum, the optimization problem requires sampling and finding the set of minima and/or lowest minimum. Such problems can rapidly become very complex and such complexity is classified in computer science as solvable in *Non-deterministic Polynomial* time (NP problem). NP problems are considered to be difficult to solve with a deterministic Turing machine (i.e. conventional computers) which deals with one task at the time (i.e. function sampling and evaluation). In this section we will describe some of the local and the global optimization methods used in this thesis.

2.5.1. Local optimization

The majority of static atomistic simulations employ a local optimization technique to relax a system's geometrical coordinates. Global optimization methods are more sophisticated and rely on local optimization. The local optimization allows one to find the closest minimum in configurational space which corresponds to an equilibrium geometry. The PES is a non linear function and there are several iterative methods for its local optimization. Most commonly, geometry optimizations are performed with first and second order methods which require respectively the evaluation of the energy and gradient and energy, gradient and second order PES derivatives for a given geometrical configuration. The first order methods: *Steepest Descend* (SD) and *Conjugate Gradient* (CG) are widely used. These two methods rely on gradients which provide the direction of the configurational space with

lower energy. In the iteration process the new geometrical configuration is determined by the size step along the direction suggested by the gradient vector as shown in equation 2.29.

$$\mathbf{x}_{i+1} = -\mathbf{g}_i + \alpha_i * \mathbf{x}_i \tag{2.29}$$

The size step α is updated at each iteration and determines the convergence rate of the algorithm. These two algorithms are very simple and computationally cheap and can minimize the energy of systems far from the local minimum. However, the minimization can considerably slow down when approaching to the local minimum. Therefore they are mainly used as quick relaxation algorithms for systems with poor geometrical starting point before more advanced methods take over. One of the most commonly used of the more advance methods is the *Newton-Raphson* (NR). Here the PES $f(\mathbf{x})$ is expanded in a Taylor series around $\mathbf{x}_0$:

$$f(\mathbf{x}) = f(\mathbf{x}_0) + \mathbf{g}(\mathbf{x} - \mathbf{x}_0) + \frac{1}{2}\mathbf{H}(\mathbf{x} - \mathbf{x}_0)^2 + \dots \tag{2.30}$$

$\mathbf{g}$ is the first derivative around the equilibrium and $\mathbf{H}$ is the hessian matrix containing second derivatives with respect to positions. Requiring the first order derivative of $f(\mathbf{x})$ to be zero, as we are looking for the minimum stationary point, and with a bit of rearrangement of the equation 2.30, we obtain the following expression:

$$\Delta\mathbf{x} = (\mathbf{x} - \mathbf{x}_0) = -\mathbf{H}^{-1}\mathbf{g} \tag{2.31}$$

The step size $\Delta\mathbf{x}$ is determined by the projection of gradients onto the hessian eigenvalues. Different control schemes are applied to the step size in order to avoid very large steps when one of the hessian eigenvalues is close to zero. Notice that this method does not assure finding the PES minimum as it can also step towards a saddle point if no checks are done of the hessian eigenvalues. Specifically, only if all hessian eigenvalues are positive is there is a guarantee to be in a local minimum and, if one of the eigenvalues is negative, the system is in a saddle point. When the PES is approximated by an IP, it is possible to analytically define the hessian matrix but when the PES is directly computed with QM methods the $\mathbf{H}$ is estimated. At the first optimization step, $\mathbf{H}$ can be set to be a unitary matrix and thus it is

equivalent to make a SD step. Afterwards, having the gradient of previous steps allows one to better estimate the hessian matrix. One of the most common scheme for updating the hessian matrix is the *Broyden-Fletcher-Goldfarb-Shanno* (BFGS). NR method is considered very robust for finding local minima and it requires very few optimization steps but only if the initial geometry is relatively close to the optimal configuration. Using an estimated hessian matrix instead of the exact one, the method is labeled as *pseudo Newton-Raphson* when updated hessian matrix is used.

2.5.2. Global optimization

In computational (bio)chemistry and (bio)physics Global Optimization (GO) techniques are applied in order to explore the PES of biomolecules, clusters surfaces and solid state systems. Thermodynamic properties of a given system will depend on occupied configurational isomers according to a Boltzmann distribution and therefore is fundamental for identifying those isomers. Exploring the PES can also lead to the discover and prediction of new stable and possibly synthesizable materials. GO algorithms are dived into deterministic and probabilistic methods. Deterministic methods such the brute force grid search allow to explore the entire configurational space and therefore to certainly find the global minimum. However, such techniques are limited to system with very low degrees of freedom. Usually, the dimensionality is generally quite high (i.e. 3N-6 degrees of freedom where N is the number of atoms) and the number of possible isomers can rapidly diverge with increasing number of atoms. In such a situation only probabilistic methods are practically employable and there is no mathematical certainty to find the global minimum.

Some of the most important probabilistic methods are *Monte Carlo* techniques which provide numerical solutions to mathematical problems and rely on the random sampling. Application of such methods is spread over several disciplines such as in maths, engineering, finance, physical and chemical sciences, etc. In physics/chemistry there are many applications of such methods such as Monte Carlo molecular modeling (which is a sort of alternative to molecular dynamics), Quantum Monte Carlo to solve the

many-body problem in QM, kinetic Monte Carlo to study the time evolution of a system with many possible pathways, etc. Here, we will only discuss how Monte Carlo is used in structure prediction in the so-called *Monte Carlo basin-hopping* (MCBH) method. Within MCBH, the geometry is randomly distorted and subsequently locally optimized in a iterative way.

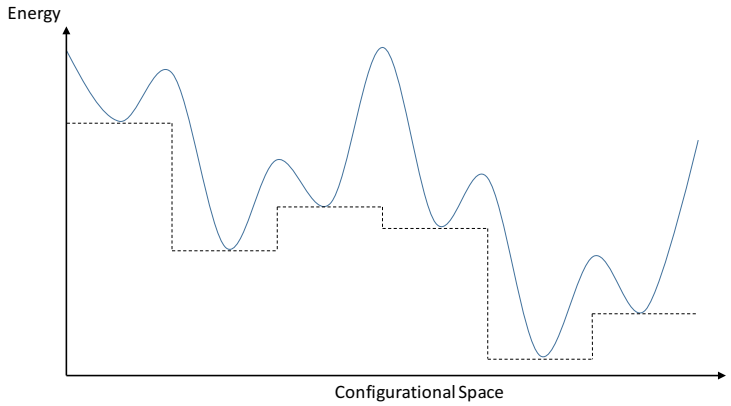

Figure 2.5: One dimensional projection of the 3N-6 configurational space. Monte Carlo basin-hopping allows to jump from one basin to the next one while exploring the PES.

In Figure 2.5 we show a schematic representation of a hypothetical 1-dimensional PES. The idea of MCBH is to overcome barriers and explore different PES regions by random distortions of systems coordinates. During the simulation, if the jump takes the system to a more stable configurations it is always accepted, otherwise there is a probability to accept the new configuration according to the energy difference and the simulation temperature. Typically, the number of iterations ranges from few tens of thousands to hundreds of thousands or millions depending on system degrees of freedom. At each cycle, a decision on whether to accept or refuse the new optimized structure is taken according to the probabilistic Metropolis criteria (eq 2.32).

$$accept: \begin{cases} \Delta E > 0,\ e^{-\frac{\Delta_E}{k_B T}} > r^{[0,1]} \\ \Delta E < 0 \end{cases} \tag{2.32}$$

where $r^{[0,1]}$ is a uniformly distributed random number between a 0 to 1 interval, ΔE is the energy difference jump between the actual and the most recently locally optimized configuration, k_B is the Boltzmann constant and

the T is a fictitious temperature. Here, the temperature has no physical meaning and it is only a simulation parameter. When the step is not accepted the process restarts from the random distortion of the last accepted configuration. At the end of the simulation all accepted configurations are ranked by energy and a certain number of them is written to a file and/or post-processed. The energy can be evaluated in principle both classically and quantum mechanically. However, quantum mechanical energy evaluation is relatively expensive and in practice is affordable for only for very small systems (for instance less than 10 atoms depending on computational resources available). Moreover, the local optimization procedure right after the random distortion could be particularly difficult due to SCF convergence problems. In the majority of cases the energy and the local optimization is done with an IP in the IP-based MCBH method. Notice that in equation 2.32, the higher the energy difference the lower the probability to accept the new structure. However, the probability to accept higher energy configurations increases if the temperature is high enough. This allows one to explore and sample the several minima inside a basin and to jump into nearby basins. A typical problem in MCBH is to get trapped in a very deep low energy minimum during the simulation avoiding further PES search. To resolve such problem, there are improved MCBH schemes where the temperature is self adapted in order to have a constant accept ratio. In such schemes, when the acceptance ratio is lower than a certain value (typically 0.5-0.7 within 100 steps) the temperature is increased accordingly in order to increase the probability of accepting a new structure, and *vice versa*, if the acceptance ratio increases too much. The geometrical distortion is provided by random moves of atomic coordinates with a maximum displacement of about 80% of the average bond length in the system. The quality of the IP heavily affects the accuracy of the GO simulation by introducing biases in the configurational space and in the energy ordering of accepted structures. To compensate for these biases, a certain number of low lying energy structures are relaxed with more accurate methods at the end of each simulation. Multicascade local optimizations schemes with increasingly accurate methods are also possible either during and/or after the MCBH simulation. As already mentioned, with probabilistic methods it is not possible to certainty find the global minimum. In practice, several simulations are done with different starting structures. If at the end of each simulation the set of energetically

low lying structures is very similar, the global optimization simulation is considered over and we strictly refer to the most stable configuration as the global minimum candidate. MCBH limits are mainly the structural bias when and IP is used, and the system size. The number of minima increases exponentially upon the increase of the system size. As such, a higher number of iterations is needed and the energy evaluation at each step is more energetically costly with increased system size.

Genetic algorithms (GA), belonging to a larger class of *Evolutionary algorithms*, are another common global optimization method. They are not utilized in this thesis but due to their importance we will briefly describe here the general underlying concept. Such methods are inspired from biological species evolution: there is a population of parents that by crossover and mutations generate children which, after a natural selection, become new parents, and so on. Only individuals possessing genetic features that adapt the best to their environmental conditions are propagated. From a computational point of view, the initial parental populations are randomly generated and the structures are allowed to "procreate" with probability according to their energetic stability. The procreation consists in structural features/motifs taken from both parents and with random mutations to create "child" structures. In each cycle, the most stable locally optimized structures are selected typically according to a Darwinian "survival of the fittest" principle and only those fitter structures are allowed to procreate for the next generation. After a certain number of generations only energetically low lying structures "survive". All unique structures that are allowed to procreate are conserved and at the end, a set of energetically low lying configurations are obtained. Different GA variants can be selected according to the crossover process, population size, mutation rate, surviving rate etc. The computational cost may limit the number of structures within the population to be generated and the number of generations to evolve which might limit the search.

Our choice of MCBH for global optimization mirrors the expertise in our research group and due to the fact that it has been shown to be very effective for cluster systems (e.g. it is efficiently capable in finding global minima of Lennard-Jones clusters up to 110 atoms.[39]). We note that there are several other global optimization methods such as *Simulated Annealing*,

Diffusion Methods, *Distance Geometry* etc. but to describe them all would be out of the scope of this thesis.

2.6. *Ab initio* statistical thermodynamics

In this section we will briefly describe how to calculate some thermodynamical properties of macroscopic systems. For this, statistical thermodynamics acts as bridge between atomic scale properties which can be computed from first principles and macroscopic classical thermodynamics. For such calculations, Gibbs introduced the concept of a statistical ensemble of a very large number of identical and non interacting molecules or microstates that can be in different accessible energetic states. The observed thermodynamical properties are the result of average behavior of a large number of molecules. Classical thermodynamic properties are therefore extracted by statistical analysis from molecular properties. There are several type of ensembles and here we will describe one of the most common which is also used in this thesis; the canonical ensemble.

2.6.1. The canonical ensemble

The canonical ensemble describes thermodynamical properties of a collection of large N molecules/particles in a fixed volume V and in thermal equilibrium with an environment (heat bath) that has constant temperature T. The equilibrium state of such ensemble displays minimum Helmholtz free energy and the energy probability density follows the Boltzmann distribution. The ensemble partition function $Q(V,T)$ is as key quantity from which all thermodynamic properties can be derived. $Q(V,T)$ can be described in terms of non-interacting indistinguishable molecular partition functions $q(V,T)$ as shown in equation 2.33.

$$Q(V,T) = \frac{[q(V,T)]^N}{N!} \tag{2.33}$$

The molecular partition function gives an indication of the number of molecular states that are thermally accessible at the temperature T. The partition function of a given molecule can be factorized in terms of translations, vibrations, rotations and electronic contributions as show in equation 2.34. This can be done assuming no coupling between these different contributions.

$$q(V,T) = q(V,T)_t \; q(T)_v \; q(T)_r \; q(T)_e \tag{2.34}$$

Notice that here other terms may be also considered such as spin multiplicity for systems possessing open shell electronic configurations. Under some assumptions, all terms in equation 2.34 have an explicit mathematical form and can be derived from first principles.

$$\begin{aligned} q_t &= \left(\frac{2\pi m k_B T}{h^2}\right)^{-\frac{3}{2}} V \\ q_v &= \prod_i \frac{e^{(-\frac{\Theta_{v,i}}{2T})}}{1 - e^{(-\frac{\Theta_{v,i}}{T})}} \\ q_r &= \frac{\sqrt{\pi}}{\sigma}\left(\frac{T^{\frac{3}{2}}}{(\Theta_{r,x}\,\Theta_{r,y}\,\Theta_{r,z})^{\frac{1}{2}}}\right) \\ q_e &= \omega_0 \; e^{-\varepsilon_0/k_B T} \end{aligned} \tag{2.35}$$

where m is the total mass of the molecule, $\Theta_{v,i} = h\nu_i/k_B$ are vibrational temperatures for the frequency of i-th normal mode under the harmonic oscillator approximation, $\Theta_{r,x,y,z} = h^2/8\pi^2 I_{x,y,z} k_B$ are rotational temperatures for a non linear molecule under the rigid rotor approximation as function of inertia moments $I_{x,y,z,}$ along the three reference axes, σ is the symmetry number and represent the number of indistinguishable orientation and q_e is the ground state electronic partition function with ω_0 degeneracy assuming electronic exited states thermally inaccessible. q_r can have the closed form shown in equation 2.35 only if Θ_r/T is relatively small (i.e. on the order of 10^{-1} or less). However, for most of the molecules at ambient temperatures this condition is satisfied. Notice that everything can be derived from first principles: m is known, $I_{x,y,z,}$ depends only from the system geometry, the set of $\{\nu_i\}$ normal modes can be derived from frequency calculations assuming harmonic approximation. Moreover, harmonic frequency calculations allows one to compute the IR-spectrum of the system which it self is directly

comparable with experimental one. Once all contributions to molecular partitions are calculated, all thermodynamic state functions such as Helmholtz and Gibbs free energy, internal energy and entropy can be derived. For instance, practically, the Helmholtz free energy, which is the potential that is minimum at the equilibrium conditions for the canonical ensemble, can be defined as follow:

$$\begin{aligned} F(V,T) &= -RT\ln(q(V,T)) \\ F(V,T) &= -\frac{3}{2}RT\ln\left(\frac{2\pi m k_B T}{h^2}\right) - RT\ln(V) \\ &\quad + \sum_i \left[R\frac{\Theta_{v,i}}{2} + RT\ln\left(1 - e^{(-\frac{\Theta_{v,i}}{T})}\right)\right] \\ &\quad - \frac{1}{2}RT\ln\left(\frac{\pi}{\Theta_{r,x}\,\Theta_{r,y}\,\Theta_{r,z}}\right) - \frac{3}{2}RT\ln(T) + RT\ln(\sigma) \end{aligned} \tag{2.36}$$

considering an Avogadro number N_A of molecules and being the gas constant $R = N_A k_B$. The equation 2.36 is nothing but the thermal corrections and *Zero Point Energy* (ZPE) correction to electronic energy of the system that can be calculated for instance with DFT. Such corrections allow to calculate energies and free energies of a system at specific temperatures which, in turn, allows to better compare with experimental observations. With similar equations it is possible to derive other thermodynamic quantities. Notice that the term V in equation 2.36 and 2.35 is the reference ensemble volume and it is unknown but in some situations can be estimated or even neglected. For instance, when considering a chemical reaction which occurs without volume change, the term V cancels out when taking the difference between products and reactants. When considering a gaseous species (G) in equilibrium with a substrate (S) it is possible to calculate the reaction Gibbs free energy ΔG as shown in equation 2.37

$$\begin{aligned} S + G &\leftrightarrows SG \\ \Delta G(P,T) &= F_{SG}(T) - F_S(T) - \mu_G(P,T) \end{aligned} \tag{2.37}$$

Here the gas chemical potential μ_G is calculated from equation 2.36 where the V is expressed in terms of the pressure P according to the ideal gas law. The equation 2.37 allows one to determine the theoretical reaction Gibbs free energies for a wide temperatures and pressures.

2.7. Computational and visualization packages

During the entire PhD thesis, FHI-AIMS[40] (*Fritz Haber Institute ab initio molecular simulations*) was the main quantum package employed. It is an all-electron full-potential code that uses atom-centered NAO. It supports semilocal and hybrid DFT and many body perturbation theory calculations. It can be used for gas-phase, surface and bulk types of system. It is particularly efficient for gas-phase calculations and scales very well with the number of computational cores (up to thousands of cores). In few cases, other quantum computational packages have also been used such as GAUSSIAN[41], VASP[42] and SIESTA[43]. For the global optimization simulation, we initially employed an in-house modified version of GMIN[39] developed in the group of Prof. D.J. Wales. The modification has been previously done in our research group and implements the Buckingham potential with relative analytic derivatives, introduction of atoms type and the "swap cation/anion" function. Subsequently we have created our own version of global optimization code written in Python and using mostly *Atomic Simulation Environments* (ASE)[44] set of libraries interfaced with the *General Utility Lattice Program* (GULP)[45] for the structure local optimization. For calculations with the ANN we employed the *Atomistic Machine-Learning Package* (AMP)[46]. Finally several visualization tools have been used such as GDIS[47], VMD[48], MOLDRAW[49] and VESTA[50] for structure visualization and manipulation.

2.8. Computational tools used in this thesis

In this section we give an overview on where the theoretical methods described in this chapter are applied in this thesis. An IP-based MCBH global optimization method has been used to find most stable cluster structures in all the projects presented in the remaining chapters. We use mainly the Buckingham potential IP to represent the cation-anion interactions. However, the Morse potential is also used to describe the OH interaction in hydroxylated systems. All IPs used are attached in the Appendix at the end of the thesis. After the global optimization procedure, a set of isomers are fully relaxed

at DFT level of theory employing firstly with PBE light/tier1 settings and secondly, a selection of them, at PBE0 tight/tier1 level. The results presented in each chapter are the outcome of fully relaxed structures with the hybrid PBE0 functional (in very few cases with B3LYP) with a tight/tier1 NAO basis set in most of cases. In chapter 3 and 6, we also perform frequency calculations in order to extract thermodynamic quantities and obtain calculated IR-spectra. In the first case we employed the Gaussian09 package using the Ahlrichs triple-ζ plus polarization basis functions (TZPV)[51] on all atoms, while in the second case we employed FHI-AIMS with PBE0 functional with a tight/tier1 NAO basis set. Further information will be given in each specific chapter.

Chapter 3

Titanosilicates mixing

In this chapter we present the structural and energetic properties of mixed titanosilicates at the nanoscale as compared with those at bulk scale. The nanoscale energetic of mixing is found to be profoundly different from the bulk one and is mainly driven by defective centers naturally present in the nanoclusters. The results presented in this chapter have been published and the full paper is included at the end of the thesis. Moreover, we also present preliminary results of an ongoing project about the chemical reducibility of selected nanoclusters.

A. Cuko, M. Calatayud, S. Bromley, "Stability of mixed-oxide titanosilicates: dependency on size and composition from nanocluster to bulk", *Nanoscale*, 2018, **10**, 832.

3.1. Introduction

Oxides based on mixing titania (TiO_2) and silica (SiO_2), titanosilicates, represent an important class of materials which are widely studied and used for many technologically and environmentally friendly applications such as solar cells, self cleaning systems, gas sensors, selective molecular sieves, material for removing water pollutants and photocatalysts for many reactions [52–57]. In these applications, titanosilicates not only take advantage

of the properties of pure titania (i.e. a photoactive semiconductor) and silica (i.e. high thermal stability and high mechanical strength) but also from the synergystic properties which emerge from their TiO_2-SiO_2 interaction (e.g. formation of new catalytic sites). As an example, one of the most industrially important mixed TiO_2-SiO_2 materials, known from early 80s, is the synthetic titanosilicate-1 (TS-1)[58]. It is used as industrial redox catalyst for oxidizing organic molecules under mild conditions with the presence of hydrogen peroxide. The active site is an isolated 4-fold titanium uniformly dispersed in a porous silica structure with 1.0-2.5% of TiO_2 molar inclusion. In such systems, increasing the amount of TiO_2 content leads to titania segregation; a phase separation that indicates the metastability of mixed titanosilicates. Despite the great industrial success of such materials, very little is known about their behavior, particularly concerning their mixing at the nanoscale.

In this chapter we show that, unlike in bulk materials, the mixing of the two materials is energetically favorable at the (sub)nanoscale. We analyze the structural features to better understand the driving force behind the mixing, and we characterize mixed titanosilicate nanocluster from a physico-chemical point of view. Finally, we provide spectroscopic (IT spectra) and structural (average coordination number) information that might help experimentalists to characterize them.

3.2. Methodology

In a first step we focus on finding the most stable structures of titanosilicates that will serve to study their structural and thermodynamic properties. We investigate the following sets of systems:

i) crystalline bulk, based on existing systems reported in databases. In particular, we consider few titanosilcates as shown in Figure 3.1. The choice of such small set of crystalline structures is justified by the fact that bulk macroscopic mixing is known to be thermodynamically unfavourable.
ii) (sub)nanoparticles, starting from previously reported pure $(SiO_2)_n$ [59–62] and pure $(TiO_2)_n$ [63,64] globally optimized. The pure and mixed titanosil-

icates $(Ti_xSi1-_xO2)_n$ have system size $n = 2 - 10, 12, 14, 16$ and 24, and mixing compositions of titania molar fractions $x = 0 - 1$.

To obtain the structures, we employ the IP-based MCBH global optimization method with in-house customisations, such as the cation Ti/Si swaps and the self adapted accept ratio. We used two different IPs in order to better sample the PES and reduce the bias on the empirical potential. Then the lowest-energy isomers are selected and their structure and energy refined using DFT calculated at a PBE0 tight/tier1 level of theory. For more detail see section 2.5.2 of the chapter 2, and the publication. Both IPs are reported in the Table A1 of the Appendix. The Cartesian coordinates for the entire set of structures can be also found in the NOMAD repository.

In a second step, we characterize the stability of the most stable nanotitanosilicates found. The mixing energy of titanosiliacte system can be obtained from the following equation:

$$\Delta E_{mix} = E_{(\mathrm{Ti}_x\mathrm{Si1}-_x\mathrm{O2})_n} - [(1\text{-x})E_{(\mathrm{SiO2})_n} + \mathrm{x}E_{(\mathrm{TiO2})_n}] \tag{3.1}$$

where $E_{(\mathrm{SiO2})_n}$, $\mathrm{x}E_{(\mathrm{TiO2})_n}$ and $E_{(\mathrm{Ti}_x\mathrm{Si1}-_x\mathrm{O2})_n}$ are electronic energies (as first estimate of ΔE_{mix}) of respectively pure silica, pure titania and titanosilicates. Notice that for nanocluster systems n denotes the effective system size while for bulk systems n is the number of oxide units in the unit cell as the system is infinitely extended. In order to check the stability of the mixed structures with the temperature we calculated free energies as determined through *ab initio* statistical thermodynamics (see section 2.6 of the chapter 2).

In a third step we provide measurable data for a better link with experiments: we performed frequency calculations under the harmonic approximation for a set of nanoclusters employing the Gaussian09 package using the Ahlrichs triple-ζ plus polarization basis functions (TZPV)[51] on all atoms.

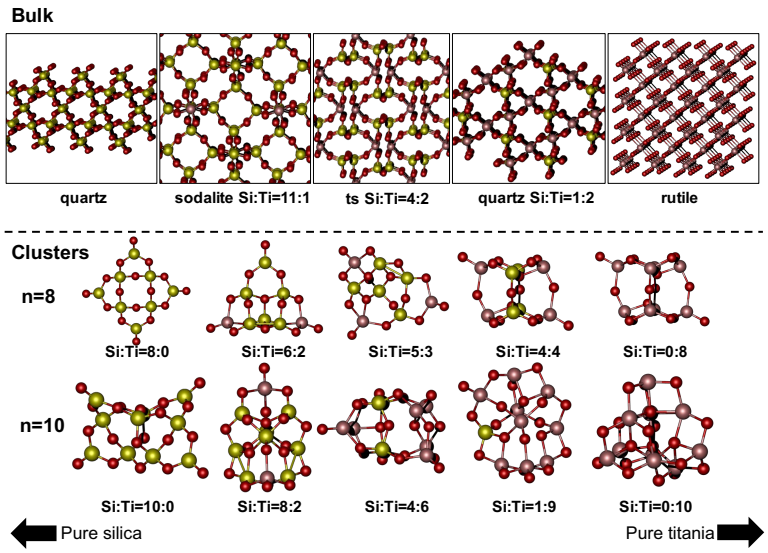

Figure 3.1: On the top side, bulk crystalline structures of pure silica (quartz), titanosilicates and pure titania (rutile) considered here. The **ts Si:Ti=4:2** it is referred to a structure found in Materials Project database (ID: mp-766596). On the bottom side some examples of globally optimized titanosilicates and the pure components for systems with size $n = 8$ and 10.

3.3. Results and Discussions

3.3.1. Structure and stability of mixed titanosilicates

In Figure 3.1 there is an example of the type of structures obtained from the basin hopping search. Silica nanoparticles are found to be very different from titania ones: the former tend to be quite symmetric and open while the latter tend to be compact and with low symmetry.

Titanosilicates are found to be very often structurally different from both pure components even if their cation coordination environments is similar. Terminal oxygen play a very important role for such nanoclusters and they are found to be of two different types: (i) three coordinated silicon "double-bonde. Si=O, but arguably more accurately: $Si^{+}-O^{-}$) and (ii) terminal oxygen atoms bonded to 4-coordinated cation also known as Non Bridging Oxygens (NBOs). In the most stable mixed systems, when possible, silicon atoms tend to avoid bonding with defective oxygens. In Figure

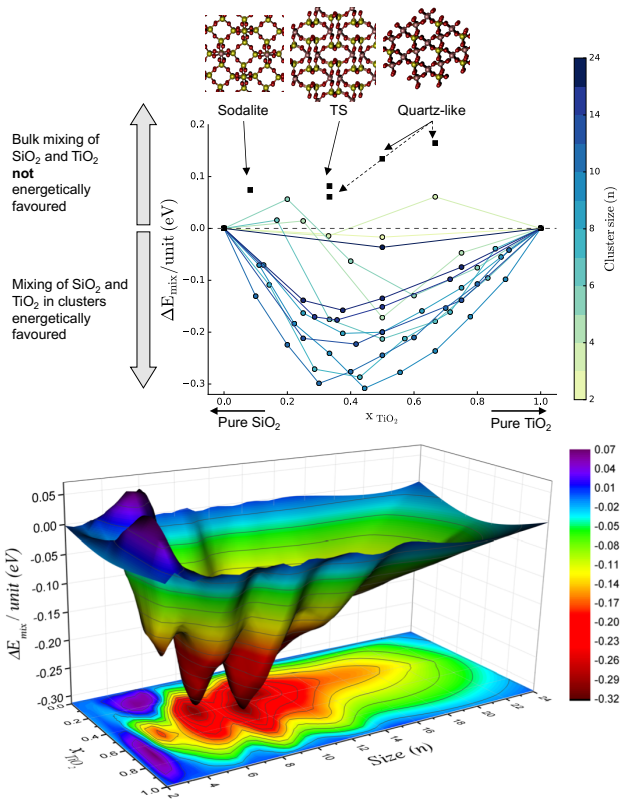

Figure 3.2: Top side: mixing energy per formula unit (eV) versus the TiO_2 molar fraction. The black filled squares denote the mixing energy of the bulk periodic structures. The filled colored circles denote the mixing energy of the globally optimized nanoclusters. The color bar ranging from light green to dark blue represents different system size repectivelly from the smallest ($n = 2$) to the largest ($n = 24$). Bottom side: 3-dimensional plot of the nanoclusters mixing energy emphasizing the size dependent mixing favourability. All numerical values of total and mixing energies of these graphs are reported in the Tables A2 and A3 of the Appendix.

3.2 we plot the ΔE_{mix}/units for all titanosilicates considered in this work. Consistently, with experimental observations, silica and titania bulk mixing is thermodynamically unfavorable since the mixing energy is in all cases positive. However, at the nanoscale their mixing is thermodynamically favorable for almost all nanoclusters for the full range of compositions. Only few small systems show near-zero or slghtly positive mixing energies. For a better visualization of the size dependency of mixing energies we also plot the a 3D solid surface as a function of x_{TiO_2} and the system size (n) interpolated from the discrete set of nanoclusters mixing energy values. The thermodynamic favourability is maximum for systems with size $n = 9, 10$ with mixing composition between 30, 44% Ti and it progressively reduces with the system size approaching nearly zero for $n = 24$.

The stability of titanosilicates nanoclusters with respect to pure counterparts oxides is driven by the competition of several electronic and structural features. One of the main factors favouring the mixing is the presence of dangling oxygens, that when bonded to Ti atoms (i.e. Ti-NBO species) are less destabilizing than when bonded to Si atoms due to the higher ionicity of the Ti-O bond. Pure silica nanoclusters heal their defective terminal oxygens by mixing with titania. Other factors such as the tetrahedral distortion of SiO_4 groups and different the cation-oxygen bond strength (i.e. Ti-O bond dissociation energy is 666.5±5.6 kJ/mol^{-1} while that of Si-O is 799.6±13.4 kJ/mol^{-1}) play a minor role, in the energetics of mixing.

3.3.2. Signatures of mixing

Since our predicted nano-titanosilicate structures have never been synthesized before, and in order to help their experimental characterization, we report the calculated infrared (IR) harmonic vibrational frequencies spectra for pure silica (Figure 3.3a), pure titania (Figure 3.3c) as compared with mixed titanosilicate clusters with $x = 0.5$ mixing composition (Figure 3.3b). These are collective IR spectra of a set of clusters with size $n = 2 - 16$ units (even numbers) whose intensities are normalized by the system size n such that all nanoclusters have about the same signal intensity. The main feature found is the presence of two unique, distinct and highly intense peaks for

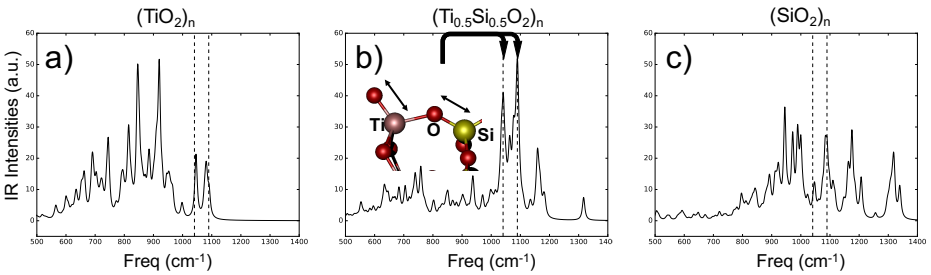

Figure 3.3: Calculated infrared (IR) harmonic vibrational frequencies (in cm^{-1}) of pure titania (a), titanosilicate (b) and silica (c) nanoclusters obtained by summing size-scaled IR spectra for nanocluster sizes n (for $n = 2, 4, 6, 8, 10, 12, 14$ and 16 units). In (b) the anti-symmetric normal mode coupling between Ti-NBO and the vicinal Si-O is shown relative to the most intense peaks.

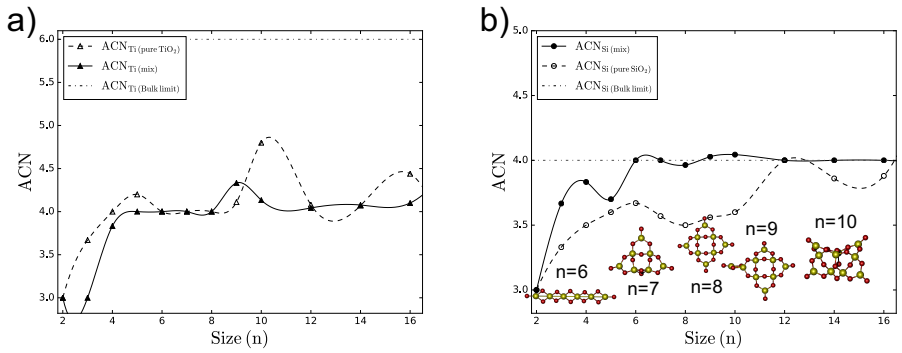

Figure 3.4: Average cation coordination numbers (ACN) for: (a) titanium centers in pure TiO_2 (dashed line) and mixed titanosilicate (solid line) nanoclusters; (b) for silicon centers in pure SiO_2 (dashed line) and mixed titanosilicate (solid line) nanoclusters. All coordination numbers are taken by counting oxygens within a maximum cut-off distance of 2.2 Å from each Ti or Si center.

titanosilicate systems (at 1035 and 1090 cm^{-1} indicated with vertical dashed lines in Figure 3.3). These peaks originate from the anti-symmetric stretching of the Ti-NBO and the vicinal Si-O. They are also present in pure systems but with much lower intensity in the case of pure TiO_2 and they are not distinct in the case of pure SiO_2.

Another property that could be detected experimentally is the average Si and Ti coordination numbers. The coordination environment can be investigated by X-Ray techniques such as EXAFS spectroscopy. The Figure 3.4 shows the average coordination numbers (ACN)s of Ti (a) and Si (b) atoms in nanoclusters as a function of the system size. Both values of the

pure (dashed lines) and the mixed (solid lines) are reported. Moreover, the values of corresponding ACN at bulk macroscopic level are also reported in dashdotted line. The main feature to highlight here is the fact that the silicon ACN in pure silica nanoclusters is persistently lower than in mixed titanosilicates for nearly all sizes. In other words Si atoms take advantage of mixing with titania in order to reach the ideal bulk coordination number of 4. Thus, for a range of sizes, the silicon ACN could be used as sign of the presence of mixed titanosilicates. For Si atoms, reaching the ideal ACN bulk value of 4 at smaller sizes in titanosilicates than in pure silica can be seen as one of the driving forces for mixing in such nanoclusters.

3.4. Chemical reactivity of Titania, Silica and Titanosilicate nanoparticles

The aim of the previous project was to find the most stable titania, silica and titanosilicates nanoparticles and to study their structural, energetic and size-dependent properties. In this section, we will give an overview of our research on the chemical properties of such systems. More specifically we explore the chemical reducibility of nanoparticles in order to predict their possible reactivity towards reducing agents as a way to characterize their redox behavior. Many of the systems predicted here to be stable (especially titanosilicates), have never been synthesized and characterized before to best of our knowledge. Therefore, we hope to elucidate their reactivity from theoretical investigations.

From the chemical point of view, the reducibility of an element is its tendency to acquire electrons and to reduce its formal oxidation number. For instance, in ordinary oxide materials Ti atoms have a +IV formal charge and the corresponding electronic configuration of Argon (i.e. $1s^2 2s^2 2p^6 3s^2 3p^6$). Since $4s$ and $3d$ orbitals are energetically accessible, Ti atoms can take one electron from the environment to become +III. This affects, for instance, the macroscopic optical properties of the system, transforming rutile crystals from white into colored minerals depending on either the presence of Ti^{3+} or the presence of dopant species. Moreover, this can be further confirmed from experimental techniques sensitive to unpaired electrons such as Elec-

tronic Paramagnetic Resonance (EPR) since Ti^{3+} has a radical nature. As an opposite tendency example, magnesia (MgO) is considered not reducible since Mg^{2+} atoms hardly reduce their formal oxidation number. Mg^{2+} has the electronic configuration of Neon (i.e. $1s^2 2s^2 2p^6$) and $3s$ orbitals are not energetically easily accessible and thus it does not tend to acquire electrons. If forcing the bulk magnesia reduction, electrons will be stabilized from the lattice Madelung field forming the so called F-centers (i.e. localized electrons in the crystal lattice)[65–68]. Two of the most common ways to study material reducibility are based on: (i) creation of oxygen vacancy defects in the system, and (ii) upon hydrogenation reaction where H_2 is the reducing agent. In these two cases, reducible oxides are expected to exhibit cations whose oxidation state is reduced, in the case of titanium two sites Ti^{3+} per O-vacancy. On the contrary, irreducible materials would exhibit electrons stabilized in F-centers in bulk or surfaces[65], or hydride species[69,70]

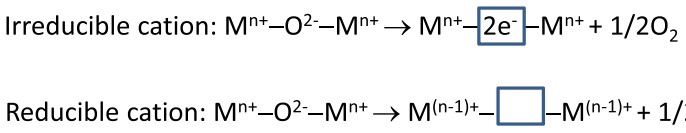

Figure 3.5: A schematic representation of reducibility and irreducibility of materials by removal of a neutral lattice oxygen.

In Figure 3.5 there is a schematic representation indicating the behavior of reducible and irreducible materials upon removal of an oxygen atom. Our idea here is to explore the size dependency of reducibility in silica, titania and titanosilicate nanoparticles. This work is still in progress therefore only results obtained so far relative to oxygen vacancy formation will be summarized here.

Oxygen vacancy formation. At the beginning of this study we selected the globally optimized $(Ti_xSi_{1-x}O)_{10}$ with $0 < x < 1$ systems and we removed a single oxygen atom from these structures in a systematic way exploring the removal of all possible O sites. Non-stoichiometric structures are then fully relaxed at the same level of theory of stoichiometric ones (i.e. PBE0 with tight/tier1 basis set) and with spin-polarized calculations. Afterwards the oxygen vacancy formation energy, $\Delta E^f_{O_v}$, relative to the following chemical

equation was calculated as

$$\mathrm{M}_n\mathrm{O}2n \rightleftarrows \mathrm{M}_n\mathrm{O}2n-1+\frac{1}{2}\,\mathrm{O}2$$

$$\Delta E^f_{O_v} = E_{M_nO_{2n-1}} + \frac{1}{2}E_{O_2} - E_{M_nO_{2n}}$$

The oxygen vacancy formation energy quantifies the energetic cost of removing an oxygen from the system. When the energetic cost of removing an oxygen is high, in principle, it indicates that the system is not easily reducible. Contrarily, when the oxygen removal energy cost is low, the system tends to be easily reducible. In this work we discuss: i) the energetic cost and the role of relaxation, ii) the environment of the vacancy (the neighboring sites) that play a role in its stabilization, and iii) the electronic structure of the defective clusters. We explore first the impact of composition in a 10 unit titanosilicate cluster, and secondly, the size dependence in pure silica and titania materials.

3.4.1. Oxygen vacancy in $(\mathrm{Ti}_x\mathrm{Si}_{1-x}\mathrm{O}2)_{10}$

In Figure 3.6a) we show the structures of our nanocluster global minima candidates used in this first part of our study. For these systems we firstly calculated the $\Delta E^f_{O_v}$ and the results are shown in Figure 3.6b). The values of energy reported here are relative of the systems displaying the less costly oxygen vacancy formation and including the effects of geometry relaxation (i.e. red part of each bar). From our results, surprisingly the pure nanosilica system is found to have a lower oxygen vacancy formation than the pure titania system: the $(\mathrm{SiO}2)_{10}$ cluster has a $\Delta E^f_{O_v} = 2.60$ eV, $(\mathrm{TiO}2)_{10}$ cluster 3.70 eV. This is surprising because the reducibility and therefore the oxygen vacancy formation energy at bulk scale of such systems is known to be the reverse: $3.7-4.8$ eV for the $\mathrm{TiO}2$ rutile structure, $4.2-5.3$ eV for the anatase structure, depending on the oxygen vacancy dilution, and 8.2 eV for the alpha-quartz structure (calculated at B3LYP level with VASP)[65]. In the titania bulk materials the formation of an oxygen vacancy results in the reduction of 2 Ti^{+4} sites into 2 Ti^{3+} as corresponds to a reducible material, whereas in silica bulk the electrons left are located between two silicon sites

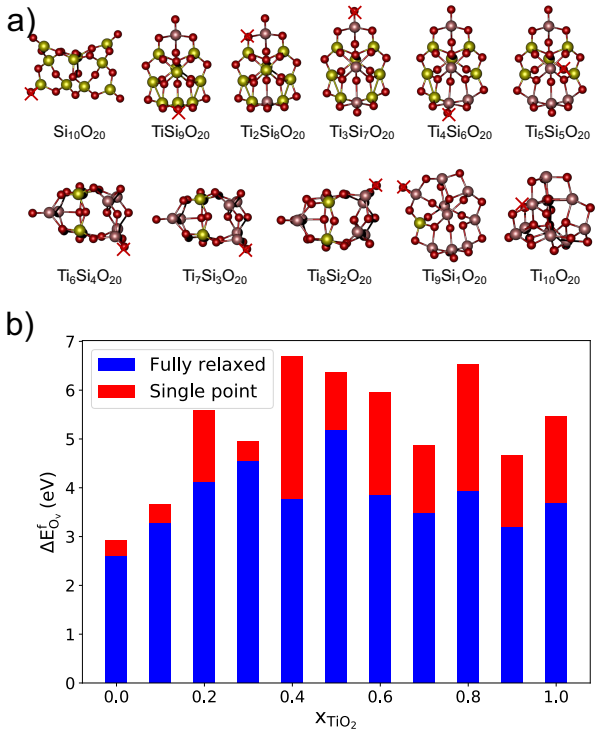

Figure 3.6: a) Global minima isomers for $(Ti_xSi_{1-x}O)_{10}$ with $0 < x < 1$ titanosilicate nanoclusters. Red crosses indicate the easiest oxygen atom to be removed. b) The corresponding oxygen vacancy formation energy $\Delta E^f_{O_v}$ with respect to nanoclusters mixing composition. The red bar indicates the energy gained after relaxing the structure from the initial geometry (removal of an oxygen from the stoichiometric cluster), the blue bar indicates the $\Delta E^f_{O_v}$ after relaxation.

(like a covalent bond). As for the mixed clusters they exhibit values between 3.29 and 5.18 eV, with no clear trend besides the fact that the cost to remove an oxygen is always larger than pure silica.

The oxygen sites that cost the least energy to remove are the terminal ones. In the Si-rich clusters with 0, 10 and 30 % the removal leads to a small relaxation and the geometry of the stoichiometric structures is almost conserved. For Ti-content of 20, 40 % and beyond the relaxation involves more energy (up to 3 eV) where in some cases the initial structure is strongly modified. For the systems with the small TiO_2 content $(0-40\%)$ the value of $\Delta E^f_{O_v}$ seems to initially increase with the TiO_2 content whereas for higher mixing compositions it seems to oscillate around 4 eV.

3.4.2. Oxygen vacancy in $(TiO_2)_n$ and $(SiO_2)_n$, n = 2 - 24

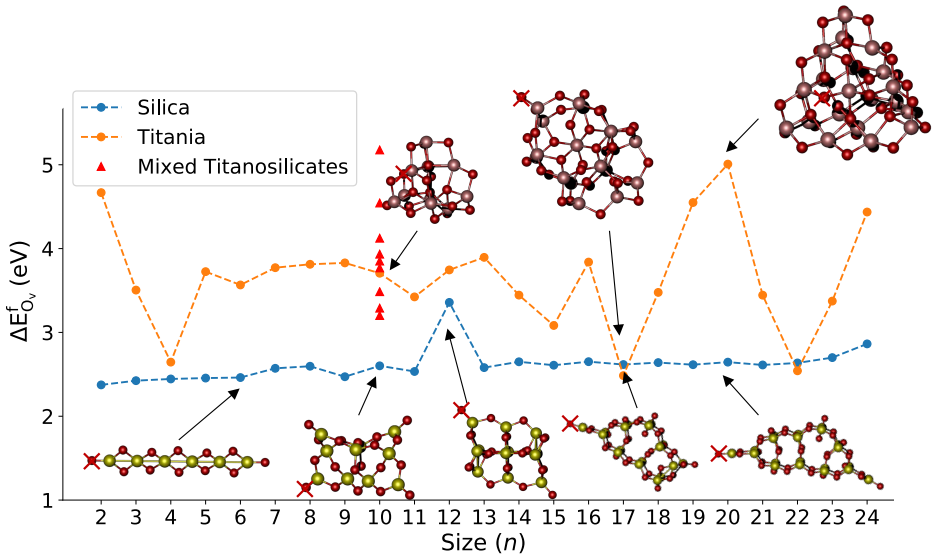

Figure 3.7: Size dependency of $\Delta E^f_{O_v}$ in silica and titania nanoclusters. In all reported cases, only $\Delta E^f_{O_v}$ arising from the best oxygen removal site are shown (i.e. the energetically easiest oxygen to remove). Such oxygen atoms are marked with a red cross.

As a second step we wanted to study the size dependency of the $\Delta E^f_{O_v}$ only of pure systems expecting to find the size at which this "anomalous" nanoscale tendency recover the behavior of bulk materials. To do so, we consider $(TiO_2)_n$ and $(SiO_2)_n$ global minima nanoclusters with $n = 2 - 24$ reported in literature. For small sizes up to 10 units we sampled all possible oxygen removal sites from stoichiometric systems while for relatively large systems we performed a random sampling. Moreover, for all systems, we have included the removal of defective dangling oxygens in our sample set in the case they were not selected. In all cases non-stoichiometric systems are fully relaxed with the spin polarized PBE0 method using tight/tier1 atom centered numerical basis functions. The results of such study are reported in Figure 3.7 which shows that pure silica nanoclusters are persistently more reducible than titania for the system sizes considered here, with the exception of $n = 17$ and $n = 22$. The $\Delta E^f_{O_v}$ for the silica systems exhibits a weak increase with the size (i.e going from 2.37 eV for $n = 2$ system to 2.86 eV $n = 24$). The titania clusters show a different behavior, with a sharp

decrease for small sizes $n = 2$ to $n = 4$ (from 4.66 eV to 2.65 eV), a plateau around 3.6 eV between $n = 5 - 13$, then larger oscillations ($n = 17$: eV, $n = 20$: 5.01 eV, $n = 22$: 2.54 eV, $n = 24$: 4.43 eV).

In all silica systems, the vacancy site responsible for such low $\Delta E^f_{O_v}$ is the dangling oxygen bonded to an under coordinated 3-fold silicon atoms which leave a 2-fold silicon after its removal. Such terminal defective sites are present in most of the stoichiometric global minima with the only exception for $(SiO_2)_{12}$ system which displays NBO terminal defects. In the titania clusters the Ti-NBO terminal oxygen or a vicinal one are found to the be the energetically easies to be removed.

In summary, in most cases removing an oxygen was found to be less costly for silica nanoparticles than from titania. Only few titania systems display a comparable $\Delta E^f_{O_v}$ to the silica one: $n = 4$, $n = 17$ and $n = 22$. In such systems the oxygen removed was either the terminal one or the one close to the terminal defective site. In the last case, during the structure relaxation, the terminal oxygen migrates into the vacancy position.

3.4.3. Electronic structure of reduced nanoparticles

We have further investigated the origin of higher silica chemical reducibility than the titania one from electronic structure prospective. We tried to rationalize why terminal dangling oxygens have such low $\Delta E^f_{O_v}$ compared to other oxygens in the structure. Generally, the removal of a neutral oxygen atom yields an excess of two electrons that reduce two cation centers. The cost of removing different oxygens can vary depending on their site in the nanocluster, on their coordination and on the system size. In titania nanoparticles, in most of the cases, the oxygen removal would yield to the reduction of two Ti atoms, and the electronic state found is that of either a triplet or an open-shell singlet (2 unpaired electrons). In the silica case, the cost of removing the terminal dangling oxygen is much lower than that of other oxygens. The dangling oxygen possesses electronic states associated to the HOMO while other oxygens have electronic states lower in energy. Thus, removing an oxygen with deep laying electronic states

affects more the system stability than removing an oxygen contributing only to the system highest energy states. To illustrate this, in Figure 3.8 we

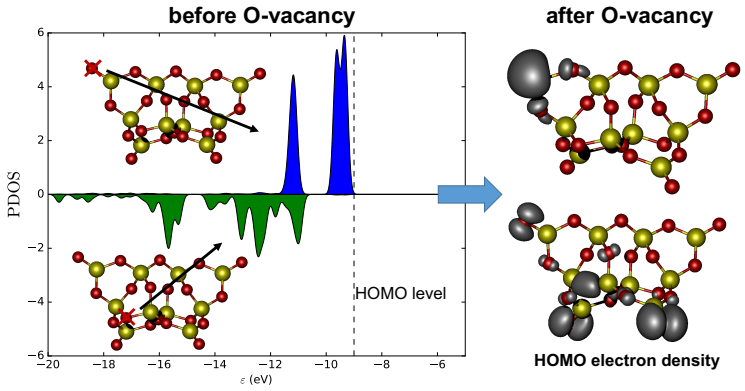

Figure 3.8: Projected density of states (PDOS) on O vacancy sites, in blue the terminal dangling oxygen while in green the internal bridging oxygen before the removal (left) and the respective electron density relative to the HOMO orbital after the removal (right)

plot the atom projected density of states of only oxygens that are going to be removed, the dangling (blue) and the internal bridging oxygen (green). After removing dangling oxygens (top side of the Figure 3.8) we obtain that the two electrons are localized around the closest silicon atom which is being reduced. The shape of the HOMO is that of an sp^2 orbital as indicated from the corresponding electron density (shown in the right side of Figure 3.8). Instead, while removing any other bridging oxygen (bottom side of the Figure 3.8) the electrons left are delocalized between the other dangling oxygens and no Si cations are reduced. This indicates that only silicon atoms bonded with defective dangling oxygens are effectively reduced in SiO_2 nanoparticles upon the removal of the defective oxygen.

3.5. Conclusions

In this chapter we have shown that the mixing between TiO_2 and SiO_2 at the nanoscale is thermodynamically favorable for a wide range of compositions contrarily to the bulk. Such energetically favorable mixing is found to be maximum for systems with size $n = 10$ with mixing compositions approximately between $x = 0.3 - 0.5$ and slowly vanishes approaching zero

at size $n = 24$ oxide units (i.e. to nanoclusters with diameters less than 1.5 nm). The favorability of mixing is mainly driven by the relative stabilities of O-dangling bonds at Si-O and Ti-O terminal sites.

We provide two measurable signatures of mixing in order to eventually help the experimental characterization of such nanoclusters. Firstly, harmonic frequency calculations show unique and distinct IR fingerprints (intense peaks at around 1090 and 1035 cm^{-1} in IR spectra) exhibited by mixed titanosilicate nanoclusters. Secondly, Si centres in mixed nanoclusters show on average a higher coordination compared to pure silica nanoclusters which in principle, could be observed in EXAFS experiments.

We have shown that the oxygen vacancy energy formation can give a qualitative indication of nanoparticle reducibility. The silica nanoclusters are found to be more reducible than the titania nanoclusters contrary to the behavior observed for the bulk. A detailed electronic structure analysis shows that the terminal oxygen sites possess levels close to the HOMO. We are expanding our study on O-vacancy formation also to titanosilicates systems, and including hydrogenation, hoping that our results can eventually help with their experimental characterization.

Our work can further be improved by considering the effect of the explicit environment such as water, oxygen, etc.. on the stability of titanosilicates We hope that this work will inspire experimental researchers to explore the properties of nanoscale mixed titanosilicate nanoclusters. This could lead the synthesis of new titanosilicate materials with enhanced catalytic properties.

Chapter 4

Titania nanoparticles

In this chapter we study the structural size dependency of titania nanoparticles with respect to their amorphous to crystalline transition. This work has been published in the reference below, therefore only a brief summary will be presented here.

Oriol Lamiel-Garcia, Andi Cuko, Monica Calatayud, Francesc Illas and Stefan T. Bromley, "Predicting size-dependent emergence of crystallinity in nanomaterials: titania nanoclusters versus nanocrystals" *Nanoscale*, 2017, **9**, 1049.

4.1. Introduction

Titanium dioxide materials are widely used and studied in both industry and in academia for their exceptional electronic properties. Indeed, they are photoactive systems with applications as photocatalyst, solar cells, water splitting systems, sunscreens, antipollution building materials etc. [73–77] Titania materials exhibit a strong size-dependency of both structure and properties as shown in Figure 4.1. At ambient conditions, the rutile structure is the most thermodynamically stable phase. Upon decreasing the system size, when the average nanoparticle diameter is lower than 14 nm, a phase transition occurs, in which the anatase structure becomes more stable[78].

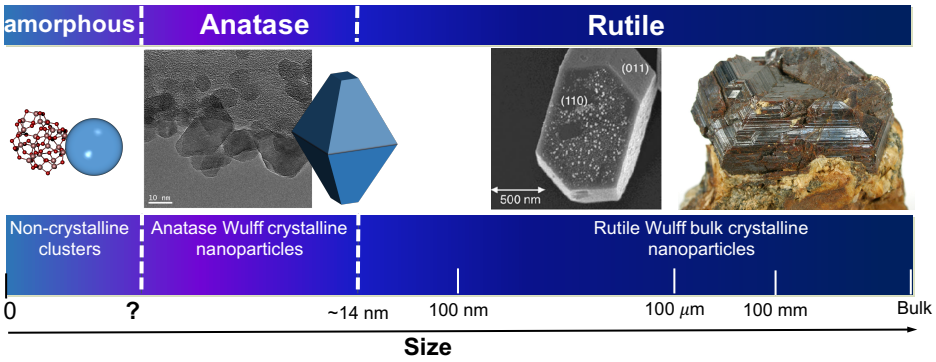

Figure 4.1: TiO_2 structural size-dependency. The system size increases from left to right. Anatase TEM images are taken from ref[71], rutile SEM image is taken from ref[72] and the macroscopic rutile mineral image is taken from Wikipedia (`https://commons.wikimedia.org/wiki/File:Rutile-tuc1055c.jpg`)

Anatase nanocrystals are highly photoactive and they typically exhibit a bi-pyramidal shape with exposed $\{101\}$ facets with some degree of $\{001\}$ truncation of the apices. Such phase transition has been rationalized by the effect of size-dependent surface energy and stress acting on the nanoparticle. A further reduction in size of anatase nanocrystals will eventually give rise to nanoclusters which generally do not possess crystalline order and do not display photochemical activity. There is experimental evidence that anatase nanoscystals persist thermally when particle diameters are roughly 5 nm, nevertheless it is unclear if nanoparticles retain a faceted noncrystalline morphology[79]. Nanoparticles with size between $2 - 3$ nm, from both experimental and theoretical evidence, display a crystalline core and an amorphous shell morphology[80]. A further decrease of the system size leads eventually to completely amorphous nanoparticles which are found to be non photoactive[81].

The aim of this work is to determine the transition size between amorphous-to-crystalline nanoparticle which in turn can be seen as the transition size between non-photoactive to highly photoactive nanoparticle. Such a transition is considered to be the crossover between the relative stability of a set of nanocrystals with decreasing size (top-down approach) and a set of amorphous globally optimized nanoclusters with increasing size (bottom-up approach). Their relative stabilities are accurately evaluated by quantum me-

chanical calculations, and we predict the amorphous to crystalline transition to occur at at $2 - 2.6$ nm.

4.2. Methodology

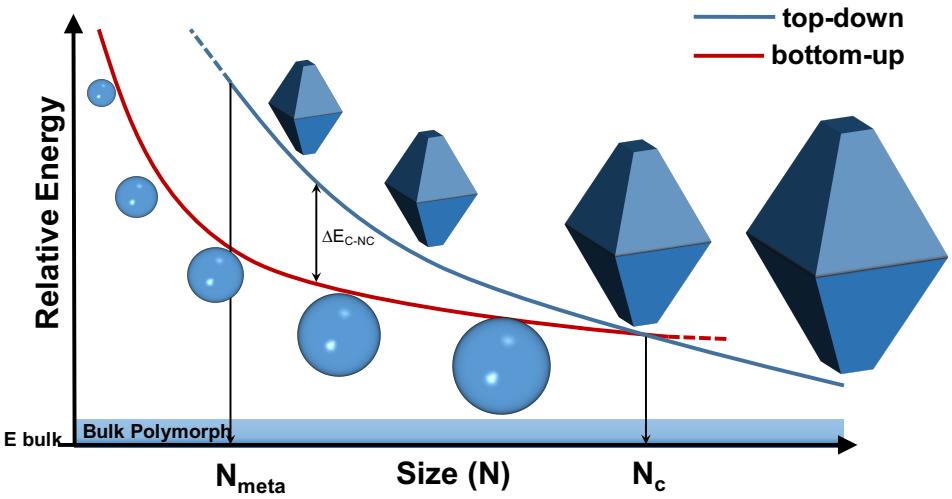

Figure 4.2: Schematic representation of energetic stability of crystalline (C) top-down nanoparticles (blue line) versus non-crystalline (NC) structures.

We aim at determining the size for the amorphous-crystalline transition, where the expected behavior of the energy as a function of the size is displayed in Figure 4.2. We describe separately the size dependent energetic stability of nanocrystals (blue line) and non-crystalline nanoparticles (red line). N_{meta} is the size limit for a bulk-cut nanocrystal, lower size involves that the crystal is too small and undergoes amorphization after geometry relaxation. Here we do not consider crystalline nanoparticles under such size limit. The energetic difference, ΔE_{C-NC}, quantifies the metastability of crystalline (C) with respect to non-crystalline (NC) nanoparticles i.e. if the system size is smaller than N_c and *vice versa* if it is bigger than N_c. Thus, the the $NC \leftrightarrow C$ crossover size is defined as the nanoparticles size, N_c, at which ΔE_{C-NC} becomes 0.

Top-down. Herein, we employ five nanocrystals derived from stoichiometric anatase bulk cuts with sizes between $N = 28 - 84$ TiO_2 units as shown in Figure 4.3 (i.e. corresponds to $84 - 252$ atoms). All such nanocrystals

retain their original bulk crystalline structure reasonably well after geometrical relaxation. Systems with $N = 28$ and $N = 38$ are considered in previous studies[82,83] and are derived from anatase bulk cuts requiring the nanocrystal net dipole moment to be zero. The reminding structures are generated according to the Wulff construction[84] morphology obtained by minimizing the nanoparticles total surface energy. For gas-phase anatase nanoparticles such a morphology corresponds to a bi-pyramidal and/or to a truncated bi-pyramidal shape. All our structures are fully relaxed using DFT calculations employing the PBE0 functional with a tight/tier1 basis, and relative energies are calculated with respect to the anatase bulk.

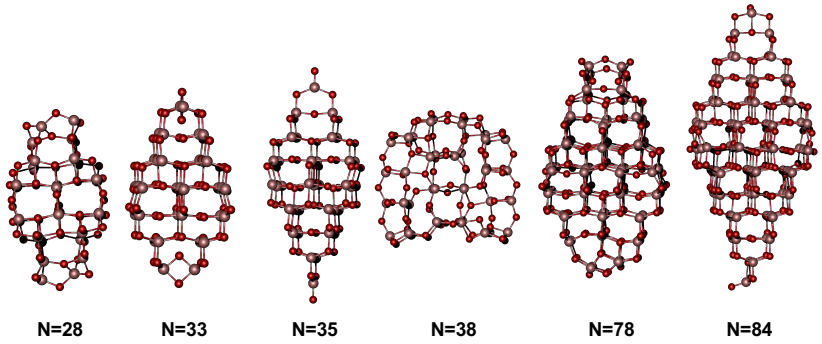

Figure 4.3: Top-down anatase cut $(TiO_2)_N$ nanocrystals.

Bottom-up. Herein, we consider nanoparticles with increasing size with $N = 1 - 24, 28, 35$ and 38 where N is the number of oxide units as shown in Figure 4.4. All such bottom-up nanoparticles are obtained with the IP-based MCBH global optimization method. We employ two different IPs based on the Buckingham potential during the global optimization procedure.

The first IP uses a mixed parameterization between the previously reported IPs for bulk titania (MA)[85] and nano-silica (FB)[59] adapted for the longer Ti-O bond length. We refer to this as the MA-FB IP. The MA IP tends to provide bulk-like highly coordinated Ti centers (i.e. 6-folded) while the FB IP tends to provide silica-like tetrahedrally coordinated cations.
The second IP is entirely re-parameterized, in which the O-O repulsion is found to have intermediate values between FB and MA. This new IP tends to provide structures where cations located in the inner part of the cluster are penta- and hexa-coordinated while those located in the outer parts are

tetra-coordinated. Both IPs are reported in the Appendices at the end of this thesis. Parameters of both IPs are reported in the Table A4 of the Appendix.

Several MCBH runs of $10^5 - 10^6$ cycles for each nanocluster size were performed using the custom scheme introduced in the previous chapter in which the temperature is self-adapted to keep the acceptance ratio between 64-80%. A selection of 40-50 globally optimized structures from each run was subsequently post refined with unconstrained DFT optimization in a cascade approach, first with PBE light/tier1 settings, and secondly with PBE0 tight/tier1 setting. Moreover, to further extend our sampling, we also used data mining of $(SiO2)_N$ and $(CeO2)_N$ structures previously generated with global optimization procedure in our lab, and we re-optimized them as $(TiO2)_N$ nanoclusters.

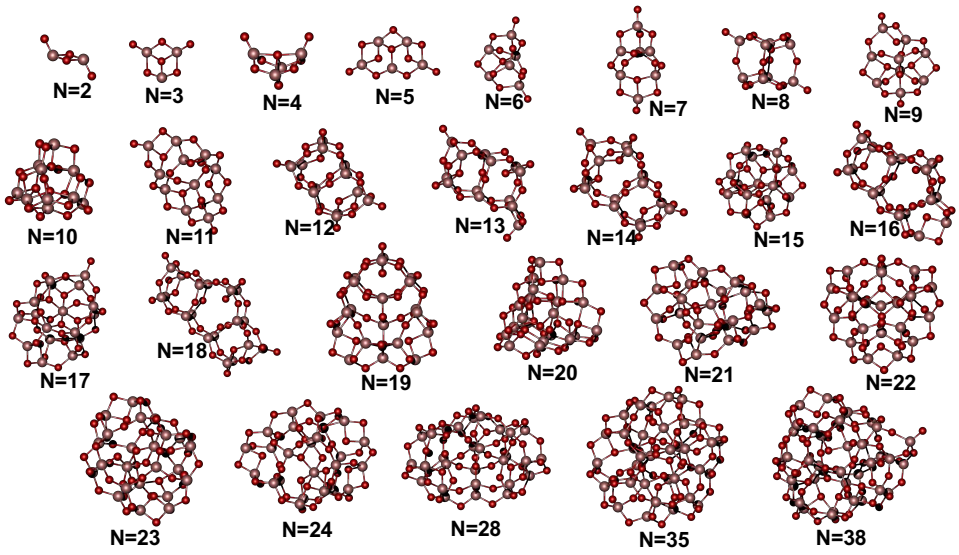

Figure 4.4: Bottom-up globally optimized $(TiO2)_N$ nanoclusters.

4.3. Structure and Energetics of titania nanoparticles

The top-down structures, as mentioned above, are derived from anatase cuts and are shown in Figure 4.3 while all the resulting bottom-up globally optimized structures are shown in Figure 4.4. The most stable $(TiO2)_N$ nanoparticles with $N < 9$ are well established in the literature. For all the

other sizes we report either new structures or global minima candidates that concur with one those found in the literature. Generally, the nanoparticles are relatively compact with low symmetry, exhibiting mainly 4-fold Ti centers and displaying dangling oxygens, especially in relatively small nanoclusters. As the system size increases there is a general trend to obtain fully saturated nanoparticles especially when $N > 18$. Moreover, we notice that nanoparticles with sizes $N = 28, 35$ and 38 are significantly more stable (by $8 - 10$ eV total energy) than their corresponding anatase-like structures from the top-down approach. Because of the low symmetry and structural differences with TiO_2 bulk-like structures we consider the bottom-up generated nanoparticles as effectively amorphous. Total energy and relative stability of both bottom-up and top-down nanoparticles are reported in Tables A5 and A5 of the Appendix.

Generally, the structural stability of nanoparticles in the scalable regime scales linearly with the surface-to-bulk ratio as the system size increases. The surface-to-bulk ratio, in turns, scales as approximately an inverse cube low with number of atoms depending on the nanoparticle shape. In the non-scalable regime, it has been shown that other factors such as the nanoparticle compressibility begin to play a significant role in the nanoparticle stability which can be expressed by a polynomial expansion of the scalable regime stability law (for more details see Figure 1.1 in chapter 1) as shown in equation 4.1 [86,87].

$$E(N) = E_{bulk} + a_1 N^{-1/3} - a_2 N^{-2/3} \tag{4.1}$$

where a1 and a2 are constants relative to the nanocrystal shape and structure. Here, $a_1 N^{-1/3}$ quantifies the surface-to-volume effects while $a_2 N^{-2/3}$ represents the structural contraction due to the surface stress. We fitted the relative stability (with respect to anatase bulk) of our top-down nanocrystals to equation 4.1. For bottom-up globally optimized structures, structural effects on the system stability are less well established and the use of equation 4.1 it is not well justified. Since the equation 4.1 captures the effect of geometry and surface stress on the total energy, we assume that an expansion of such an equation could describe more finer surfaces effects related with morphology changes. The equation 4.1 can be seen as the first polynomial expansion of the scalable regime and the general expansion expression can

be defined as following:

$$E(N) = a_0 + a_1 x + a_2 x^2 + a_3 x^3 \ldots \tag{4.2}$$

where $a_0 = E_{bulk}$, $x = N^{-1/3}$ and a_n are (possibly N dependent) constants. We have fitted the relative stability of our bottom-up structures to the equa-

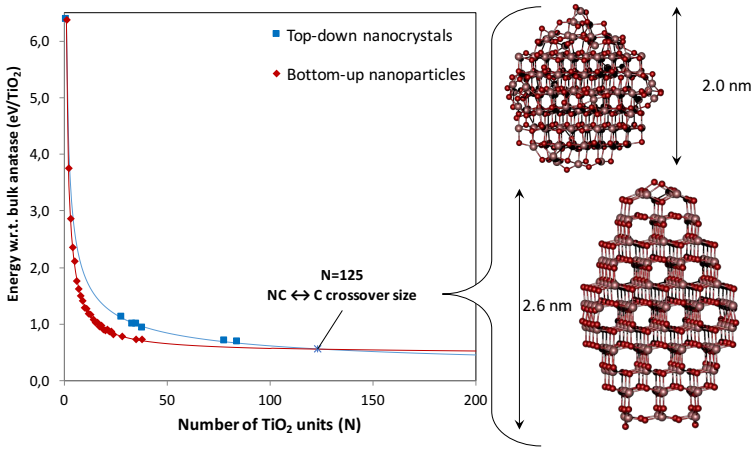

Figure 4.5: Top-down (blue squares) and bottom-up (red squares) relative stability with respect to the anatase bulk polymorph against the nanoparticle size (N). Blue line indicates the fit to an inverse power law shown in equation 4.1 and red line indicates the 5^{th} polynomial fit of equation 4.2. The $NC \leftrightarrow C$ crossover size is indicated by a cross at 125 TiO_2 units (i.e. 375 atoms). On the right hand side, we provide a tenative estimate of a nanocrystal structure close to the crossover size.

tion 4.2, the 5^{th} order polynomial fit has been chosen as the most convenient. In Figure 4.5 we report top-down and bottom-up relative stabilities with respect to anatase bulk and relative fitting lows as describe respectively in the 5^{th} order of equation 4.2 and in equation 4.1. The $NC \leftrightarrow C$ crossover size between bottom-up 5^{th} polynomial fit and top-down inverse power lows is estimated to be at $N = 125$ TiO_2 units which corresponds to systems with 375 atoms. A probable nanoparticle at the crossover size either could be semi-crystalline roughly 2 nm of diameter and displaying an anatase-like core and an amorphous shell or could have a faceted truncated by-pyramid morphology with $2.0 - 2.6$ nm.

4.4. Conclusions

In this chapter we estimated the non-crystalline to crystalline ($NC \leftrightarrow C$) crossover size for titania nanoparticles to occur at a particle diameter of roughly $2 - 2.6$ nm. This prediction seem to be consistent with experimental observations[80]. From a bottom-up approach we globally optimize nanoparticles with sizes $N = 1 - 38$ finding new global minima candidates never reported before especially for systems with $N \geq 10$. Also, a new parameterization of IP has been carried out for an efficient and accurate TiO_2 nanocluster global optimization. The approach shown here is quite general and can be applied to study size dependent properties for other materials. A continuation of this work would be to study the effect of water containing environment on the $NC \leftrightarrow C$ crossover size. In this regard, our work in chapter 6 can be considered as an early stage research for the study of such effects.

Chapter 5

Refined Monte Carlo basin hopping approaches

In this chapter we propose two approaches in order to improve the global optimization procedure using IP-based MCBH. The first approach provides an efficient way for finding energetically low laying minima for hydrated systems and specifically developed for silica nanoclusters. Here we will provide a brief description of the main idea and a summary of obtained results since this work has been published and attached to this thesis.

Andi Cuko, Antoni Maciá, Monica Calatayud, Stefan T. Bromley, "Global optimisation of hydroxylated silica clusters: A cascade Monte Carlo Basin Hopping approach" *Computational and Theoretical Chemistry* 2017, **1102**, 38-43.

The second approach relies on the use of Machine Learning algorithms to post refine and correct the IP energetic bias providing better isomer energy. This work has not been published at the time of the writing of this thesis therefore we will describe it in detail here.

5.1. Introduction

The IP-based MCBH algorithm we have used so far can be considered as our standard approach that allows us to efficiently explore the PES of a given system. In Figure 5.1 there is a schematic representation of this procedure as is also explained in section 2.5.2 of chapter 2. According to a specific

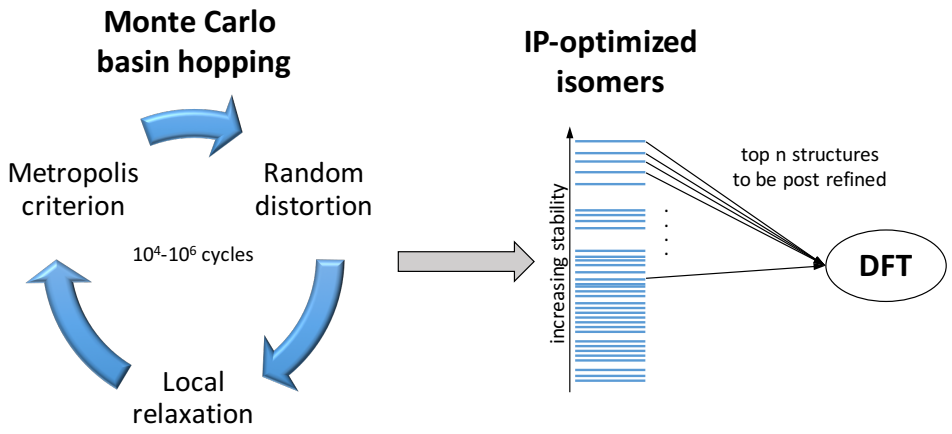

Figure 5.1: Schematic description of the standard basin hopping approach employed in this thesis.

system one might need to employ a modified version of the standard MCBH approach. For instance, in mixed titanosilicates nanoparticles we have employed the cation swapping (i.e. Ti $\leftrightarrow$ Si) in order to favor the sampling of new geometrical configurations. Improvements of such procedure can be either in-cycle refinements or post refinements of obtained isomers. In this chapter we present two approaches that can improve the search for stable isomers in two different situations. Our first approach, cascade MCBH, is an in-cycle refinement procedure and is meant to be for hydrated systems which potentially have different H-bond surface networks that may affect isomers stability. In the second approach we employ Machine Learning algorithm as a MCBH post refinement procedure to improve the energetic stability and ordering of the isomers obtained.

5.2. Cascade Monte Carlo basin hopping approach

The interaction of a nanocluster with the environment can profoundly change its properties. As considered to be a common environment molecule, water can react and hydroxylate oxide nanoparticles even in trace amounts. Nanosized silica is a typical example known to be particularly prone to react with water and the resulting degree of hydroxylation is found to determine many of its properties. For instance, the solubility of small silicate nanoparticles is determined by their hydroxylation which in turn is affected by the pH in solution. Such species are central to the synthesis of technologically important nanoporous silicate materials such as zeolites[88]. Using IP-based MCBH to find the most stable structure for hydroxylated systems can be difficult especially for highly hydrated systems. Such difficulties can derive from the choice of the IP describing the system. Accurate IPs, typically rely on a different parameterization of hydroxyl groups oxygen atom types (i.e. OH) from the bridging oxygen atoms (e.g. Si-O-Si). Assigning whether an oxygen belongs to an hydroxyl group or to non-bridging group in a randomly distorted systems where connections between atoms are lost is rather problematic. IPs that treat all oxygen atoms type (e.g. both hydroxyls or to non-bridging oxygens) with the same parameterization typically do not provide a good description of hydroxyl groups and therefore they can miss isomers whose stability is driven by the H-bonding network. Our approach consists in employing two consecutive energy minimization steps in each MCBH cycle: (i) a lightly parameterized but computationally efficient IP (FFSiOH*) which does not distinguish between H-bonded conformational isomers, and then (ii) a more sophisticated IP (FFSiOH) which accounts for polarization and H-bonding. Parameterizations of such IPs are reported in the Table A7 of the Appendix.

Silica nanoparticles provide a perfect case study for several reasons: (i) it is known that the system is highly prone to react with water due to a high number of defective centers, (ii) there is the availability of both accurate and lightly parameterized IPs suited for the system, (iii) for specific system sizes and hydration degrees global minima candidates are already reported from previous studies therefore we have the necessary data to validate our procedure.

5.2.1. Cascade approach: Methodology

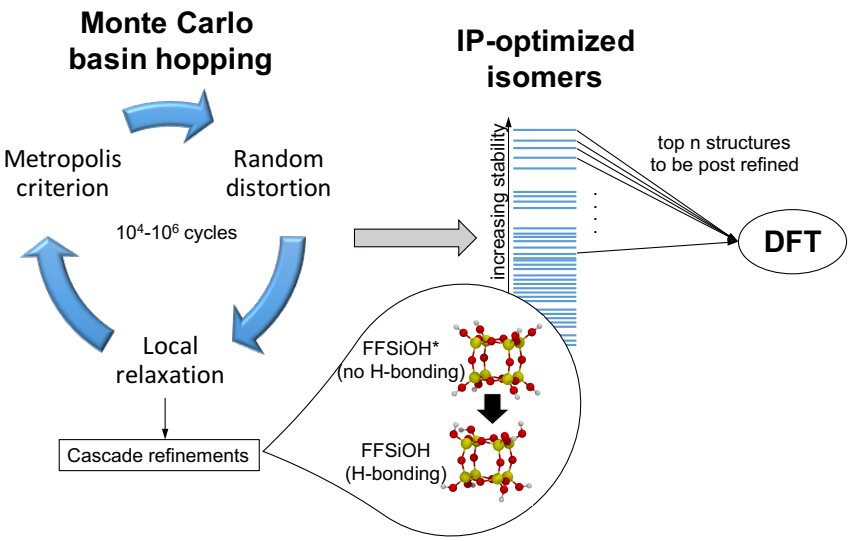

Figure 5.2: Schematic description of the Cascade Monte Carlo basin hopping approach.

The schematic description of the cascade approach is shown in Figure 5.2. Here we apply the cascade MCBH approach to $(SiO_2)_M(H_2O)_N$ systems with $M = 6, 8, 10$ and 12 and with different hydroxylation degree ($R_{N/M} \times 100$) up to ∼65%. In order to more efficiently explore the PES we use a self-correcting temperature technique to keep the acceptance ratio between 60-80% as in our previous studies. For each MCBH cycle, atomic displacements are set to a maximum of ±0.8 Å. In order to remove isomers replica we filter out structures having energy difference less than 1 kJ/mol. Several runs (at least three) of fifty thousand steps each are performed for all considered systems. The ten most energetically stable isomers resulting from the global optimization procedure for each system are subsequently fully relaxed using DFT. This final geometrical optimization is done employing the FHI-AIMS package, using the B3LYP hybrid functional and a tier1 atomic centered numerical basis set with a light integration grid.

5.2.2. Cascade approach: Validation

A number of recent studies have focused on attempting to find the most stable structures of hydroxylated silica nanoclusters, $(SiO_2)_M(H_2O)_N$, in the approximate size range of 10–100 atoms[89–92]. We compare our resulting most stable structures $(SiO_2)_8(H_2O)_N$ with $N = 2 - 5$ with ones found in previous works[90,91]. As we can see from structures in Figure 5.3 we could

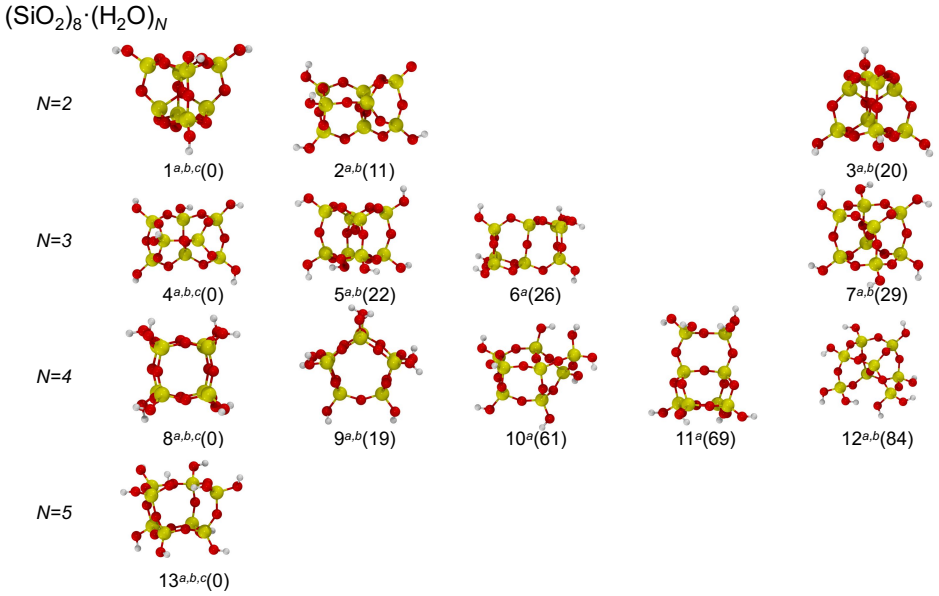

Figure 5.3: Globally optimized $(SiO_2)_8(H_2O)_N$ hydroxylated nanoclusters. From left to right isomers with decreasing stability as found in this work are reported while from top to down system with increasing water content (N) is shown. Numbers in parenthesis is the isomer relative stability with respect to the global minima candidate in kJ/mol while numbers outside are used as label for each structure. Isomers are also labeled as $^{a)}$ if found in this work, $^{b)}$ if found in ref[91]and $^{c)}$ if found in ref[90].

find all global minima candidates reported in other studies (first column on left side). This further enhances the possibility for such structures to be the real global minima. For systems with N=3 and 4 we could also find new hydroxylated nanoclusters as third most stable structures which were not reported before (i.e. system numbers 6, 10 and 11 in Figure 5.3).

5.2.3. Cascade approach: New hydroxylated silica nanoclusters

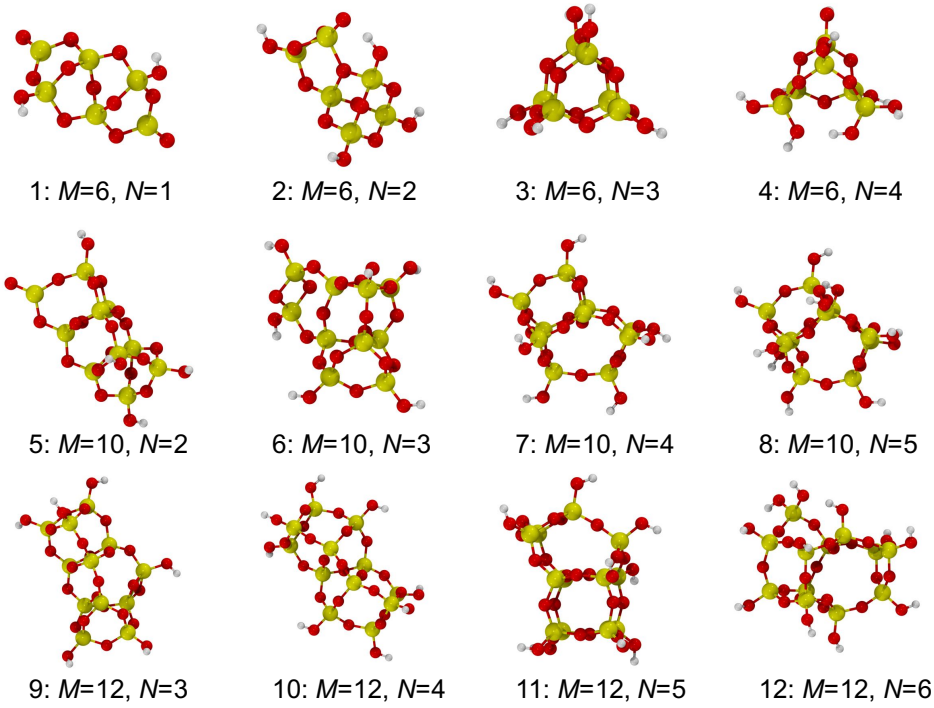

Figure 5.4: New global minima candidates of $(SiO_2)_M(H_2O)_N$ hydroxylated nanoclusters.

Once our approach had been validated we used it to find new hydroxylated silica global minima candidates for $(SiO_2)_M(H_2O)_N$ systems with $M = 6, 10$ and 12, each with with $N = 1-4$, $N = 2-5$ and $N = 3-6$ water molecules respectively, which had not been reported previously. The new generated global minima candidates are reported in Figure 5.4. In all cases, water is dissociated and chemisorbed H_2O. In the systems considered here, at least two water molecules are needed to completely heal the defective dangling oxygen atoms present in pure silica. In Figure 5.5a) and 5.5b) we report respectively the energetics of nanocluster hydration as the result of electronic structure calculations at 0 K and the effect of the hydration on structural features such as the tetrahedral distortion of SiO_4 groups. As the hydroxylation degree increased there is a general tendency for both hydroxylation energy and tetrahedral distortion of SiO_4 groups to first rapidly decrease, and then subsequently level off to a constant value

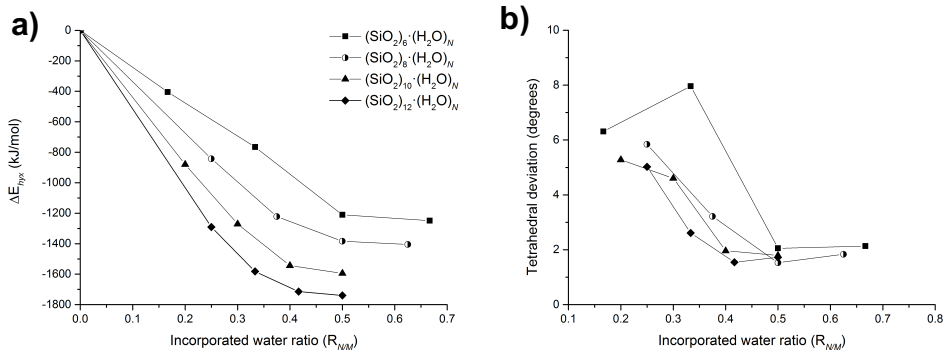

Figure 5.5: a) Hydroxylation energy of $(SiO_2)_M(H_2O)_N$ and b) as a tetrahedral distortion of SiO_4 groups as a function of the hydration degree $R_{N/M}$.

The value of the system hydroxylation degree at which the tetrahedral distortion of SiO_4 groups and the hydroxylation energy level off is identified as the optimal hydration ($R^{opt}_{N/M}$). Values of optimal hydration degree of silica nanoclusters varies with the system size M by following an inverse power low of $R^{opt}_{N/M} = 2M^{-2/3}$ which is consistent with what has been found in a previous study[90] (i.e. $R^{opt}_{N/M}$ ranging from 0.75 for $M = 4$ systems to $\sim$0.3 for $M = 16$ systems). Finding the number of optimal hydroxylated silica systems could help to rationalize the size dependency of silica hydration which so far has not been fully understood.

5.2.4. Conclusions

In this work we present a new approach for globally optimizing hydrated systems with the MCBH algorithm. Here, in each basin hopping cycle, atomic coordinates are optimized with two IPs in a cascade manner in which the second IP gives a better description of the system. We have validated this approach on already known systems $(SiO_2)_8(H_2O)_N$ and we have used it to find new global minima candidates for systems with different sizes and hydroxylation degrees (i.e. $M = 6$ and $N = 1 - 4$, $M = 10$ and $N = 2 - 5$, $M = 12$ and $N = 3 - 6$). Although this approach has been used for hydrated silica systems, it can be employed in principle for any system for which accurate IPs need an atomic configuration not so far from the minimum in order to correctly assign atom types. We have also used

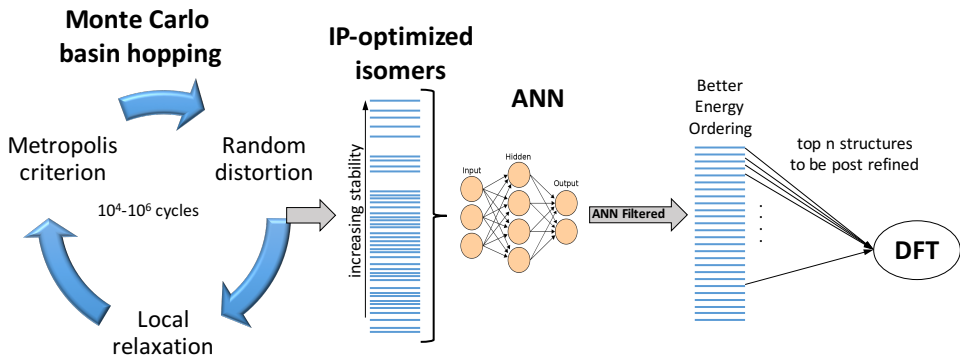

Figure 5.6: Schematic description of the ANN post refinement procedure.

this approach for the global optimization of some of the hydrated titania nanoclusters presented in chapter 6.

5.3. Machine Learning post refinements

The global optimization procedure with the IP-based MCBH algorithm can be problematic for relatively large systems. On one side the IP allows for an efficient sampling of the vast number of configurational isomers, but, on the other side, the sampling is biased to the IP PES which is generally different from the one of higher accurate methods (e.g. DFT quantum mechanical PES). Typically, to account for such IP bias a certain number of most stable isomers is post refined with more accurate methods as is also shown in Figure 5.1. In large systems, in order to prevent losing stable isomers, the number of structures to be post refined with more accurate and computationally more expensive methods could be relatively high and sometimes not easily affordable. In order to have a better energetic evaluation of IP-optimized isomers with a computationally low cost we employ a Machine Learning (ML) based algorithm known as an Artificial Neural Network (ANN). More details about ML and ANN can be found in section 2.3 of chapter 2. In principle ANNs are capable of fitting any mathematical function with an arbitrary degree of accuracy. It has been shown that ANN models have greatly been able to represent high-dimensional PES with a very good accuracy [33,35,93]. In Figure 5.6 there is a schematic description on how we use the ANN to improve the global optimization procedure. The

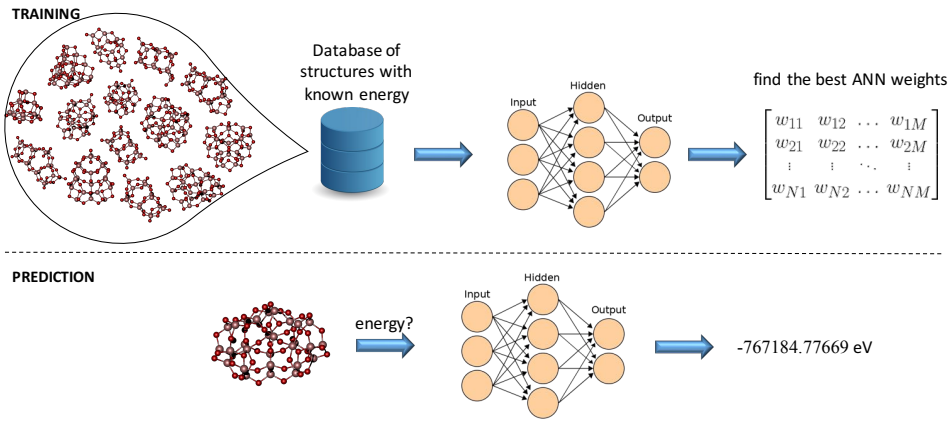

Figure 5.7: Schematic representation of how the ANN works. Top: the training procedure. Bottom: application procedure. For further details see section 2.3 of the chapter 2.

idea is to use the ANN as a sort of filter that provides better isomers energy at a very low computational cost. Thanks to this approach, not only the number of structures that undergo post refinements is reduced but also the efficacy in finding low energy structures that may be incorrectly labeled as high energy from the IP is increased. We have developed and applied this procedure specifically for $(TiO_2)_N$ nanoparticles but in principle it can be used for IP-based global optimization of any system.

5.3.1. Methodology

Here we will qualitatively describe how the the ANN functions as it is schematized in Figure 5.6. As a first step, the ANN model has to be trained, typically using a large amount of data. In our case the data is made from a set of different $(TiO_2)_N$ isomers with different sizes whose energy has been calculated with the desired reference method (PBE in our case). The training dataset can be generated from scratch or can be recycled from personal or external repository of structures. We notice that global optimization methods are particularly suited for creating databases since they generate a large number of different isomers. Moreover, in standard optimization methods, typically, only few energetically most stable isomers are conserved while all the other structures are discarded. Such discarded isomers could

be employed to train an ANN instead of being discarded.

In this specific case, to build the training data set, we consider isomers generated with the standard IP-based MCBH procedure for $(TiO_2)_N$ nanoparticles with $N = 10 - 20, 22, 24$ and 28 oxide units. The IP used in this work has been developed in chapter 4 specifically to describe $(TiO_2)N$. Such IP is also reported in table A4 of the appendix (named as IP2). A single run of fifty thousand cycles has been performed to generate isomers. Notice that here our scope is only to generate different isomers and not to find the global minima, therefore the search does not need to be extensive. For each $(TiO_2)_N$ system we perform a full geometrical relaxation of the $20 - 40$ most stable isomers depending on their size, with DFT calculations employing the PBE functional and a light/tier-1 numerical basis set with FHI-AIMS code. The training set is not composed by only PBE-optimized structures, but rather taking all intermediate local optimization steps that differ by more than 0.01 eV for each of post refined isomers. The overall dataset in this way is composed by 3521 $(TiO_2)_N$ images out of which the 80% (i.e. 2816) are randomly selected for the actual ANN training and the rest for the ANN testing. The choice of such procedure is to ensure that the ANN can correctly evaluate IP-optimized structures that might be different from the PBE-optimized ones.

5.3.2. ANN training

Training of the ANN basically means finding the weights that reduce the most errors in determining the total energy of nanoparticles in the training set. The ANN architecture is composed of the input layer of 20 nodes plus two hidden layers of 5 nodes each and the output layer of one node for each atom. The ANN input is represented by the feature vector of symmetry functions of which 8 of the type G^I (equation 2.6) and 12 of the type G^{II} (equation 2.7) determine the fingerprint of the local environment of each atom (see section 2.3.2 of chapter 2 for more details). Both training and usage of the ANN are done employing the AMP and ASE python packages. The ANN is trained on images of the training set by minimizing the energy loss function with BFGS optimization algorithm

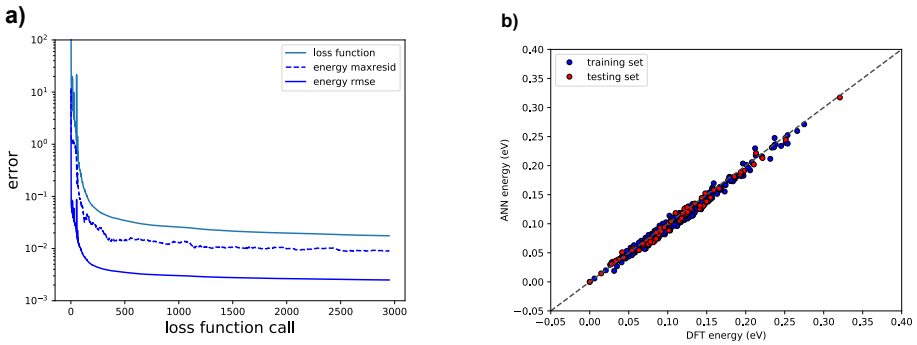

Figure 5.8: a) Convergence plot of the ANN training. b) Predicted ANN energies versus the DFT energies on training data set (blue) and testing data set (red) structures.

until the convergence threshold of 0.0025 eV for root mean square energy errors (rmse) per atom. The evolution of the loss function, energy rmse and maximum residual error are shown in Figure 5.8a). The convergence criteria were met after 2949 steps. As the Figure 5.8b) shows, the prediction accuracy of the trained ANN is found to be very good as compared with PBE energies for both the training and the testing set. We can use now the ANN to predict the energy of unknown structures.

5.3.3. Performance of ANN aided basin hopping

In order to evaluate the ANN improvements we globally optimize $(TiO2)_{26}$ and $(TiO2)_{30}$ nanoclusters with the standard IP-based MCBH and we compare how the ANN post refinements help identifying a set of the most stable isomers. These two systems are both considered relatively large and their sizes are outside the ANN training set. Moreover, systems with $N = 26$ are within to the size range used during the training, while systems with $N = 30$ are outside this range. This choice may have implications for the reliability of the ANN results arising from both energy interpolation and/or extrapolation. More generally, on fitted models such as the ANN the interpolation of data could be accepted with relatively low risk while the extrapolation of data should be carefully examined. By choosing these two examples we want to address how well the ANN can interpolate and extrap-

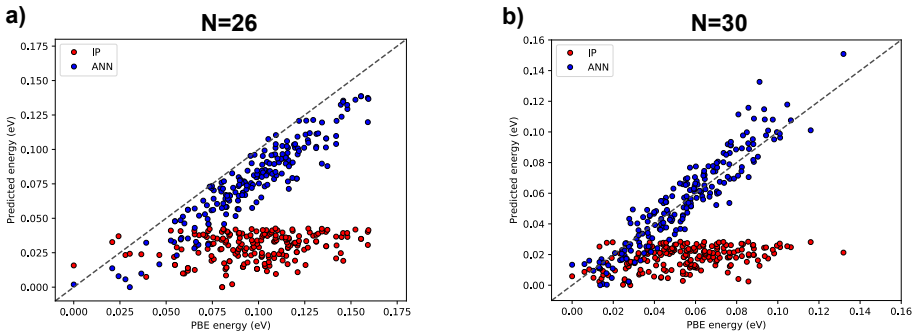

Figure 5.9: ANN (blue) and IP (red) predicted relative energies plotted against the DFT (PBE) relative energies for $(TiO_2)_{26}$ in a) and $(TiO_2)_{30}$ in b). In all cases energies calculated for IP-optimized isomers are scaled with respect to the most stable isomer and normalized by the number of oxide units.

olate system energies. For both $(TiO_2)_{26}$ and $(TiO_2)_{30}$ we perform three MCBH runs of 500 thousand cycles each staring from randomly selected initial structures. A selection of the 200 most stable IP-optimized isomers are subsequently fully relaxed with DFT calculations employing the PBE functional using a light/tier1 numerical basis set.

As a first analysis, the performance of the ANN is compared with the one of the IP in predicting nanoparticle energetic stability calculated using PBE as a reference. In order to simplify our analysis, we consider only single point calculations on fixed IP-optimized nanoparticle geometries. For each level of accuracy, isomer energies are scaled with respect to most stable isomer and normalized by the system size (i.e. N). The results of our analysis for both $(TiO_2)_{26}$ and $(TiO_2)_{30}$ are shown in the parity plot in Figure 5.9 respectively in a) and b). For both systems, the IP (red dots) tends to overestimate the isomer stability with respect to the PBE reference. Moreover the whole set of isomers is found to be in the energy range of 0.05 eV/oxide-units while ANN evaluated isomers are distributed in a much wider range of 0.150 eV/oxide-units in agreement with PBE. Thus, the IP energetic stability evaluated for a set of nanoparticles possesses strong deviations from the reference method and tends to overestimate the density of isomers per energetic range. Nanocluster stability is found to be in much better agreement when evaluated with ANN and compared with the PBE level of accuracy (blue dots). Such agreement seems to be better for $(TiO_2)_{30}$ than for $(TiO_2)_{26}$, which was found to systematically overestimate the

isomers stability with respect to PBE (i.e. blue dots are below the diagonal). The systematic error in $(TiO_2)_{26}$ originates from an under estimation of the energy with the ANN on the most stable structure, which is then used as reference to scale energetic values of all the other isomer. Nevertheless, the ANN energy evaluation of IP-optimized clusters greatly corrects their stability, thus allowing a smaller number of isomers to be fully relaxed at the computationally expensive DFT level of theory. For instance, in order to obtain the top 10% of most stable DFT(PBE) isomers a selection of 183 IP-optimized isomers vs 35 ANN filtered must be considered for $(TiO_2)_{26}$ systems and 192 IP-optimized vs 28 ANN filtered isomers, respectively, in the case of $(TiO_2)_{30}$.

So far we have considered only single point energy calculations for IP-optimized nanoclusters in order to study the ANN and the IP performances and accuracies with respect to the PBE reference. This allows a direct comparison between methods purely from energetic accuracy perspective. However, in a real MCBH simulation we are interested in finding the most stable isomer(s) after an unconstrained geometry relaxation with DFT which can further shuffle the isomer energy ordering. The magnitude of the structure relaxation with DFT starting from the IP-optimized one is an indication of the IP capability to provide accurate geometries. In order to qualitatively analyze the effectiveness of the ANN we firstly track the isomer energy ordering going from IP to single point calculation with PBE to a fully relaxed isomer at the PBE level (i.e. the standard IP-based MCBH approach). We refer to such fully optimized isomers at PBE level as PBEf in order to distinguish them from isomers evaluated with single point calculation. Secondly, the energy order of the same set of structures is shown when introducing the ANN energy correction right after the IP.

In Figure 5.10 we have reported such analysis for $(TiO_2)_{26}$ nanoparticles. As we can see from the graph 5.10a), the energy ordering in the standard IP-based MCBH approach dramatically changes starting from IP and going to PBE as suggested from the high intercrossing of colored lines. When introducing the ANN, as in the graph 5.10b), first the isomer energy ranking changes from IP to ANN and subsequently is found to be qualitatively preserved going from ANN to PBE. This can be seen from the colour map which represents the isomer energy ordering according to the ANN

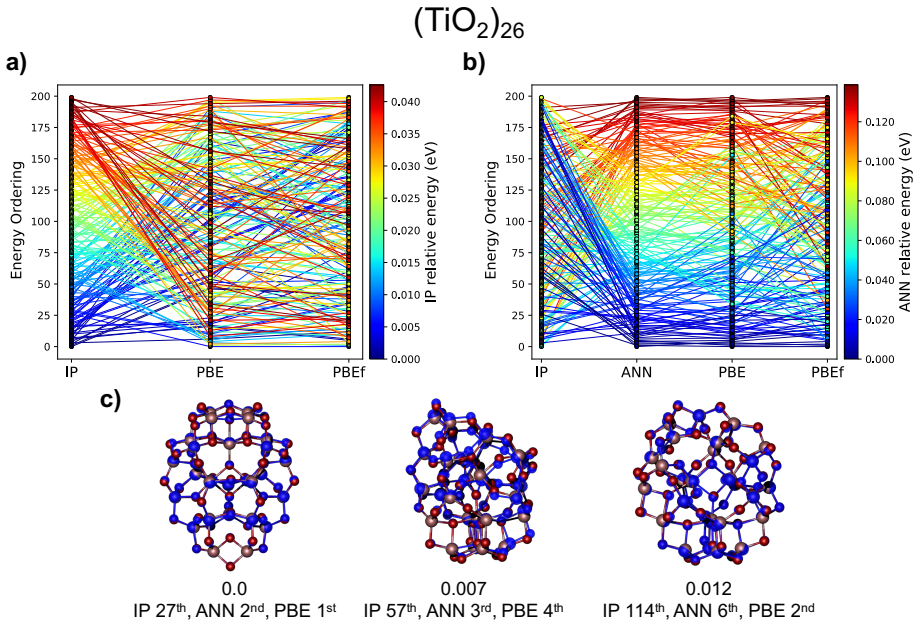

Figure 5.10: $(TiO_2)_{26}$ nanoparticles: a) energy ordering evolution of the standard MCBH approach. The colour bar refers to IP energetic order. b) Energy ordering evolution of the ANN aided MCBH approach. The colour bar refers to the ANN energetic order. c) Structure of the top three most stable isomers after full relaxation, PBEf, showing in transparent blue the initial structure (i.e. IP-optimized structure) and coloured - the fully relaxed one. Relative energy in eV per oxide unit is reported below each isomer. In the second line is the rank history tracking stability order with the different methods of each isomer.

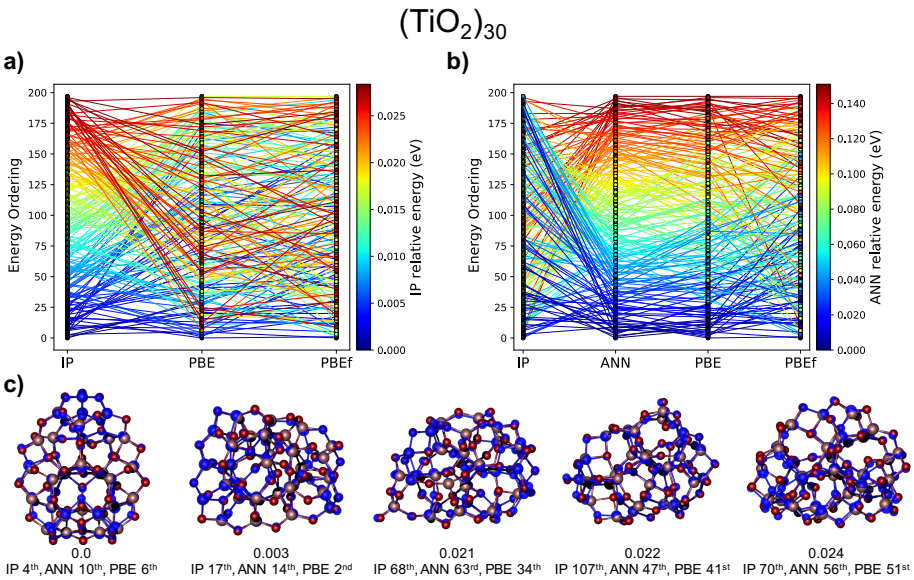

Figure 5.11: $(TiO_2)_{30}$ nanoparticles: a) energy ordering evolution of the standard MCBH approach. The color bar refers to IP energetic order. b) Energy ordering evolution of the ANN-aided MCBH approach. The colour bar refers to ANN energetic order. c) Structure of the top five most stable isomers after full relaxation PBEf showing in transparent blue the initial structure (i.e. IP-optimized structure) and colored the fully relaxed one. Relative energy in eV per oxide unit is reported below each isomer. In the second line is the ranking history, tracking stability order with the different methods of each isomer.

energy, going from dark blue for the most stable to red for the least stable isomer. Going from ANN to PBE the intercrossing of coloured lines is much reduced with respect to the one occurring in graph 5.10a) from IP to PBE. Finally the full isomers relaxation, PBEf, is found to slightly shuffle the PBE isomer stability. The three most stable isomers found after the geometry relaxation with DFT (i.e. PBEf) are also reported in Figure 5.10c). Here, in order to show the effect of coordinates relaxation, we superpose the initial structure (i.e. IP-optimized one) in transparent blue with the final DFT (i.e. PBEf) one. The two superposed images suggest that the geometrical change is rather small between the initial structure (IP-optimized) and the DFT relaxed one (PBEf). Generally, this is true for also other isomers, indicating that the IP provides reasonable structures for $(TiO_2)_{26}$ nanoparticles. Notice that the global minimum candidate (left side of Figure 5.10c) originates from the isomer found to be 2^{nd} in the ANN energy ranking and 27^{th} in the IP energy ranking. The third most stable isomer instead was 6^{th} in the ANN ranking and 114^{th} in IP ranking.

A similar analysis is also presented for $(TiO_2)_{30}$ nanoparticles in Figure 5.11. The considerations made for $(TiO_2)_{26}$ are still valid with the only difference being that in this case, to find the two most stable isomers both the IP and the ANN yield relatively good results. However, both the IP and the ANN were not able to easily find the 3^{rd}, the 4^{th} and the 5^{th} most stable isomers. We notice that also the PBE ranking is affected when isomers are fully relaxed (i.e. going from PBE to PBEf) while the agreement between ANN and PBE ranking is consistent with $(TiO_2)_{26}$ case. Despite the strong change in the PBEf energy ordering, again the structural relaxation does not seem to dramatically change the atomic positions as we can see from the superposition of initial and relaxed structures in Figure 5.11c). This indicates that for such system size, due to a high density of isomers, small changes in isomer atomic positions causes a large change in the isomer stability order. What remains remarkable from the ANN aided MCBH approach is that the ANN is able to provide a similar energetic description as PBE as indicated from blue lines of graphs 5.10b) and 5.11b). Moreover, the ANN is able to correctly identify as stable isomers which were labeled as not stable from the IP.

5.3.4. Conclusions

We have shown here that artificial neural networks can be used to accurately predict $(TiO_2)_N$ isomer energies at low computational cost. The strength of such approach is the capability of the ANN to find isomers that are relatively unstable according to the IP but actually are highly stable according to DFT. Since these predictions were made for systems with different nanoparticle sizes from those used during the training, we can assert that symmetry functions can capture the underling geometrical features of local atomic environments affecting the energetic stability of nanosized titania. Despite the good results shown for the $(TiO_2)_{30}$ system whose size was slightly larger than the largest nanoparticle in the training set (i.e. $N = 28$), further larger systems should be carefully evaluated each time.

Chapter 6

Hydrated titania and silica nanoparticles

In this chapter we report on the structural stability of silica and titania nanoclusters in the presence of water. Our study is focused on determining how nanoparticle structure and stability changes upon including water molecules in the system. We employ global optimization techniques to find the most stable structure with several hydration degrees. Subsequently we apply *ab initio* statistical thermodynamics to determine the most favoured degree of nanoparticle hydration at each temperature and water vapor condition. This work has been submitted for publication and will soon be available.

6.1. Introduction

As introduced in chapter 3 and 4, silica and titania based nano materials are used in a vast number of applications. In many of these applications such materials come into contact with water containing environments. Understanding how water interacts and affects the properties of these materials is therefore essential in order to optimize their performances. Moreover, water-nanoparticle interactions can determine the aqueous chemistry and exo-toxicity of nano-SiO_2 and nano-TiO_2 and therefore their bottom-up

synthetic process[94–96]. We have already mentioned in the section 5.2 of the previous chapter about the importance of hydration on nanosilica. Following that part, we stress the importance of the hydration effects in nanosilica indicated by a number of works trying to tackle the problem of the early stage aggregation of small nanoparticles in a dynamic equilibrium environment[97–100]. For such systems, processes occurring during the early stages of the formation of large nanoparticles or crystalline materials such as zeolites are not well understood, preventing therefore their rational synthesis. From theoretical perspective, several studies have been attempting to determine most stable structures with approximate size range of 10-100 atoms mainly through IP-based MCBH[89–92] including ours with the cascade Monte Carlo basin hopping approach[101].

Regarding titania nanoparticles, many studies have focused on their photoactivity under UV-light as already mantioned in chapter 4. Several others, focuse more specifically towards photo-dissociative water splitting reaction important for cheap production of Hydrogen and Oxygen to used in fuel cells[102,103]. From theoretical perspective, several studies focused on top-down bulk cut TiO_2 nanoparticles[104–107] and their interaction with water[108–113] containing up to a few thousands of atoms which roughly corresponds to 4.4 nm in diameter. Such calculations have attempted to provide new insight on photocatalytic process of such big nanoparticles although in most cases. Although such great efforts in simulating realistic nanoparticles, typical experimental systems are much larger and complex than simulated ones. Some other experimental studies have characterized the hydration of very small titania nanoclusters in order to emulate the interaction of water with bulk defective sites such as corners and edges containing lowly coordinated cation centers[114]. This was a laser beam experiment in which they isolated $[(TiO_2)_M(D_2O)_N]^-$ clusters with $M = 2-4$ and $N = 1-3$ and measured their vibrational frequencies. Here the structural assignments was only possible through theoretical global optimization methods[115]. The role of globally optimized structures is again crucial in helping experimental observations. In this work we perform an extensive search for $(TiO_2)_M(H_2O)_N$ titania nanoparticles with $M = 4, 8, 12, 16$ and with hydration degrees ($R_{N/M} \times 100$) up to 100% for smallest system and up to 50% for the largest one. Our aim is to study structural

and thermodynamic properties of hydrated TiO_2 and compare them with hydrated SiO_2 which have been already previously studied [90–92,101].

6.2. Methodology

$(TiO_2)_M(H_2O)_N$ structures were obtained with IP-based MCBH global optimization using both the standard and the cascade method developed in the previous chapter. We have parameterized two new IP suited for describing titania nanoparticles. We firstly parameterized an accurate IP (FFTiOH) including core-shell ion models, Buckingham, Morse potentials and a 4-body H-bond description able to correctly describe hydroxyls groups. Secondly we introduced a simpler version of the FFTiOH but a more robust one (FFTiOH*) based only Buckingham potential able to optimize a randomly distorted structure. In developing these IPs we took inspirations from (i) the structural similarities between anhydrous low energy silica and titania nanoclusters and (ii) the well established IP developed for hydroxylated silica nanoparticles [116,117] adapting them to reproduce the correct structural flexibility of titania nanoparticles. All parameters of such IPs are reported in the Table A8 of the Appendix. Extensive search was performed for $(TiO_2)_M(H_2O)_N$ structures with $M = 4, 8, 12, 16$ and $N = 1, 2, 3 \ldots$ To identify the most stable structure we post refine a large number of isomers with a full geometry optimization in a cascade fashion firstly with PBE and finally with PBE0 functional using the tight/tier-1 numerical basis set. We perform frequency calculations for all most stable isomers in order to provide vibrational spectra and thermodynamic properties including temperature and entropic effects. All calculations were performed with FHI-AIMS code.

6.3. Results and Discussions

We have performed global optimization on $(TiO_2)_M(H_2O)_N$ and $(SiO_2)_M(H_2O)_N$ systems with $M = 4$ and $N = 1 - 4$, $M = 8$ and $N = 1 - 5$, $M = 12$ and $N = 1 - 6$ and finally $M = 16$ and $N = 1 - 8$. Only a selection of

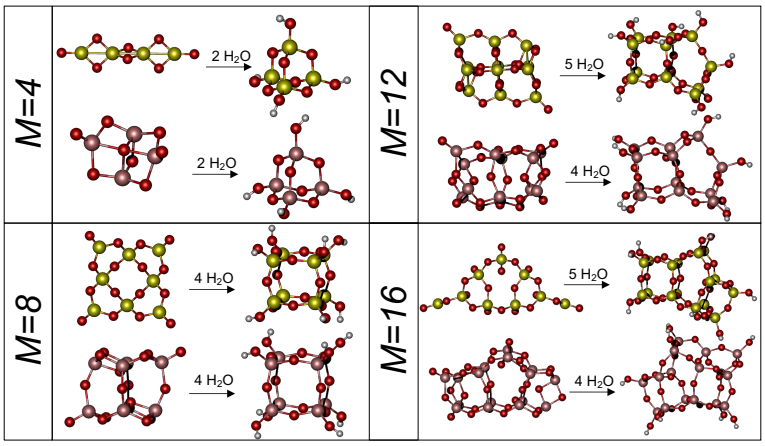

Figure 6.1: Selection of few hydrated nano-TiO_2 and nano-SiO_2 as a result of the hydration reaction from anhydrous particles for each system size M.

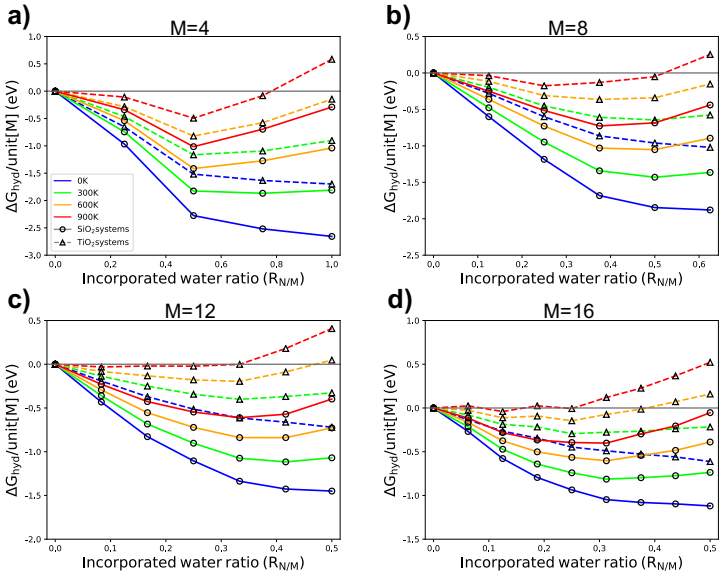

Figure 6.2: Hydration energies free energies of silica and titania nanoclusters for sizes: a) $M = 4$, b) $M = 8$, c) $M = 12$, d) $M = 16$. Hydration free energies are reported at different temperatures while keeping the water partial pressure at 1 Pa which is sufficiently low to consider water as an ideal gas even at ambient conditions. Values of total energy and hydration free energy (at 0 and 300 K at 1 Pa) of both silica and titania nanoclusters are reported in the Table A9 of the Appendix

structures is shown In Figure 6.1. The most relevant hydration effects can be summarized as follow.

1. The most evident effect on the nanoparticles structure is the healing of

terminal defective oxygens naturally present in anhydrous systems.

2. The water adsorption in a dissociation way occurring on cases shown in Figure 6.1. We find that the water is adsorbed in a molecular way only in $(TiO_2)_4(H_2O)_4$, $(TiO_2)_{16}(H_2O)_8$ and $(SiO_2)_{16}(H_2O)_8$ which may indicate a remarkable reactivity of these nanoclusters toward Lewis bases such as the water molecule.
3. Some hydrated nanoclusters including the ones in Figure 6.1 display topologically similar isomers although the significant differences of the corresponding anhydrous structures.
4. Generally, highly hydrated titania clusters are found to be profoundly different with respect to silica especially for the largest systems due to ability of Ti atoms to assume different coordinations ranging from 4 to 6.

In order to study the thermodynamics of the nanoclusters hydration we have calculated the corresponding hydration energy and free energy according the equation 6.1.

$$\Delta G_{hyd} = G_{(\mathrm{XO_2})\mathrm{M}(\mathrm{H_2O})\mathrm{N}} - G_{(\mathrm{XO_2})\mathrm{M}} - NG_{\mathrm{H_2O}} \tag{6.1}$$

where G is the temperature and pressure dependent Gibbs free energy as calculated through *ab initio* statistical thermodynamics (see section 2.6 of chapter 2 for more details) and X is the Si or Ti cation specie.

In Figure 6.2 we plot hydration free energy different temperatures (i.e. 300, 600, 900 K) and the hydration energy at 0 K of all $(TiO_2)_M(H_2O)_N$ and $(SiO_2)_M(H_2O)_N$ systems considered in this work as a function of the incorporated water ratio ($R_{N/M}$). The reported hydration energies at 0 K are calculated simply electronic energy rather the Gibbs free energy for each system. At 0 K, the hydraton energy is found to be increasingly exothermic as the number of incorporated water molecules increases up to -0.5 eV for the in SiO_2 and -1.5 eV for TiO_2 clusters. However, these quantities does not account for thermal end entropic contributions affecting the hydration reaction. Indeed, as the temperature increase, especially in highly hydrated systems which possess a higher entropy ΔG_{hyd} increases consequently towards more positive values. For instance, in several high temperature cases (at 900 K) specially in some titania systems such as $M = 8, 12$ and 16

with $N > 4$ the hydration reaction is even found to be endothermic.

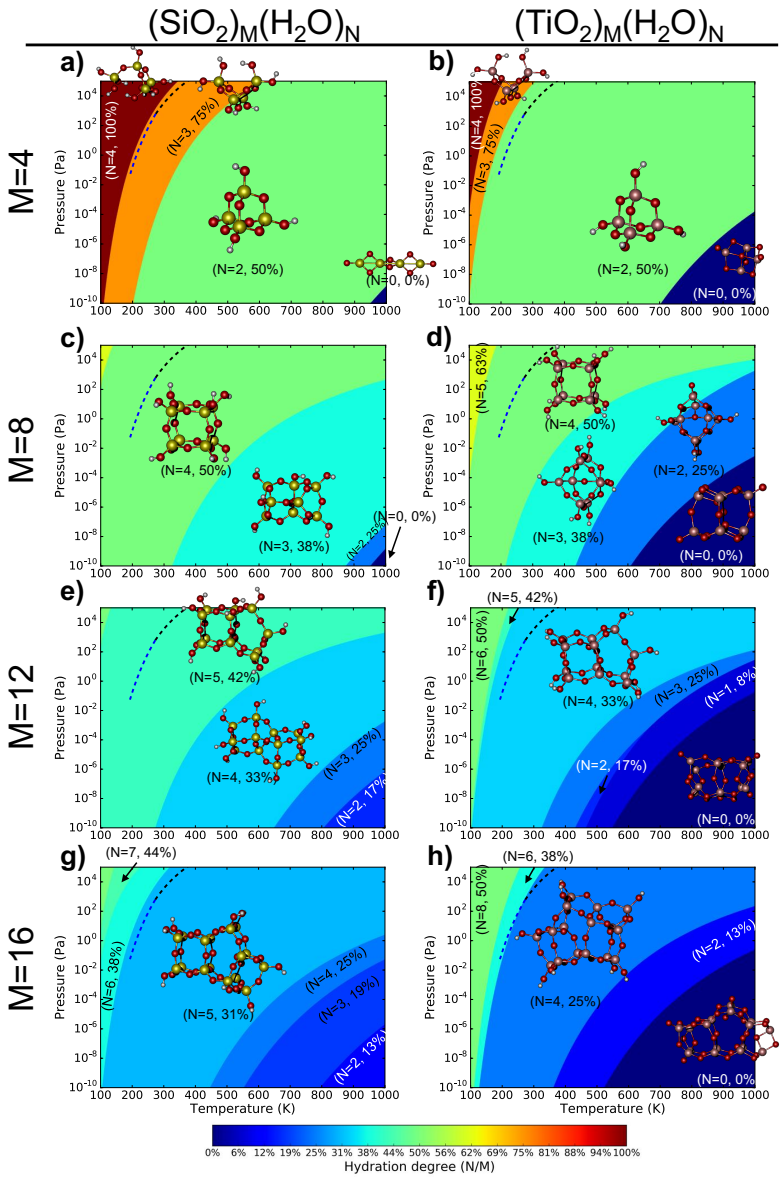

Figure 6.3: Water vapour partial pressure P (Pa) against temperature T (K) phase diagrams for silica in the left side and titania nanoparticles in right side (1×10^5Pa$\simeq$ 1 atm). Blue and black dashed line indicate the equilibrium vapour pressure with respectively ice and liquid water. The phase diagrams colors indicates the most stable structures hydration degree at that specific T and Pa as indicated from the label in parenthesis. Towards blue systems are lowly hydrated while towards red are highly hydrated.

In order to better show the effects of the environmental temperature

and water vapor partial pressure on the nanoparticles hydration we report phase diagrams for each system size in Figure 6.3. Phase diagrams represent the nanoparticle hydration degree at specif temperature and water vapor partial pressure. Regions with colors toward the blue indicates that nanoparticles prefers to be progressively less hydrated while red regions indicate that nanoparticles with high hydration degree are favorable. In each diagram, regions with low pressure and high temperatures (bottom left side) favors anhydrous nanoparticles consistently with the experience. Contrarily, high pressure and low temperature up to the water vapor-to-liquid phase transition, nanoparticles with high hydration degree will be favored. We notice that as the system size (M) increases (going from top diagrams to bottom), highly hydrated nanoparticles tends to be less favored and this behavior is more pronounces in titania systems rather than in silica. This emphasizes the higher tendency of silica nanoparticles to be generally more hydrated then titania.

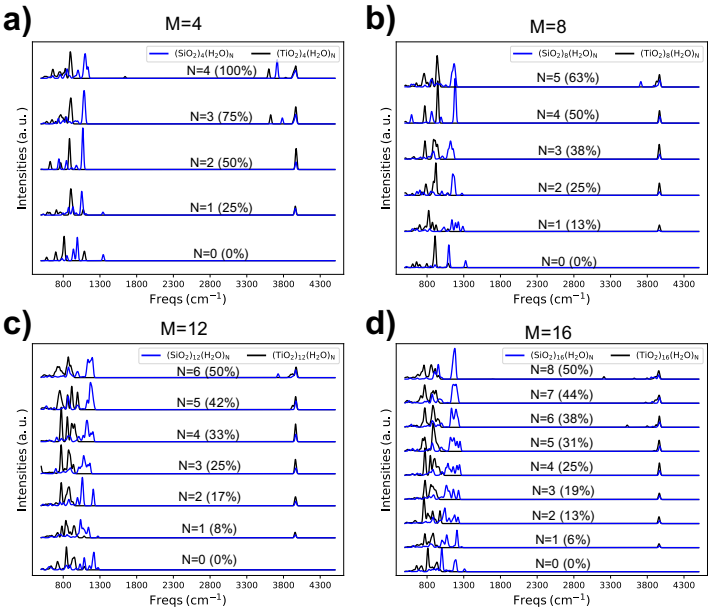

Figure 6.4: Simulated, infrared harmonic vibrational frequencies of silica (blue line) and titania (black line) line systems at different N incorporated water molecules (hydration degrees in parenthesis). a), b), c), d) represents IR spectra of respectively $M = 4, 8, 12, 16$ system sizes. Each graph is scaled with respect to the most intense peak. Intensities are in arbitrary units.

In Figure 6.4 we report the calculated harmonic frequencies of all global

minima titania (black line) and silica (blue line) nanoclusters. In all the spectra the region associated to hydroxyl OH stretching, ν(OH), is around 3900 cm^{-1} and is present for all hydrated systems. OH groups involved in a hydrogen bond (OH–O), likely in highly hydrated clusters, have red-shifted vibration modes in the range of 3000-3900 cm^{-1} proportionally its strength. Cation-O vibrational modes fall in a region between 600 to 1400 cm^{-1} and are relative to complex coupling between stretching and bending modes often involving several atom centres. Ti-O-Ti vibrational modes are found to be more red-shifted (i.e. mostly with vibrational modes lower than 1000 cm^{-1}) with respect to Si-O-Si one (i.e. mostly with vibrational modes higher than 1000 cm^{-1}) reflecting the weaker force constant of Ti-O bonds. Moreover, these modes are found to be slightly blue shifted when increasing the system size and hydration in the case of silica. When the water molecule absorbs in a molecular way it should be a peak around 1600 cm^{-1} which is associated to the water bending mode. This bending mode could be shifted depending on whether the water is involved in a dative bond with titanium centers or in interacts with nanoclusters OH groups forming hydrogen bonds. In our case where water is adsorbed in a molecular way (i.e. titania systems with $M = 4$ and $N = 4$ and both silica and titania systems with $M = 16$ and $N = 8$) such peak exists but is hardly spotted due to its low intensity.

6.4. Conclusions

In this study we have reported several global minima candidates from an extensive global optimization structural search for hydrated titania systems which are little known in litterateur. To do so, we have parametrized a new accurate interatomic potential suited for the study of nano sized hydrated titania system. We have compared energetic and structural properties between $(TiO_2)_M(H_2O)_N$ and $(SiO_2)_M(H_2O)_N$ systems showing in both cases their tendency to be hydrated. Moreover, we have reported also phase diagrams showing thermodynamically preferred hydration degree at specific environmental conditions such as water vapour pressure and temperature. Calculated harmonica vibrational frequencies are also reported for both systems in order eventually help the experimental characterization of

such nanoparticles. We hope that our study on such small hydrated titania and silica systems can inspire other theoretical and experimental works in order to better understand solution chemistry of such nanoparticles.

Thesis conclusions

In this thesis we studied properties of technologically relevant SiO_2 and TiO_2 based materials at nanoscale where experimental characterization is rather difficult. One of the main problems at this size scale is the structural determination of nanoclusters. Here we attempt to determine the most stable structures by performing global optimization studies and providing realistic structural models. Such models have been used subsequently to study the systems size dependent properties such as the structural stability. From such studies we came up with several important predictions and we improved the methods for a better selection of realistic structures in vacuum and in the presence of water. The main results are summarized as follows:

1. We predicted that the mixing between titania and silica is thermodynamically favorable at nanoscale for a wide range of mixing compositions contrary to the bulk. Such materials are used in industry as catalysts for many reactions and their activity is limited by a very little possible mixing composition. For such nanoscale mixed oxide materials we also attempted to predict their possible reactivity towards chemical reduction.

2. Another interesting prediction is related with the titania nanoparticle system size at which occurs the emergence of crystallinity. This prediction gives an estimate on how small titania nanoparticles should be without losing their crystallinity which allows them to have a high photocatalytic activity, that we estimate to be $2.0 - 2.6$ nm.

3. In order to study more complex systems and to find the corresponding most stable structures by global optimization methods we also

propose new approaches such as the cascade Monte Carlo basin hopping and the Machine Learning post refinements. The former is particularly suited for global optimization of complex systems such as hydrated nanoparticles while the later is better suited for large anhydrous nanoparticles with high isomers density. Moreover, we have also developed new IPs suited for titanosilicates, titania and hydrated titania nanoparticles.

4. Finally, we focus on the effect of the water environment on titania systems structural and thermodynamic properties as compared with those of hydrated silica which is better known in literature. Here we report phase diagrams which show the hydration degree of nanoparticles as a function of the temperature and water vapor. We hope with our studies to inspire experimental investigations on such small nanoparticles. A better understanding of the nanoscale behavior of such materials could help developing new ones with enhanced properties with respect to existing ones.

Resumen en español y conclusiones

Introducción

Los materiales óxidos son ampliamente utilizados en la tecnología moderna debido a su amplia variedad de propiedades, como la actividad (foto)catalítica, el magnetismo, la superconductividad y la actividad óptica, mientras son químicamente estables. Al mezclar materiales de óxido, la efectividad y el rango de propiedades se pueden mejorar debido a su cooperación sinérgica. Este efecto es muy conocido, por ejemplo, en catálisis heterogénea y en compuestos cerámicos de alta temperatura[118]. Existen diferentes tipos de materiales mixtos según la aplicación que uno pueda necesitar. Primero, compuestos donde las diferentes fases se mezclan de forma heterogénea. Segundo, materiales dopados donde usualmente una pequeña fracción de uno o más elementos se diluye en la matriz. En tercer lugar, soluciones sólidas, donde los componentes se mezclan homogéneamente en una amplia variedad de composiciones. En este último caso, a veces puede ser difícil obtener un material mezclado homogéneamente o una mezcla con composición especifica debido a diferentes límites de solubilidad recíproca.

Curiosamente, la solubilidad recíproca de dos materiales puede cambiar de acuerdo con el tamaño del sistema. Por ejemplo, los materiales que apenas se mezclan a escala masiva en la composición deseada, se pueden estabilizar en una fase mixta a escala nanométrica[119]. Una nanopartícula posee un diámetro promedio entre 1 y 100 nanómetros (1 nm = 10^{9} m).

Además, es posible identificar tres regímenes de tamaño de material que poseen diferentes características: 1) el régimen escalable donde las propiedades genéricas se amplían con una ley lineal con respecto al tamaño del sistema que alcanza al límite las del bulk, 2) el régimen a nanoescala se describe fenomenológicamente como el régimen en el que los sistemas comienzan a mostrar propiedades diferentes de las del bulk a la reducción de tamaño, 3) y el régimen de clúster en el que las propiedades oscilan en gran medida con pequeños cambios en el tamaño del sistema [9]. Este último régimen también se conoce como la escala en la que cada átomo cuenta. Los nanomateriales exhiben propiedades que son muy diferentes a las del bulk y están atrayendo gran atención debido a sus aplicaciones en nanotecnologías. El origen de sus peculiares propiedades radica principalmente en el aumento de las relaciones superficie-volumen y en la presencia de esquinas y bordes para nanopartículas no esféricas. Además, más allá de las propiedades estructurales y morfológicas, los nanomateriales muestran propiedades electrónicas únicas y distintas.

A pesar del gran impacto de los materiales de nano-óxido en la tecnología actual, la caracterización estructural experimental a menudo es muy difícil, especialmente en el régimen de clúster. El papel de la teoría en la descripción de tales materiales de tamaño nanométrico es esencial para proporcionar modelos estructurales realistas que puedan caracterizarse a partir de sus propiedades, como la estructura electrónica, la reactividad química, etc.

En esta Tesis Doctoral nos hemos centrado en los nanomateriales de óxido a base de titania y sílice, y mezclas de los mismos, es decir, titanosilicatos. Estos materiales fueron elegidos entre muchos otros debido a sus propiedades únicas y su gran uso en la tecnología moderna. Estudiamos sus propiedades en el régimen de tamaño de nanoescala donde la caracterización experimental es difícilmente accesible. Durante gran parte de esta Tesis, nos centramos en las propiedades estructurales y energéticas dependientes del tamaño de las nanopartículas optimizadas globalmente. Además, también caracterizamos la reactividad química de algunos sistemas que se centran principalmente en la reducción de tales nanopartículas. En las siguientes secciones presento un breve resumen de los proyectos de investigación trabajados durante este programa de doctorado de 3 años.

Nanopartículas de titaniosilicatos

Los óxidos basados en la mezcla de titania (TiO_2) y sílice (SiO_2), a saber, titanosilicatos, representan una clase importante de materiales ampliamente estudiados y utilizados para muchas aplicaciones tecnológicas y ecológicas, como células solares, sistemas autolimpiantes, sensores de gas, tamices moleculares selectivos, material para eliminar contaminantes del agua y fotocatalizadores para un abanico de reacciones[52–57]. En muchas aplicaciones, los titanosilicatos no solo aprovechan las propiedades de la titania pura (semiconductor) y la sílice (alta estabilidad térmica y alta resistencia mecánica), sino de las propiedades sinérgicas que surgen de la interacción TiO_2 - SiO_2 (por ejemplo, formación de nuevos sitios catalíticos). Como ejemplo, uno de los materiales mixtos TiO_2 - SiO_2 más importantes desde el punto de vista industrial, conocido a principios de los 80, es el titanosilicato-1 sintético (TS-1)[58]. Se utiliza como catalizador redox industrial para oxidar moléculas orgánicas en condiciones suaves en presencia de peróxido de hidrógeno. El sitio activo es un titanio tetracoordinado uniformemente disperso en una estructura de sílice porosa con una inclusión molar de 1,0-2,5 % de TiO_2. En tales sistemas, aumentar la cantidad de contenido de TiO_2 conduce a una segregación de titania, por lo tanto, se produce una separación de fases que indica la metaestabilidad termodinámica de los titanosilicatos mixtos. A pesar del gran éxito industrial de dichos materiales, se sabe muy poco sobre su comportamiento, particularmente en lo que respecta a su mezcla, en escala nanométrica.

En este proyecto, queremos lograr una mejor comprensión de la fuerza impulsora detrás de la mezcla de titania con sílice en un nivel microscópico fundamental. Para hacerlo, utilizamos una gama de métodos de modelado computacional, como optimización global y métodos *ab initio* para estudiar la estabilidad de la estructura variando de la composición de la mezcla y de el tamaño del sistema. Nuestro objetivo principal es comprender por qué y cómo se mezclan estos materiales en escala nanométrica. El objetivo secundario es caracterizarlos (teóricamente) desde un punto de vista químico-físico y proporcionar información útil para sintetizarlos experimentalmente.

Métodos. Empleamos el método de optimización global Monte Carlo

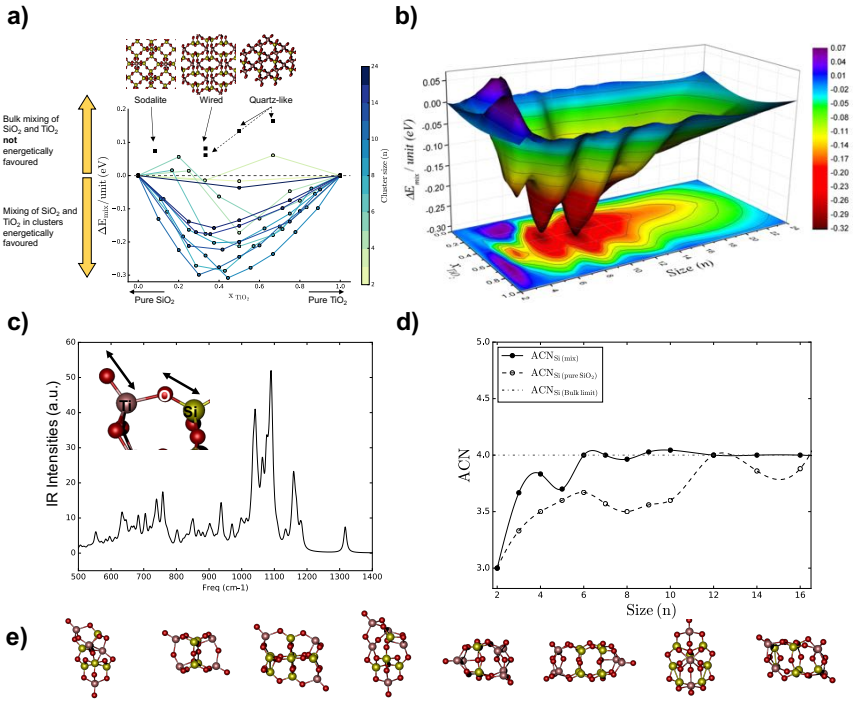

Figura E1: a) La energía de mezcla de titanosilicatos de bulk y de nanoclusters optimizados globalmente se indica en función de la fracción molar de TiO_2. b) Energía de mezcla de nanopartículas trazada en superficie tridimensional respecto a la fracción molar de TiO_2 y el tamaño de los nanoclusters. Todas las energías están normalizadas por el número de unidades de óxido. c) Espectro armónico infrarrojo (IR) calculado de un conjunto de nanopartículas de titanosilicatos. d) Número promedio de coordinación de átomos de silicio en sílice pura (línea discontinua) y en nanopartículas de titanosilicato (línea continua). e) Algunos de los modelos predichos más estables de nanoclusters de titanosilicato. Clave de color: Ti en gris, Si amarillo y O en rojo.

Basin Hopping (MCBH)[39] basado en los Potencial Interatómicos (IPs) para encontrar el isómero más estable. Tal método permite explorar la superficie de energía potencial (PES) de nanoclusters mediante distorsión aleatoria y relajación de la geometría del sistema de forma iterativa. En cada iteración, la geometría se relaja con un IP basado en el potencial de Buckingham y luego, el criterio probabilístico de Metrópolis, que se basa en el cambio en la energía total y una temperatura ficticia, se aplica para determinar si se acepta o rechaza el nuevo isómero. El IP se deriva de parametrizaciones previamente conocidas utilizadas a partir de nanoclusters de sílice y titania y adaptadas para los titanosilicatos mixtos. Aunque la descripción intrínseca

es pobre con el IP, tal enfoque permite de muestrear de manera eficiente hasta varios cientos de miles de isómeros diferentes. Para compensar esa naturaleza aproximada del IP, varias estructuras que resultan más estables se refinan posteriormente por medio de métodos DFT que emplean el funcional híbrido PBE0 y los orbitales atómicos numéricos tight / tier-1. Usamos FHI-AIMS para cálculos de DFT que se considera un código de alta precisión. Este enfoque permite encontrar eficientemente el isómero de titanosilicato más estable mientras que describe su estabilidad con un método altamente preciso que también asegura predicciones precisas.

Resultados. Proporcionamos, mediante un estudio sistemático, estructuras modelo de nano-titanosilicatos para toda la gama de composiciones (es decir, TiO_2 fracción molar incorporada que va de 0 a 1) y tamaños hasta 24 formula MO_2 unidades (M = Si, Ti). Predecimos que, a diferencia de los sistemas de bulk macroscópicos, a escala nanométrica, la mezcla entre sílice y titania es termodinámicamente favorable (Fig. E1a). Esto se muestra claramente a partir de la energía de mezcla (ΔE_{mix}) que es negativa cuando la mezcla se produce a nivel de nanoescala mientras que es positiva a nivel de bulk. La máxima favorabilidad de mezcla está asociada a grupos con un tamaño de aproximadamente 1.0 nm (entre 9 y 12 unidades) y con una composición de mezcla entre 0.3 y 0.4 TiO_2fracción molar. Al aumentar el tamaño de los clusters, la ventaja energética para mezclar se agota lentamente. Este efecto es particularmente evidente en la Fig. E1b) en la que la energía de mezcla se traza en función de la composición de mezcla y el tamaño del sistema en un gráfico de superficie sólida tridimensional. Además, las energías libres de mezcla de Gibbs se estiman a partir de cálculos de frecuencia vibracional *ab initio* para una mejor evaluación de la estabilidad termodinámica. Los resultados sugieren que la mezcla es favorable hasta temperaturas de 900 K para todos los tamaños de agregados considerados.

El factor estructural más importante asociado con la mezcla favorable se relaciona con los centros defectuosos (oxígenos monocoordinados) presentes naturalmente en la superficie de estos nanoclusters en este régimen de tamaño. Nuestras estructuras predichas, en parte mostradas en la Fig. E1e), nunca han sido sintetizadas antes. Por lo tanto, esperamos inspirar a los grupos experimentales en esta tarea para una clase de material tan importante.

Para ayudar a caracterizar experimentalmente los nanoclusters de titanosilicatos, reportamos los espectros de frecuencia armónica calculados para sílice pura, titania pura y cluster mezclados de titanosilicatos (Fig. E1 c). Los espectros muestran la presencia de picos únicos y intensos a 1035 y 1090 cm-1 que son una signatura de titanosilicatos mezclados y que permite distinguirlos de nanoparticulas pura. Además, damos los numeros promedio de coordinación atómica ya que esta información estructural puede ser accesible a través de la técnica experimental EXAFS. En nuestros sistemas, el número promedio de coordinación de silicio en nanoclusters mixtos es significativamente diferente del de nanoclusters de sílice pura. Esto persiste para una amplia gama de tamaños evaluados aquí y podría usarse como un signo de la presencia de titanosilicatos mixtos.

Este trabajo ha sido publicado: Andi Cuko, Monica Calatayud y Stefan T. Bromley. "Stability of mixed-oxide titanosilicates: dependency on size and composition from nanocluster to bulk."*Nanoscale*, **10**,832–842, 2018.

Reactividad química de las nanopartículas de Titania, sílice y titanosilicato

El objetivo del proyecto anterior era encontrar nanopartículas de titania, sílice y titanosilicatos que son enérgicamente más estables y estudiar sus propiedades estructurales, energéticas y dependientes del tamaño. En esta sección, daremos una visión general de nuestra investigación sobre las propiedades químicas de dichos sistemas. Más específicamente, exploramos la reducibilidad química de las nanopartículas con el fin de predecir su posible reactividad hacia los agentes reductores por caracterizar su comportamiento redox. Muchos de los sistemas aquí predichos para ser estables (especialmente titanosilicatos), hasta donde sabemos, nunca se han sintetizado y caracterizado antes. Por lo tanto, esperamos dilucidar su reactividad a partir de investigaciones teóricas.

Desde el punto de vista químico, la reducibilidad de un material es su tendencia a adquirir electrones y a reducir su número de oxidación formal. Por ejemplo, en los materiales de óxido ordinarios, los átomos de Ti

tienen una carga formal +IV y la configuración electrónica correspondiente a la del Argón (es decir,$1s^2 2s^2 2p^6 3s^2 3p^6$). Como los orbitales $4s$ y $3d$ son energéticamente accesibles, los átomos de Ti pueden tomar un electrón del entorno para convertirse en +III. Esto afecta, por ejemplo, las propiedades ópticas macroscópicas del sistema que transforma los cristales de rutilo blancos en minerales coloreados, dependiendo de la presencia de Ti^{3+} o la presencia de especies dopantes. Además, esto puede confirmarse con técnicas experimentales sensibles a electrones desapareados, como la Resonancia Paramagnética Electrónica (EPR), ya que Ti^{3+} tiene una naturaleza radicalaria. Como ejemplo de tendencia opuesta, la magnesia (MgO) se considera un material no reducible ya que los átomos de Mg dificilmente reducen su número de oxidación formal. Mg^{2+} tiene la configuración electrónica de Neon (es decir,$1s^2 2s^2 2p^6$) y los orbitales $3s$ no estan energéticamente accesibles y, por lo tanto, tienden a evitar la adquisición de más electrones. Si se fuerza la reducción de magnesia, los electrones se estabilizarán por el campo reticular de Madelung formando los llamados centros F (es decir, electrones localizados en la red cristalina). Dos de las formas más comunes de estudiar la reducibilidad del material se basan en (i) la creación de defectos de vacantes de oxígeno en el sistema y (ii) la reacción de hidrogenación donde H_2 es el agente reductor.

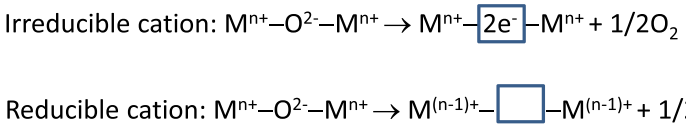

Figura E2: Una representación esquemática de la reducibilidad e irreducibilidad de los materiales.

Al comienzo de este estudio, seleccionamos los sistemas $(Ti_xSi_{1-x}O)_{10}$ (con tamaño de 10 unitades de óxido) globalmente optimizados con $0 < x < 1$ y eliminamos un solo átomo de oxígeno de estas estructuras de manera sistemática explorando la eliminación de todos los posibles sitios. Las estructuras no estequiométricas se relajan completamente al mismo nivel de teoría de las estequiométricas (es decir, PBE0 con un conjunto de set bases numericos tight/tier-1). Todos los cálculos son de tipo capa abierta restringido. La energía de formación de vacantes de oxígeno,$\Delta E^f_{O_v}$, se calcula con la

siguiente ecuación química: Al comienzo de este estudio, seleccionamos los sistemas ($Ti_xSi_{1-x}O)_{10}$ (con tamaño de 10 unitades de óxido) globalmente optimizados con $0 < x < 1$ y eliminamos un solo átomo de oxígeno de estas estructuras de manera sistemática explorando la eliminación de todos los posibles sitios. Las estructuras no estequiométricas se relajan completamente al mismo nivel de teoría de las estequiométricas (es decir, PBE0 con un conjunto de set bases numericos tight/tier-1). Todos los cálculos son de tipo capa abierta restringido. La energía de formación de vacantes de oxígeno,$\Delta E^f_{O_v}$, se calcula con la siguiente ecuación química: En la Fig. E2 hay una representación esquemática que indica el comportamiento de materiales reducibles e irreductibles tras la eliminación de un átomo de oxígeno. Nuestra idea aquí es explorar la dependencia del tamaño de la reducibilidad de las nanopartículas de sílice, titania y titanosilicato. Este trabajo aún está en progreso, por lo tanto, solo se resumirán aquí los resultados obtenidos hasta ahora en relación con la formación de vacante de oxígeno. Primero se estudia el efecto de la composición y de la relajación en un cluster de 10 unidades, después se estudia el efecto del tamaño en agregados de titania y silice puros.

Formación de vacante de oxígeno

Al comienzo de este estudio, seleccionamos los sistemas ($Ti_xSi_{1-x}O)_{10}$ (con tamaño de 10 unitades de óxido) globalmente optimizados con $0 < x < 1$ y eliminamos un solo átomo de oxígeno de estas estructuras de manera sistemática explorando la eliminación de todos los posibles sitios. Las estructuras no estequiométricas se relajan completamente al mismo nivel de teoría de las estequiométricas (es decir, PBE0 con un conjunto de set bases numericos tight/tier-1). Todos los cálculos son de tipo capa abierta no restringido. La energía de formación de vacantes de oxígeno,$\Delta E^f_{O_v}$, se calcula con la siguiente ecuación química:

$$\mathrm{M}_n\mathrm{O}2n \rightleftarrows \mathrm{M}_n\mathrm{O}2n - 1 + \frac{1}{2}\,\mathrm{O}2$$

$$\Delta E^f_{O_v} = E_{M_nO_{2n-1}} + \frac{1}{2}E_{O_2} - E_{M_nO_{2n}}$$

La energía de formación de vacantes de oxígeno cuantifica el costo energético de eliminar un oxígeno del sistema. Cuando el costo energético de eliminar un oxígeno es alto, en principio, indica que el sistema no es fácilmente reducible. Por el contrario, cuando el costo de la energía de eliminación de oxígeno es bajo, el sistema tiende a ser fácilmente reducible.

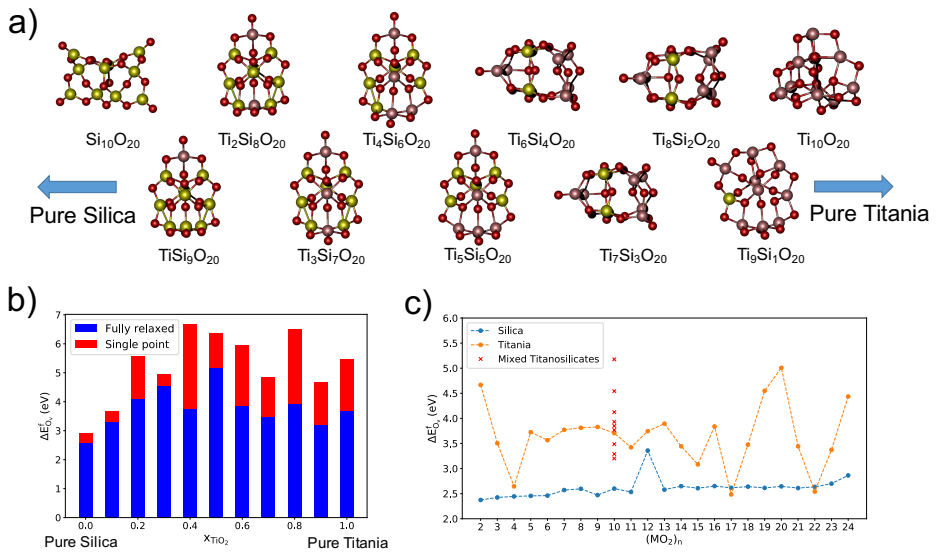

Figura E3: a) Isómeros más estable de $(\mathrm{Ti}_x\mathrm{Si}1-x\,\mathrm{O})10$ con $0 < x < 1$ y b) su correspondiente formación de vacante de oxígeno energía $\Delta E^f_{O_v}$ con respecto a la composición de lamezcla. La barra roja + azul indica el $\Delta E^f_{O_v}$ de la geometría congelada, mientras que el azul solo indica el $\Delta E^f_{O_v}$ de la geometría relajada. c) Dependencia de tamaño de $\Delta E^f_{O_v}$ en nanoclusters de sílice y de titania. En todos los casos reportados, se muestran solo las $\Delta E^f_{O_v}$ que surgen del mejor sitio de eliminación de O (es decir, el oxígeno con la energía de formación de vacante más baja).

Vacante de oxígeno en $(\mathrm{Ti}_x\mathrm{Si}1-x\,\mathrm{O})10$

En la Figura E3 a) mostramos las estructuras de nanopartículas mas estables utilizados en esta primera parte de nuestro estudio. En dichos sistemas, primero calculamos $\Delta E^f_{O_v}$ y los resultados se muestran en la Figura E3 b).

Los valores de energía presentados aquí son relativos a los sistemas que muestran la formación de vacante de oxígeno menos costosa e incluyen los efectos de la relajación de la geometría (es decir, la parte roja de cada barra). De nuestros resultados, sorprendentemente, se encontró que el sistema de nanosílice puro tiene una energía de formación de vacantes de oxígeno menor que los titanosilicatos mixtos y el sistema de titania puro. Esto es sorprendente porque se sabe que la reducibilidad de sistemas bulk es inversa y, por lo tanto, la energía de formación de vacantes de oxígeno es la inversa[65] : $\Delta E^f_{O_v}$ 3.7-4.8 eV para el cristal rutilo, 4.2-5.3 para anatasa y 8.2 para quartz.

Es interesante ver que la relajación es poco importante para los sistemas ricos en silicio mientras que para la titania puede implicar hasta 40 % de la energía: alrededor de 0.2 eV para 0 y 10 % de silicio, 3 eV para 40 % y 80 %.

Vacante de oxígeno en $(TiO_2)_N$ y $(SiO_2)_N$

Como segundo paso, queríamos estudiar la dependencia de tamaño de $\Delta E^f_{O_v}$ únicamente del sistema puro, esperando encontrar el tamaño en el que esta tendencia nanoescalar .ªnómalarecupera el comportamiento de los materiales de bulk. Para tamaños relativamente pequeños, se tomaron muestras de todas las posibles eliminaciones de oxígeno de los sistemas estequiométricos, mientras que para sistemas relativamente grandes se realizó un muestreo aleatorio. En todos los casos, los sistemas no estequiométricos se relajan completamente con el método PBE0 con tipo de calculo open-shell no restringido y utilizando funciones de base numérica centrada en el átomo tight/tier-1. Los resultados de tal estudio se informan en la figura E3c) que muestra que los nanoclusters de sílice pura son persistentemente más reducibles que la titania para los tamaños del sistema considerados aquí. En todos los sistemas de sílice, el sitio vacante responsable de un valor tan bajo de $\Delta E^f_{O_v}$ es el oxígeno terminal de un átomo de silicio tricoordinado, que dejan un silicio dicoordinado después de su eliminación. Dichos sitios terminales defectuosos están presentes en la mayoría de los mínimos globales con la única excepción del sistema $(SiO_2)_{12}$ que muestra un tipo diferente de defectos terminales llamado Non Bridging Oxygen (NBO) donde cada uno de los oxígenos terminales esta unido a un centro de silicio tetracoordinado. Sin embargo, en la mayoría de los casos, la eliminación de oxígeno resultó menos costosa para las nanopartículas de sílice que para la titania. Solo unos pocos sistemas de titania muestran un $\Delta E^f_{O_v}$ comparable a la

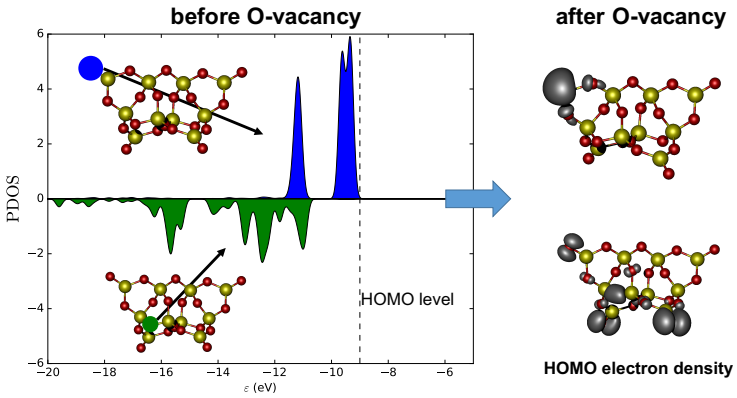

Figura E4: Densidad proyectada de los estados enegeticos (PDOS) de dos atoms de O, en azul el oxígeno terminal mientras que en verde el oxígeno interno antes de la eliminación (izquierda) y la respectiva densidad electrónica relativa al orbital HOMO después de la eliminación (derecha)

sílice. En tales sistemas, las estructuras de titania se relajan de forma tal que la vacancia se mueve fuera de la nanopartícula reemplazando al oxígeno terminal existente.

Estructura electrónica de nanopartículas reducidas.
Hemos investigado más a fondo el origen de una mayor reducibilidad química de sílice que la titania desde un análisis de la estructura electrónica. Intentamos racionalizar por qué los oxígenos terminales tienen un valor tan bajo $\Delta E^{f}_{O_v}$ con respecto a otros oxígenos en la estructura. Generalmente, la eliminación de un átomo de oxígeno neutro produce un exceso de dos electrones que reducen dos centros de cationes. El costo de eliminar diferentes oxígenos puede variar dependiendo de su sitio en el nanocluster y de su coordinación. En las nanopartículas de titania, la eliminación de oxígeno siempre conduciría a la reducción de dos átomos de Ti. En el caso de la sílice, el costo de eliminar el oxígeno terminal es mucho menor que el de otros oxígenos. El oxígeno terminal posee estados electrónicos asociados al HOMO mientras que otros oxígenos tienen estados a valores energéticos más bajos. Por lo tanto, la eliminación de oxígeno con estados electrónicos menos energéticos afecta más la estabilidad del sistema que la eliminación de un oxígeno que contribuye solo a los estados de energía más altos del sistema. Para ilustrar esto, en la figura E4 graficamos la densidad proyectada de estados de solo oxígenos que se van a eliminar, el oxígeno terminal (azul)

y el oxígeno interno (verde). Después de eliminar los oxígenos terminales (parte superior de la figura E4) obtenemos que los 2 electrones están localizados alrededor del silicio más cercano que se está reduciendo. En su lugar, al eliminar cualquier otro oxígeno puenteado (lado inferior de la figura E4), los electrones se deslocalizan entre los otros oxígenos colgantes y no se reducen los cationes de Si. Esto indica que solo los átomos de silicio unidos con oxígenos terminales defectuosos se reducen en nanopartículas de SiO_2. De la forma del HOMO de estos sistemas se deduce que el silicio posee un par libre de electrones ocupando un orbital sp2.

Como hemos demostrado, la energía de formación de vacantes de oxígeno puede dar una indicación cualitativa de la reducibilidad de las nanopartículas. Sin embargo, solo un análisis detallado de la estructura electrónica puede proporcionar información sobre la capacidad de reducción y, por lo tanto, sobre la reactividad de estos sistemas muy pequeños. Estamos ampliando nuestro estudio sobre la formación de vacantes de oxigeno también para titanosilicatos para eventualmente guiar su caracterización experimental.

Aparición de la cristalinidad en nanopartículas de titania

Los materiales de dióxido de titanio son ampliamente utilizados y estudiados tanto en la industria como en la academia por sus excepcionales propiedades electrónicas. De hecho, son sistemas fotoactivos con aplicaciones como fotocatalizador, células solares, sistemas de disociación del agua, etc.[73–77]. Los materiales de Titania poseen una fuerte dependencia de tamaño tanto de la estructura como de las propiedades. En condiciones ambientales, la estructura del rutilo es la fase más estable termodinámicamente. Al reducir el tamaño del sistema, cuando el diámetro medio de las nanopartículas es inferior a 14 nm, ocurre una transición de fase en la que la estructura de la anatasa se convierte en la fase más estable. Contrariamente a la fase de rutilo, los nanocristales de anatasa muestran una fuerte fotoactividad, así se emplean para varios materiales basados en nano titania como fotocatalizadores, protectores solares, materiales de construcción

anticontaminación, etc. Una mayor reducción en el tamaño de los nanocristales de anatasa originará nanoparticulas que generalmente no poseen un orden cristalino y no muestran actividad fotoquímica. Existen evidencias experimentales de que los nanocristales de anatasa persisten térmicamente cuando el diámetro de las partículas es aproximadamente de 4 nm[79], sin embargo, no está claro si las nanopartículas retienen o no una morfología cristalina. Las nanopartículas con un tamaño entre 2 y 3 nm, a partir de evidencias experimentales indirectas, muestran un núcleo cristalino y una morfología de corteza amorfa. Una disminución adicional del tamaño del sistema conduce al final a especies completamente amorfas[80].

El objetivo de este trabajo es determinar el tamaño de transición entre nanopartículas amorfas a cristalinas. Para estimar dicho tamaño de transición, consideramos los nanocristales TiO_2 desde un enfoque top-down y nanoclusters amorfos desde un enfoque bottom-up, cuyas estabilidades relativas se evalúan mediante cálculos mecánicos.

Estrategia y métodos. Desde un enfoque top-down, seleccionamos un conjunto de nanocristales de anatasa con diferentes tamaños, como se muestra en la Figura E5. La mayoría de las estructuras elegidas tienen la morfología de Wulff[84] obtenida deste una minimización de la energía superficial total de las nanopartículas. Para las nanopartículas de anatasa en fase gaseosa, dicha morfología corresponde a una forma bi-piramidal o bi-piramidal truncada. Desde un enfoque bottom-up, consideramos las nanopartículas optimizadas globalmente con tamaño creciente con N = 1-24, 28, 35 y 38, donde N es el número de unidades de óxido. Desde el punto de vista estructural, las nanopartículas de titania optimizadas globalmente tienden a ser bastante compactas y muestran una baja simetría. Estas características estructurales surgen de la flexibilidad intrínseca y natural de la red Ti-O en este régimen de tamaño en el que, por ejemplo, los átomos de titanio pueden estar coordinados con 4, 5 o incluso 6 aniones de oxígeno. De hecho, las nanopartículas suficientemente grandes muestran una mayor coordinación media del catión debido a un mayor número de centros de titanio penta y / o hexacoordinados. En general, los cationes más coordinados tienden a permanecer en el centro de las nanopartículas, mientras que los tetracoordinados tienden a colocarse en la superficie de las nanopartículas. Tales características hacen particularmente difícil la optimización global de

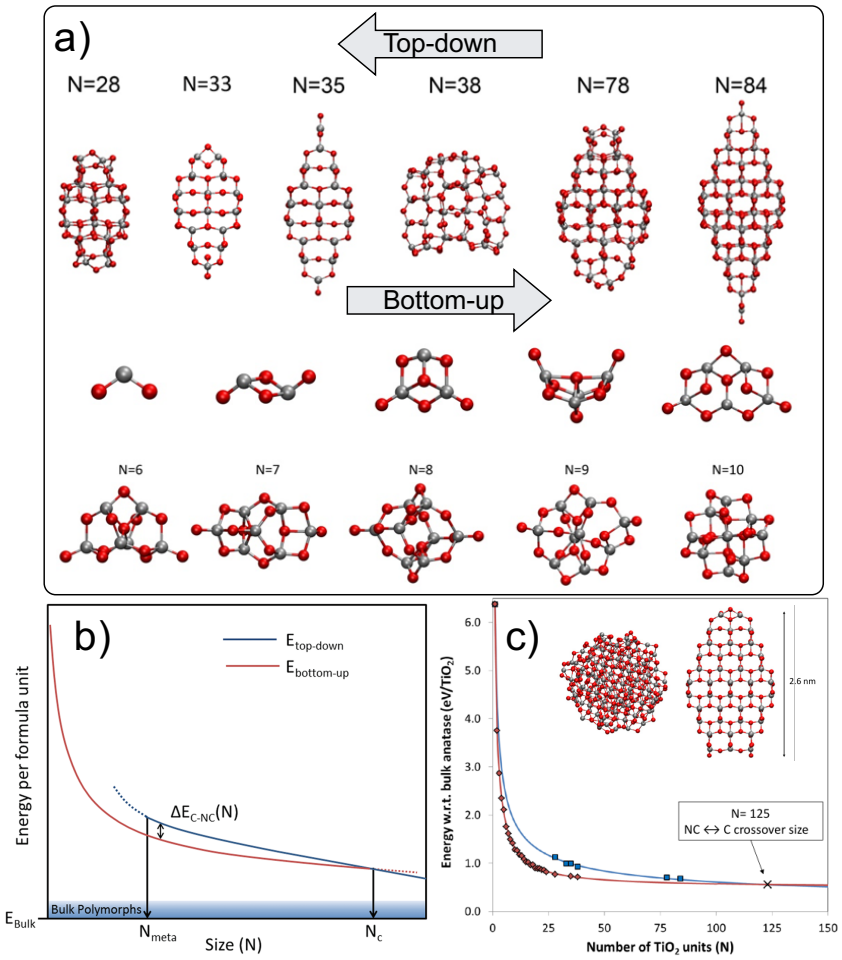

Figura E5: a) Una selección de pocas nanopartículas de TiO_2 de nanocristales de anatasa (top-down) y de nanopartículas optimizadas globalmente en este estudio. b) Una representación esquemática de las estabilidades de las nanopartículas en función del tamaño del sistema. c) Estabilidad dependiente del tamaño de nanopartículas cristalinas (azul) y no cristalinas (rojo) obtenido en nuestro estudio con el relativo tamaño de transición de fase extrapolado.

las nanopartículas de titania. De hecho, numerosos estudios previos han intentado encontrar candidatos mínimos globales para nanopartículas de TiO_2 en este régimen de tamaño. Aquí empleamos el enfoque MCBH basado en IP de manera similar a la utilizada para titanosilicatos (ver arriba). Después del enfoque de optimización global, un número relativamente grande de nanopartículas se relajan por completo a nivel de teoría DFT. Los candidatos de mínimos globales presentados aquí son el resultado de una serie de refinamientos posteriores en cascada y su estabilidad final se calcula

usando el funcional PBE0 que emplea una base numérica tight/tier-1 con el codigo FHI-AIMS.

En Figure E5 c) graficamos la estabilidad de nanopartículas no cristalinas optimizadas globalmente (puntos rojos) y la estabilidad de los nanocristales cortados con anatasa (puntos azules) con respecto a la fase de anatasa bulk. Generalmente, la estabilidad estructural de las nanopartículas en el régimen escalable se escala linealmente con la relación de superficie a volumen a medida que aumenta el tamaño del sistema. La relación superficie-volumen, a su vez, se escala aproximadamente como $N^{-}3$ donde N es el número de átomos que depende de la forma de la nanopartícula. En el régimen no escalable, otros factores como la compresibilidad de las nanopartículas comienzan a desempeñar un papel importante que se puede tener en cuenta mediante una expansión polinómica de la ley de estabilidad del régimen escalable. Por lo tanto, en primer lugar ajustamos la estabilidad de los sistemas cristalinos y no cristalinos a leyes de potencia inversa con respecto al número de átomos. En segundo lugar, estimamos que el tamaño de cruce de la transición entre nanopartículas de titania no cristalino a cristalino (NC↔C) ocurre cuando el diámetro promedio de la partícula es de alrededor de 2-2.6 nm. Esto corresponde al punto extrapolado en el que se encuentran las dos curvas de estabilidad de abajo hacia arriba y de arriba hacia abajo. A este tamaño TiO_2 las nanopartículas pueden tener una morfología Wulff construida truncada o un núcleo cristalino y una morfología esférica de corteza amorfa. Esta predicción está respaldada por observaciones experimentales indirectas[80].

Este trabajo ha sido publicado: Oriol Lamiel-Garcia, Andi Cuko, Monica Calatayud, Francesc Illas, and Stefan T. Bromley. "Predicting size-dependent emergence of crystallinity in nanomaterials: titania nanoclusters versus nanocrystals". *Nanoscale*, **9**, 1049–1058, 2017.

Procedimientos de refinamiento de *Basin Hopping*

En este trabajo hemos estudiado una mejora del método de optimización global utilizado hasta este momento. En términos generales, la opti-

mización global con el algoritmo Monte Carlo *basin hopping* basada en el IP tiene algunas limitaciones originadas, en primer lugar, por la naturaleza aproximada del IP. Por ejemplo, la geometría optimizada de un sistema en particular puede ser diferente si se obtiene con un IP en lugar de con métodos mecano-cuánticos. Además, también el orden de energía de un conjunto de isómeros puede verse afectado por una descripción deficiente de IP. Aunque la discrepancia entre la PES mecánico clásico y cuántico, solo el enfoque clásico es lo suficientemente eficiente como para permitir un muestreo amplio y exhaustivo del espacio de configuración. Con el fin de corregir dicha discrepancia, un número relativamente grande de estructuras de baja energía optimizadas para IP se someten a refinamientos posteriores con métodos cuánticos. En la figura E6 mostramos una representación esquemática del método de salto de cuenca Monte Carlo basado en IP utilizado hasta ahora.

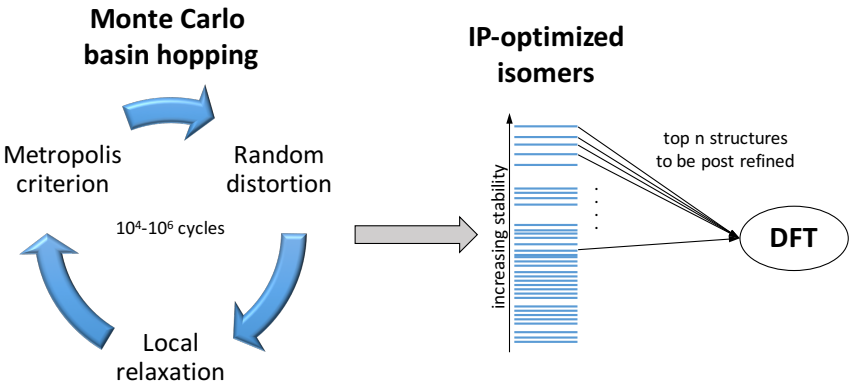

Figura E6: Una ilustración esquemática del refinamiento en cascada dentro del procedimiento de optimización global que proporciona una descripción muy mejorada de los grupos hidroxilo.

En este proyecto, presentamos dos enfoques que pueden mejorar la búsqueda de isómeros estables en dos situaciones diferentes. Nuestro primer enfoque, el Cascade Monte Carlo basin hopping, es un procedimiento de refinamiento de la estructura: internamente en el ciclo de optimización, cada movimiento de exploración corresponde a una relajación geométrica en cascada con dos o más IP cada vez más precisas. Tal enfoque es particularmente adecuado para explorar la PES de sistemas hidratados que potencialmente tienen diferentes redes de H-bond superficiales que pueden afectar la estabilidad de los isómeros y, por lo tanto, deben describirse con una IP adecuada.

En el segundo enfoque, empleamos algoritmos de Machine Learning (ML) tales como Neural Networks como un procedimiento de refinamiento de *basin hopping* para mejorar la estabilidad y el orden energético de los isómeros obtenidos.

Monte Carlo *Basin Hopping* en cascada

El primer enfoque se desarrolla con el fin de explorar la PES de la nanopartícula de óxido inmerso en un entorno específico, como el agua. En el caso de nuestras nanopartículas de óxido a base de sílice y titania, las moléculas de agua se adsorben químicamente en forma disociativa por pequeños grados de hidratación. Encontrar la estructura más estable para sistemas hidroxilados puede ser difícil, especialmente para sistemas altamente hidratados. Tales dificultades derivan especialmente de la elección del IP. IP precisas, típicamente se basan en una parametrización diferente de tipos de átomos de oxígeno de grupos hidroxilo (es decir, OH) a partir de los átomos de oxígeno puente (por ejemplo, Si-O-Si). La asignación de si un oxígeno pertenece a un grupo hidroxilo o al grupo sin puente en un sistema distorsionado aleatoriamente como paso del procedimiento de salto de cuenca donde se pierden las conexiones entre átomos es bastante problemático. Nuestro enfoque consiste en emplear dos pasos de minimización de energía consecutivos en cada ciclo de basin hopping: (i) un IP ligeramente parametrizado pero computacionalmente eficiente que no distingue entre isómeros conformacionales de H-bond, y luego (ii) un IP más sofisticado que tiene en cuenta la polarización y los H-bonds. Las nanopartículas de sílice proporcionan un estudio de caso perfecto por varias razones: (i) se sabe que el sistema es altamente propenso a reaccionar con agua debido a un gran número de centros defectuosos, (ii) existe la disponibilidad de IP precisas y ligeramente parametrizadas adecuadas para el sistema, (iii) para tamaños de sistema y grados de hidratación específicos, los candidatos mínimos globales ya se reportaron en estudios previos, por lo tanto, tenemos los datos necesarios para validar nuestro procedimiento.

En la Figura E7 hay una ilustración esquemática que describe nuestro procedimiento de optimización global mejorado. Más específicamente, el

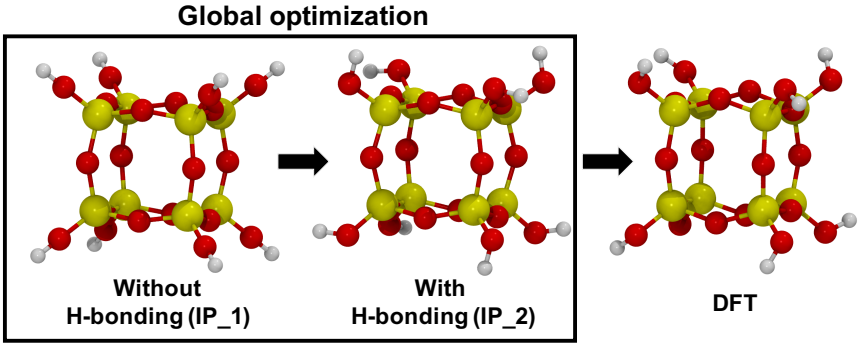

Figura E7: Una ilustración esquemática del refinamiento en cascada dentro del procedimiento de optimización global: en primer lugar la estructura es relaxada por el IP_1 que es ligeramente parametrizado pero computacionalmente eficiente y después, la estructura es refinada con el IP_2 que es más preciso.

IP_1, que ha sido usado en estudios previos, está ligeramente parametrizado y proporciona una descripción cualitativa de grupos hidroxilo[89]. El IP_2 fue parametrizado específicamente para describir con precisión los sistemas de sílice hidroxilada[116,117]. Para grados de hidratación relativamente medios a altos, la complejidad del sistema aumenta ya que cada isómero puede tener varias redes de H-bond diferentes y las moléculas de agua pueden adsorber a la superficie del grupo. Por lo tanto, se vuelve importante emplear IP_2 durante la búsqueda de PES. Probamos este nuevo enfoque con respecto a estudios previos para verificar que es capaz de encontrar estructuras ya conocidas de global mínimos de sílice hidroxilada como las $(SiO_2)_M\,(H_2O)_N$ con M = 8 y N = 2-5. En esta comparación, no solo pudimos encontrar las estructuras más estables, sino que incluso pudimos encontrar nuevos isómeros energéticamente bajos para sistemas con N = 3 y 4. Luego aplicamos este enfoque para extender el conjunto de nanopartículas de sílice hidroxiladas conocidas con sistemas con M = 6, 10 y 12 y con N = 1-6.

La energía de hidroxilación (ΔE_{hyx}) para todas las nuevas estructuras optimizadas globalmente se muestra en la Figura E8 a). Aquí, la relación de agua incorporada es equivalente al grado de hidroxilación dividido por 100. En todos los casos, la hidroxilación es una reacción exotérmica con respecto a la nanopartícula de sílice desnuda. Las estructuras que se considera que tienen un grado de hidroxilación óptimo se muestran en la figura E8 b). El grado óptimo se elige de acuerdo con la relación del agua incorporada que

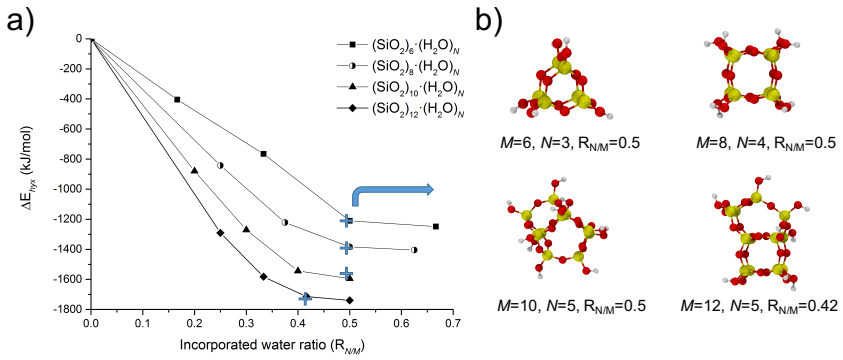

Figura E8: a) Energías de hidroxilación de nanopartículas de sílice optimizadas globalmente en función de la relación de agua incluida$R_{N/M}$. Círculos medio llenos indican estructuras ya conocidas (SiO2)8 (H2O) $_{\mathrm{N}}$ que reconfirmamos aquí con este enfoque. b) Nanopartículas de sílice con grado óptimo de hidroxilación. b) nanopartículas de sílice hidroxilada que se considera tienen un grado de hidroxilación óptimo.

causa la desviación tetraédrica mínima de los centros SiO4 del valor ideal de 109.4º. Esto también coincide con la proporción de agua incorporada donde elΔE_{hyx}se nivela a un valor constante. De esta forma al determinar el grado óptimo de hidroxilación es consistente con la elección realizada en un trabajo previo[90].

Este trabajo ha sido publicado: Andi Cuko, Antoni Macià, Monica Calatayud, and Stefan T. Bromley. "Global optimisation of hydroxylated silica clusters: A cascade Monte Carlo basin hopping approach."*Computational and Theoretical Chemistry*, **1102**, 38–43, 2017.

Post refinamientos con Neural Networks

En este trabajo, nuestro objetivo es mejorar el procedimiento de optimización global para sistemas relativamente grandes. En tales situaciones, hay una gran cantidad de isómeros dentro de un rango pequeño de energías (es decir, una gran densidad de isómeros en la PES). En estos casos, la descripción del IP a menudo no es lo suficientemente precisa como para identificar el conjunto de isómeros más estables. En este trabajo, queremos tener un mejor refinamiento energético de las estructuras optimizadas para

IP generadas a partir del procedimiento de optimización global, mientras se mantiene la eficiencia de un IP. Para hacerlo, empleamos modelos basados en ML como las Neural Networks Artificiales (ANN) como un evaluador de energía altamente preciso y eficiente. La idea básica es usar un conjunto de datos relativamente grande de configuraciones de geometría para las cuales las energías totales ya están evaluadas a nivel DFT para entrenar el modelo de ANN. Tal modelo, después del entrenamiento apropiado, es capaz de evaluar la energía de una especie desconocida en función de sus configuraciones geométricas. Además, el gran conjunto de datos de entrenamiento se puede construir usando estructuras refinadas DFT obtenidas a partir de carreras preliminares de *Basin hopping*.

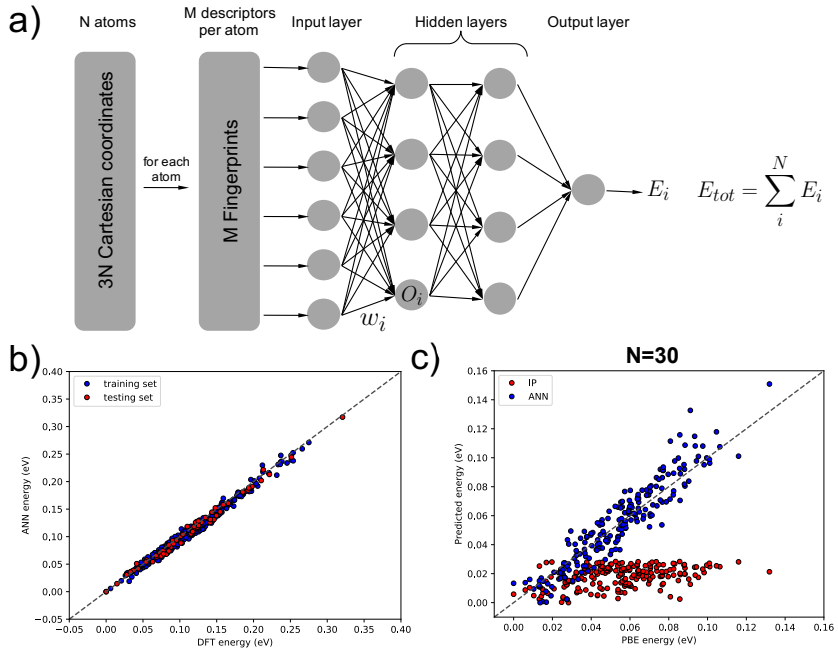

Figura E9: a) Una ilustración esquemática de las *Artificial Neural Networks* (ANN) y su uso para determinar la energía total de una molécula. b) Rendimiento de la ANN que muestra las energías relativas pronosticadas en comparación con las energías calculadas a nivel PBE para el conjunto de configuraciones geométricas en entrenamiento (azul) y prueba (rojo). La pareja perfecta entre ANN y PBE los se encuentra en la diagonal (línea punteada). c) Rendimiento de las energías relativas de los isómeros de $(TiO_2)_N$ predictoras con ANN (en azul) generadas con el método de optimización global

Este enfoque no solo reduce el número de estructuras que requieren refinamiento posterior con DFT, sino que también aumenta la eficacia de la

optimización global al seleccionar estructuras de baja energía que pueden etiquetarse incorrectamente como alta energía a partir de una evaluación incorrecta con el IP. En la figura E9 a) hay una descripción esquemática de cómo funciona la ANN. La ANN, inspirada de neuronas biológicas, se ve como una red de gráficos donde los nodos organizados en capas se conectan entre sí por los bordes. A cada nodo se asocia una función llamada función de activación (O_i) que modula la comunicación del nodo con las de la capa previa. Los bordes representan pesos o parámetros (ω_i) que determinan qué tan fuertes están conectados dos nodos. El input del ANN es una representación rotacional y traslacional invariante de las coordenadas atómicas que son in total 3N. Esta representación, tambien llamada descriptor, fue desarrollada por Behler y Parrinello[35]. Tal descriptor proporciona un vector de características para cada átomo que actúa como una huella dactilar basada en el entorno local específico del átomo. En la figura E9 b) mostramos el rendimiento de ANN en el conjunto de entrenamiento y prueba que muestra que es capaz de predecir $(TiO2)_N$ energías de configuraciones geométricas con gran precisión con respecto al nivel PBE. En la Figura E9 c) informamos el rendimiento real de la ANN en la predicción de las energías isoméricas de los sistemas $(TiO2)30$ (que están fuera del conjunto de entrenamiento) en comparación con las energías DFT / PBE para un conjunto de nanopartículas que se originan en el salto de la cuenca. El rendimiento de la ANN es mucho mejor que el IP original y, por lo tanto, se necesita un menor número de estructuras para ser refinado con DFT. Actualmente estamos preparando el manuscrito para este trabajo.

Nanopartículas de titania y sílice hidratada

Siguiendo nuestro estudio anterior sobre sistemas de sílice hidratada, aquí consideramos la interacción entre nanopartículas de titania con agua, que es una de las especies ambientales más comunes. Esto también se puede ver como la tendencia de las nanopartículas a reaccionar con el agua. Nuestro objetivo en este trabajo es estudiar y comparar las nanopartículas de sílice y titania dependientes del tamaño y la estabilidad estructural dependiente de la hidratación. En otras palabras, queremos entender cómo la interacción agua-nanopartícula afecta la estabilidad y las propiedades del sistema y

cómo cambian con el tamaño del sistema.

Se sabe que los sistemas de sílice de tamaño nanométrico son particularmente propensos a la reacción con el agua, lo que da como resultado una cobertura de superficie de nanopartículas de grupos hidroxilo (Si-OH). La proporción de dichos grupos, o el grado de cobertura/recubrimiento, afectan fuertemente a muchas de las propiedades de las nanopartículas de sílice. Las nanopartículas de sílice hidroxilada son importantes en la síntesis de silicatos nanoporosos tecnológicamente relevantes como las zeolitas[88]. Varios estudios han intentado de determinar las estructuras más estables de un rango de tamaño aproximado de 10-100 átomos principalmente a través de MCBH basado en IP.[89–92] incluida la nuestra en Cascade Monte Carlo Basin Hopping[101]. En el caso de titania, la interacción del agua con las superficies cristalinas de TiO_2 se ha investigado intensamente tanto experimentalmente como teóricamente debido a la reacción de fotodescomposición del agua que ocurre con la radiación de luz ultravioleta por la producción de hidrógeno[75]. Por lo tanto, se considera que el papel del agua fisisorbida y quimisorbida en la superficie de titania es crucial para la fotodisociación del agua. Tras la reducción del tamaño del sistema de TiO_2 a 2-5 nm este efecto se mejora[120]. A pesar de la investigación exhaustiva, el mecanismo detallado de fotodisociación con agua aún no está claro. Experimentalmente, las nanopartículas hidratadas pequeñas de titania se utilizan como sistemas modelo para comprender mejor el mecanismo de fotodisociación del agua[114]. Desde una perspectiva computacional, muy pocos trabajos han intentado de encontrar unos candidatos de mínimo global de pequeñas nanopartículas de titania hidratadas[115]. En este trabajo realizamos una búsqueda exhaustiva de nanopartículas de titania hidroxilada $(TiO_2)_M(H_2O)_N$ con M = 4, 8, 12, 16 y con grados de hidratación ($R_{N/M} \times 100$) hasta 100 % para el sistema más pequeño y hasta 50 % para el más grande. Nuestro objetivo es estudiar las propiedades estructurales y termodinámicas de TiO_2 hidratado y compararlas con aquellas de SiO_2 hidratado que ya se han estudiado previamente.

Desde un punto de vista metodológico, empleamos el MCBH basado en el IP. Hemos desarrollado nuevas parametrizaciones de IP para describir nano titania hidratada. También empleamos el enfoque de Monte Carlo basin hopping en cascada desarrollado previamente por nosotros para siste-

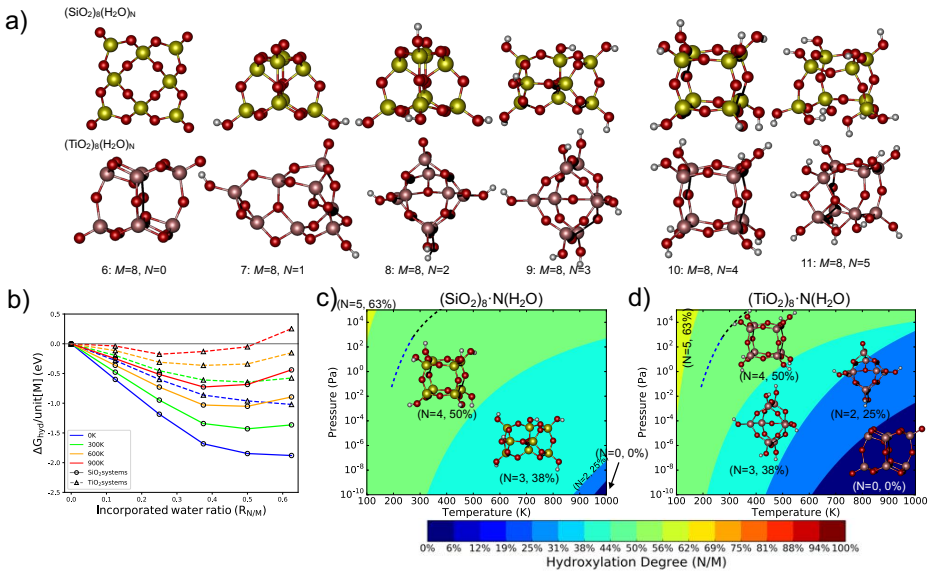

Figura E10: a) $(SiO_2)_8\,(H_2O)_N$ optimizados globalmente ya informado en la bibliografía [90,91] y $(TiO_{28})\,(H_2O)_N$ encontrados en este estudio. b) Energía libre de hidratación por unidad para todos los nanoclusters de titania (líneas discontinuas) y sílice (líneas continuas) informados en a) a diferentes temperaturas. c) y d) son diagramas de fase de sistemas de nanosilica y nanotitania respectivamente hidratados en equilibrio térmico con ambiente de agua gaseosa. La línea punteada en la parte superior izquierda de los gráficos indica las condiciones experimentales de la transición de fase gas-sólido del agua.

mas con alto grado de hidratación (es decir $R_{N/M} > 0{,}4$). Consecutivamente, post-refinamos un conjunto de estructuras de baja energía en primer lugar con PBE y finalmente con PBE0 empleando el conjunto de base numérica tight /tier-1 con el código FHI-AIMS. Aquí mostraremos un ejemplo de nuestro análisis para sistemas con M = 8, pero se derivan conclusiones similares para los otros sistemas con diferentes M considerados en este estudio. En la figura E10 a) mostramos las estructuras más estables obtenidas de la búsqueda estructural de sistemas con M = 8. En la figura E10 b), informamos las energías libres de hidratación que son exotérmicas en titania y sílice a cualquier relación de agua incorporada. Sin embargo, en el caso de la sílice, la reacción de hidratación es más energéticamente exotérmica. A medida que la temperatura aumenta, la energía libre de hidratación se vuelve menos exotérmica y específicamente para el sistema de titania con M = 8 y N = 5 se convierte en un proceso endotérmico. En la figura E10 c) y E10 d) se muestra un ejemplo de diagrama de fase respectivamente de sistemas

de $(SiO_2)_8(H_2O)_N$ y de $(TiO_2)_8(H_2O)_N$. Cada región de dicho diagrama define las condiciones de temperatura y presión parcial del agua que estabilizan una estructura con un grado de hidratación específico. Aunque existen algunas similitudes estructurales entre la sílice hidratada y la titania (como las nanopartículas con M = 8 y N = 4), su interacción con el agua es muy diferente. Las nanopartículas de sílice prefieren estar mayormente hidratadas para una amplia gama de presiones y temperaturas de vapor de agua contrarias a la titania, que tiende a ser más hidrófoba. Presentamos en este estudio, ademas, las frecuencias de vibración para cada sistema y el efecto de la inclusión de agua en el espacio de banda de las nanopartículas. Esperamos con este trabajo facilitar la interpretación de los datos obtenidos a partir de los experimentos de "laser ablation cluster beam"del tipo mostrado en ref[114]. Esto podría proporcionar una mayor comprensión en el mecanismo de fotodisociación de agua. Un artículo esta en preparación.

Conclusiones

En esta Tesis Doctoral estudiamos las propiedades de los materiales basados en SiO_2y TiO_2 tecnológicamente relevantes a nanoescala donde la caracterización experimental es difícil. Uno de los principales problemas en esta escala de tamaño es la determinación estructural de los nanoclusters. Aquí intentamos determinar las estructuras más estables realizando estudios de optimización global y proporcionando modelos estructurales realistas. Dichos modelos se han utilizado posteriormente para estudiar las propiedades dependientes del tamaño del sistema, como la estabilidad estructural. A partir de tales estudios, obtuvimos varias predicciones importantes y mejoramos los métodos para una mejor selección de estructuras realistas en el vacío y en presencia de agua. Los principales resultados se resumen de la siguiente manera:

1. Predijimos que la mezcla entre titania y sílice es termodinámicamente favorable a nanoescala para una amplia gama de composiciones, contrariamente a lo que se observa a nivel macroscopico. Dichos materiales *bulk* se usan en la industria como catalizadores para muchas reacciones y su actividad está limitada por la gama altamente restringida de composiciones

de mezclado. Para tales materiales de óxido mixto a escala nanométrica también hemos realizado cálculos para predecir su posible reactividad hacia la reducción química.

2. Otra predicción interesante está relacionada con el tamaño del sistema de nanopartículas de titania en el cual ocurre la aparición de la cristalinidad. Nuestros cálculos proporcionan una estimación de cómo pueden ser las nanopartículas de titania pequeñas sin perder su cristalinidad y, por lo tanto, su alta actividad fotocatalítica. Estimamos que este tamaño de cruce sea para nanopartículas de 2-2.6 nm.

3. Para encontrar las estructuras más estables mediante métodos de optimización global, de modo que para estudiar sistemas más complejos también proponemos nuevos enfoques, como el Monte Carlo basin hopping en cascada y el basin hopping mejorado con Neural Networks. El primero es particularmente adecuado para la optimización global de sistemas complejos como las nanopartículas hidratadas, mientras que el último es más adecuado para grandes nanopartículas anhidras con una alta densidad de isómeros de baja energía.

4. Finalmente, nos enfocamos en el efecto del ambiente acuoso en las propiedades estructurales y termodinámicas de los sistemas de titania en comparación con los de la sílice hidratada que es mejor conocida en la literatura. Aquí presentamos diagramas de fases que muestran el grado de hidratación de las nanopartículas en función de la temperatura y del vapor de agua. Esperamos que nuestros estudios inspiren investigaciones experimentales sobre este pequeñas nanopartículas. Una mejor comprensión del comportamiento a nanoescala de dichos materiales podría ayudar a desarrollar otros nuevos con propiedades mejoradas con respecto a los existentes.

Résumé en française et conclusions

Introduction

Les Matériaux à base d'oxydes sont largement utilisés dans la technologie moderne en raison de leur grande diversité de propriétés comme l'activité (photo)catalytique, le magnétisme, la supraconductivité ou l'activité optique, tout en apportant une grande stabilité chimique. En mélangeant des matériaux d'oxyde, l'efficacité et la gamme de propriétés peuvent être améliorées en raison de leur effet synergique. Cet effet est très bien connu, par exemple, dans la catalyse hétérogène et chez les composés céramiques résistants à haute température[118]. Il peut y avoir plusieurs types différents de matériaux mélangés selon les applications recherchées. D'abord, des composés où des phases différentes sont mélangées de façon hétérogène. Deuxième, des matériaux dopés où une petite fraction d'un ou plusieurs éléments est diluée dans la matrice. Troisième, les solutions solides, où les composants sont mélangés de façon homogène dans une large variété de compositions. Dans ce dernier cas, il peut être, parfois, difficile d'obtenir un matériel mixte de manière homogène ou une composition de mélange particulière en raison des limites de solubilité réciproques différentes.

Curieusement, la solubilité réciproque de deux matériaux peut changer selon la taille de système. Par exemple, les matériaux qui se mélangent à peine à grande échelle, peuvent être stabilisés dans une phase mélangée à l'échelle nanométrique[119]. Une nano particule est typiquement mentionnée

comme un avec un diamètre moyen entre 1 et 100 nanomètres (1 nm = 10^9 m). En outre, il est possible d'identifier les régimes de taille de trois matériaux qui possèdent des caractéristiques différentes : 1) le régime évolutif où l'évolution des propriétés génériques est linéaire en ce qui concerne la taille de système, avec pour limite le massif ou bulk. 2) le régime nanométrique, qui est phénoménologiquement décrit comme le régime où les systèmes commencent à montrer des propriétés différentes de celles de bulk sur la réduction de taille. 3) et le régime de l'agrégat ou cluster dans lequel les propriétés oscillent grandement avec la taille de système[9]. Ce dernier régime est aussi mentionné comme l'échelle où chaque atome compte.

Le nanomateriaux présentent donc des propriétés qui diffèrent grandement de celles du bulk et attirent de plus en plus d'attention en raison de leurs applications dans des nanotechnologies. Leurs propriétés particulières proviennent principalement des ratios surface-à-bulk accrus et la présence de coins et de bords pour la nanoparticule non-sphérique. En plus des propriétés structurelles et morphologiques, le nanomatériau montre des propriétés électroniques uniques et distinctes. Malgré le grand impact de nanomatériaux d'oxyde dans la technologie de nos jours, la caractérisation structurelle expérimentale est souvent très difficile, particulièrement dans les dimensions petites des agrégats. Le rôle de la théorie dans la description de tels matériaux est essentiel afin de fournir des modèles structurels réalistes qui peuvent être caractérisés par leurs propriétés comme la structure électronique, réactivité chimique etc. accessibles par l'expérience.

Dans ce doctorat, nous nous sommes concentrés sur le nanomateriaux d'oxyde basés sur l'oxyde de titane et la silice et leurs mélanges, titanosilicates. Ces matériaux ont été choisis parmi plusieurs autres à cause de leur utilisation dans les technologiee modernes par leurs propriétés uniques. Nous étudions leurs propriétés au régime de taille nanométrique où la caractérisation expérimentale est à peine accessible. Pendant une bonne partie de cette thèse, nous nous concentrons sur les propriétés structurelles et énergiques qui dépendant de la taille de nanoparticules. De plus, nous caractérisons aussi la réactivité chimique de quelques systèmes sélectionnés en se focalisant principalement sur la réductibilité. Dans les sections suivantes, je présente un résumé des résultats de recherche obtenus dans ce programme de doctorat pendant ces trois ans.

Ce doctorat a été réalisé en cotutelle entre l'Université de Barcelona (directeur : Stefan Bromley, 16 mois) et Sorbonne Université (directeur : Monica Calatayud, 20 mois), avec un court séjour chez Simune atomistics (supervision : Monica Garcia, 2 mois), dans le cadre du doctorat européen en chimie théorique EJD-TCCM.

Nanoparticules de titanosilicates

Les oxydes basés sur le mélange d'oxyde de titane (TiO_2) et silice (SiO_2), titanosilicates, représentent une classe importante de matériaux largement étudiés et utilisés dans les applications respectueuses de l'environnement comme des cellules solaires, des systèmes autonettoyants, des capteurs de gaz, des tamis moléculaires sélectifs, des matériaux dépolluants de l'eau ou encore les photocatalyseurs pour beaucoup de réactions[52–57]. Dans de nombreuses applications, les titanosilicates profitent non seulement des propriétés de l'oxyde de titane pur (semi-conducteur) et la silice (haute stabilité thermique et haute force mécanique) mais des propriétés synergiques qui naissent de l'interaction mutuelle TiO_2-SiO_2 (par exemple, la formation de nouveaux sites catalytiques). Par example, un des plus importants matérieux pour l'industrie est à base de TiO_2-SiO_2, le titanosilicate-1 (TS-1)[58], connu dès années 80. Il est utilisé comme un catalyseur redox industriel pour oxyder des molécules organiques dans des conditions douces avec la présence d'eau oxygénée. Le site actif est composé par des centres de titane tetracoordonnés dispersés dans une structure de silice poreuse avec 1.0-2.5% de fraction malaire de TiO_2. Dans ces systèmes, augmenter la quantité de TiO_2 mène à une ségrégation de l'oxyde de titane, avec séparation de phase indiquant la metastabilité thermodynamique de titanosilicates mélangés. Malgré le grand succès industriel de ces matériaux, on connait très peu leur comportement, particulièrement concernant leur mélange, à l'échelle nanométrique.

Objectif. Dans ce projet nous voulons obtanir une meilleure compréhension du mélange de l'oxyde de titane avec la silice à niveau microscopique fondamental. Pour ce faire, nous utilisons une gamme de méthodes de modélisation computationnelle comme l'optimisation globale et l'utilisa-

tion des méthodes *ab initio* pour étudier la stabilité structurelle en variant la composition du mélange et la taille de système. Notre but primaire est de comprendre pourquoi et comment ces matériaux se mélangent ensemble à l'échelle nanométrique. L'objectif secondaire est de les caractériser (théoriquement) d'un point de vue physico-chimique, et fournir des informations utiles pour les synthétiser et le caractériser expérimentalement.

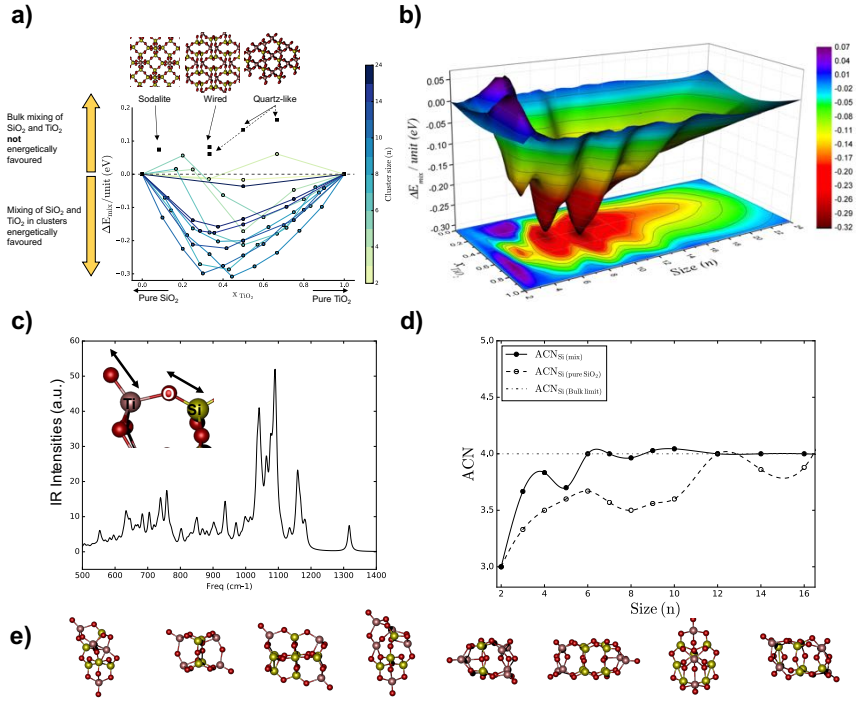

FIGURE F1: a) Énergie de Mélange de titanosilicates massifs et des nanoagrégats globalement optimisés en fonction de la fraction molaire de TiO_2. b) Graph 3D de l'énergie de mélange des nanoparticules versus la fraction molaire de TiO_2 et la taille de système. Toutes les énergies sont normalisées par le nombre d'unités d'oxyde. c) Spectre des fréquences vibrationnelles infrarouge (IR) harmoniques calculée pour un ensemble des nanoparticules de titanosilicate. d) Numéro de coordination moyen d'atomes de silicium dans silice pure (ligne pointillée) et dans nanoparticules de titanosilicate (ligne pleine). e) Certains des modèles prévus stables de titanosilicate nanoclusters. Colours : Ti en gris, Si jaune et O en rouge.

Méthodologie. Nous employons une méthode d'optimisation globale, Monte Carlo Basin Hopping (MCBH)[39] avect un Potentiel Interatomique (PI) pour trouver l'isomère le plus stable. Telle méthode permet d'explorer la surface

d'énergie potentielle (SEP) des nanoagrégats par les déplacements aléatoires d'atomes et la relaxation géométrique consécutive de façon itérative. À chaque itération, la géométrie est détendue avec un PI basé sur le potentiel de Buckingham et puis, le critère de Métropolis probabiliste, basé sur le calcul de l'énergie totale à une température fictive, est appliqué pour déterminer s'il faut accepter ou rejeter le nouvel isomère. Le PI est tiré de paramétrages précédemment connus utilisés pour les nanoclusters purs de silice et d'oxyde de titane. Il est adapté pour les titanosilicates mixtes. Bien que la description intrinsèque avec le PI est pauvre, une telle approche permet d'échantillonner efficacement jusqu'à plusieurs centaines de milliers d'isomères différents. Pour pallier à la nature approximative du PI, un certain nombre de structures stables obtenues à ce stade sont par la suite raffinées au moyen des méthodes DFT employant le fonctionnelles hybride PBE0 et un ensemble des functions base atomique numérique tight/tier-1. Nous avons utilisé le paquet de FHI-AIMS pour les calculs DFT. Cette approche permet de trouver efficacement l'isomère titanosilicate le plus stable en décrivant sa stabilité avec une méthode de calcul précise qui assure aussi des prévisions réalistes.

Résultats. Nous fournissons, par une étude systématique, des structures de nano-titanosilicates pour la gamme entière de compositions (i.e. TiO_2 Fraction molaire incorporée allant de 0 à 1) et des tailles jusqu'à 24 unités MO_2 (M= Si, Ti). Nous prévoyons que, contrairement aux systèmes massifs macroscopiques, au niveau nanoscopique le mélange entre la silice et titania est thermodynamique favorable (Fig. F1a). Ceci est montré clairement par l'énergie de mélange (ΔE_{mix} qui a des valeurs négatives pour les nanoagrégats tandis qu'elle est positive pour les massifs. La plus favorable énergie de mélange est associée aux agrégats de taille environ 1.0 nm (entre 9 et 12 unités) et avec une composition se mélangeant entre 0.3 et 0.4 fraction de molaire TiO_2.

En augmentant la taille des agrégats, la stabilité énergétique pour les systèmes mixtes diminue. Cet effet est particulièrement évident dans la Fig. F1b dans laquelle l'énergie de mélange est tracée en fonction de la composition et de la taille. De plus, les énergies de mélange de Gibbs sont estimées à partir des calculs de fréquence de vibration *ab initio* pour une meilleure évaluation de la stabilité thermodynamique. Les résultats suggèrent que

la stabilité des mélanges persiste avec la températures allant jusqu'à 900 K pour toutes les tailles d'agrégat considérées.Le facteur structurel, le plus important, associé au mélange favorable, est lié à la nature des centres défectueux (oxygènes pendants), naturellement présents à la surface de ces agrégats à ce régime de taille.

Nos structures prédites, en partie montrées dans Fig. F1e), n'ont jamais été synthétisées auparavant. Afin d'aider à la caractérisation expérimentale des nanoclusters de titanosilicates mixtes, nous rapportons aussi les spectres de vibration harmonique calculés pour la silice pure, l'oxyde de titane pur et les agrégats de titanosilicate mixtes (Fig. F1c). A partir de ces spectres, une signature de titanosilicates intimement mélangés peut être distinguée par la présence de pics uniques et très intenses (1035 et 1090 cm-1). De plus, nous rapportons les nombres moyens de coordination atomique puisque cette information structurale peut être accessible par la technique expérimentale EXAFS. Dans nos systèmes, le nombre moyen de coordination du silicium dans les nanoparticules mixtes est significativement différent de celui des nanoparticules de silice pure. Ceci persiste pour un large éventail de tailles évaluées ici et il pourrait être utilisé comme signe de la présence de titanosilicates mixtes.Nous espérons inspirer et guider les expérimentateurs pour travailler sur cette catégorie de matérieau aussi importante.

Ce travail a été publiée par : Andi Cuko, Monica Calatayud, and Stefan T. Bromley. "Stability of mixed-oxide titanosilicates : dependency on size and composition from nanocluster to bulk." *Nanoscale*, **10**,832–842, 2018.

Réactivité chimique des nanoparticules de TiO_2, SiO_2 et titanosilicates

L'objectif du projet précédent était de trouver des nanoparticules d'oxyde de titane, de silice et de titanosilicates les plus stables énergétiquement et d'étudier leurs propriétés structurelles, énergétiques et dépendant de la taille. Dans cette section, nous donnerons un aperçu de nos recherches sur les propriétés chimiques de tels systèmes. Plus spécifiquement, nous explorons la réductibilité chimique des nanoparticules afin de prédire et de

caractériser leur comportement redox à partir des méthodes théoriques basées sur la DFT.

D'un point de vue chimique, la réductibilité d'un matériau est sa tendance à acquérir des électrons et à réduire le nombre d'oxydation formel du cation impliqué. Elle est associée également à la perte d'oxygène ou au gain d'hydrogène, et quand cela arrive des électrons dits de réduction sont disponibles au sein du matériau, comme schématisé ci-dessous. Par exemple,

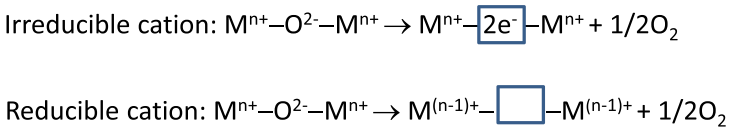

FIGURE F2: Représentation schématique du système réductible et irréductible.

dans TiO_2, les atomes de Ti ont une charge formelle + IV et une configuration électronique de l'argon ($1s^2 2s^2 2p^6 3s^2 3p^6$). Puisque les orbitales $4s$ et $3d$ sont énergétiquement accessibles, les atomes de Ti peuvent prendre un électron de l'environnement pour devenir + III. Ceci affecte par exemple les propriétés optiques macroscopiques du système qui transforme les cristaux de rutile de couleur blanche en minéraux colorés selon la présence de Ti^{3+} ou la présence d'espèces dopantes. En outre, cela peut être confirmé par des techniques expérimentales sensibles aux électrons non appariés tels que la résonance paramagnétique électronique (EPR) puisque Ti^{3+} a une nature radicalaire. En tant qu'exemple de tendance opposée, l'oxyde de magnésium (MgO) est considéré comme un matériau non réductible car les atomes de Mg ne réduisent pas leur nombre d'oxydation formel. Mg^{2+} a la configuration électronique du Neon ($1s^2 2s^2 2p^6$) et les orbitales $3s$ ne sont pas facilement accessibles énergétiquement et tendent donc à éviter d'acquérir d'autres électrons. Si l'on force la réduction de MgO par élimination d'oxygène, les électrons seront stabilisés à partir du réseau de Madelung formant les centres dits F, où les électrons sont localisés dans le réseau cristallin.

Objectif. La silice est connue pour être très peu réductible alors que l'oxyde de titane est réductible au niveau massif. Mais qu'en est-il du niveau nanométrique, et des mélanges ? Notre but ici est d'explorer la dépendance de

taille de la réductibilité dans la silice, l'oxyde de titane et les nanoparticules de titanosilicate. Deux approches ont été utilisées pour réduire les systèmes : (i) la création d'une lacune d'oxygène dans le système et (ii) sur la réaction d'hydrogénation par addition de H_2. Ce travail étant toujours en cours, seuls les résultats obtenus jusqu'ici par rapport à la formation de lacune d'oxygène seront résumés ici.

Formation de lacune d'oxygène

Nous avons sélectionné les systèmes globalement optimisés $(Ti_xSi_{1-x}O)_{10}$ avec $0 < x < 1$ et nous avons éliminé un seul atome d'oxygène de ces structures, de manière systématique en explorant tous les sites O possibles. Les structures non stoechiométriques sont ensuite complètement relaxées au même niveau de théorie que les structures stoechiométriques (c'est-à-dire PBE0 avec un ensemble de bases tight/tier-1 avec FHI-AIMS). Tous les calculs sont spin polarisés de spin à enveloppe ouverte. Ensuite, on calcule l'énergie de formation de lacune d'oxygène, $\Delta E^f_{O_v}$, par rapport à l'équation chimique suivante comme suit :

$$M_nO_{2n} \rightleftarrows M_nO_{2n-1} + \frac{1}{2}O_2$$
$$\Delta E^f_{O_v} = E_{M_nO_{2n-1}} + \frac{1}{2}E_{O_2} - E_{M_nO_{2n}}$$

L'énergie de formation de la lacune d'oxygène quantifie le coût énergétique de l'élimination de l'oxygène du système. Lorsque le coût énergétique de l'élimination d'un oxygène est élevé, il indique en principe que le système n'est pas facilement réductible. Au contraire, lorsque le coût de l'énergie d'élimination de l'oxygène est faible, le système a tendance à être facilement réductible. Nous reportons également le gain énergétique dû à la relaxation géométrique. Dans un premier temps nous allons étudier l'effet de la teneur en Ti dans un agrégat de 10 unités MO_2, puis évaluer l'effet de taille dans les systèmes purs.

Lacune d'oxygène dans $(Ti_xSi_{1-x}O_2)_{10}$

Dans la figure F3a) nous montrons les structures de minima globales des

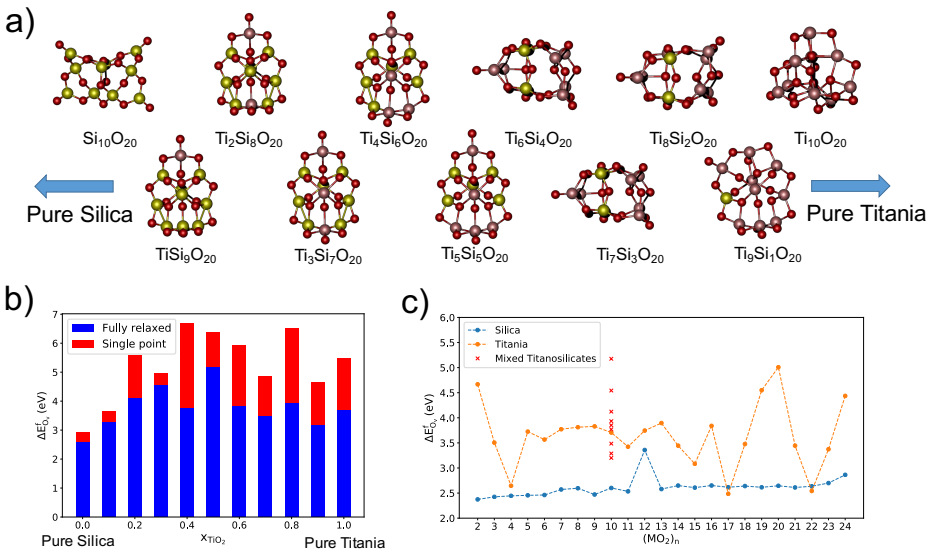

FIGURE F3: a) Les isomères stoechiométriques des minima globaux pour $(Ti_xSi1-_xO)10$ avec $0 < x < 1$ et b) leur énergie de formation de lacune d'oxygène $\Delta E^f_{O_v}$ par rapport à leur composition de mélange. La barre rouge + bleue indique le $\Delta E^f_{O_v}$ de la géométrie gelée tandis que le bleu indique seulement le $DeltaE^f_O$ de la géométrie relaxée. c) Dépendance de taille de $\Delta E^f_{O_v}$ dans les nanoclusters de silice et d'oxyde de titane. Dans tous les cas signalés, seuls $\Delta E^f_{O_v}$ provenant du meilleur site d'élimination de O sont indiqués (c'est-à-dire l'oxygène le plus facile à éliminer).

nanoparticules utilisées dans cette première partie de notre étude. Sur de tels systèmes nous avons tout d'abord calculé le $\Delta E^f_{O_v}$ et les résultats sont montrés dans la figure F3b). Les valeurs d'énergie rapportées ici sont relatives aux systèmes présentant la formation de lacune d'oxygène moins coûteuse et incluant les effets de relaxation de la géométrie (c'est-à-dire la partie rouge de chaque barre). La valeur d'énergie de formation de lacune pour silice pure est de 2.5 eV, TiO_2 pur 3.7 eV. Ceci est surprenant parce que la silice est connue pour être très peu réductible au niveau massif. Les valeurs calculées au niveau PBE dans une étude précedente[65] sont : 5.15 eV pour le quartz, 4.21 eV pour rutile et 4.23 eV pour anatase TiO_2. Les compositions mixtes présentent dans plusieurs cas des valeurs au-dessus de la valeur de 3.7 eV. Ceci voudrait dire que certains systèmes mixtes sont mois réductibles que l'oxyde de titane pur, et d'autres plus réductibles. Une analyse des géométries optimisées des systèmes mixtes avec défaut d'oxygène montre que les oxygènes "pendants" ou dangling liés à Si ou Ti

sont, de façon générale, les moins couteux à éliminer.

Lacune d'oxygène dans $(TiO_2)_N$ and $(SiO_2)_N$
Dans un second temps, nous avons voulu étudier la dépendance de taille du système pur $\Delta E^f_{O_v}$ pour trouver la taille à laquelle cette tendance nanométrique "anormale" récupère le comportement des matériaux massifs. Pour des tailles relativement petites, nous avons échantillonné tous les sites d'oxygène possible à partir de systèmes stoechiométriques, tandis que pour des systèmes relativement grands nous avons effectué un échantillonnage aléatoire. Dans tous les cas, les systèmes sont entièrement optimisés avec la méthode PBE0 non restreinte avec des fonctions de base numérique tight/tier-1 centrées sur l'atome. Les résultats d'une telle étude sont rapportés dans la figure F3c) qui montre que les nanoclusters de silice pure ont des valeurs constamment plus faibles pour l'énergie de formation de lacune que l'oxyde de titane pour les tailles de système considérées ici. Dans tous les systèmes à base de silice, le site qui correspond aux valeurs les plus faibles de $\Delta E^f_{O_v}$ est l'oxygène pendant lié à un atome de silicium initialement tri-coordonné, qui devient di-coordonné après avoir enlevé l'oxygène. De tels sites défectueux terminaux sont présents dans l aplupart des agrégats obtenus par l'optimisation globale, avec la seule exception pour le système $(SiO_2)_{12}$ qui affiche un type différent de défauts terminaux appelé Oxygène Non Bridant (ONB) où chacun des oxygènes pendants est collé à un centre de silicium tetra-coordonné. Néanmoins, dans la plupart des cas, l'élimination de l'oxygène est moins coûteuse pour les nanoparticules de silice que pour l'oxyde de titane. Seuls quelques systèmes d'oxyde de titane affichent un $\Delta E^f_{O_v}$ comparable à celui de la silice. Dans de tels systèmes, si un oxygène interne est éliminé, un oxygène terminal voisi viendra combler la lacune. Ceci implique une forte énergie de relaxation et une structure finale proche de celle d'un terminal éliminé.

Structure électronique des nanoparticules réduites
Nous avons étudié l'origine de la réductibilité chimique de la silice qui a été trouvée plus élevée (moindre énergie de formation de lacune) que celle de l'oxyde de titane. Nous avons essayé de rationaliser pourquoi les oxygènes pendants terminaux ont une valeur si faible $\Delta E^f_{O_v}$ par rapport aux autres oxygènes de la structure. Généralement, l'élimination d'un atome d'oxygène neutre donne un excès de deux électrons pour le substrat. Le coût

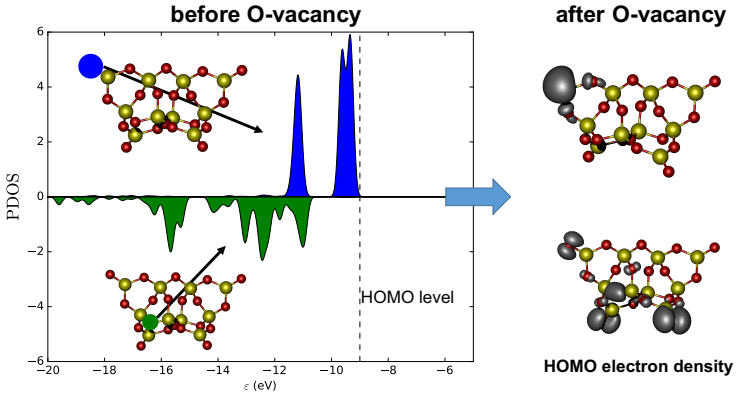

FIGURE F4: Densité d'états projetée (PDOS) sur les sites d'inoccupation O, en bleu l'oxygène ballotté terminal en vert l'oxygène de pont interne avant l'élimination (gauche) et la densité électronique respective par rapport à l'orbitale HOMO après l'enlèvement (droite)

d'élimination des différents oxygènes peut varier en fonction de leur site dans le nanocluster et de leur coordinance. Dans les nanoparticules d'oxyde de titane, l'élimination de l'oxygène conduit toujours à la réduction de deux atomes de Ti^{4+} en Ti^{3+}. Dans le cas de la silice, le coût de l'élimination de l'oxygène terminal est beaucoup plus faible que celui des autres oxygènes. L'oxygène terminal possède des états électroniques associés à la HOMO tandis que les autres oxygènes ont des états plus bas en énergie. Ainsi, l'élimination d'un oxygène avec des états électroniques internes affecte plus la stabilité du système que l'élimination d'un oxygène contribuant uniquement aux états d'énergie élevée du système. Pour illustrer ceci, dans la figure F4 nous traçons la densité d'états projetée des atomes d'oxygène qui vont être enlevés : le terminal ou pendant (bleu) et l'oxygène pontant interne (vert). Après avoir enlevé les oxygènes pendants (en haut de la figure F4) on obtient que les 2 électrons sont localisés autour du silicium le plus proche, comme une paire libre. En revanche, l'élimination d'un oxygène pontant (côté inférieur de la figure F4) conduit à la délocalisation des électrons entre les autres oxygènes pendants, sans participation des sites de silicium. Ceci indique que seuls les atomes de silicium liés à des oxygènes pendants défectueux sont réduits dans les nanoparticules de SiO_2.

Comme nous l'avons montré, l'énergie de formation de lacune d'oxygène donne une indication de la réductibilité des nanoparticules. D'après nos

résultats la réductibilité est élevée pour les nanoagrégats de silice pure, et décropit dans l'oxyde de titane pur. Les titanosilicats montrent des valeurs soit plus élevées, soit intermédiaires entre les systeèmes purs, selon la composition. Une analyse détaillée de la structure électronique montre que les niveaux énergétiques des oxygènes terminaux du silicium contribuent majoraitairement à la HOMO, transferant les électrons de réduction au silicium voisin après élimination, et ceci serait relié à leur faible valeur d'énergie de formation de lacune.

Émergence de la cristallinité dans les nanoparticules de TiO_2

Les matériaux de dioxyde de titane sont largement utilisés et étudiés dans l'industrie et l'académie pour leurs propriétés électroniques exceptionnelles. En effet, ce sont des systèmes photoactifs avec des applications comme photocatalyseur, cellules solaires, systèmes de dépollution, etc..[73–77]. Les matériaux à base de TiO_2 possèdent une forte dépendance de la structure et des propriétés. Dans les conditions ambiantes, la structure rutile est la phase la plus thermodynamiquement stable. En réduisant la taille du système, lorsque le diamètre moyen des nanoparticules est inférieur à 14 nm, une transition de phase se produit dans laquelle la structure anatase devient la phase la plus stable. Contrairement à la phase de rutile, les nanocristaux d'anatase présentent une photoactivité plus élevée et sont donc utilisés pour plusieurs matériaux à base de nano-oxyde de titane tels que les photocatalyseurs, les écrans solaires, les matériaux de construction antipollution, etc. Une réduction supplémentaire de la taille des nanocristaux d'anatase va éventuellement donner naissance à des nanoclusters qui ne possèdent généralement pas d'ordre cristallin et ne présentent pas d'activité photochimique. Il existe des preuves expérimentales que les nanocristaux d'anatase persistent thermiquement lorsque le diamètre des particules est d'environ 4 nm, mais il n'est pas clair si les nanoparticules conservent une morphologie non cristalline. Des nanoparticules de taille comprise entre 2 et 3 nm, d'après des preuves expérimentales et théoriques, présentent un noyau cristallin et une morphologie de coque amorphe. Une diminution

supplémentaire de la taille du système conduit à des espèces complètement amorphes.

Objectif. Le but de ce travail est de déterminer la taille de transition entre une nanoparticule amorphe et cristalline. Afin d'estimer cette taille de transition, nous considérons les nanocristaux de TiO_2 à partir d'une approche descendante et de nanoclusters amorphes à partir d'une approche ascendante dont les stabilités relatives sont évaluées avec précision par des calculs de mécanique quantique.

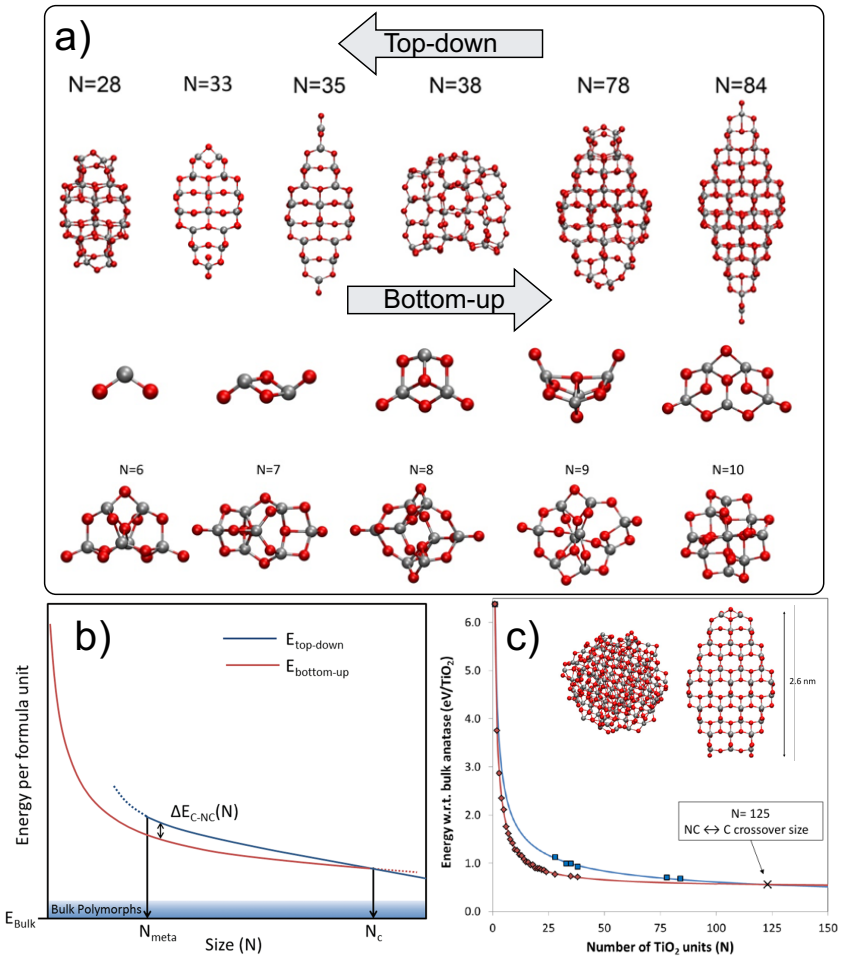

FIGURE F5: a) Une sélection de quelques nanoparticules top-down et bottom-up TiO_2 utilisées dans cette étude. b) Une représentation schématique des stabilités des nanoparticules en fonction de la taille du système. c) Stabilité dépendante de la taille de non-cristalline (en rouge) et cristalline (en bleu) obtenue dans notre étude.

Stratégie et méthodologie. A partir d'une approche descendante, nous

sélectionnons un ensemble de nanocristaux d'anatase de différentes tailles, comme le montre la figure F5. La bulk des structures massives choisies ont la morphologie de construction de Wulff[84] obtenue en minimisant l'énergie de surface totale des nanoparticules. Pour les nanoparticules d'anatase en phase gazeuse, une telle morphologie correspond à une forme bi-pyramidale et / ou à une forme bipyramidale tronquée. A partir d'une approche ascendante, nous considérons des nanoparticules globalement optimisées avec une taille croissante avec N = 1-24, 28, 35 et 38 où N est le nombre d'unités d'oxyde. D'un point de vue structurel, les nanoparticules d'oxyde de titane optimisées globalement ont tendance à être assez compactes et présentent une faible symétrie. Ces caractéristiques structurelles découlent de la flexibilité intrinsèque et naturelle du réseau Ti-O à ce régime de taille dans lequel, par exemple, les atomes de titane peuvent être 4-, 5- ou même 6-coordonnés. En effet, des nanoparticules suffisamment grandes présentent une coordination cationique moyenne plus élevée due à un nombre plus élevé de centres de titane coordonnés penta et / ou hexa. Généralement, les cations les plus coordonnés ont tendance à rester au centre des nanoparticules tandis que les cations sous-coordonnés ont tendance à se poser sur la surface des nanoparticules. De telles caractéristiques rendent l'optimisation globale des nanoparticules de dioxyde de titane particulièrement difficile. En effet, de nombreuses études précédentes ont tenté de trouver des minima globaux pour les nanoparticules de TiO_2 dans ce régime de taille. Ici, nous utilisons l'approche MCBH basée sur PI de manière similaire à celle utilisée pour les titanosilicates (voir ci-dessus). Après l'approche d'optimisation globale, un nombre relativement important de nanoparticules sont ensuite calculées au niveau de la théorie DFT. Les minima globaux présentés ici sont le résultat d'une série de post-raffinement en cascade et leur stabilité finale est calculée à l'aide de la fonctionnelle PBE0 en utilisant l'ensemble de base numérique tier-1 tel que calculé avec le code FHI-AIMS.

Dans la figure F5c) nous présentons la stabilité des nanoparticules optimisées globalement non cristallines (points rouges) et la stabilité des nanocristaux coupés en anatase (points bleus) par rapport à la phase anatase. En règle générale, la stabilité structurelle des nanoparticules dans le régime évolutif évolue linéairement avec le rapport surface-volume à mesure que la taille du système augmente. Le rapport surface-à-bulk, à son

tour, s'échelonne en inverse du cube avec le nombre d'atomes dépendant de la forme de la nanoparticule. Dans le régime non-scalable, d'autres facteurs tels que la compressibilité des nanoparticules commencent à jouer un rôle significatif qui peut être considéré par une expansion polynomiale de la loi de stabilité de régime évolutif. Par conséquent, nous ajustons d'abord la stabilité des systèmes cristallins et non cristallins à des lois de puissance inverse par rapport au nombre d'atomes. Deuxièmement, nous estimons que la taille de transition de non-cristallin à cristallin (NC $\leftrightarrow$ C) de nanoparticules d'oxyde de titane se produit lorsque le diamètre moyen de la particule est d'environ 2-2,6 nm. Ceci correspond au point extrapolé où les deux courbes de stabilité descendante et descendante se croisent. A cette taille les nanoparticules TiO_2 peuvent avoir soit une morphologie tronquée de Wulff, soit un noyau cristallin et une morphologie sphérique amorphe. Cette prédiction est en outre soutenue par des observations expérimentales indirectes[80].

Ce travail a été publié par : Oriol Lamiel-Garcia, Andi Cuko, Monica Calatayud, Francesc Illas, and Stefan T. Bromley. "Predicting size-dependent emergence of crystallinity in nanomaterials : titania nanoclusters versus nanocrystals". *Nanoscale*, **9**, 1049–1058, 2017.

Procédures de raffinement de *Basin Hopping*

Dans ce travail, nous avons étudié un moyen d'améliorer la précision de la procédure d'optimisation globale utilisée dans la première partie. D'une manière générale, l'optimisation globale du Monte Carlo *Basin Hopping* basée sur PI, a quelques limites qui découlent d'abord de la nature approximative de la propriété à mesurer elle-même. Par exemple, la géométrie optimisée d'un système particulier peut être différente si elle est obtenue avec une PI classique plutôt qu'avec des méthodes de mécanique quantique. De plus, l'ordre d'énergie d'un ensemble d'isomères peut également être affecté par une mauvaise description de PI. Bien que l'écart entre les SEP classiques et quantique soit limité, seule l'approche classique est suffisamment performante pour permettre un échantillonnage large et exhaustif de l'espace de configuration. Afin de corriger une telle divergence, un nombre

relativement important de structures de basse énergie optimisées par PI subissent des post-raffinements avec des méthodes de mécanique quantique. Dans la figure F6 nous montrons une représentation schématique de la méthode de saut de *Basin Hopping* Monte Carlo basée sur PI utilisée jusqu'ici.

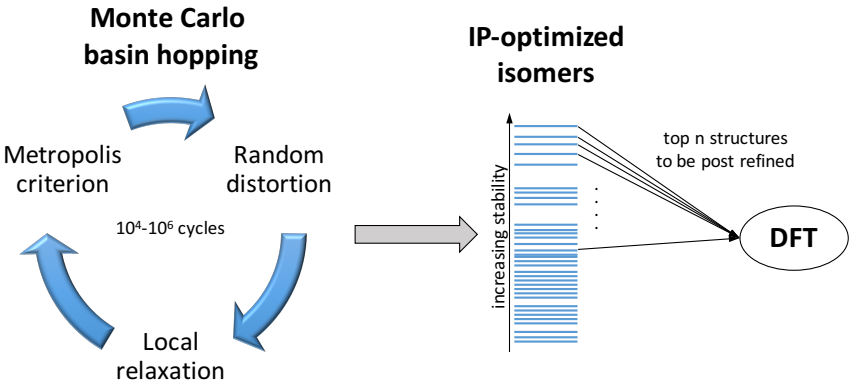

FIGURE F6: Une illustration schématique du raffinement en cascade dans la procédure d'optimisation globale qui fournit une description grandement améliorée des agrégats hydroxyles.

Objetcif. Dans ce projet, nous présentons deux approches qui peuvent améliorer la recherche d'isomères stables dans deux situations différentes. Notre première approche, cascade de Monte Carlo, est une procédure de raffinement de structure en cycle dans laquelle chaque mouvement d'exploration correspond à une relaxation de géométrie en cascade avec deux ou plusieurs PI de plus en plus précis. Une telle approche est particulièrement appropriée pour explorer le SEP de systèmes hydratés qui ont potentiellement différents réseaux de surface de liaison H qui peuvent affecter la stabilité des isomères et doivent donc être décrits avec une propriété appropriée. Dans la seconde approche, nous utilisons des algorithmes de Machine Learning tels que des réseaux de neurones artificiels comme procédure de post-raffinement de houblonnage de *Basin Hopping* pour améliorer la stabilité énergétique et l'ordre des isomères obtenus.

Cascade Monte Carlo Monte Hopping

La première approche améliorée est développée afin d'explorer le SEP d'une nanoparticule d'oxyde immergée dans un environnement spécifique tel que l'eau. Dans le cas de nos nanoparticules d'oxyde à base de silice et d'oxyde de titane, les molécules d'eau se chimisorbent de manière dissociative pour des degrés d'hydratation relativement faibles. Trouver la structure la plus stable pour les systèmes hydroxylés peut être difficile, en particulier pour les systèmes fortement hydratés. Ces difficultés découlent notamment du choix de la propriété à mesurer. Les PI précis reposent typiquement sur une paramétrisation différente des types d'atomes d'oxygène des agrégats hydroxyle (c'est-à-dire OH) des atomes d'oxygène pontants (par exemple Si-O-Si). L'attribution d'un oxygène à un agrégat hydroxyle ou à un agrégat non pontant dans un système déformé de façon aléatoire en tant qu'étape de la procédure de saut de *Basin Hopping* où les connexions entre les atomes sont perdues est plutôt problématique. Notre approche consiste à utiliser deux étapes de minimisation d'énergie consécutives dans chaque cycle de sauts de *Basin Hopping*. D'abord, un potentiel interatomique (PI) légèrement paramétré mais efficace sur le plan des calculs qui ne distingue pas les isomères conformationnels liés à H reliés à la polarisation et la liaison hydrogène, puis une deuxième étape plus précise qui tient compte de ces propriétés explicitement. Les nanoparticules de silice fournissent un cas d'étude parfait pour plusieurs raisons : (i) on sait que le système est très enclin à réagir avec l'eau en raison d'un nombre élevé de centres défectueux, (ii) il existe des PI précis et légèrement paramétrés adaptés pour le système, (iii) pour des tailles de système et des degrés d'hydratation spécifiques, les candidats minima globaux sont déjà rapportés dans des études antérieures, nous avons donc les données nécessaires pour valider notre procédure.

Dans la figure F7 il y a une illustration schématique décrivant notre procédure d'optimisation globale améliorée. Plus spécifiquement, le PI_1 est utilisé dans des études précédentes, est légèrement paramétré et fournit une description qualitative des agrégats hydroxyles[89]. Le PI_2 a été paramétré spécifiquement pour décrire précisément les systèmes de silice hydroxylée[116,117]. Pour des degrés d'hydratation relativement moyens à élevés, la complexité du système augmente car chaque isomère peut avoir

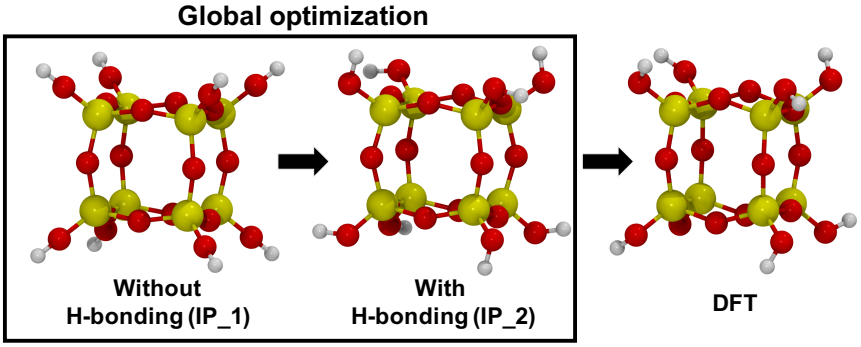

FIGURE F7: Une illustration schématique du raffinement en cascade dans la procédure d'optimisation globale qui fournit une description grandement améliorée des agrégats hydroxyles.

plusieurs réseaux de liaison H différents et les molécules d'eau peuvent physisorber à la surface de l'agrégat. Il devient donc important d'utiliser PI_2 pendant la recherche de SEP. Nous avons testé cette nouvelle approche par rapport à des études antérieures afin de vérifier qu'elle est capable de trouver des systèmes déjà connus $(SiO_2)_M(H_2O)_N$ avec M = 8 et N = 2-5 silice hydroxylée globale minima. Dans cette comparaison, non seulement nous pourrions trouver les structures les plus stables, mais nous pourrions même trouver de nouveaux isomères énergétiquement bas pour les systèmes N = 3 et 4. Nous avons ensuite appliqué cette approche pour étendre l'ensemble des nanoparticules de silice hydroxylées connues avec d'autres systèmes M = 6, 10 et 12 et avec N = 1-6.

L'énergie d'hydroxylation (ΔE_{hyx}) pour toutes les nouvelles structures optimisées globalement est représentée sur la figure F8a). Ici, le rapport d'eau incorporé est équivalent au degré d'hydroxylation divisé par 100. Dans tous les cas, l'hydroxylation est une réaction exothermique par rapport à la nanoparticule de silice nue. Les structures considérées comme ayant un degré d'hydroxylation optimal sont représentées sur la figure F8b). Le degré optimal est choisi en fonction du rapport d'eau incorporée qui provoque la déviation tétraédrique minimale des centres SiO_4 par rapport à la valeur idéale de 109,4°. Cela coïncide également avec la ratio d'eau incorporée où le ΔE_{hyx} se stabilise à une valeur constante. Cette façon de déterminer le degré d'hydroxylation optimal est cohérente avec le choix fait dans un travail antérieur [90].

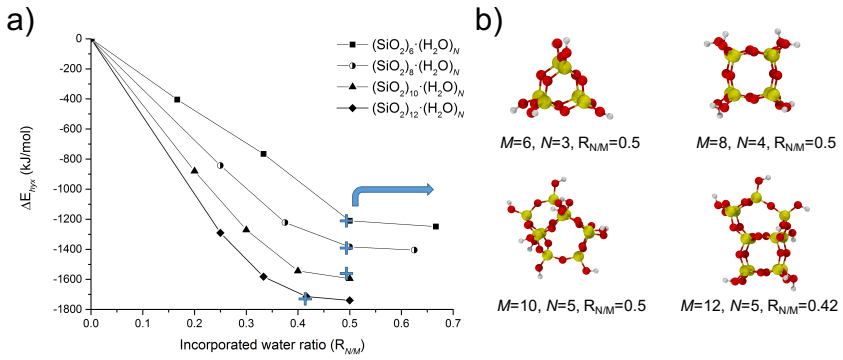

FIGURE F8: a) Les énergies d'hydroxylation des nanoparticules de silice optimisées globalement en fonction du rapport eau inclus $R_{N/M}$. Les cercles à moitié pleins indiquent des structures déjà connues de $(SiO_2)_8(H_2O)_N$ que nous reconfirmons ici avec cette approche. b) Nanoparticules de silice avec un degré d'hydroxylation optimal. b) Nanoparticules de silice hydroxylées considérées comme ayant un degré d'hydroxylation optimal.

Ce travail a été publié par : Andi Cuko, Antoni Macià, Monica Calatayud, and Stefan T. Bromley. "Global optimisation of hydroxylated silica clusters : A cascade Monte Carlo basin hopping approach." *Computational and Theoretical Chemistry*, **1102**, 38–43, 2017.

Post-raffinements par Neural Networks

Lorsque les systèmes sont grands il y a un grand nombre d'isomères dans une petite gamme d'énergies (c'est-à-dire une grande densité d'isomères sur le SEP). Dans ces cas, la description du PI n'est souvent pas assez précise pour identifier l'ensemble des isomères les plus stables. Dans ce travail, notre objectif est d'améliorer la procédure d'optimisation globale pour les systèmes relativement importants en taille, comme les nanoparticules d'oxyde de titane.

Objectif. Dans ce travail, nous voulons avoir un meilleur raffinement énergétique des structures optimisées avec PI générées à partir de la procédure d'optimisation globale, tout en maintenant l'efficacité de la procédure. Pour ce faire, nous utilisons des modèles basés sur l'apprentissage automatique tels que le neural networks (NN) en tant qu'évaluateur d'énergie hautement précis et

efficace. L'idée de base est d'utiliser un ensemble de données relativement grand de configurations de géométrie pour lequel les énergies totales sont déjà évaluées au niveau de DFT pour former le modèle NNA. Un tel modèle, après une formation appropriée, est capable d'évaluer l'énergie d'une espèce inconnue en fonction de ses configurations géométriques. De plus, le grand ensemble de données d'entraînement peut être construit en utilisant des structures raffinées post-DFT obtenues à partir d'essais préliminaires de saut en *Basin Hopping*.

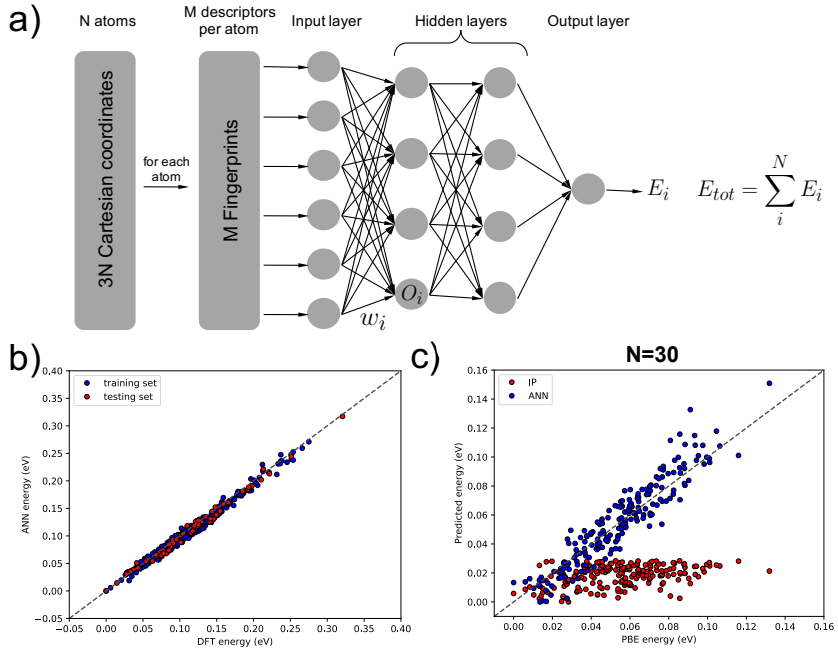

FIGURE F9: a) Une illustration schématique du neural networks (NN) et son utilisation pour déterminer l'énergie totale d'une molécule. b) Performance du NN montrant les énergies relatives prédites par rapport aux énergies PBE pour l'ensemble des configurations géométriques dans l'ensemble d'entraînement (bleu) et d'essai (rouge). La correspondance parfaite entre les deux se trouve dans la diagonale (ligne pointillée). c) Performance du NN qui prédit les énergies relatives aux isomères $(TiO_2)_N$ (en bleu) générés à partir de la procédure de saut de *Basin Hopping*s par rapport aux isomères PI.

Cette approche réduit non seulement le nombre de structures qui nécessitent un post-raffinement avec DFT, mais augmente également l'efficacité de l'optimisation globale en sélectionnant des structures à basse énergie qui peuvent être incorrectement étiquetées comme étant à haute énergie d'une mauvaise évaluation PI. Dans la figure F9a) il y a une description

schématique du fonctionnement du NN. Le NN, inspiré des neurones biologiques, est considéré comme un réseau de graphes où les nœuds organisés en couches sont reliés entre eux par des arêtes. A chaque noeud est associée une fonction appelée fonction d'activation (O_i) qui module la communication du noeud avec celles de la couche précédente. Les extrêmes représentent les poids ou les paramètres (ω_i) qui déterminent la façon dont deux nœuds forts sont connectés. L'entrée NN est une représentation invariante rotationnelle et translationnelle des coordonnées atomiques 3N. Nous sélectionnons le descripteur *symmetry functions* développé par Behler et Parrinello[35]. Un tel descripteur fournit un vecteur de caractéristiques pour chaque atome agissant comme une empreinte digitale basée sur l'environnement local spécifique de l'atome. Dans la figure F9b) nous rapportons la performance NN dans l'ensemble de formation et de test montrant qu'il est capable de prédire les énergies géométriques de $(TiO_2)_N$ avec une grande précision par rapport à PBE. Dans la figure F9c) nous rapportons les performances réelles du NN dans la prédiction des énergies isomères des systèmes $(TiO_2)_{30}$ (qui sont en dehors de l'ensemble d'apprentissage) par rapport aux énergies DFT / PBE un ensemble de nanoparticules provenant du *Basin Hopping* de saut. La performance du NN est bien meilleure que la PI d'origine et donc un nombre inférieur de structures est nécessaire pour être affiné avec DFT. Actuellement nous préparons le manuscrit pour ce travail.

Nanoparticules hydratées de TiO_2 vs SiO_2

Suite à notre étude précédente sur les systèmes de silice hydratée, nous considérons ici l'interaction entre les nanoparticules d'oxyde de titane et l'eau qui est l'une des espèces environnementales les plus courantes. Cela peut également être vu comme la tendance des nanoparticules à réagir avec l'eau. Notre objectif dans ce travail est d'étudier et de comparer les nanoparticules de silice et de dioxyde de titane en fonction de leur stabilité structurelle et de leur stabilité hydrique. En d'autres termes, nous voulons voir comment l'interaction eau-nanoparticules affecte la stabilité et les propriétés du système et comment elles changent avec la taille du système.

On sait que les systèmes de silice nanostructurée sont particulièrement sujets à la réaction avec l'eau, ce qui se traduit par un recouvrement de surface par des groupements hydroxyle (Si-OH). La proportion de ces agrégats, ou le degré de recouvrement, affectent fortement de nombreuses propriétés des nanoparticules de silice. Les nanoparticules de silice hydroxylées sont importantes dans la synthèse de silicates nanoporeux technologiques tels que les zéolithes[88]. Plusieurs études ont tenté de déterminer les structures les plus stables avec une gamme de taille approximative de 10-100 atomes principalement par MCBH basé sur PI.[89–92] y compris les nôtres sur le Cascade Monte Carlo[101]. Dans le cas de l'oxyde de titane, l'interaction de l'eau avec les surfaces cristallines de TiO_2 a été étudiée intensivement par l'expérience et la théorie en raison de la réaction de *photosplitting* de l'eau qui se produit avec le rayonnement UV[75]. Ainsi, le rôle de l'eau physisorbée et chimisorbée sur la surface de l'oxyde de titane est considéré comme crucial pour la photodissociation de l'eau. En réduisant la taille du système TiO_2 à 2-5 nm, cet effet est amélioré[120]. Malgré la recherche intensive, le mécanisme détaillé de photodisociation de l'eau reste encore peu clair. Expérimentalement, de petites nanoparticules hydratées de titane sont utilisées comme systèmes modèles afin de mieux comprendre le mécanisme de photodisociation de l'eau[114].

Objectif. D'un point de vue calculatoire, très peu de travaux ont tenté de trouver les candidats minima globaux pour les petites nanoparticules d'oxyde de titane hydraté[115]. Dans ce travail, nous effectuons des recherches approfondies pour les $(TiO_2)_M(H_2O)_N$ nanoparticules de titane avec M = 4, 8, 12, 16 et avec des degrés d'hydratation ($R_{N/M} \times 100$) jusqu'à 100% pour les plus petits systèmes et jusqu'à 50% pour les plus grands. Notre but est d'étudier les propriétés structurales et thermodynamiques du TiO_2 hydraté et de les comparer avec le SiO_2 hydraté qui a déjà été étudié.

D'un point de vue méthodologique, nous utilisons le Monte Carlo Basin Hopping basé sur le PI. Nous avons développé de nouveaux paramétrages PI pour décrire l'agrégat de nano-oxyde de titane hydratée. Nous utilisons également l'approche de cascade de Monte Carlo développée précédemment par nos soins pour des systèmes à haut degré d'hydratation (i.e. $R_{N/M} > 0.4$). Consécutivement, nous post affinons un ensemble de structures à basse énergie d'abord avec PBE et enfin avec PBE0 en utilisant l'ensemble de base

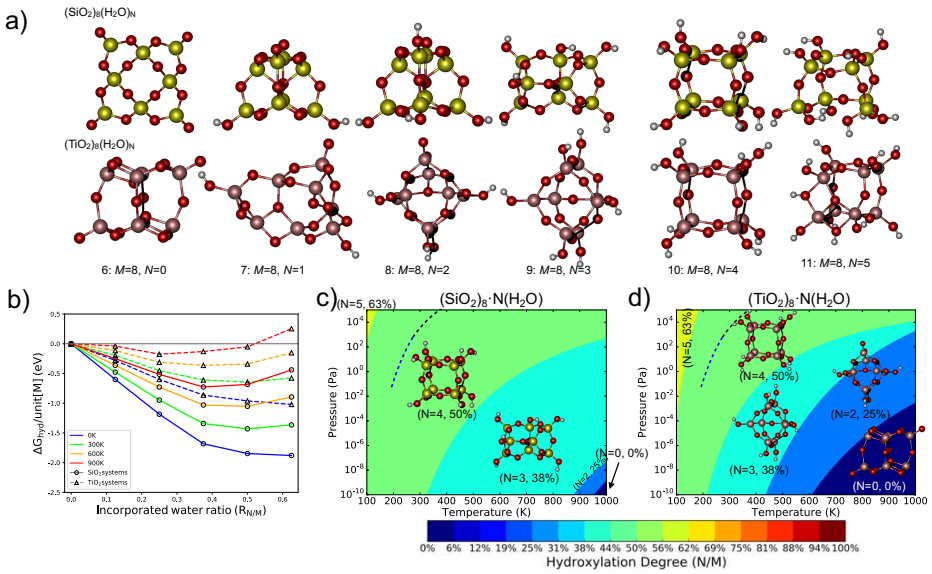

FIGURE F10: a) Agrégat de $(SiO_2)_8(H_2O)_N$ optimisé globalement déjà rapporté dans la littérature[90,91] et $(TiO_2)_8(H_2O)_N$ trouvé dans cette étude. b) Énergie en fonction du degré d'hydratation par unité MO_2 pour tous les nanoclusters d'oxyde de titane (lignes pointillées) et la silice (lignes pleines) rapportés en a) à différentes températures. c) et d) sont des diagrammes de phases de systèmes de nanosilice et de nanooxyde de titane respectivement hydratés en équilibre thermique avec un milieu aqueux gazeux. La ligne pointillée en haut à gauche des graphiques indique les conditions expérimentales de la transition de phase solide-gaz eau.

numérique de niveau 1 et en utilisant le code FHI-AIMS.

Ici, nous allons montrer un exemple de notre analyse pour les systèmes avec M = 8 mais des conclusions similaires sont dérivées pour les autres systèmes avec M différent considéré dans cette étude. Dans la figure F10a) nous montrons les structures les plus stables obtenues à partir de la recherche structurelle pour les systèmes avec M = 8. Dans la figure F10b), nous rapportons les énergies sans hydratation qui sont exothermiques à la fois dans l'oxyde de titane et la silice à tout rapport d'eau incorporé. Cependant, dans le cas de la silice, la réaction d'hydratation est plus énergétiquement exothermique. À mesure que la température augmente, l'énergie sans hydratation devient moins exothermique et, spécifiquement pour le système de titane avec M = 8 et N = 5, elle devient un processus endothermique. Dans la figure F10c) et F10d) On montre un exemple de diagramme de phase des systèmes $(SiO_2)_8(H_2O)_N$ et $(TiO_2)_8(H_2O)_N$ respectivement. Chaque

région du diagramme définit les conditions de température et de pression partielle de l'eau qui stabilisent une structure avec un degré d'hydratation spécifique. Bien qu'il y ait quelques similitudes structurelles entre la silice hydratée et l'oxyde de titane (comme les nanoparticules avec M = 8 et N = 4), leur interaction avec l'eau est très différente. Les nanoparticules de silice préfèrent être principalement hydratées pour une large gamme de pressions de vapeur d'eau et de température contrairement à l'oxyde de titane, qui tend à être plus hydrophobe. Nous rapportons dans cette étude les fréquences vibrationnelles pour chaque système et l'effet de l'inclusion de l'eau sur la bande interdite des nanoparticules.

Un manuscript est en préparation pour être soumis dnas les semaines qui viennent. Nous espérons avec ce travail pouvoir fournir une interprétation plus facile des données obtenues à partir des expériences de faisceau d'ablation laser du type montré dans ref[114] afin d'éclairer sur les mécanismes de photodissociation de l'eau.

Conclusions

Dans cette thèse, nous avons étudié les propriétés de matériaux à base de SiO_2 et de TiO_2 technologiquement importants à l'échelle nanométrique, où la caractérisation expérimentale est plutôt difficile. L'un des principaux problèmes à cette échelle de taille est la détermination structurelle des nanoclusters. Ici, nous essayons de déterminer les structures les plus stables en effectuant des études d'optimisation globale et en fournissant des modèles structurels réalistes. De tels modèles ont été utilisés par la suite pour étudier les propriétés dépendantes de la taille du système telles que la stabilité structurelle. A partir de ces études, nous avons obtenu plusieurs prédictions importantes et nous avons amélioré les méthodes pour une meilleure sélection de structures réalistes dans le vide et en présence d'eau. Les principaux résultats sont résumés comme suit :

1. Nous avons prédit que le mélange entre l'oxyde de titane et la silice est thermodynamiquement favorable à l'échelle nanométrique pour une large gamme de compositions de mélange contrairement aux systèmes

massifs. Ceci ouvre de nouvelles perspectives pour de des matériaux déjà largement utilisés dans l'industrie en tant que catalyseurs pour de nombreuses réactions, car leur activité est limitée par la gamme très restreinte de compositions de mélange. Pour de tels matériaux d'oxyde mixte à l'échelle nanométrique, nous avons également effectué des calculs pour prédire leur réactivité possible à la réduction chimique.

2. Une autre prédiction intéressante est liée à la taille du système de nanoparticules de titane à laquelle se produit l'émergence de la cristallinité. Nos calculs donnent une estimation de la taille des nanoparticules de titane sans perdre leur cristallinité et donc leur haute activité photocatalytique. Nous estimons que cette taille de croisement est pour des nanoparticules de 2-2.6 nm.

3. Afin de trouver des structures plus stables par des méthodes d'optimisation globales, nous proposons également de nouvelles approches telles que la cascade Monte Carlo et le réseau de neurones. Le premier est particulièrement adapté à l'optimisation globale de systèmes complexes tels que les nanoparticules hydratées tandis que le second est mieux adapté pour les grandes nanoparticules anhydres avec une densité élevée d'isomères à faible énergie.

4. Enfin, nous nous intéressons à l'effet de l'environnement hydrique sur les propriétés structurales et thermodynamiques des systèmes en titane par rapport à ceux de la silice hydratée, mieux connue dans la littérature. Nous présentons ici des diagrammes de phase qui montrent le degré d'hydratation des nanoparticules en fonction de la température et de la vapeur d'eau. Nous espérons que nos études inspireront des expérimentateurs sur de telles petites nanoparticules. Une meilleure compréhension du comportement à l'échelle nanométrique de ces matériaux pourrait aider à en développer de nouveaux avec des propriétés améliorées par rapport à celles existantes.

Bibliography

[1] Jacques Védrine. Heterogeneous catalysis on metal oxides. *Catalysts*, 7(11):341, nov 2017.

[2] Zhenwei Wang, Pradipta K. Nayak, Jesus A. Caraveo-Frescas, and Husam N. Alshareef. Recent developments in p-type oxide semiconductor materials and devices. *Advanced Materials*, 28(20):3831–3892, feb 2016.

[3] H. Y. Hwang, Y. Iwasa, M. Kawasaki, B. Keimer, N. Nagaosa, and Y. Tokura. Emergent phenomena at oxide interfaces. *Nature Materials*, 11(2):103–113, feb 2012.

[4] J.H. Ngai, F.J. Walker, and C.H. Ahn. Correlated oxide physics and electronics. *Annual Review of Materials Research*, 44(1):1–17, 2014.

[5] Sharma Bhupendra K. and Ahn Jong-Hyun. Flexible and stretchable oxide electronics. *Advanced Electronic Materials*, 2(8):1600105, 2016.

[6] Haomiao Xu, Naiqiang Yan, Zan Qu, Wei Liu, Jian Mei, Wenjun Huang, and Songjian Zhao. Gaseous heterogeneous catalytic reactions over mn-based oxides for environmental applications: A critical review. *Environmental Science & Technology*, 51(16):8879–8892, jul 2017.

[7] Mohammad Mansoob Khan, Syed Farooq Adil, and Abdullah Al-Mayouf. Metal oxides as photocatalysts. *Journal of Saudi Chemical Society*, 19(5):462 – 464, 2015. Special Issue: Nanomaterials as Photocatalysts.

[8] C. Richard A. Catlow, Stefan T. Bromley, Said Hamad, Miguel Mora-Fonz, Alexey A. Sokol, and Scott M. Woodley. Modelling nano-clusters and nucleation. *Phys. Chem. Chem. Phys.*, 12:786–811, 2010.

[9] Stefan T. Bromley, Iberio de P. R. Moreira, Konstantin M. Neyman, and

Francesc Illas. Approaching nanoscale oxides: models and theoretical methods. *Chem. Soc. Rev.*, 38:2657–2670, 2009.

[10] H. W. Kroto, J. R. Heath, S. C. O'Brien, R. F. Curl, and R. E. Smalley. C60: Buckminsterfullerene. *Nature*, 318(6042):162–163, nov 1985.

[11] K Wegner, P Piseri, H Vahedi Tafreshi, and P Milani. Cluster beam deposition: a tool for nanoscale science and technology. *Journal of Physics D: Applied Physics*, 39(22):R439, 2006.

[12] Shelley A. Claridge, A. W. Castleman, Shiv N. Khanna, Christopher B. Murray, Ayusman Sen, and Paul S. Weiss. Cluster-assembled materials. *ACS Nano*, 3(2):244–255, 2009. PMID: 19236057.

[13] Khalaf Mai, Mostafa, Ibrahimov Hikmet, Gamal, and Ismailov Etibar, Hummat. Nanostructured materials: Importance, synthesis and characterization-a review. *Chemistry Journal*, 2:118–125, 2012.

[14] D. L. Peng, T. Asai, N. Nozawa, T. Hihara, and K. Sumiyama. Magnetic properties and magnetoresistance in small iron oxide cluster assemblies. *Applied Physics Letters*, 81(24):4598–4600, dec 2002.

[15] Norifusa Satoh, Toshio Nakashima, Kenta Kamikura, and Kimihisa Yamamoto. Quantum size effect in TiO2 nanoparticles prepared by finely controlled metal assembly on dendrimer templates. *Nature Nanotechnology*, 3(2):106–111, feb 2008.

[16] Tianbo Liu, Ekkehard Diemann, Huilin Li, Andreas W. M. Dress, and Achim Müller. Self-assembly in aqueous solution of wheel-shaped mo154 oxide clusters into vesicles. *Nature*, 426(6962):59–62, nov 2003.

[17] Thakur Prasad Yadav, Ram Manohar Yadav, and Dinesh Pratap Singh. Mechanical milling: a top down approach for the synthesis of nanomaterials and nanocomposites. *Nanoscience and Nanotechnology*, 2(3):22–48, aug 2012.

[18] Byung Hyo Kim, Michael J. Hackett, Jongnam Park, and Taeghwan Hyeon. Synthesis, characterization, and application of ultrasmall nanoparticles. *Chemistry of Materials*, 26(1):59–71, oct 2013.

[19] Frank Jensen. *Introduction to Computational Chemistry*. John Wiley & Sons, 2006.

[20] Donald A. McQuarrie and John D. Simon. *Physical chemistry : a molecular approach*. University Science Books, 1997.

[21] Peter Atkins and Julio de Paula. *Physical Chemistry*. W. H. Freeman, 2006.

[22] Chandler A. Becker, Francesca Tavazza, Zachary T. Trautt, and Robert A. Buarque de Macedo. Considerations for choosing and using force fields and interatomic potentials in materials science and engineering. *Current Opinion in Solid State and Materials Science*, 17(6):277 – 283, 2013. Frontiers in Methods for Materials Simulations.

[23] Scott Woodley. Database of Published Interatomic Potential Parameters. `http://www.ucl.ac.uk/klmc/Potentials/`.

[24] H. Balamane, T. Halicioglu, and W. A. Tiller. Comparative study of silicon empirical interatomic potentials. *Phys. Rev. B*, 46:2250–2279, Jul 1992.

[25] Norman L. Allinger. Conformational analysis. 130. mm2. a hydrocarbon force field utilizing v1 and v2 torsional terms. *Journal of the American Chemical Society*, 99(25):8127–8134, 1977.

[26] Junmei Wang, Romain M. Wolf, James W. Caldwell, Peter A. Kollman, and David A. Case. Development and testing of a general amber force field. *Journal of Computational Chemistry*, 25(9):1157–1174, 2004.

[27] Riccardo Miotto, Fei Wang, Shuang Wang, Xiaoqian Jiang, and Joel T. Dudley. Deep learning for healthcare: review, opportunities and challenges. *Briefings in Bioinformatics*, may 2017.

[28] Yann LeCun, Yoshua Bengio, and Geoffrey Hinton. Deep learning. *Nature*, 521(7553):436–444, may 2015.

[29] Matthias Rupp, Alexandre Tkatchenko, Klaus-Robert Müller, and O. Anatole von Lilienfeld. Fast and accurate modeling of molecular atomization energies with machine learning. *Phys. Rev. Lett.*, 108:058301, Jan 2012.

[30] Edward O. Pyzer-Knapp, Kewei Li, and Alan Aspuru-Guzik. Learning from the harvard clean energy project: The use of neural networks to accelerate materials discovery. *Advanced Functional Materials*, 25(41):6495–6502, Sep 2015.

[31] Felix A. Faber, Alexander Lindmaa, O. Anatole von Lilienfeld, and Rickard Armiento. Machine learning energies of 2 million elpasolite (abC_2D_6) crystals. *Phys. Rev. Lett.*, 117:135502, Sep 2016.

[32] Paul Raccuglia, Katherine C. Elbert, Philip D. F. Adler, Casey Falk, Malia B. Wenny, Aurelio Mollo, Matthias Zeller, Sorelle A. Friedler, Joshua Schrier, and Alexander J. Norquist. Machine-learning-assisted materials discovery using failed experiments. *Nature*, 533:73, May 2016.

[33] Jörg Behler. First principles neural network potentials for reactive simulations of large molecular and condensed systems. *Angewandte Chemie International Edition*, 56(42):12828–12840, 2017.

[34] Thomas B. Blank, Steven D. Brown, August W. Calhoun, and Douglas J. Doren. Neural network models of potential energy surfaces. *The Journal of Chemical Physics*, 103(10):4129–4137, 1995.

[35] Jörg Behler and Michele Parrinello. Generalized neural-network representation of high-dimensional potential-energy surfaces. *Phys. Rev. Lett.*, 98:146401, Apr 2007.

[36] Trevor Hastie, Robert Tibshirani, and Jerome Friedman. *The Elements of Statistical Learning*. Springer New York, 2009.

[37] Stefan Grimme. Accurate description of van der waals complexes by density functional theory including empirical corrections. *Journal of Computational Chemistry*, 25(12):1463–1473, 2004.

[38] Stefan Grimme. Semiempirical GGA-type density functional constructed with a long-range dispersion correction. *Journal of Computational Chemistry*, 27(15):1787–1799, 2006.

[39] David J. Wales and Jonathan P. K. Doye. Global optimization by basin-hopping and the lowest energy structures of lennard-jones clusters containing up to 110 atoms. *The Journal of Physical Chemistry A*, 101(28):5111–5116, 1997.

[40] Volker Blum, Ralf Gehrke, Felix Hanke, Paula Havu, Ville Havu, Xinguo Ren, Karsten Reuter, and Matthias Scheffler. Ab initio molecular simulations with numeric atom-centered orbitals. *Computer Physics Communications*, 180(11):2175 – 2196, 2009.

[41] M. J. Frisch, G. W. Trucks, H. B. Schlegel, G. E. Scuseria, M. A. Robb, J. R. Cheeseman, G. Scalmani, V. Barone, B. Mennucci, G. A. Petersson, H. Nakatsuji, M. Caricato, X. Li, H. P. Hratchian, A. F. Izmaylov, J. Bloino, G. Zheng, J. L. Sonnenberg, M. Hada, M. Ehara, K. Toyota,

R. Fukuda, J. Hasegawa, M. Ishida, T. Nakajima, Y. Honda, O. Kitao, H. Nakai, T. Vreven, J. A. Montgomery, Jr., J. E. Peralta, F. Ogliaro, M. Bearpark, J. J. Heyd, E. Brothers, K. N. Kudin, V. N. Staroverov, R. Kobayashi, J. Normand, K. Raghavachari, A. Rendell, J. C. Burant, S. S. Iyengar, J. Tomasi, M. Cossi, N. Rega, J. M. Millam, M. Klene, J. E. Knox, J. B. Cross, V. Bakken, C. Adamo, J. Jaramillo, R. Gomperts, R. E. Stratmann, O. Yazyev, A. J. Austin, R. Cammi, C. Pomelli, J. W. Ochterski, R. L. Martin, K. Morokuma, V. G. Zakrzewski, G. A. Voth, P. Salvador, J. J. Dannenberg, S. Dapprich, A. D. Daniels, Ö. Farkas, J. B. Foresman, J. V. Ortiz, J. Cioslowski, and D. J. Fox. Gaussian09 Revision E.01. Gaussian Inc. Wallingford CT 2009.

[42] G. Kresse and J. Furthmüller. Efficient iterative schemes for ab initio total-energy calculations using a plane-wave basis set. *Phys. Rev. B*, 54:11169–11186, Oct 1996.

[43] José M Soler, Emilio Artacho, Julian D Gale, Alberto García, Javier Junquera, Pablo Ordejón, and Daniel Sánchez-Portal. The siesta method for ab initio order- n materials simulation. *Journal of Physics: Condensed Matter*, 14(11):2745, 2002.

[44] Ask Hjorth Larsen, Jens Jørgen Mortensen, Jakob Blomqvist, Ivano E Castelli, Rune Christensen, Marcin Dułak, Jesper Friis, Michael N Groves, Bjørk Hammer, Cory Hargus, Eric D Hermes, Paul C Jennings, Peter Bjerre Jensen, James Kermode, John R Kitchin, Esben Leonhard Kolsbjerg, Joseph Kubal, Kristen Kaasbjerg, Steen Lysgaard, Jón Bergmann Maronsson, Tristan Maxson, Thomas Olsen, Lars Pastewka, Andrew Peterson, Carsten Rostgaard, Jakob Schiøtz, Ole Schütt, Mikkel Strange, Kristian S Thygesen, Tejs Vegge, Lasse Vilhelmsen, Michael Walter, Zhenhua Zeng, and Karsten W Jacobsen. The atomic simulation environment—a python library for working with atoms. *Journal of Physics: Condensed Matter*, 29(27):273002, 2017.

[45] Julian D. Gale. Gulp: A computer program for the symmetry-adapted simulation of solids. *J. Chem. Soc., Faraday Trans.*, 93:629–637, 1997.

[46] Alireza Khorshidi and Andrew A. Peterson. Amp: A modular approach to machine learning in atomistic simulations. *Computer Physics Communications*, 207:310 – 324, 2016.

[47] Sean Fleming and Andrew Rohl. GDIS: a visualization program

for molecular and periodic systems. *Zeitschrift für Kristallographie - Crystalline Materials*, 220(5/6), jan 2005.

[48] William Humphrey, Andrew Dalke, and Klaus Schulten. VMD – Visual Molecular Dynamics. *Journal of Molecular Graphics*, 14:33–38, 1996.

[49] P. Ugliengo, D. Viterbo, and G. Chiari. MOLDRAW: Molecular graphics on a personal computer. *Zeitschrift für Kristallographie - Crystalline Materials*, 207(1), jan 1993.

[50] Koichi Momma and Fujio Izumi. *VESTA3* for three-dimensional visualization of crystal, volumetric and morphology data. *Journal of Applied Crystallography*, 44(6):1272–1276, Dec 2011.

[51] Ansgar Schäfer, Christian Huber, and Reinhart Ahlrichs. Fully optimized contracted gaussian basis sets of triple zeta valence quality for atoms li to kr. *The Journal of Chemical Physics*, 100(8):5829–5835, apr 1994.

[52] The-Vinh Nguyen, Hyun-Cheol Lee, M. Alam Khan, and O-Bong Yang. Electrodeposition of tio2/sio2 nanocomposite for dye-sensitized solar cell. *Solar Energy*, 81(4):529 – 534, 2007.

[53] Kaihong Qi, Xianqiong Chen, Yuyang Liu, John H. Xin, C. L. Mak, and Walid A. Daoud. Facile preparation of anatase/sio2 spherical nanocomposites and their application in self-cleaning textiles. *J. Mater. Chem.*, 17:3504–3508, 2007.

[54] Steven M. Kuznicki, Valerie A. Bell, Sankar Nair, Hugh W. Hillhouse, Richard M. Jacubinas, Carola M. Braunbarth, Brian H. Toby, and Michael Tsapatsis. A titanosilicate molecular sieve with adjustable pores for size-selective adsorption of molecules. *Nature*, 412(6848):720–724, aug 2001.

[55] Chaoran Jiang, Ki Yip Lee, Christopher M.A. Parlett, Mustafa K. Bayazit, Chi Ching Lau, Qiushi Ruan, Savio J.A. Moniz, Adam F. Lee, and Junwang Tang. Size-controlled tio2 nanoparticles on porous hosts for enhanced photocatalytic hydrogen production. *Applied Catalysis A: General*, 521:133 – 139, 2016. SI:Photocatalysis.

[56] Sihui Zhan, Dairong Chen, Xiuling Jiao, and Yang Song. Mesoporous tio2/sio2 composite nanofibers with selective photocatalytic proper-

ties. *Chem. Commun.*, pages 2043–2045, 2007.

[57] Pei Cao, Guowei Zhou, Yixian Ren, and Hong Xiao. Fabrication and photoactivity of short rod-shaped mesoporous sio2@tio2 composites with tio2 shell. *RSC Adv.*, 6:6551–6561, 2016.

[58] Taramasso Marco, Perego Giovanni, and Notari Bruno. Preparation of porous crystalline synthetic material comprised of silicon and titanium oxides. *U.S. Patent*, (4410501), 1983.

[59] E Flikkema and S.T Bromley. A new interatomic potential for nanoscale silica. *Chemical Physics Letters*, 378(5-6):622–629, sep 2003.

[60] E. Flikkema and S. T. Bromley. Dedicated global optimization search for ground state silica nanoclusters: (SiO2)n(n= 6-12). *The Journal of Physical Chemistry B*, 108(28):9638–9645, jul 2004.

[61] Stefan T. Bromley and Edwin Flikkema. Columnar-to-disk structural transition in nanoscale(SiO2)NClusters. *Physical Review Letters*, 95(18), oct 2005.

[62] E. Flikkema and Stefan T. Bromley. Defective to fully coordinated crossover in complex directionally bonded nanoclusters. *Physical Review B*, 80(3), jul 2009.

[63] S. Hamad, C. R. A. Catlow, S. M. Woodley, S. Lago, and J. A. Mejías. Structure and stability of small TiO2nanoparticles. *The Journal of Physical Chemistry B*, 109(33):15741–15748, aug 2005.

[64] Mingyang Chen and David A. Dixon. Tree growth—hybrid genetic algorithm for predicting the structure of small (TiO2)n, n = 2–13, nanoclusters. *Journal of Chemical Theory and Computation*, 9(7):3189–3200, jun 2013.

[65] Z. Helali, A. Jedidi, O. A. Syzgantseva, M. Calatayud, and C. Minot. Scaling reducibility of metal oxides. *Theoretical Chemistry Accounts*, 136(9), aug 2017.

[66] Francesc Illas and Gianfranco Pacchioni. Optical properties of surface and bulk f centers in MgO from ab initio cluster model calculations. *The Journal of Chemical Physics*, 108(18):7835–7841, may 1998.

[67] Anna Maria Ferrari and Gianfranco Pacchioni. Electronic structure of f and v centers on the MgO surface. *The Journal of Physical Chemistry*, 99(46):17010–17018, nov 1995.

[68] Carmen Sousa, Gianfranco Pacchioni, and Fransesc Illas. Ab initio study of the optical transitions of f centers at low-coordinated sites of the MgO surface. *Surface Science*, 429(1-3):217–228, jun 1999.

[69] Julia Vecchietti, Miguel A. Baltanás, Christel Gervais, Sebastián E. Collins, Ginesa Blanco, Olivier Matz, Monica Calatayud, and Adrian Bonivardi. Insights on hydride formation over cerium-gallium mixed oxides: A mechanistic study for efficient h 2 dissociation. *Journal of Catalysis*, 345:258–269, jan 2017.

[70] Olga A. Syzgantseva, Monica Calatayud, and Christian Minot. Revealing the surface reactivity of zirconia by periodic DFT calculations. *The Journal of Physical Chemistry C*, 116(11):6636–6644, mar 2012.

[71] David G. Calatayud, Teresa Jardiel, Marco Peiteado, Cristina Fernandez Rodriguez, M. Rocio Espino Estevez, Jose M. Dona Rodriguez, Francisco J. Palomares, Fausto Rubio, Daniel Fernandez-Hevia, and Amador C. Caballero. Highly photoactive anatase nanoparticles obtained using trifluoroacetic acid as an electron scavenger and morphological control agent. *J. Mater. Chem. A*, 1:14358–14367, 2013.

[72] Gang Liu, Jimmy C. Yu, Gao Qing (Max) Lu, and Hui-Ming Cheng. Crystal facet engineering of semiconductor photocatalysts: motivations, advances and unique properties. *Chemical Communications*, 47(24):6763, 2011.

[73] Xiaobo Chen and Annabella Selloni. Introduction: Titanium dioxide (tio2) nanomaterials. *Chemical Reviews*, 114(19):9281–9282, 2014. PMID: 25294394.

[74] Yu Bai, Iván Mora-Seró, Filippo De Angelis, Juan Bisquert, and Peng Wang. Titanium dioxide nanomaterials for photovoltaic applications. *Chemical Reviews*, 114(19):10095–10130, mar 2014.

[75] Akira Fujishima and Kenichi Honda. Electrochemical photolysis of water at a semiconductor electrode. *Nature*, 238(5358):37–38, jul 1972.

[76] Mukes Kapilashrami, Yanfeng Zhang, Yi-Sheng Liu, Anders Hagfeldt, and Jinghua Guo. Probing the optical property and electronic structure of TiO2 nanomaterials for renewable energy applications. *Chemical Reviews*, 114(19):9662–9707, aug 2014.

[77] Jenny Schneider, Masaya Matsuoka, Masato Takeuchi, Jinlong Zhang,

Yu Horiuchi, Masakazu Anpo, and Detlef W. Bahnemann. Understanding TiO2 photocatalysis: Mechanisms and materials. *Chemical Reviews*, 114(19):9919–9986, sep 2014.

[78] Hengzhong Zhang and Jillian F. Banfield. Thermodynamic analysis of phase stability of nanocrystalline titania. *J. Mater. Chem.*, 8:2073–2076, 1998.

[79] J. F. Banfield and H. Zhang. Nanoparticles in the environment. *Reviews in Mineralogy and Geochemistry*, 44(1):1–58, jan 2001.

[80] Hengzhong Zhang, Bin Chen, Jillian F. Banfield, and Glenn A. Waychunas. Atomic structure of nanometer-sized amorphous tio$_2$. *Phys. Rev. B*, 78:214106, Dec 2008.

[81] Bunsho Ohtani, Yoshimasa Ogawa, and Sei-ichi Nishimoto. Photocatalytic activity of amorphous-anatase mixture of titanium(iv) oxide particles suspended in aqueous solutions. *The Journal of Physical Chemistry B*, 101(19):3746–3752, 1997.

[82] Sami Auvinen, Matti Alatalo, Heikki Haario, Juho-Pertti Jalava, and Ralf-Johan Lamminmäki. Size and shape dependence of the electronic and spectral properties in TiO2 nanoparticles. *The Journal of Physical Chemistry C*, 115(17):8484–8493, apr 2011.

[83] Petter Persson, J. Christof M. Gebhardt, and Sten Lunell. The smallest possible nanocrystals of semiionic oxides. *The Journal of Physical Chemistry B*, 107(15):3336–3339, apr 2003.

[84] G. Wulff. XXV. zur frage der geschwindigkeit des wachsthums und der auflösung der krystallflächen. *Zeitschrift für Kristallographie - Crystalline Materials*, 34(1-6), jan 1901.

[85] Masanori Matsui and Masaki Akaogi. Molecular dynamics simulation of the structural and physical properties of the four polymorphs of tio2. *Molecular Simulation*, 6(4-6):239–244, 1991.

[86] A. S. Barnard and P. Zapol. Effects of particle morphology and surface hydrogenation on the phase stability of Tio_2. *Phys. Rev. B*, 70:235403, Dec 2004.

[87] A. S. Barnard and P. Zapol. A model for the phase stability of arbitrary nanoparticles as a function of size and shape. *The Journal of Chemical Physics*, 121(9):4276–4283, sep 2004.

[88] Colin S. Cundy and Paul A. Cox. The hydrothermal synthesis of zeolites: Precursors, intermediates and reaction mechanism. *Microporous and Mesoporous Materials*, 82(1):1–78, 2005.

[89] S. T. Bromley and E. Flikkema. Novel structures and energy spectra of hydroxylated (SiO2)8-based clusters: Searching for the magic (SiO2)8o2h3- cluster. *The Journal of Chemical Physics*, 122(11):114303, mar 2005.

[90] Kim E. Jelfs, Edwin Flikkema, and Stefan T. Bromley. Hydroxylation of silica nanoclusters (sio2)m(h2o)n, m = 4, 8, 16, 24: stability and structural trends. *Phys. Chem. Chem. Phys.*, 15:20438–20443, 2013.

[91] Edwin Flikkema, Kim E. Jelfs, and Stefan T. Bromley. Structure and energetics of hydroxylated silica clusters, (sio2)m(h2o)n, m=8, 16 and n=1–4: A global optimisation study. *Chemical Physics Letters*, 554:117 – 122, 2012.

[92] Kim E. Jelfs, Edwin Flikkema, and Stefan T. Bromley. Evidence for atomic mixingvia multiple intermediates during the dynamic interconversion of silicate oligomers in solution. *Chem. Commun.*, 48:46–48, 2012.

[93] Albert P. Bartók, Mike C. Payne, Risi Kondor, and Gábor Csányi. Gaussian approximation potentials: The accuracy of quantum mechanics, without the electrons. *Phys. Rev. Lett.*, 104:136403, Apr 2010.

[94] Colin S. Cundy and Paul A. Cox. The hydrothermal synthesis of zeolites: Precursors, intermediates and reaction mechanism. *Microporous and Mesoporous Materials*, 82(1):1 – 78, 2005.

[95] Matteo Cargnello, Thomas R. Gordon, and Christopher B. Murray. Solution-phase synthesis of titanium dioxide nanoparticles and nanocrystals. *Chemical Reviews*, 114(19):9319–9345, 2014. PMID: 25004056.

[96] Laura K. Adams, Delina Y. Lyon, and Pedro J.J. Alvarez. Comparative eco-toxicity of nanoscale tio2, sio2, and zno water suspensions. *Water Research*, 40(19):3527 – 3532, 2006.

[97] Nicole Pienack and Wolfgang Bensch. In-situ monitoring of the formation of crystalline solids. *Angewandte Chemie International Edition*, 50(9):2014–2034, feb 2011.

[98] Christopher T. G. Knight, Raymond J. Balec, and Stephen D. Kinrade. The structure of silicate anions in aqueous alkaline solutions. *Angewandte Chemie International Edition*, 46(43):8148–8152, nov 2007.

[99] Mohamed Haouas and Francis Taulelle. Revisiting the identification of structural units in aqueous silicate solutions by two-dimensional silicon-29 INADEQUATE. *The Journal of Physical Chemistry B*, 110(7):3007–3014, feb 2006.

[100] Stefan A. Pelster, Wolfgang Schrader, and Ferdi Schüth. Monitoring temporal evolution of silicate species during hydrolysis and condensation of silicates using mass spectrometry. *Journal of the American Chemical Society*, 128(13):4310–4317, apr 2006.

[101] Andi Cuko, Antoni Macià, Monica Calatayud, and Stefan T. Bromley. Global optimisation of hydroxylated silica clusters: A cascade monte carlo basin hopping approach. *Computational and Theoretical Chemistry*, 1102:38 – 43, 2017.

[102] Yi Ma, Xiuli Wang, Yushuai Jia, Xiaobo Chen, Hongxian Han, and Can Li. Titanium dioxide-based nanomaterials for photocatalytic fuel generations. *Chemical Reviews*, 114(19):9987–10043, aug 2014.

[103] Tahereh Jafari, Ehsan Moharreri, Alireza Amin, Ran Miao, Wenqiao Song, and Steven Suib. Photocatalytic water splitting—the untamed dream: A review of recent advances. *Molecules*, 21(7):900, jul 2016.

[104] Kyoung Chul Ko, Stefan T. Bromley, Jin Yong Lee, and Francesc Illas. Size-dependent level alignment between rutile and anatase TiO2 nanoparticles: Implications for photocatalysis. *The Journal of Physical Chemistry Letters*, 8(22):5593–5598, nov 2017.

[105] Francesca Nunzi, Saurabh Agrawal, Annabella Selloni, and Filippo De Angelis. Structural and electronic properties of photoexcited TiO2 nanoparticles from first principles. *Journal of Chemical Theory and Computation*, 11(2):635–645, jan 2015.

[106] Gianluca Fazio, Lara Ferrighi, and Cristiana Di Valentin. Spherical versus faceted anatase TiO2 nanoparticles: A model study of structural and electronic properties. *The Journal of Physical Chemistry C*, 119(35):20735–20746, aug 2015.

[107] Oriol Lamiel-Garcia, Kyoung Chul Ko, Jin Yong Lee, Stefan T. Bromley,

and Francesc Illas. When anatase nanoparticles become bulklike: Properties of realistic TiO2 nanoparticles in the 1–6 nm size range from all electron relativistic density functional theory based calculations. *Journal of Chemical Theory and Computation*, 13(4):1785–1793, mar 2017.

[108] Amilcare Iacomino, Giovanni Cantele, Domenico Ninno, Ivan Marri, and Stefano Ossicini. Structural, electronic, and surface properties of anatase tio$_2$ nanocrystals from first principles. *Phys. Rev. B*, 78:075405, Aug 2008.

[109] Enrico Berardo and Martijn A. Zwijnenburg. Modeling the water splitting activity of a TiO2 rutile nanoparticle. *The Journal of Physical Chemistry C*, 119(24):13384–13393, jun 2015.

[110] Erik G. Brandt, Lorenzo Agosta, and Alexander P. Lyubartsev. Reactive wetting properties of TiO2 nanoparticles predicted by ab initio molecular dynamics simulations. *Nanoscale*, 8(27):13385–13398, 2016.

[111] Kenji Shirai, Gianluca Fazio, Toshiki Sugimoto, Daniele Selli, Lorenzo Ferraro, Kazuya Watanabe, Mitsutaka Haruta, Bunsho Ohtani, Hiroki Kurata, Cristiana Di Valentin, and Yoshiyasu Matsumoto. Water-assisted hole trapping at the highly curved surface of nano-TiO2 photocatalyst. *Journal of the American Chemical Society*, 140(4):1415–1422, jan 2018.

[112] Daeheum Cho, Kyoung Chul Ko, Oriol Lamiel-García, Stefan T. Bromley, Jin Yong Lee, and Francesc Illas. Effect of size and structure on the ground-state and excited-state electronic structure of TiO2 nanoparticles. *Journal of Chemical Theory and Computation*, 12(8):3751–3763, jul 2016.

[113] Daniele Selli, Gianluca Fazio, and Cristiana Di Valentin. Using density functional theory to model realistic TiO2 nanoparticles, their photoactivation and interaction with water. *Catalysts*, 7(12):357, nov 2017.

[114] Marissa L. Weichman, Sreekanta Debnath, John T. Kelly, Sandy Gewinner, Wieland Schöllkopf, Daniel M. Neumark, and Knut R. Asmis. Dissociative water adsorption on gas-phase titanium dioxide cluster anions probed with infrared photodissociation spectroscopy. *Topics in Catalysis*, 61(1-2):92–105, nov 2017.

[115] Mingyang Chen, Tjerk P. Straatsma, and David A. Dixon. Molecular

and dissociative adsorption of water on (TiO2)n clusters n = 1–4. *The Journal of Physical Chemistry A*, 119(46):11406–11421, nov 2015.

[116] Alfonso Pedone, Gianluca Malavasi, M. Cristina Menziani, Ulderico Segre, Federico Musso, Marta Corno, Bartolomeo Civalleri, and Piero Ugliengo. FFSiOH: a new force field for silica polymorphs and their hydroxylated surfaces based on periodic b3lyp calculations. *Chemistry of Materials*, 20(7):2522–2531, apr 2008.

[117] Antoni Macià Escatllar, Piero Ugliengo, and Stefan T. Bromley. Modeling hydroxylated nanosilica: Testing the performance of ReaxFF and FFSiOH force fields. *The Journal of Chemical Physics*, 146(22):224704, jun 2017.

[118] Eric W. McFarland and Horia Metiu. Catalysis by doped oxides. *Chemical Reviews*, 113(6):4391–4427, 2013. PMID: 23350590.

[119] Ksenia Fominykh, Gülen Ceren Tok, Patrick Zeller, Hamidreza Hajiyani, Thomas Miller, Markus Döblinger, Rossitza Pentcheva, Thomas Bein, and Dina Fattakhova-Rohlfing. Rock salt ni/co oxides with unusual nanoscale-stabilized composition as water splitting electrocatalysts. *Adv. Funct. Mater.*, 27(8):1605121, 2017.

[120] Saurabh Srivastava, Joseph Palathinkal Thomas, Md. Anisur Rahman, Marwa Abd-Ellah, Mamata Mohapatra, Debabrata Pradhan, Nina F. Heinig, and Kam Tong Leung. Size-selected TiO2 nanocluster catalysts for efficient photoelectrochemical water splitting. *ACS Nano*, 8(11):11891–11898, nov 2014.

Appendix

Titanosilicates nanoparticles, IPs and energetics of mixing

Table A1: Buckingham parameters for IPs used in the Monte Carlo basin hopping global optimization searches in Chapter 3. Ionic charges for both IPs are: Q(Si, Ti) = 2.4 and Q(O) = -1.2

	IP1			IP2		
	A_{ij}	B_{ij}	C_{ij}	A_{ij}	B_{ij}	C_{ij}
Si-O	10454.2	0.208	63.05	10386.97	0.210372	63.45
Ti-O	2454.2	0.211	-55.05	14719.71	0.200783	65.90
Si-Si	79502.1	0.220	446.78	74316.65	0.220	446.78
Si-Ti	69000.0	0.210	500.00	104167.92	0.220	446.78
Ti-Ti	69000.0	0.210	480.59	74316.65	0.220	446.78
O-O	2828.5	0.297	16.48	2828.5	0.297	16.48

Table A2: Total and mixing energy (eV) of titanosilicate and corresponding pure silica and titania structures at PBE0 tight/tier-1 level of theory.

System	$\mathbf{x}_{\mathrm{TiO_2}}$	**Total energy (eV)**	ΔE_{mix}**/unit**
$(SiO_2)_2$	0.000	-23998.628948781	0.0000
$Ti_1Si_1O_4$	0.500	-39395.821093405	-0.0167
$(TiO_2)_2$	1.000	-54792.946306103	0.0000
$(SiO_2)_3$	0.000	-36000.645793516	0.0000
$Ti_1Si_2O_6$	0.330	-51397.838677881	-0.0145
$Ti_2Si_1O_6$	0.667	-66794.761616984	0.0609
$(TiO_2)_3$	1.000	-82192.093849742	0.0000
$(SiO_2)_4$	0.000	-48002.639028013	0.0000
$Ti_1Si_3O_8$	0.250	-63399.803085355	0.0144
$Ti_2Si_2O_8$	0.500	-78797.770370337	-0.1719
$Ti_3Si_1O_8$	0.750	-94194.492950979	-0.0471
$(TiO_2)_4$	1.000	-109591.52638539	0.0000
$(SiO_2)_5$	0.000	-60004.627962668	0.0000
$Ti_1Si_4O_{10}$	0.200	-75401.541009197	0.0564
$Ti_2Si_3O_{10}$	0.400	-90799.333800403	-0.0631
$Ti_3Si_2O_{10}$	0.600	-106196.86047662	-0.1294
$Ti_4Si_1O_{10}$	0.800	-121593.78698265	-0.0757

$(TiO_2)_5$	1.000	-136990.60356196	0.0000
$(SiO_2)_6$	0.000	-72006.617106618	0.0000
$Ti_1Si_5O_{12}$	0.167	-87403.888230548	0.0159
$Ti_2Si_4O_{12}$	0.333	-102802.40371295	-0.1754
$Ti_3Si_3O_{12}$	0.500	-118199.99675263	-0.2131
$Ti_4Si_2O_{12}$	0.667	-133597.15947250	-0.1791
$Ti_5Si_1O_{12}$	0.833	-148994.02466230	-0.0955
$(TiO_2)_6$	1.000	-164390.81850687	0.0000
$(SiO_2)_7$	0.000	-84008.482129892	0.0000
$Ti_1Si_6O_{14}$	0.143	-99406.641652290	-0.1088
$Ti_2Si_5O_{14}$	0.286	-114805.17581770	-0.2713
$Ti_3Si_4O_{14}$	0.429	-130202.68151404	-0.2867
$Ti_4Si_3O_{14}$	0.571	-145599.55783254	-0.2123
$Ti_5Si_2O_{14}$	0.714	-160996.59754615	-0.1612
$Ti_6Si_1O_{14}$	0.857	-176393.13931644	-0.0390
$(TiO_2)_7$	1.000	-191790.26328829	0.0000
$(SiO_2)_8$	0.000	-96011.405525393	0.0000
$Ti_1Si_7O_{16}$	0.125	-111409.27556127	-0.0706
$Ti_2Si_6O_{16}$	0.250	-126807.32170324	-0.1632
$Ti_3Si_5O_{16}$	0.375	-142204.94048643	-0.2024
$Ti_4Si_4O_{16}$	0.500	-157602.22671239	-0.2000
$Ti_5Si_3O_{16}$	0.625	-172999.20477183	-0.1591
$Ti_6Si_2O_{16}$	0.750	-188396.15253490	-0.1144
$Ti_7Si_1O_{16}$	0.875	-203792.98287985	-0.0550
$(TiO_2)_8$	1.000	-219189.84754442	0.0000
$(SiO_2)_9$	0.000	-108013.52540721	0.0000
$Ti_1Si_8O_{18}$	0.111	-123411.42645541	-0.0706
$Ti_2Si_7O_{18}$	0.222	-138809.70683876	-0.1834
$Ti_3Si_6O_{18}$	0.333	-154207.48989963	-0.2410
$Ti_4Si_5O_{18}$	0.444	-169605.36116046	-0.3083
$Ti_5Si_4O_{18}$	0.556	-185002.34976334	-0.2776
$Ti_6Si_3O_{18}$	0.667	-200399.24311390	-0.2363
$Ti_7Si_2O_{18}$	0.778	-215795.91258780	-0.1701
$Ti_8Si_1O_{18}$	0.889	-231192.52948979	-0.0980

$(TiO_2)_9$	1.000	-246589.33391945	0.0000
$(SiO_2)_{10}$	0.000	-120016.05808241	0.0000
$Ti_1Si_9O_{20}$	0.100	-135414.67096072	-0.1306
$Ti_2Si_8O_{20}$	0.200	-150812.91539109	-0.2243
$Ti_3Si_7O_{20}$	0.300	-166210.96628318	-0.2987
$Ti_4Si_6O_{20}$	0.400	-181608.04766648	-0.2762
$Ti_5Si_5O_{20}$	0.500	-197005.03857150	-0.2446
$Ti_6Si_4O_{20}$	0.600	-212402.00237762	-0.2103
$Ti_7Si_3O_{20}$	0.700	-227798.74224502	-0.1536
$Ti_8Si_2O_{20}$	0.800	-243195.58402226	-0.1071
$Ti_9Si_1O_{20}$	0.900	-258592.23642913	-0.0416
$(TiO_2)_{10}$	1.000	-273989.44301377	0.0000
$(SiO_2)_{12}$	0.000	-144022.25380481	0.0000
$Ti_3Si_9O_{24}$	0.250	-190216.38898834	-0.2120
$Ti_5Si_7O_{24}$	0.417	-221010.91476169	-0.2229
$Ti_6Si_6O_{24}$	0.500	-236407.83444198	-0.1998
$Ti_9Si_3O_{24}$	0.750	-282598.13722054	-0.1385
$(TiO_2)_{12}$	1.000	-328788.61783104	0.0000
$(SiO_2)_{14}$	0.000	-168029.35750224	0.0000
$Ti_4Si_{10}O_{28}$	0.286	-229619.94416664	-0.1705
$Ti_5Si_9O_{28}$	0.357	-245017.07648010	-0.1764
$Ti_7Si_7O_{28}$	0.500	-275810.82349600	-0.1512
$Ti_{10}Si_4O_{28}$	0.714	-322001.22704360	-0.0980
$(TiO_2)_{14}$	1.000	-383588.05321771	0.0000
$(SiO_2)_{16}$	0.000	-192035.44996292	0.0000
$Ti_4Si_{12}O_{32}$	0.250	-253625.63452931	-0.1386
$Ti_6Si_{10}O_{32}$	0.375	-284419.92512328	-0.1578
$Ti_8Si_8O_{32}$	0.500	-315213.54039826	-0.1348
$Ti_{12}Si_4O_{32}$	0.750	-376800.54162855	-0.0745
$(TiO_2)_{16}$	1.000	-438387.21836150	0.0000
$(SiO_2)_{24}$	0.000	-288060.06629464	0.0000
$Ti_{12}Si_{12}O_{48}$	0.500	-472823.84752340	-0.0363
$(TiO_2)_{24}$	1.000	-657585.88426394	0.0000

Table A3: Total and mixing energy (eV) of SiO_2 (quartz), TiO_2 (rutile) and of titanosilicate bulk systems studied in Chapter 3 at PBE0 tight/tier-1 level of theory.

System	$\mathbf{x}_{TiO_2}$	**Total energy (eV)**	ΔE_{mix}**/unit (eV)**	**n of units/cell**
(SiO_2) quartz	0.000	-36010.12399679	0.0000	3
Sodalite-like	0.083	-159436.37868418	0.0742	12
quartz-like2:1	0.333	-51406.65217968	0.0817	3
TS11:1	0.333	-102813.42794212	0.0611	6
quartz-like3:3	0.500	-118209.76116476	0.1344	6
quartz-like1:2	0.667	-66803.17680510	0.1646	3
(TiO_2) rutile	1.000	-54800.29585748	0.0000	2

Titania nanoparticles: IPs and structure stability

Table A4: Buckingham parameters for IPs used in the Monte Carlo basin hopping global optimization searches in Chapter 4. Ionic charges for both IPs are: Q(Ti, Ti1, Ti2) = 2.4 and Q(O, O1, O2) = -1.2

IP1				
	A_{ij}	B_{ij}	C_{ij}	
Ti-O	69000.0	0.210	500	this work
Ti-Ti	22054.2	0.185	5.05	this work
O-O	3328.5	0.297	16.48	this work
IP2				
	A_{ij}	B_{ij}	C_{ij}	
Ti1-Ti1	31120.2	0.15400	5.25	MA-IP[85]
Ti1-O1	16957.5	0.19400	12.59	MA-IP[85]
Ti1-O2	16957.5	0.19400	12.59	MA-IP[85]
O1-O1	11782.7	0.23400	30.22	MA-IP[85]
Ti2-Ti2	79502.1	0.20101	446.78	FB-IP[59]
Ti2-O2	10454.2	0.20759	63.05	FB-IP[59]
Ti2-O1	10454.2	0.20759	63.05	FB-IP[59]
O1-O2	1428.4	0.35773	41.37	FB-IP[59]
Ti1-Ti2	79502.1	0.20101	446.70	FB-IP[59]
O1-O2	2100.0	0.32000	0.00	-

Table A5: From the bottom-up approach, total energy, total energy per unit and total energy per unit relative to anatase bulk of globally optimized nanoclusters. All energies are in eV and are obtained with PBE0 funtional using tight/tier-1 numerical basis set. Anatase bulk system's energy is -109600.914 eV and it has 4 unit per cell (standard anatase unitcell) [a]Total energy/unit - Anatase-bulk/unit.

$(TiO_2)_N$	**Total energy (eV)**	**Total energy/unit (eV)**	**Relative to Bulk[a]**
$(TiO_2)_1$	-27393.850	-27393.850	6.378
$(TiO_2)_2$	-54792.946	-27396.473	3.755
$(TiO_2)_3$	-82192.094	-27397.365	2.864
$(TiO_2)_4$	-109591.527	-27397.882	2.347
$(TiO_2)_5$	-136990.604	-27398.121	2.108
$(TiO_2)_6$	-164390.819	-27398.470	1.759
$(TiO_2)_7$	-191790.264	-27398.609	1.619
$(TiO_2)_8$	-219189.848	-27398.731	1.497

$(TiO_2)_9$	-246589.334	-27398.815	1.414
$(TiO_2)_{10}$	-273989.443	-27398.944	1.284
$(TiO_2)_{11}$	-301388.641	-27398.967	1.261
$(TiO_2)_{12}$	-328788.618	-27399.052	1.177
$(TiO_2)_{13}$	-356187.9635	-27399.074	1.154
$(TiO_2)_{14}$	-383588.0532	-27399.147	1.082
$(TiO_2)_{15}$	-410988.1054	-27399.207	1.021
$(TiO_2)_{16}$	-438387.3154	-27399.207	1.021
$(TiO_2)_{17}$	-465787.5716	-27399.269	0.960
$(TiO_2)_{18}$	-493186.6659	-27399.259	0.969
$(TiO_2)_{19}$	-520587.3355	-27399.333	0.895
$(TiO_2)_{20}$	-547986.8223	-27399.341	0.887
$(TiO_2)_{21}$	-575386.0346	-27399.335	0.894
$(TiO_2)_{22}$	-602785.896	-27399.359	0.870
$(TiO_2)_{23}$	-630185.5407	-27399.371	0.857
$(TiO_2)_{24}$	-657585.884	-27399.412	0.817
$(TiO_2)_{28}$	-767184.7767	-27399.456	0.772
$(TiO_2)_{35}$	-958982.5525	-27399.502	0.727
$(TiO_2)_{38}$	-1041181.3996	-27399.511	0.718

Table A6: From the top-dwon approach, total energy, total energy per unit and total energy per unit relative to anatase bulk of anatase cut nanoparticles. All energies are in eV and are obtained with PBE0 funtional using tight/tier-1 numerical basis set. Anatase bulk system's energy is -109600.914 eV and it has 4 unit per cell (standard anatase unitcell). [a] Truncated Bipyramidal Wulff morphology. [b]Total energy/unit - Anatase-bulk/unit.

$(TiO_2)_N$	**Total energy**	**Total energy/unit**	**Relative to Bulk[b]**
$(TiO_2)_{28}$ ref[82]	-767174.8733	-27399.103	1.126
$(TiO_2)_{33}$ T-Wulff[a]	-904174.6708	-27399.232	0.996
$(TiO_2)_{35}$ Wulff	-958973.366	-27399.239	0.989
$(TiO_2)_{38}$ ref[83]	-1041173.491	-27399.302	0.926
$(TiO_2)_{78}$ TWulff	-2137163.031	-27399.526	0.702
$(TiO_2)_{84}$ Wulff cut	-2301561.73	-27399.544	0.684

Hydrated Silica and Titania nanoparticles: IPs and hydration energies

Table A7: Parameters for the FFSiOH and FFSiOH* (simplified FFSiOH) IPs used in the Monte Carlo basin hopping global optimization searches of hydrated silica clusters (Chapter 5 and Chapter 6). [a] the Morse potential acting only between bonded atoms where the bonding cutoff threshold is determined according to their Van der Waals radii. [b] the Morse potential acting only between bonded all pars of atoms within a cutoff distance of 4.00 Å expect on bonded species. [c] the hydrogen bond three-body interaction parameters according the formula $E_{H-bond} = A_{2,3}/r_{2,3}^{12} - B_{2,3}/r_{2,3}^{10} \times \cos\theta_{3,1,2}{}^4$ if $\theta_{3,1,2} < 90^o$, $E_{H-bond} = 0.0$ otherwise. Cutoff interactions are: 1,2=1.00Å, 1,3=2.00Å and 2,3= 2.71Å

FFSiOH* used in ref[89,90]			
Buckingham	A_{ij}	B_{ij}	C_{ij}
Si-O	18003.8	0.205204	133.54
H-O	10907.0	0.125393	4.09
O-O	1388.8	0.362318	175.00
Charges	Q(Si) = 2.4, Q(O) = -1.2 and Q(H)=0.6		
FFSiOH used in ref[117]			
Buckingham	A_{ij}	B_{ij}	C_{ij}
$O1_{shel}$-$O1_{shel}$	15039.909	0.227708	0.0
$O1_{shel}$-$O2_{shel}$	6768.7644	0.245932	0.0
$O2_{shel}$-$O2_{shel}$	1688.1482	0.292545	0.0
Si_{core}-$O1_{shel}$	8166.2632	0.193884	0.0
Morse	D_e	a	r_e
Si_{core}-$O2_{shel}$	0.045897	2.6598	2.33921
Morse (intra bond)[a]			
H_{core}-$O2_{shel}$	0.009359	3.2461	1.76617
H_{core}-$O1_{shel}$	0.009359	2.5461	2.36617
Morse (X12)[b]			
H_{core}-$O2_{shel}$	0.1109733	1.0230	2.33429
H_{core}-$O1_{shel}$	0.006439	1.8794	3.17953
hydrogen-bond[c]	A	B	
H_{core}-$O2_{shel}$-$O2_{shel}$	3653.26	0.00	
Spring	K(O1) = 256.71027, K(O2) = 160.84247		
Charges: Si_{core}= 2.7226, $O1_{core}$= 1.919810, $O1_{shel}$=-3.281110, $O2_{core}$= 1.429114, $O2_{shel}$=-2.767837, H $_{core}$= 0.658073			

Table A8: Parameters for the FFTiOH and FFTiOH* (the simpler version of FFTiOH) IPs used in the Monte Carlo basin hopping global optimization searches of hydrated titania clusters (Chapter 6). [a] and [b] Morse potential acting between atoms pairs with different cutoff distances: 0.0 - 1.2 Å for the interaction in [a] and 1.2 - 2.5 Å for the interaction in [b]. The meaning of the interaction [c] is reported in Table A7 right above.

FFTiOH* used in this work			
Buckingham	A_{ij}	B_{ij}	C_{ij}
Ti-O	22054.2	0.190000	0.00
H-O	1054.2	0.145000	0.00
O-O	15039.9	0.227708	0.00
Charges	Q(Ti) = 2.7226, Q(O) = 1.3613 and Q(H)=0.68065		
FFTiOH used in this work			
Buckingham	A_{ij}	B_{ij}	C_{ij}
$O1_{shel}$-$O1_{shel}$	15039.909	0.227708	0.0
$O1_{shel}$-$O2_{shel}$	6768.7644	0.245932	0.0
$O2_{shel}$-$O2_{shel}$	1688.1482	0.292545	0.0
Ti_{core}-$O1_{shel}$	22054.2000	0.190000	0.0
Morse	D_e	a	r_e
Ti_{core}-$O2_{shel}$	0.045897	2.6598	2.33921
(H_{core}-$O2_{shel}$)[a]	0.009359	3.2461	1.76617
(H_{core}-$O2_{shel}$)[b]	0.11097337	1.6830	2.48921
Morse (X12)[c]			
H_{core}-$O1_{shel}$	0.006439	1.8794	3.17953
hydrogen-bond	same as in Table A7		
Spring	K(O1) = 256.71027, K(O2) = 130.84247		
Charges: same as in Table A7 with Q(Ti)=Q(Si)			

Table A9: Total energy and hydration (free)energy of silica and titania global minima candidate clusters at 0K and 300K as reported in Chapter 6. All data reported here are the result of PBE0 calculations employing tight / tier-1 basis set. All energies are in eV. To calculate the hydration energy for each cluster we use the water total energy which is -2080.824623837 eV.

$(XO_2)_M(H_2O)_N$ (X=Si, Ti)	**Total energy**	$\Delta E_{hyd}/unit[M]$	$\Delta G_{hyd}/unit[M]$ (300K, 1Pa)
$(SiO_2)_4(H_2O)_0$	-48002.6390278160	0.000	0.000
$(SiO_2)_4(H_2O)_1$	-50087.3335856515	-0.967	-0.744
$(SiO_2)_4(H_2O)_2$	-52173.3910310210	-2.275	-1.825
$(SiO_2)_4(H_2O)_3$	-54255.1869114091	-2.518	-1.867

$(SiO_2)_4(H_2O)_4$	-56336.5647800218	-2.656	-1.810
$(SiO_2)_8(H_2O)_0$	-96011.4043516400	0.000	0.000
$(SiO_2)_8(H_2O)_1$	-98097.0278750840	-0.599	-0.358
$(SiO_2)_8(H_2O)_2$	-100182.535852963	-1.185	-0.683
$(SiO_2)_8(H_2O)_3$	-102267.338674625	-1.682	-0.902
$(SiO_2)_8(H_2O)_4$	-104349.476285513	-1.846	-1.074
$(SiO_2)_8(H_2O)_5$	-106430.564603840	-1.894	-1.116
$(SiO_2)_{12}(H_2O)_0$	-144022.253805869	0.000	-1.069
$(SiO_2)_{12}(H_2O)_1$	-146108.262282385	-0.431	0.000
$(SiO_2)_{12}(H_2O)_2$	-148193.837840203	-0.827	-0.477
$(SiO_2)_{12}(H_2O)_3$	-150277.983224293	-1.104	-0.947
$(SiO_2)_{12}(H_2O)_4$	-152361.599422819	-1.337	-1.342
$(SiO_2)_{12}(H_2O)_5$	-154443.495096819	-1.426	-1.430
$(SiO_2)_{12}(H_2O)_6$	-156524.598700983	-1.449	-1.381
$(SiO_2)_{16}(H_2O)_0$	-192035.449961704	0.000	0.000
$(SiO_2)_{16}(H_2O)_1$	-194120.574716013	-0.268	-0.214
$(SiO_2)_{16}(H_2O)_2$	-196206.349746144	-0.578	-0.471
$(SiO_2)_{16}(H_2O)_3$	-198290.633880571	-0.794	-0.640
$(SiO_2)_{16}(H_2O)_4$	-200373.732834230	-0.936	-0.740
$(SiO_2)_{16}(H_2O)_5$	-202456.332524720	-1.047	-0.813
$(SiO_2)_{16}(H_2O)_6$	-204537.676764259	-1.079	-0.797
$(SiO_2)_{16}(H_2O)_7$	-206618.763454576	-1.096	-0.774
$(SiO_2)_{16}(H_2O)_8$	-208699.966734881	-1.119	-0.736
$(TiO_2)_4(H_2O)_0$	-109591.526384618	0.000	0.000
$(TiO_2)_4(H_2O)_1$	-111674.964415884	-0.653	-0.464
$(TiO_2)_4(H_2O)_2$	-113759.247100736	-1.517	-1.163
$(TiO_2)_4(H_2O)_3$	-115840.533332674	-1.633	-1.093
$(TiO_2)_4(H_2O)_4$	-117921.621538981	-1.699	-0.902
$(TiO_2)_8(H_2O)_0$	-219189.847545120	0.000	0.000
$(TiO_2)_8(H_2O)_1$	-221272.915420889	-0.191	-0.136
$(TiO_2)_8(H_2O)_2$	-223356.299783769	-0.370	-0.249
$(TiO_2)_8(H_2O)_3$	-225439.226319991	-0.512	-0.343
$(TiO_2)_8(H_2O)_4$	-227520.835847176	-0.614	-0.401
$(TiO_2)_8(H_2O)_5$	-229602.136873834	-0.661	-0.369
$(TiO_2)_{12}(H_2O)_0$	-328788.617828857	-0.720	-0.326

$(TiO_2)_{12}(H_2O)_1$	-330871.745529406	0.000	0.000
$(TiO_2)_{12}(H_2O)_2$	-332954.718314729	-0.280	-0.196
$(TiO_2)_{12}(H_2O)_3$	-335037.247621494	-0.600	-0.452
$(TiO_2)_{12}(H_2O)_4$	-337119.289873198	-0.863	-0.609
$(TiO_2)_{12}(H_2O)_5$	-339200.683946106	-0.961	-0.644
$(TiO_2)_{12}(H_2O)_6$	-341282.207339540	-1.020	-0.576
$(TiO_2)_{16}(H_2O)_0$	-438387.315807357	0.000	0.000
$(TiO_2)_{16}(H_2O)_1$	-440470.305785652	-0.135	-0.080
$(TiO_2)_{16}(H_2O)_2$	-442553.214281150	-0.265	-0.187
$(TiO_2)_{16}(H_2O)_3$	-444635.299203332	-0.344	-0.216
$(TiO_2)_{16}(H_2O)_4$	-446717.771656194	-0.447	-0.293
$(TiO_2)_{16}(H_2O)_5$	-448799.271203031	-0.489	-0.277
$(TiO_2)_{16}(H_2O)_6$	-450880.708071367	-0.527	-0.265
$(TiO_2)_{16}(H_2O)_7$	-452962.039211837	-0.559	-0.237
$(TiO_2)_{16}(H_2O)_8$	-455043.707090292	-0.612	-0.216

APPENDIX

List of Publications

1. Stability of mixed-oxide titanosilicates: dependency on size and composition from nanocluster to bulk. Andi Cuko, Monica Calatayud and Stefan T. Bromley, *Nanoscale*, 2018, 10, 832. DOI: 10.1039/c7nr05758j

2. Predicting size-dependent emergence of crystallinity in nanomaterials: titania nanoclusters versus nanocrystals. Oriol Lamiel-Garcia, Andi Cuko, Monica Calatayud, Francesc Illas and Stefan T. Bromley, *Nanoscale*, 2017, 9, 1049. DOI: 10.1039/C6NR05788H

3. Global optimisation of hydroxylated silica clusters: A cascade Monte Carlo Basin Hopping approach. Andi Cuko, Antoni Macià, Monica Calatayud, Stefan T.Bromley, *Comp. Theor. Chem.* 2017, 1102, 38-43. doi.org/10.1016/j.comptc.2016.12.030

4. Dissociative water adsorption on TiO_2 and SiO_2 nanoclusters: dependence on temperature and water vapour pressure. This work is in its final stage preparation and the manuscript is reported here. (In preparation)

5. Development of artificial neural networks for binary and ternary oxide nanoparticles: the case of titania and magnesium silicate nanoparticles. (In preparation)

5. Oxygen vacancy formation in Titania and Silica: from nanoscale to bulk. (In preparation)

The author actively participated in doing calculations, analyzing and discussing results, and in writing the manuscripts of articles 1, 3 and 4. For the article 2, the author actively participated in doing calculations relative

to the bottom-up approach. He developed an interatomic potential for the global optimization of $(TiO_2)_N$ nanoclusters able to find and revise many of the previously reported global minima candidates. He also participated to analysis and discussions during the project and to the final review of the article. The article 4 is in its last stage of preparation and the manuscript is reported in this thesis while articles 5 and 6 are at their early stage of preparation and thus not reported here.

Stability of Mixed-oxide Titanosilicates: Dependency on Size and Composition from Nanocluster to Bulk

Andi Cuko[1,2], Monica Calatayud[2,3,*], Stefan T. Bromley[1,4,*]

[1] *Departament de Química Física and Institut de Química Teòrica i Computacional (IQTCUB), Universitat de Barcelona, E-08028 Barcelona, Spain*

[2] *Sorbonne Universités, UPMC Univ Paris 06, CNRS, Laboratoire de Chimie Théorique CC 137 - 4, place Jussieu F. 75252 PARIS CEDEX 05 - France*

[3] *Institut Universitaire de France, France*

[4] *Institució Catalana de Recerca i Estudis Avançats (ICREA), E-08010 Barcelona, Spain*

* Corresponding authors: s.bromley@ub.edu, calatayu@lct.jussieu.fr

Nanostructured titanosilicate materials based upon interfacing nano-TiO_2 with nano-SiO_2 have drawn much attention due to their huge potential for applications in a diverse range of important fields including gas sensing, (photo)catalysis, solar cells, photonics/optical components, tailored multi-(bio)functional supports and self-cleaning coatings. In each case it is the specific mixed combination of the two SiO_2 and TiO_2 nanophases that determines the unique properties of the final nanomaterial. In the bulk, stoichiometric mixing of TiO_2 with SiO_2 is limited by formation of segregated TiO_2 nanoparticles or metastable glassy phases and more controlled disperse crystalline mixings only occur at small fractions of TiO_2 (< 15 wt%). In order to more fully understand the stability nano-SiO_2 and nano-TiO_2 combinations with respect to composition and size, we employ accurate all-electron density functional calculations to evaluate the mixing energy in $(Ti_xSi_{1-x}O_2)_n$ nanoclusters with a range of sizes (n = 2 - 24) having different titania molar fractions (x = 0 - 1). We derive all nanoclusters from a dedicated global optimisation procedure to help ensure that they are the most energetically stable structures for their size and composition. We also consider a selection of representative intimately mixed crystalline solid phase $(Ti_xSi_{1-x}O_2)_{bulk}$ systems for comparison. In agreement with experiment, we find that intimate mixing of SiO_2 and TiO_2 in bulk crystalline phases is energetically unfavourable. Conversely, we find that SiO_2-TiO_2 mixing is energetically favoured in small $(Ti_xSi_{1-x}O_2)_n$ nanoclusters. Following the evolution of mixing energy with nanocluster size and composition we find that mixing is most favoured in nanoclusters with a diameter of 1 nm with a TiO_2 molar fraction of 0.3-0.4. Thereafter, mixed nanoclusters with increasing size have progressively less negative mixing energies up to diameters of approximately 1.5 nm. We propose some chemical-structural principles to help rationale this energetically favourable nanoscale mixing. As a guide for

experimentalists to observe and characterize these mixed nano-species we also provide two measurable signatures of mixing based on their unique vibrational and structural characteristics.

Introduction

Almost all elements of the periodic table form stable oxide compounds. Due to the importance and diversity of properties exhibited by oxides (e.g. (photo)catalytic activity, multiferroic and memristive effects, superconductivity, magnetism) they play an essential role in our society in established technologies, while continuing to be a focus of frontier research in many fields. The effectiveness and range of properties of an application based on a single oxide material can often be enhanced by using mixed oxides (i.e. materials comprised by the combination of two or more oxides). Examples of such synergistic behaviour in mixed oxides are well established in, for instance, cases of catalytic activity[1] and high temperature composites[2]. Depending on the application, one may need to mix the constituent oxides in a more or less intimate fashion. In some cases, homogeneously mixing oxides can be difficult due to their tendency to segregate into separate phases, typically occurring when the structures and properties of the respective bulk phases are very different. Moreover, it can be also difficult to obtain specific compositions of two oxides, for instance when high temperature calcination is involved in the mixed oxide synthesis. These effects can, however, be very dependent on sample size. For example, some materials that hardly mix at bulk macroscopic level at desired composition, can be synthesized and stabilized in mixed phases at the nanoscale[3,4,5,6]. Furthermore, at the nanoscale, system properties can often be more finely tuned by varying both size and composition. Here, we focus on a particular mixed oxide system, titanosilicates (i.e. mixed titania (TiO_2) and silica (SiO_2) systems). Titanosilicates are robust low cost materials that can combine mechanical strength, chemical stability, nanoporosity, controllable optical characteristics, photoactivity and high redox potential properties. This combination of features make titanosilicates ideal candidates for thermally stable high surface area materials that can be tailored for a range catalytic and optical applications (e.g. industrial heterogeneous catalysis, solar cells, optical components, self-cleaning systems, selective molecular sieves, water remediation, and photocatalysis[7,8,9,10,11,12,13]). One important class of titanosilicates is that of the ETS (Engelhard Titanium Silicate) family of microporous titanosilicates introduced by Kuznicki *et al*.[14,15]. Among the numerous interesting properties of these materials, due to their tailorable pore dimensions, some are able to selectively adsorb and separate gas mixtures of small molecules with similar size, such as that of N_2/CH_4, Ar/O_2 and N_2/O_2. Formally, the titanosilicate frameworks of the ETS materials do not possess a stoichiometric mix of TiO_2 and SiO_2, but as with the related aluminosilicate zeolites, have a net negative charge which must be compensated by cations.

Generally, it is relatively difficult to synthesize homogeneous stoichiometric mixed TiO_2-SiO_2 bulk phases due to the tendency of the constituent oxides to segregate into two respective phases

with increasing temperature. In crystalline systems, bulk homogeneous mixing seems to be only possible by the inclusion of a very small percentage of TiO_2 in a silica framework. For higher TiO_2 molar fractions homogeneous mixed TiO_2-SiO_2 oxides seem only to be possible in amorphous bulk phases, which are metastable with respect to the separate respective pure oxide polymorphs.[16,17,18] There are several ways to synthesize titanosilicates. From a top down synthesis of mechanically crushing separate bulk phases of silica and titania and heating it is possible to obtain macroscopically homogeneous mixing. In order to have microscopically homogeneous mixing, however, bottom up synthetic methods such as sol-gel techniques are needed.[19] When larger proportions of titania (typically > 15 wt%) are employed these syntheses tend to lead to segregated (nano)composites of two distinct phases of TiO_2 and SiO_2. Dong et al.[20], for example, have synthesized a highly ordered 2D hexagonal mesoporous crystalline TiO_2-SiO_2 nanocomposite with anatase TiO_2 nanocrystals embedded in silica pore walls which is thermally stable at 600-850ºC. This material exhibits an improved photocatalytic activity in the degradation of rhoamine B (RhB) compared to the commercial pure TiO_2 Degussa P25 catalyst. Jiang C. et al.[21] have also synthesized TiO_2-SiO_2 titanosilicate composites via sol-gel routes where small TiO_2 anatase nanocrystals are incorporated into microporous ZSM-5 and mesoporous SBA-15 silica frameworks in order to better control their size and improve the titania photoactivity for hydrogen production by water splitting. In the class of non-segregated mixed TiO_2-SiO_2 bulk oxides, one of the most industrially important materials, known from early 80s, is the synthetic titanosilicate-1 (TS-1)[7]. The active sites in TS-1 are uniformly dispersed and isolated four-fold titanium centers incorporated in a zeolitic silica MFI structure with 1.0-2.5% of TiO_2 molar inclusion. TS-1 is used as industrial redox catalyst for oxidizing organic molecules in mild conditions in the presence of hydrogen peroxide.

In this work we theoretically investigate the size-dependency of the energetics of TiO_2-SiO_2 mixing. In particular, we focus on TiO_2-SiO_2 mixing in small nanoclusters (i.e. <100 atoms) and how it compares with, and evolves with increasing size, towards the situation in corresponding bulk systems. In principle titanosilicate nanoparticles could be synthesised through use of ionized nanocluster beams but to the best of our knowledge no mixed silica-titania nanoclusters of the size studied herein have been reported to date. nanocluster beams are, however, becoming an important method for generating selected nanoclusters for catalytic and technological applications,[22,23,24] Takeuchi et al.[25], for example, have synthesized thin layers of titanosilicates by deposition of TiO_2 and SiO_2 nanoclusters generated by a laser beam in which they observe a high photocatalytic activity towards decomposition of NO in N_2 and O_2 due to highly disperse Ti-sites embedded in a silica framework.

Previous theoretical studies of stoichiometric mixed TiO_2-SiO_2 systems have tended to focus on crystalline bulk mixed oxide materials having a very small fraction of TiO_2 (e.g. TS-1) – see ref. 26 for an overview of theoretical and experimental studies in this area. Only very few works are present in the literature on the theoretical modelling of TiO_2-SiO_2 mixing in systems with relatively high percentages of TiO_2. Recently, Landmann et al.[27] reported an extensive and detailed computational modelling study of the structure of bulk amorphous titanosilicate glasses. Miroshnichenko *et al*.[28] have studied the effect of SiO_4 groups on optical, electronic, and structural properties when present in TiO_2 anatase-structured nanoparticles. For very small nanoclusters, Bandyopadhyay and Aikens[29] have studied a series of mixed $Ti_xSi_yO_{2(x+y)}$ oxide nanoclusters with up to five formula units (i.e. $x+y \leq 5$).

Confirming experiment, our calculations show that TiO_2-SiO_2 mixing is energetically unfavourable in bulk crystalline systems. However, surprisingly, in nanoclusters possessing up to 70 atoms we predict that the mixing of TiO_2 and SiO_2 is thermodynamically favourable. Our results point to a number of important factors which determine the higher stability of nano-titanosilicates with respect to pure nano-silica and nano-titania. Linking the results for bulk and the nanoscale we also show that the energetics of TiO_2-SiO_2 mixing depends on size; becoming less favourable with increasing size after a nanocluster size of ~30 atoms. With this work, we hope to inspire experimental groups, especially from the nanocluster beam community, to attempt the synthesis of the titanosilicate nanoclusters predicted here. To assist in the identification of mixed TiO_2-SiO_2 nanoclusters in such experiments we provide calculated vibrational frequency and average coordination number signatures that indicate when intimate nano-oxide mixing is occurring.

Methodology

We consider both mixed titanosilicates nanoclusters $(Ti_xSi_{1-x}O_2)_n$, with a range of sizes (n = 2 - 24) having different titania molar fractions (x = 0 - 1), and a selection of crystalline solid phase systems $(Ti_xSi_{1-x}O_2)_{bulk}$. In the case of the nanoclusters, great efforts were made to try to find the most energetically stable isomer for each n and x. In order to find low energy nanocluster structures on the multidimensional potential energy surface (PES) we used the Monte Carlo basin-hopping (MCBH) global optimization algorithm[30] with classical interatomic potentials (IPs) to efficiently explore the PES as implemented in an in-house modified version of the GMIN 1.x code.[31] Previously, IPs have been employed for global optimisation of separate $(TiO_2)_n$[32,33,34] and $(SiO_2)_n$[35,36,37,38] nanoclusters. However, to our knowledge, IPs for mixed titanosilicate nanoclusters have not been reported. Specifically, we use the Buckingham pair interaction IP together with interionic electrostatic interactions:

$$V_{ij}(r_{ij}) = \frac{q_i q_j}{4\pi\varepsilon_0 r_{ij}} + A_{ij} exp\left(-\frac{r_{ij}}{B_{ij}}\right) - \frac{C_{ij}}{r_{ij}^6} \quad (1)$$

where q_i, q_j are ionic charges, ε_0 is the vacuum dielectric constant, r_{ij} is the interatomic distance between atoms i and j and A, B, C are fitted parameters. Due to the structural complexity of the $(Ti_xSi_{1-x}O_2)_n$ system we were not able to find one IP parameter set that could provide reliably in finding low energy nanoclusters for the full range of x considered. Thus, in order to resolve this issue, we employed two different Buckingham-type IPs (IP1 and IP2) with the respective parameters reported in table 1. These IPs are largely derived from modifications to parameters used in previously reported IPs for $(SiO_2)_n$ nanoclusters[35] and bulk TiO_2[39]. IP1 typically provides better low energy cluster isomer candidates than IP2 for systems with a higher content of TiO_2 and tends to give structures where Ti-centres are 4, 5 and rarely 6 coordinated depending on nanocluster size. For systems with a lower incorporation of TiO_2 this IP tends to yield 3-coordinated Ti atoms which are highly unstable. IP2 instead, generally yields lower energy isomer structures than IP1 for lower content of TiO_2. In both cases, Si-centres tend to occupy 4-fold O-coordinated positions which are known to be to be the most energetically favourable for pure silica systems. We note that both IPs are able to provide reasonable structures for intermediate TiO_2 content thus the low energy PES of this compositional range is probably most well sampled by our approach. A comparison of the performance of both IP1 and IP2 with respect to the refined energetic stabilities of the isomers coming from a typical global optimisation run over the full range of TiO_2 content and for three system sizes (N= 8, 9 10) is proved in the Supplementary Information.

With both IPs there is a tendency to produce nanoclusters with Si-O terminations. It is known that for small nanoclusters both pure TiO_2 and SiO_2 prefer open structures with terminating oxygen defects compared to compact fully coordinated ones[33,36]. However, due to the relatively higher ionicity of Ti-O bonds, Ti-O terminations tend to be less energetically costly compared to Si-O terminations. Also, for relatively larger nanoclusters (n ≥ 12) there is a tendency for the IPs to produce some low energy nanocluster structures containing 5- or 6-fold coordinated silicon atoms which are relatively high in energy according to density DFT-based calculations (see details below). Instead of simply discarding these anomalous nanoclusters, we found that they could be converted into more reliably low energy candidate nanocluster structures after the MCBH search by simple interchange of cations within the respective nanocluster following: 1) Si centres in terminating Si-O defects with a 4-coordinated Ti atoms, 2.) Highly coordinated Si centres (5- and 6-coordinated) with 4-coordinated Ti centres.

	IP1 (x > 0.30 TiO_2)			IP2 (x < 0.30 TiO_2)		
	A_{ij}	B_{ij}	C_{ij}	A_{ij}	B_{ij}	C_{ij}
Si-O	10454.2	0.208	63.05	10386.97	0.210372	63.45
Ti-O	2454.2	0.211	-55.05	14719.71	0.200783	65.90
Si-Si	79502.1	0.220	446.78	74316.65	0.220	446.78
Ti-Si	69000.0	0.210	500.00	104167.92	0.220	446.78
Ti-Ti	69000.0	0.210	480.59	74316.65	0.220	446.78
O-O	2828.5	0.297	16.48	2828.5	0.297	16.48

Table 1. Buckingham parameters for IPs used in the MCBH global optimization searches. Ionic charges for both IPs are: Q(Si, Ti)=2.4 and Q(O) = -1.4

We used MCBH with both IP1 and IP2 for finding low energy nanocluster isomers. We typically use several MCBH runs for each nanocluster composition (up to five for the larger nanoclusters) and for each run we use a different initial structure. With increasing nanocluster size, we correspondingly increase the number of MCBH steps in each run from fifty thousand to one million. In addition to the usual random atomic displacements we also apply Ti/Si cation interchange moves in a small percentage (1 - 5%) of the steps. From each run of this IP-based global optimization procedure, for each nanocluster composition, the forty lowest energy structures were then fully optimized employing all electron, relativistic, DFT based calculations using the FHI-AIMS code.[40] Firstly, we employed the general gradient approximation PBE[41] functional with a light/tier-1 basis of numerical atom-centred basis functions, to optimise the IP-optimised nanocluster structures coming directly from the global optimisations. We note that light/tier-1 basis of numerical atom-centred orbitals approximately provides results of a similar or higher quality to those obtained with valence triple-zeta plus polarization Gaussian type orbitals. Subsequently, from these forty isomers, the seven most stable isomers were further optimized using the hybrid PBE0 functional[42] with tight/tier-1 basis. This cascade optimisation approach has been successfully used in previous studies[33,34,37,43,44].

For the selected periodic $(Ti_xSi_{1-x}O_2)_{bulk}$ crystals we performed an initial full optimization of both atom coordinates and cell lattice vectors at a PBE light/tier-1 level of theory with atom coordinates then further refined at a PBE0 tight/tier-1 level also using FHI-AIMS. For these periodic calculations, depending on the unit cell size, we used an appropriate Monkhort-Pack grid of k-points, going from 7x7x7 for the smallest system (pure rutile and quartz) to a 2x2x2 points grid for the largest one.

In order to compare relative stabilities of a specific mixed system with respect to the pure oxides, we consider the mixing energy, ΔE_{mix}, which we take to be difference in the energy of the system with respect to the proportional sum of the energies of the two pure systems of the same

size. Specifically, for a generic titanosilicate we refer to the chemical reaction between pure oxide systems as defined in equation 2 and the corresponding mixing energy in equation 3.

$$(1-x)\,SiO_2 + x\,TiO_2 \rightarrow Ti_xSi_{1-x}O_2 \quad (2)$$

$$\Delta E_{mix} = E_{Ti_xSi_{1-x}O_2} - [(1-x)\,E_{(SiO_2)} + x\,E_{TiO_2}] \quad (3)$$

where x is the TiO_2 molar fraction in the nanocluster. $E_{Ti_xSi_{1-x}O_2}$ is the total DFT energy of the mixed system, $E_{(SiO_2)}$ and $E_{(TiO_2)}$ are energies of the respective pure silica and pure titania global minima structures. ΔE_{mix} can be either positive, which means that the silica and titania mixing is energetically unfavourable, or negative, which means that the mixing is favourable. Mixing energies are then normalized by the number of MO_2 (M=Si, Ti) oxide units. In the case of nanoclusters the number of units corresponds to its size n, while in the case of bulk systems we employ the number of oxide units in the unit cell. We note that normalization factor could also be chosen to be the number of the smallest titanosilicate units according to a specific composition (e.g. when x=0.5 the fundamental unit is $TiSiO_4$, when x=0.333 the fundamental unit is $TiSi_2O_6$ etc.). This normalisation choice unit is typically employed for reporting experimental mixing enthalpies of bulk systems. For example, conventionally, experimental mixing enthalpies of two common mixed MgO-SiO_2 magnesium silicates forsterite (Mg_2SiO_4) and enstatite ($MgSiO_3$) are usually given relative to moles of Mg_2SiO_4 and moles of $MgSiO_3$ respectively.[45] For titanosilicates, to the best of our knowledge, there are no experimental enthalpies of mixing because of the tendency of the constituent oxide phases to segregate. We note that the use of the MO_2 (M=Si, Ti) oxide unit also allows us to directly compare systems with different compositions on the same footing. In the Supplementary Information we report $\Delta E_{mix}/unit$ (eV) according to both definitions of normalisation unit for a range of $Ti_{0.5}Si_{0.5}O_2$ systems. We note that the mixing energy in equation 3 is a thermodynamic quantity, therefore formally all terms used should be thermally corrected at finite temperatures. As a first approximation, we mainly consider ΔE_{mix} in terms of 0K internal electronic energies directly coming from DFT calculations. However, in order to account for the effect of finite temperature we have also estimated the free mixing energies (ΔG_{mix}) for a set of mixed titanosilicates nanoclusters with with 1:1 stoichiometry (x=0.5). For these calculations we evaluated the harmonic vibrational frequencies and resulting free energies with the Gaussian09 package[46] using the PBE0 functional with the Ahlrichs triple-ζ plus polarizations basis functions (TZPV)[47] on all atoms.

Results and Discussions

1) Bulk mixed TiO_2-SiO_2 systems

Firstly we took a selection of mixed $(Ti_xSi_{1-x}O_2)_{bulk}$ crystalline systems where one or more 4-fold coordinated Si-centres were replaced with Ti atoms to generate mixed oxide bulk phases with different degrees of mixing (i.e. x=0.08, 0.33, 0.50 and 0.67 TiO_2 molar fraction). Specifically, we consider the quartz (Fig. 1a) and sodalite (Fig. 1b) crystal structure types. We choose quartz as representative of dense titanosilicates where we examined structures with x=0.33, 0.50 and 0.67. The sodalite crystal with low (x=0.08) TiO_2 inclusion is taken to represent low density zeolitic titanosilicates such as TS-1. In the latter case we did not consider TS-1 directly because of the prohibitive computational cost of PBE0 DFT calculations with the large unit cell involved. In our selected set of bulk crystal titanosilicates, we also include a hypothetical phase having 4-fold Si-centres and 6-fold Ti-centres and an intermediate inclusion of TiO_2 (x=0.33, see Fig. 1c). This hypothetical structure was found in the Materials Project database (ID: mp-766596)[48]. We note that unlike quartz and sodalite, this latter structure exhibits one dimensional "wires" of linked TiO_6 units as found in the experimentally synthesised non-stoichiometric ETS-10 structure[10]. This high 6-fold coordination environment of Ti is also similar to that found in the most stable rutile TiO_2 bulk polymorph. We refer to this structure as the "wired" phase.

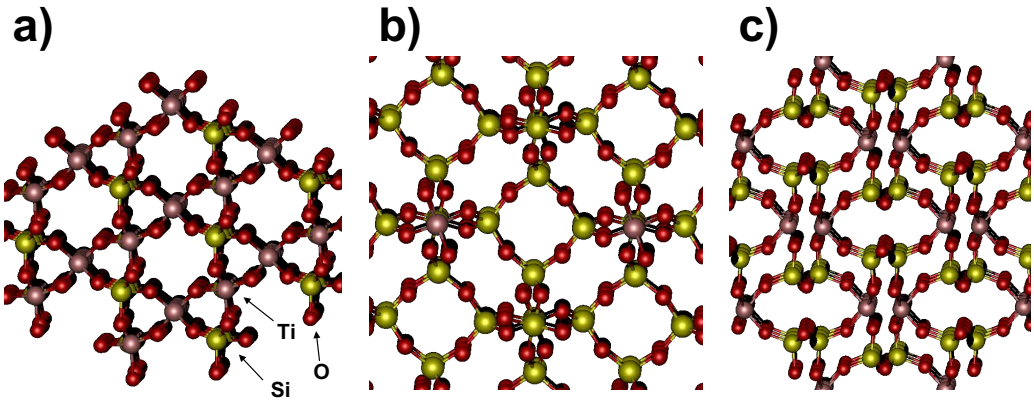

Fig 1. Crystalline mixed titanosilicates models: a) quartz-like structures (there are three quartz-like systems with different TiO_2 molar fractions: x=0.33, 0.50 (shown here) and 0.67, b) a sodalite-like system where in the unit cell, one Si atom is replaced with a Ti atom which corresponds to x=0.08, c) is the "wired" titanosilicate structure found in the Materials Project database having 4-fold silicon and 6-fold titanium atoms with x=0.33.

2) Global optimized mixed nanocluster structures

We report a set of global optimized mixed $(Ti_xSi_{1-x}O_2)_n$ titanosilicate nanoclusters with *n* = 2 - 24 units. For n = 2 - 10 we consider all possible values of molar fraction *x*. We also consider some larger nanoclusters with n = 12, 14, 16 and 24, for which selected mixing ratios have been chosen.

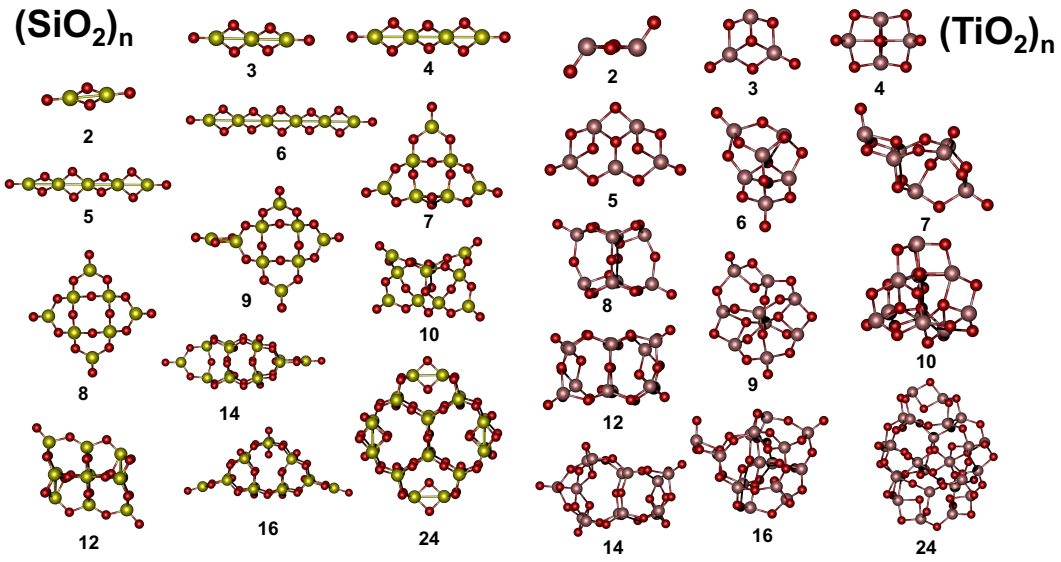

Fig 2. Structures of globally minimised nanoclusters of silica (left) and titania (right), each labelled with the respect to the corresponding number of MO_2 (M=Si or Ti) units. All these structures have been previously reported in the literature by us and other authors.[32,33,34,36,37,38,49,50,51,52] Atom key: yellow – silicon, grey – titanium, red – oxygen.

In Fig. 2 we show the lowest energy pure nanoclusters of silica and titania found previously [32,33,34,36,37,38,49,50,50,51] used here to calculate mixing energies for our set of titanosilicates. The global minima silica nanoclusters in this size range tend to be quite symmetric and open, and typically possess two or more terminal oxygen defects. Notice that for size n = 24 we have taken the very low energy fully-coordinated structure reported in ref. 38 structure rather than the reported global minimum structure in ref. 37 which possesses terminal oxygens. In fact, as noted in ref. 38, these two structures are almost degenerate in energy and the use of the PBE0 functional in the present work slightly favours the fully coordinated structure. All pure silica nanocluster structures display both 3- and 4-fold coordinated silicon atoms. Three-fold coordinated silicon atoms are present only when bound to a terminally "double-bonded" oxygen (i.e. formally: >Si=O, but arguably more accurately: $>Si^{+}\text{-}O^{-}$).[53,54] Such defective terminations are very common in the global minima silica nanoclusters in this size range and are found for all sizes apart from n = 12 and n = 24. For n = 12 the terminal oxygen atoms are bonded to 4-coordinated silicon atoms. In this case they are known as non-bridging oxygen (NBO) atoms where, for each NBO, the nanocluster also possesses a compensating triple coordinated oxygen-site. The combination of these two sites is also known as a compensated NBO or a valence alternation pair[55,56]. Titania nanoclusters tend to have relatively more compact and amorphous structures with respect to their silica counterparts. Most of them tend to have two NBO-type terminal oxygen defects. Unlike for the pure silica nanoclusters 3-fold coordinated titanium centres (i.e. >Ti=O species) appear to be energetically unstable and the

majority of the oxygen-terminated global minima nanoclusters exhibit only NBOs (except for $(TiO_2)_2$ where, due to the extremely small system size, only 3-coordinated Ti centres are possible). The global minima structures for $(TiO_2)_{10}$ and the largest n = 24 titania nanocluster considered are fully coordinated. As for silica this probably indicates a tendency for low energy nanoclusters to exhibit less energetically costly terminal defects with increasing size.[38] Generally, the respective global minima nanoclusters of $(TiO_2)_n$ and $(SiO_2)_n$ are quite distinct, with both systems displaying similar nanocluster structures only for sizes n = 2 and 12.

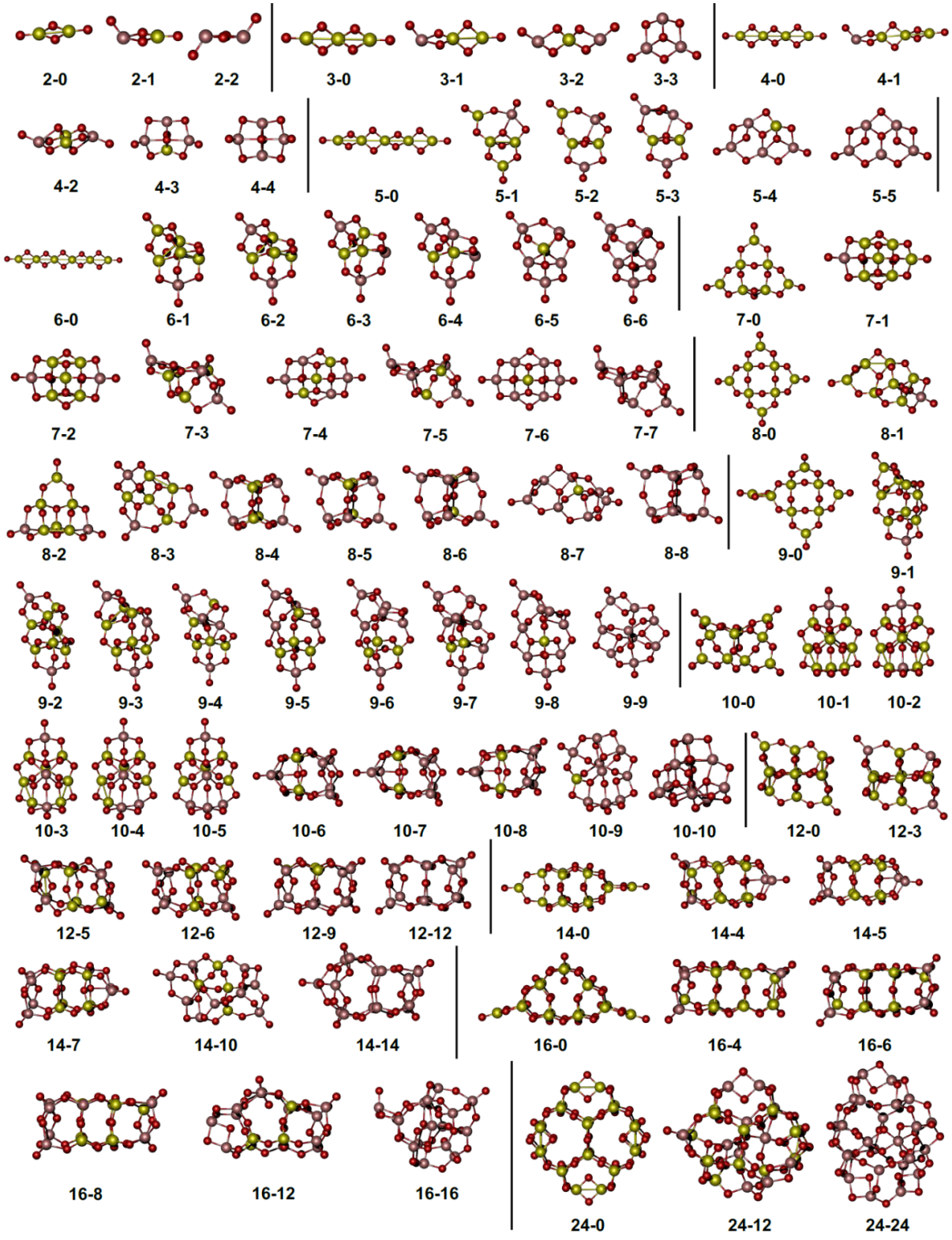

Fig 3. Globally optimized titanosilicate nanoclusters. Pure silica and titania nanoclusters from Fig 2 are also included for completeness. The two numbers assigned for each nanocluster are relative to the total number of units (n) and the number of incorporated TiO_2 units, respectively. Structures with sizes n = 2 - 5 were previously reported in literature[29], while all others are new to this study.

In Fig. 3 we report the lowest energy titanosilicate $(Ti_xSi_{1-x}O_2)_n$ nanocluster structures found in the present study (i.e. global minima candidates) for a range of different mixing ratios, x, and sizes, n. We note that only structures with sizes n = 2 - 5 were previously reported.[29] Almost all of the titanosilicate nanoclusters present two terminal oxygen defects, mainly of the NBO type at Ti centres (Ti-NBOs). Typically, the titanosilicate nanocluster structures have little or no symmetry unlike the global minima of pure silica nanoclusters. Even at very small TiO_2 content, there appear to be a strong influence towards more "titania-like" nanoclusters structures, especially for nanoclusters with sizes n = 5 - 14. We note that in several cases there are just a few dominant isomers that cover the whole composition range for a particular system size. The structural similarity of the mixed nanoclusters to those of pure titania can be so strong that in some cases the mixed nanoclusters exhibit the same bonding topology as the respective titania global minimum structure, with only replacements of titanium atoms by silicon atoms (e.g. structures 4-3, 5-4, 6-5, 7-3, 7-5, 8-4, 8-5, 8-6 in Fig. 3). This similarity between mixed $(Ti_xSi_{1-x}O_2)_n$ nanoclusters and pure $(TiO_2)_n$ might suggest that could be possible to obtain low energy titanosilicate nanoclusters simply by replacing titanium with silicon atoms in pure titania nanoclusters. However, in many cases, we find that the global minima of the mixed nanoclusters have different structures with respect to the pure counterparts (e.g. structures 8-2, 8-3, 9-1⋯9-6, 10-1⋯10-5, 10-6⋯10-8 in Fig. 3:) demonstrating the need for our global optimisation approach.

3) Thermodynamics of mixing

3.1) Mixing energy

As a first approximation, we use total internal electronic energies at 0K directly from our DFT based calculations for our evaluations of ΔE_{mix} of our global optimized nanoclusters and periodic crystalline titanosilicates. In Fig. 4 we plot mixing energies, calculated according equation 3, for all global optimized $(Ti_xSi_{1-x}O_2)_n$ nanoclusters in Fig. 3 and bulk systems in Fig. 1, as a function of x. We can clearly see in Fig. 4 that the mixing between quartz and rutile to form bulk crystalline titanosilicates is energetically unfavourable (i.e. ΔE_{mix} values are positive). This result tends to confirm experiments where crystalline titanosilicates have only been successfully synthesised with very small proportions of TiO_2 (e.g. TS-1), and otherwise form metastable mixed oxide glasses. However, at the nanoscale, the mixing of pure silica and titania nanoclusters is generally energetically favourable (i.e. ΔE_{mix} values are generally negative). The nanocluster mixing energy size dependency is also shown in the 3D graph in Fig. 5. Here we use a smoothed continuum surface to represent the discrete set of data points of the mixing energies with respect to TiO_2 ratios and nanocluster size. From Figs. 4 and 5 it is clear that for very small nanocluster sizes (n = 1 - 5) the

mixing energies are quite modest in magnitude (≤ 0.15 eV) and can be positive (for n = 3) or negative (for n = 4 - 5). In the latter cases, the most favourable mixing energies are found for x values between 0.5 - 0.6. With increasing nanocluster size from n = 6 – 12 we observe a rapid increase in the overall energetic favourability of mixing with the most favourable region of mixing occurring for nanoclusters possessing 7, 9, 10 units (i.e. nanoclusters of approximately 1 nm diameter) and for x values between 0.4 – 0.5. For larger nanocluster sizes the mixing composition for the most favourable mixing is maintained, but the magnitude of ΔE_{mix} slowly reduces with increasing nanocluster size.

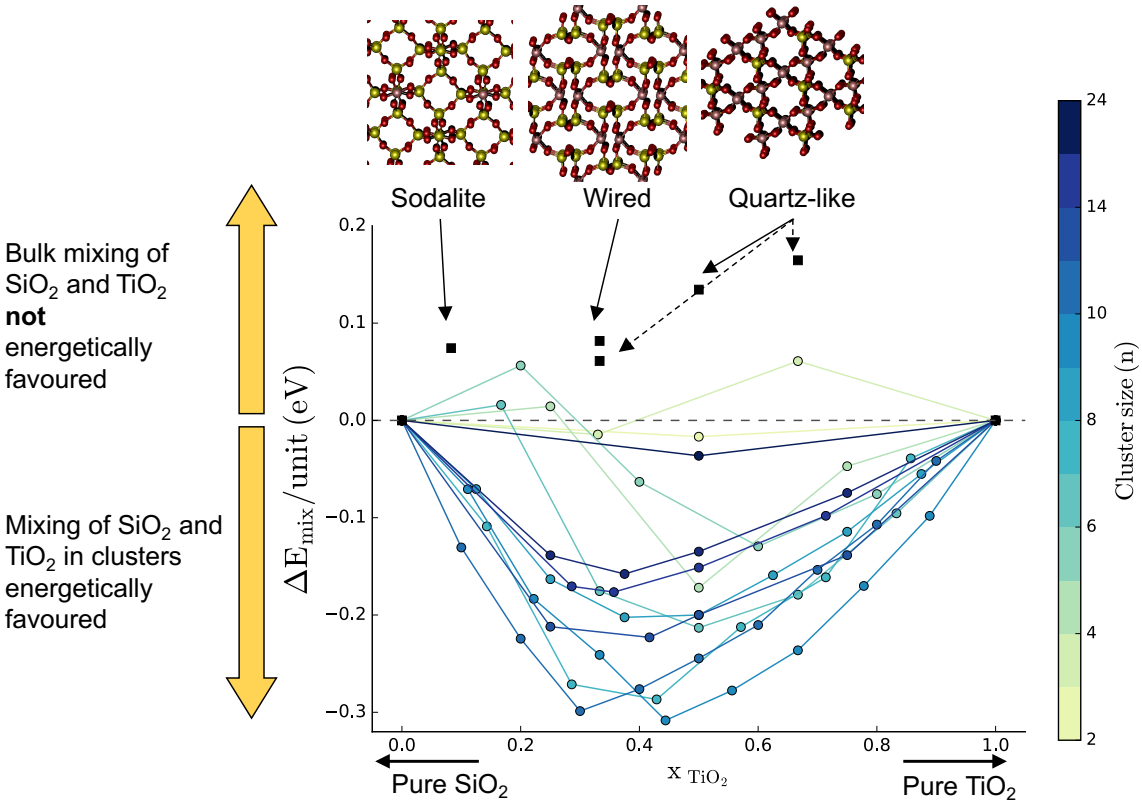

Fig 4. Mixing energy per formula unit versus the TiO_2 molar fraction. The black filled squares denote the mixing energies of the bulk periodic structures shown in Fig. 1. The filled coloured circles denote the mixing energies of the globally optimized nanoclusters shown in Fig. 3. Nanocluster sizes are represented by a colour map ranging from light green for smaller nanoclusters to dark blue for larger sizes.

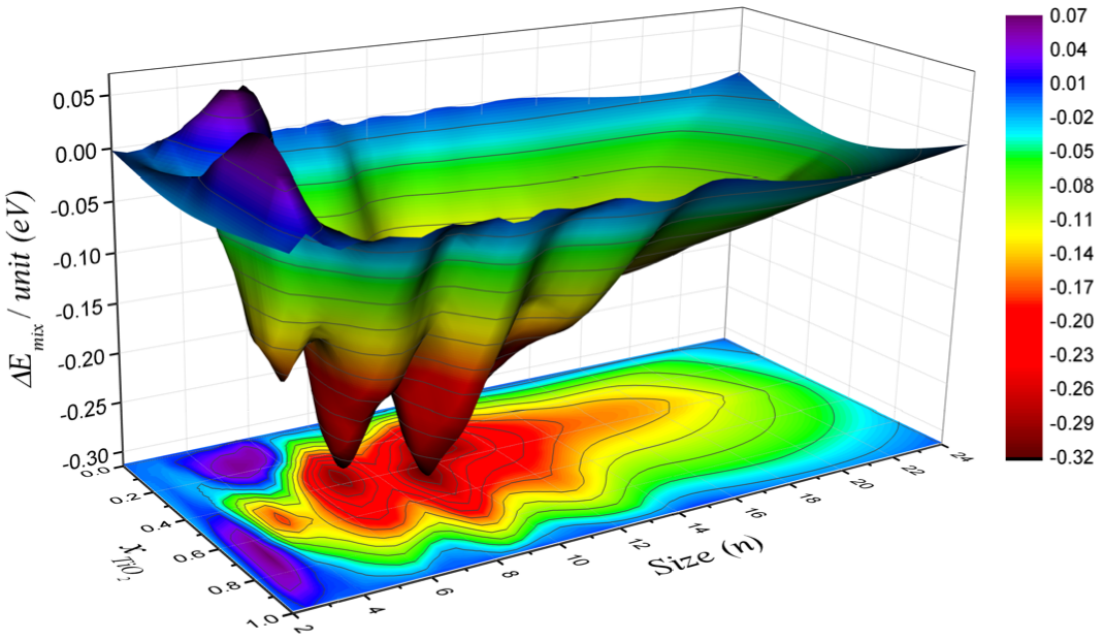

Fig 5. Three-dimensional surface representation of the mixing energy per unit for globally optimized titanosilicates nanoclusters versus the TiO_2 molar fraction (x) and system size (n). This 3D surface shows the size dependency of the nanocluster mixing energies reported in the 2D graph in Fig. 4. A 2D contoured projection of the mixing energy map is also shown. The colour map indicating mixing energies ranges from dark blue (energetically unfavourable mixing) to red (energetically favourable mixing). We note that for ease of visualisation the contours and surface have been smoothed by interpolating through their respective underlying sets of discrete data points.

The sign and magnitude of the mixing energies of titanosilicate nanoclusters arises from the competition between several electronic and/or structural factors. For example, the presence of terminating defective oxygen sites and distorted tetrahedral SiO_4 groups are both energetically destabilizing factors. In low energy mixed $(Ti_xSi_{1-x}O_2)_n$ nanoclusters, terminal NBO defects are preferentially found at titanium centres (Ti-NBO) rather than at silicon centres (Si-NBO). This can probably be explained due to the higher ionicity of Ti-O bonds with respect to Si-O bonds whereby rupture of the former is relatively less electronically, and thus energetically, destabilizing. Although this tends to favour terminal Ti-NBO groups over Si-NBO groups, Ti centres can also take advantage of internal positions in a nanocluster with high oxygen coordination spheres (making 5-6 Ti-O bonds). The strong tendency of silicon to have directional tetrahedral oxygen coordination means that such positions are not energetically favourable for Si centres. However, taking into account the higher Si-O bond strength with respect to Ti-O (bond dissociation energies for Ti-O is 666.5 ± 5.6 kJ/mol while for Si-O it is 799.6 ± 13.4 kJ/mol)[57] Si centres in tetrahedrally coordinated oxygen environments lower the total nanocluster energy more that Ti centres in the same position. These considerations can inform us as to how mixed nanoclusters can more effectively avoid the energetic

cost of terminating NBO-Si defects and internal SiO_4 strain while taking advantage of strong unstrained Si-O bonding and highly coordinated Ti centres by the following set of general structural principles: nanoclusters should possess (i) Ti-NBO rather than Si-NBO terminations, (ii) Ti centres rather than Si centres in positions having either high oxygen coordination (i.e. >4) or distorted tetrahedrally coordinated oxygen environments, (iii) Si centres rather than Ti centres in positions with relatively undistorted tetrahedrally coordinated oxygen environments. Consequently, Si-rich nanoclusters can often be stabilised by following principles (i) and (ii), and Ti-rich nanoclusters may be stabilised by following principle (iii). As a concrete example, for the case of n=12 nanoclusters we show in figure 6 how pure and $(SiO_2)_{12}$ and $(TiO_2)_{12}$ nanoclusters can be stabilised by following these principles when moving to mixed nanoclusters.

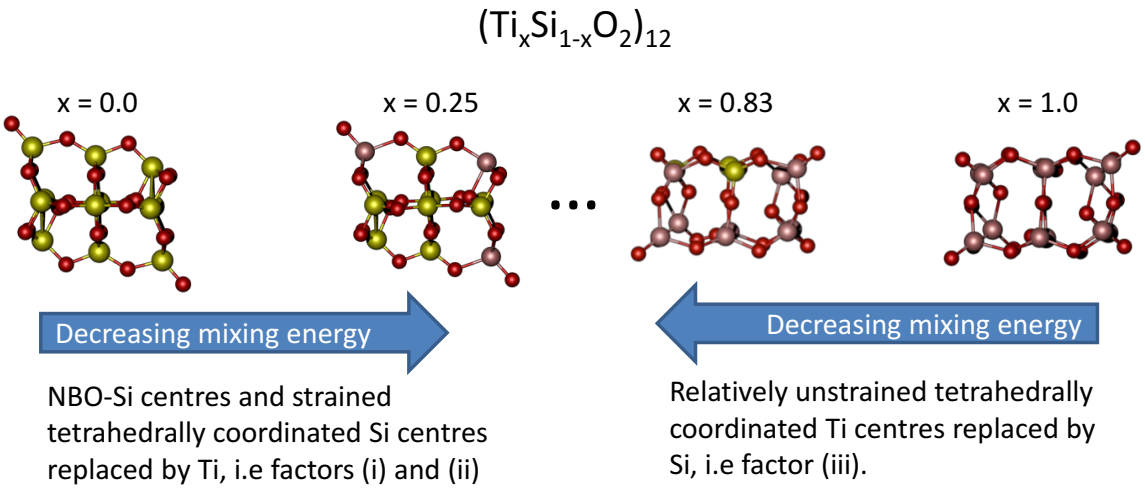

Fig 6. Example of how negative mixing energy can be rationalised when moving from pure phase $(SiO_2)_n$ and $(TiO_2)_n$ nanoclusters to mixed nanoclusters for the case of n=12 by following principles (i) - (iii) – see end of section 3.1 in main text.

Although we do not have extensive data for sizes higher than 16 units, the set of structures between 2 and 16 units allows for an analysis of some of these factors affecting the stability of mixed systems with size. We suggest that the decrease in mixing energy with increasing system size above 10 units can be largely attributed to the gradual decrease in terminal defects in the pure silica reference nanoclusters (e.g. four for $(SiO_2)_{10}$, two for $(SiO_2)_{12}$, $(SiO_2)_{14}$ and $(SiO_2)_{16}$ and none for $(SiO_2)_{24}$). Therefore, titanosilicate nanocluster stabilities are compared with less and less destabilized pure silica systems as the size increases. Finally, following the general trend in Fig. 5, we can predict that the energetic favourability of mixing in titanosilicates nanoclusters with n > 24 units would rapidly tend to zero.

3.2) Mixing free energy

For a more accurate description of the thermodynamics of TiO_2-SiO_2 mixing in titanosilicate nanoclusters we have considered the mixing Gibbs free energies at different temperatures for a set of nanoclusters with selected TiO_2 incorporation ratios. Specifically, we evaluate the free energy contributions to the mixing energies at different temperatures and at 1 atmosphere for pure oxide nanoclusters and 50% mixing for sizes n = 2 - 16 units, according to:

$$\Delta G(T) = \Delta H(T) - T\Delta S(T) \quad (4)$$

where ΔH and ΔS are respectively the enthalpy and entropy of the system including temperature dependent contributions of nanocluster translations (S_{trans}), rotations (S_{rot}), vibrations (S_{vib}) and relevant distinct nanocluster isomer atomic configurations (S_{conf}). Both S_{trans} and S_{rot} are obtained from standard thermochemical relations and we use calculated harmonic frequencies to evaluate S_{vib}[58]. In this work, we neglect the configurational entropy term (S_{conf}). This term would take into account the entropic contribution for all the different configurational isomers weighted with respect to their relative energy. Generally, we find that there is large energy separation between (configurational) isomers and global minima for the mixed nanoclusters justifying this assumption. In the Supplementary Information we report the energy separations between our global minima nanoclusters and the respective first few energetically low lying isomers and the probability for each of them to be thermally accessible.

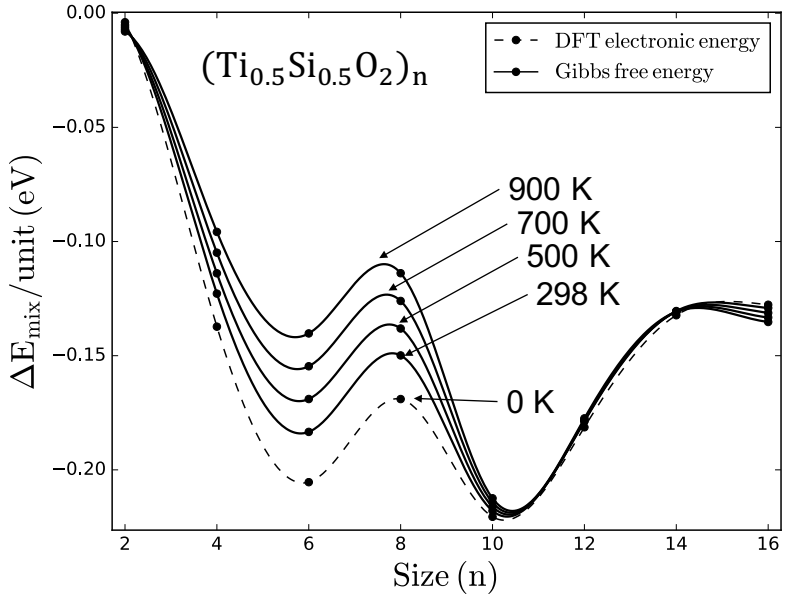

Fig 7. Total mixing electronic energy without zero point correction (dashed line) and Gibbs mixing free energies (solid lines) at different temperatures (298, 500, 700 and 900 K) relative to $(Si_{0.5}Ti_{0.5}O_2)_n$ systems versus the nanocluster size n (n= 2, 4, 6, 8, 10, 12, 14 and 16 units). Energies are plotted on smoothed lines in order to help follow the trends.

In Fig. 7 we plot the mixing free energies at different temperatures (298, 500, 700, and 900 K) calculated according to equation 3 using the calculated Gibbs free energies for each energetic term for the set of nanoclusters mentioned above. Mixing free energies are compared with mixing electronic energies. Overall, the thermodynamic favourability of mixing is found to be conserved with respect to the results for 0K when increasing the temperature. Thermal corrections affect mainly nanoclusters with sizes n = 6 and 8, but are found to be less relevant for the mixing at other sizes. Generally, thermal corrections lead to slightly less favourable mixing energies for all sizes except for the largest (n = 16) nanocluster considered where the thermally corrected mixing free energy is lower than electronic one. A deeper analysis of this effect is out of the scope of the present work, since we are primarily interested in verifying the persistence of favourable mixing in our mixed oxide nanoclusters at finite temperatures.

4) Signatures of mixing

In an effort to provide experimentally measurable signatures of TiO_2-SiO_2 mixing in $(Ti_xSi_{1-x}O_2)_n$ nanoclusters, in the following two sections, we analyse calculated harmonic frequencies and average coordination numbers of pure oxide nanoclusters as compared to mixed oxide nanoclusters.

4.1) Harmonic frequencies

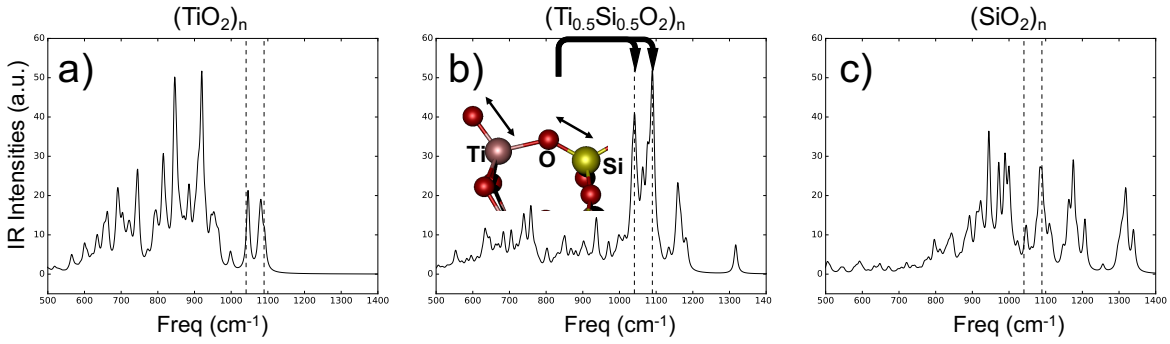

Fig 8. Calculated infrared (IR) harmonic vibrational frequencies (in cm^{-1}) of pure titania (a), titanosilicate (b) and silica (c) nanoclusters obtained by summing size-scaled IR spectra for nanocluster sizes n (n= 2, 4, 6, 8, 10, 12, 14 and 16 units). In b) the anti-symmetric normal mode coupling between Ti-NBO and the vicinal Si-O is shown relative to the most intense peaks. Calculated IR harmonic frequencies for each size are available in the Supplementary Information. All spectra were generated using the Moldraw code[59] and are made openly digitally available.

In Fig. 8 we present calculated infrared (IR) harmonic vibrational frequencies for pure titania (Fig 8a), pure silica (Fig 8c) and mixed global optimized (Fig. 8b) nanoclusters. Each spectrum is composed by the sum of size-scaled IR spectra of several $(Ti_{0.5}Si_{0.5}O_2)_n$ nanoclusters (i.e. $I^{tot}{}_{IR} =$

$\sum 1/n \cdot I^{(Ti_{0.5}Si_{0.5}O_2)_n}{}_{IR}$ where $I^{tot}{}_{IR}$ is the total IR intensity, $1/n$ is the scaling factor for the $I^{(Ti_{0.5}Si_{0.5}O_2)_n}{}_{IR}$ IR spectrum relative to $(Ti_{0.5}Si_{0.5}O_2)_n$ nanocluster). In other words, the IR spectra shown here are designed to mimic those of hypothetical samples which contain a monotonically decreasing size distribution of nanoclusters. IR spectra for each specific nanocluster size are available in the Supplementary Information. The main feature that we want to highlight from these IR spectra is the presence of two highly intense, distinct and consistent peaks in titanosilicate nanoclusters at around 1035 and 1090 cm^{-1} (highlighted with the horizontal dashed line in Fig. 7b). These peaks are also present in the pure systems but with significantly lower intensities. In titanosilicate nanoclusters the two peaks are due to couplings between stretching of the Ti-O bond in terminating oxygen defects and the vicinal Si-O bond in the "interior" of the nanocluster (see schematic in in Fig 8b). We note that these two peaks are related to the same normal mode and there is a size dependent red-shifting that generates distinct peaks going from ~1090 cm^{-1} from smaller nanoclusters to ~1035 cm^{-1} for larger ones.

In pure TiO_2 (Fig. 7a) nanoclusters there are two distinct IR peaks that overlap with the ones in titanosilicate nanoclusters. The first peak is slightly blue-shifted at 1046 cm^{-1} and is due to exclusively to the contribution from the smallest $(TiO_2)_2$ nanocluster. However, we note that the relative intensities of these two peaks are quite low with respect to the most intense peaks. Unlike for titanosilicates, there is also no size dependent red-shifting of these peaks in titania nanoclusters and all peaks around 1090 cm^{-1} are due to harmonic stretching of terminal Ti-O species. In pure silica (Fig 7c) nanoclusters, there is also an intense peak that coincides with one found for mixed titanosilicate nanoclusters. Here, there is an intense peak at 1085 cm^{-1} from systems with sizes between 8 and 12 units, due to a complex coupling between stretching and bending modes involving different parts of these nanoclusters.

We suggest that the presence of both vibrational modes at 1090 and 1035 cm^{-1}, particularly enhanced in titanosilicates nanoclusters, can be used as a signature of the presence of mixed $(Ti_xSi_{1-x}O_2)_n$ nanoclusters

4.2) Average Si and Ti coordination numbers

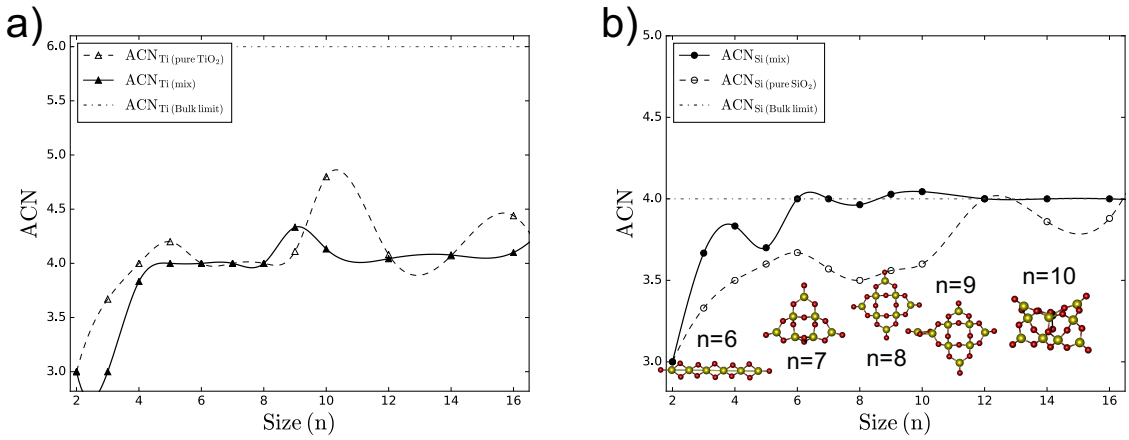

Fig 9. Average cation coordination numbers (ACN) plotted on smoothed lines for easily following trends for: a) titanium centres in pure TiO_2 (dashed line) and mixed titanosilicate (solid line) nanoclusters; b) for silicon centres in pure SiO_2 (dashed line) and mixed titanosilicate (solid line) nanoclusters. The corresponding oxygen coordination number of the respective cation in the bulk phase is indicated in both cases as a dot-dashed line. All coordination numbers are taken by counting oxygens within a maximum cut-off distance of 2.2 Å from each Ti or Si centre. In mixed systems, for each size, the ACN is averaged over all nanocluster mixing compositions. Figures shown in b) are pure silica structures with n = 6 - 10 in order to show the origin of low silicon ACN values for this size regime.

The coordination number of an atom is defined as the number of its nearest neighbours. Average coordination numbers (ACNs) can be experimentally determined by X-Ray techniques such as EXAFS (Extended X-ray Absorption Fine Structure) spectroscopy. Fig. 9 displays the average coordination numbers of titanium (a) and silicon (b) in both pure and mixed systems. In the case of titanium coordination there are no significant differences between pure and mixed systems except for few cases (e.g. for n= 10 and 16). Here, the ACN for Ti remains between 4 and 4.5 for almost all the size range studied and is well below the bulk value of 6. In the case of silicon coordination, the ACN in pure silica nanoclusters is persistently lower than in mixed titanosilicate nanoclusters for nearly all sizes. The ACN for Si atoms could thus be used as a signature of mixed titanosilicate nanoclusters. The higher value of the ACN for silicon atoms in titanosilicate nanoclusters is related to the fact that Si atoms can take advantage of mixing with titania to be tetrahedrally 4-coordinated (at the lower energetic cost of producing a terminal Ti-O defect) which is its ideal coordination number (see above discussion). We find that the ACN for Si atoms reaches the ideal bulk value of 4-coordinated at smaller sizes in titanosilicates (6 units) than in pure silica (12-16 units). Indeed, the relative ease with which a bulk-like ACN value for Si centres can be achieved in titanosilicate nanoclusters is one of the driving forces for mixing at smaller nanocluster sizes.

Conclusions

In this study we have theoretically investigated the mixing between TiO_2 and SiO_2 in both bulk phases and in nanoclusters. We employed global optimization to find mixed $(Ti_xSi_{1-x}O_2)_n$ nanoclusters in a systematic way for a wide range of sizes and mixing compositions. Several new global minima candidates of titanosilicate nanoclusters are thus reported. We observe that bulk mixing is energetically unfavourable which is in agreement with experimental observations. However, the mixing of the two oxides is found to be energetically favourable in the considered nanoclusters from 0K up to at least 900K. The size regime within which mixing is energetically favourable corresponds covers $(Ti_xSi_{1-x}O_2)_n$ nanoclusters with n= 2 - 24 (i.e. to nanoclusters with diameters less than 1.5 nm). The maximum mixing favourability is calculated to be when mixed $(Ti_xSi_{1-x}O_2)_n$ nanoclusters are around 1.0 nm in diameter (between 9 and 10 units) and when the molar fraction of TiO_2 is about 0.3-0.4. We suggest a number of structural-chemical driving forces for mixing in this size range. As a guide for experimentalists to observe and characterize these mixed nano-species we provide two measurable signatures of mixing. Firstly, harmonic frequency calculations show mixed titanosilicate nanoclusters to have a unique and distinct IR fingerprint (intense peaks at 1090 and 1035 cm^{-1} in IR spectra). Secondly, Si centres in mixed nanoclusters are found to show a higher average coordination relative to pure silica nanoclusters which could, in principle, be observed in EXAFS experiments. We hope that this work will serve as inspiration to experimental researchers to explore the fundamental properties of nanoscale titanosilicate mixed systems in order to synthesize new and highly efficient titanosilicate materials.

Supplementary Information

We report the coordinates of all global optimized titanosilicate nanoclusters used in this work. We also include a selection of metastable isomers for $(Ti_{0.5}Si_{0.5}O_2)_n$ (n= 4, 6, 8, 10, 12, 14, 16) and their probabilities to be thermally accessible at different temperatures (298, 500, 700, 900). Calculated harmonic frequencies of the most stable nanoparticles have also been included. Finally we include a table containing total energies and mixing energies for all systems appearing in Fig. 4 and an example of mixing energy normalized by two unit definitions. All structures have also been uploaded in an open access manner in both the NOMAD repository (https://repository.nomad-coe.eu/) and the WASP@N nanocluster database (https://hive.chem.ucl.ac.uk/).

Acknowledgements

This research was supported by the Spanish MINECO / AEI-FEDER grant: CTQ2015-64618-R and, in part, by Generalitat de Catalunya grants: 2014SGR97 and XRQTC. We acknowledge the Red Española de Supercomputación for provision of computing time. We also acknowledge GENCI- CINES/IDRIS

(Grant 2016- x2016082131, 2017- x2017082131) and the CCRE-DSI of Université P. M. Curie for computing resources.

References

[1] E.W. McFarland and H. Metiu, *Chem. Rev.*, 2013, **113**, 4391–4427.

[2] K. A. Keller, G. Jefferson, and R. J. Kerans, ed. N. P. Bansal, Springer US, Boston, MA, 2005, p. 377.

[3] D. Bergeron, W. A. Castleman, N. O. Jones, and S. N. Khanna, *Nano Letters*, 2004, **4**, 261–265.

[4] K. Fominykh, G. C. Tok, P. Zeller, H. Hajiyani, T. Miller, M. Döblinger, R. Pentcheva, T. Bein, D. Fattakhova-Rohlfing, *Adv. Funct. Mater.,* 2017, **27**, 1605121.

[5] K.T. Lee, A.A. Lidie, S.Y. Jeon, G.T. Hitz, and S.J. Song, *J. Mater. Chem. A*, 2013,**1**, 6199–6207.

[6] R. B. Soriano, J. Wu, and M. G. Kanatzidis, *J. Am. Chem. Soc.*, 2015, **137**, 9937–9942.

[7] Taramasso, M., Perego, G., Notari, B. U.S. Patent No. 4410501, 1983.

[8] T.V. Nguyen, H.C. Lee, M. Khan, and O.B. Yang, *Sol. Energy*, 2007, **81**, 529–534.

[9] K. Qi, X. Chen, Y. Liu, J. Xin, C. Mak, and W. Daoud, *J. Mater. Chem.*, 2007, **17**, 3504–3508.

[10] S. M. Kuznicki, V. A. Bell, S. Nair, H. W. Hillhouse, R. M. Jacubinas, C. M. Braunbarth, B. H. Toby, and M. Tsapatsis, *Nature*, 2001, **412**, 720–724.

[11] C. Jiang, K. Lee, C. Parlett, M. Bayazit, C. Lau, Q. Ruan, S. Moniz, A. Lee, and J. Tang, *Appl. Catal. Gen.*, 2016, **521**, 133–139.

[12] S. Zhan, D. Chen, X. Jiao, and Y. Song, *Chem. Commun.*, 2007, **0**, 2043–2045.

[13] P. Cao, G. Zhou, Y. Ren, and H. Xiao, *Rsc. Adv.*, 2016, **6**, 6551–6561.

[14] S. M. Kuznicki, U.S. Patent No. 4853202, 1989.

[15] S. M. Kuznicki, K. A. Thrush, F. M. Allen, S. M. Levine, M. M. Hamil, D. T. Hayhurst and M. Mansour, *Synth. Micopor. Mater.*, 1992, **1**, 427.

[16] G.S. Henderson and M.E. Fleet, *J. Non-Cryst. Solids*, 1997, **211**, 214–221.

[17] J. S. Rigden, J. K. Walters, P. J. Dirken, M. E. Smith, G. Bushnell-Wye, W. S. Howells and R. J. Newport, *J. Phys. Condens. Matter*, 1997, **9**, 4001.

[18] X. Orignac, H.C. Vasconcelos, and R.M. Almeida, *J. Non-Cryst. Solids*, 1997, **217,** 155–161.

[19] Z. Li, B. Hou, Y. Xu, D. Wu, Y. Sun, W. Hu, and F. Deng, *J. Solid. State. Chem.*, 2005, **178**, 1395–1405.

[20] We. Dong, Y. Sun, C. W. Lee, W. Hua, X. Lu, Y. Shi, S. Zhang, J. Chen, and D. Zhao, *J. Am. Chem. Soc.*, 2007, **129**, 13894-13904

[21] C. Jiang, K. Y. Lee, C. M. A. Parlett, M. K. Bayazit, C. C. Lau, Q. Ruan, S. J. A. Moniz, A. F. Lee and J. Tang, *Appl. Catal. A*, 2016, **521**, 133–139.

[22] S. Plant, L. Cao, F. Yin, Z. Wang, and R. E. Palmer, *Nanoscale*, 2013, **6**, 1258–1263.

[23] S. Plant, L. Cao, and R. E. Palmer, *J Am Chem Soc*, 2014, **136**, 7559–7562.

[24] R. E. Palmer, L. Cao, and F. Yin, *Rev. Sci. Instrum.*, 2016, **87**, 046103.

[25] M. Takeuchi, M. Matsuoka, and H. Yamashita, *J Synchrotron Radiat.*, 2001, **8**, 643–644.

[26] S. Bordiga, F. Bonino, A. Damin, C. Lamberti, *Phys. Chem. Chem. Phys.*, 2007, **9**, 4854–4878.

[27] M. Landmann, T. Köhler, E. Rauls, T. Frauenheim, and W.G. Schmidt, *J. Phys. Condens. Matter*, 2014, **26**, 253201.

[28] O. Miroshnichenko, S. Posysaev and M. Alatalo, *Phys. Chem. Chem. Phys.*, 2016, **18**, 33068–33076.

[29] I. Bandyopadhyay and C. M. Aikens, *J. Phys. Chem. A*, 2011, **115**, 868–879.

[30] D.J. Wales and J.P.K. Doye, *J. Phys. Chem. A*, 1997, **101**, 5111–5116.

[31] http://www-wales.ch.cam.ac.uk/GMIN/

[32] L. Tang, L. Linwei, J. Zhao and R. Qiu, *J. Comput. Chem.*, 2011, **33**, 163.

[33] M. Y. Chen and D. A. Dixon, *J. Chem. Theory Comput.*, 2013, **9**, 3189–3200.

[34] O. Lameil-Garcia, A. Cuko, M. Calatayud, F. Illas, S.T. Bromley, *Nanoscale*, 2017, **9**, 1049–1058.

[35] E. Flikkema and S.T. Bromley, *Chem. Phys. Lett*., 2003, **378**, 622-629.

[36] E. Flikkema and S. T. Bromley, J. Phys. Chem. B, 2004, 108, 9638–9645.

[37] S. T. Bromley and E. Flikkema, *Phys. Rev. Lett.*, 2005, **95**, 185505.

[38] E. Flikkema and S. T. Bromley, *Phys. Rev. B*, 2009, **80**, 035402.

[39] M. Matsui and M. Akaogi, *Mol. Simul.*, 1991, **6**, 239–244.

[40] V. Blum, R. Gehrke, F. Hanke, P. Havu, V. Havu, X. Ren, K. Reuter and M. Scheffler, *Phys. Commun*., 2009, **180**, 2175–2196.

[41] J. P. Perdew, K. Burke, and M. Ernzerhof, *Phys. Rev. Lett.*, 1996, **77**, 3865–3868.

[42] C. Adamo and V. Barone, *J. Chem. Phys.*, 1999, **110**, 6158–6169.

[43] S. Hamad, C. R. A. Catlow, S. M. Woodley, S. Lago, J. A. Mejias, *J. Phys. Chem. B*, 2005, **109**, 15741–15748.

[44] S. Bhattacharya, B. H. Sonin, C. J. Jumonville, L. M. Ghiringhelli and N. Marom, *Phys. Rev.*, 2015, **91**, 241115.

[45] C Brousse, R. C. Newton and O. J. Kleppa, *Geochim. Cosmochim. Acta*, 1984, **48**, 1081–1088.

[46] Gaussian 09, Revision D.01, M. J. Frisch et al., Gaussian, Inc., Wallingford CT, 2013.

[47] A. Schaefer, C. Huber, and R. Ahlrichs, *J. Chem. Phys.*, 1994, **100,** 5829-5835.

[48] A. Jain, S. Ong, G. Hautier, W. Chen, W. Richards, S. Dacek, S. Cholia, D. Gunter, D. Skinner, G. Ceder and K. Persson, *APL Mater.*, 2013, **1**, 011002.

[49] F. Aguilera-Granja, A. Vega and L. Balbás, *J. Chem. Phys.*, 2016, **144**, 234312.

[50] W. C. Lu, C. Z. Wang, V. Nguyen, and M.W. Schmidt, *J. Phys. Chem. A*, 2003, **107**, 6936–6943.

[51] S. M. Woodley, S. Hamad, J. A. Mejias, and C. Catlow, *J. Mater. Chem.*, 2006, **16**, 1927–1933.

[52] C. Catlow, S. T. Bromley, S. Hamad, M. Mora-Fonz, A. A. Sokol, S. M. Woodley, *Phys. Chem. Chem. Phys.*, 2010, **12**, 786-811.

[53] V.G. Avakyan, V.F. Sidorkin, E.F. Belogolova, S.L. Guselnikov, L.E. Guselnikov, *Organometallics*, 2006, **25**, 6007–6013.

[54] M. A. Zwijnenburg, A. A. Sokol, C. Sousa, S. T. Bromley, *J. Chem. Phys.*, 2009, **131**, 034705.

[55] S. Hamad and S. T. Bromley, *Chem. Commun.*, 2008, **0**, 4156-4158.

[56] M. A. Zwijnenburg, F. Illas, J. Chem. Phys. 137 (2012) 154313

[57] Luo, Y.-R. Bond Dissociation Energies. In CRC Handbook of Chemistry and Physics, 89th ed.; Lide, D. R., Ed.; CRC Press/Taylor and Francis: Boca Raton, FL, 2009

[58] D. A. McQuarrie and J. D. Simons, Molecular Thermodynamics, University Science Book, Sausalito, CA, 1999.

[59] P. Ugliengo, D. Viterbo, G. Chiari, *Z. Kristallogr*. 1993, **207**, 9.

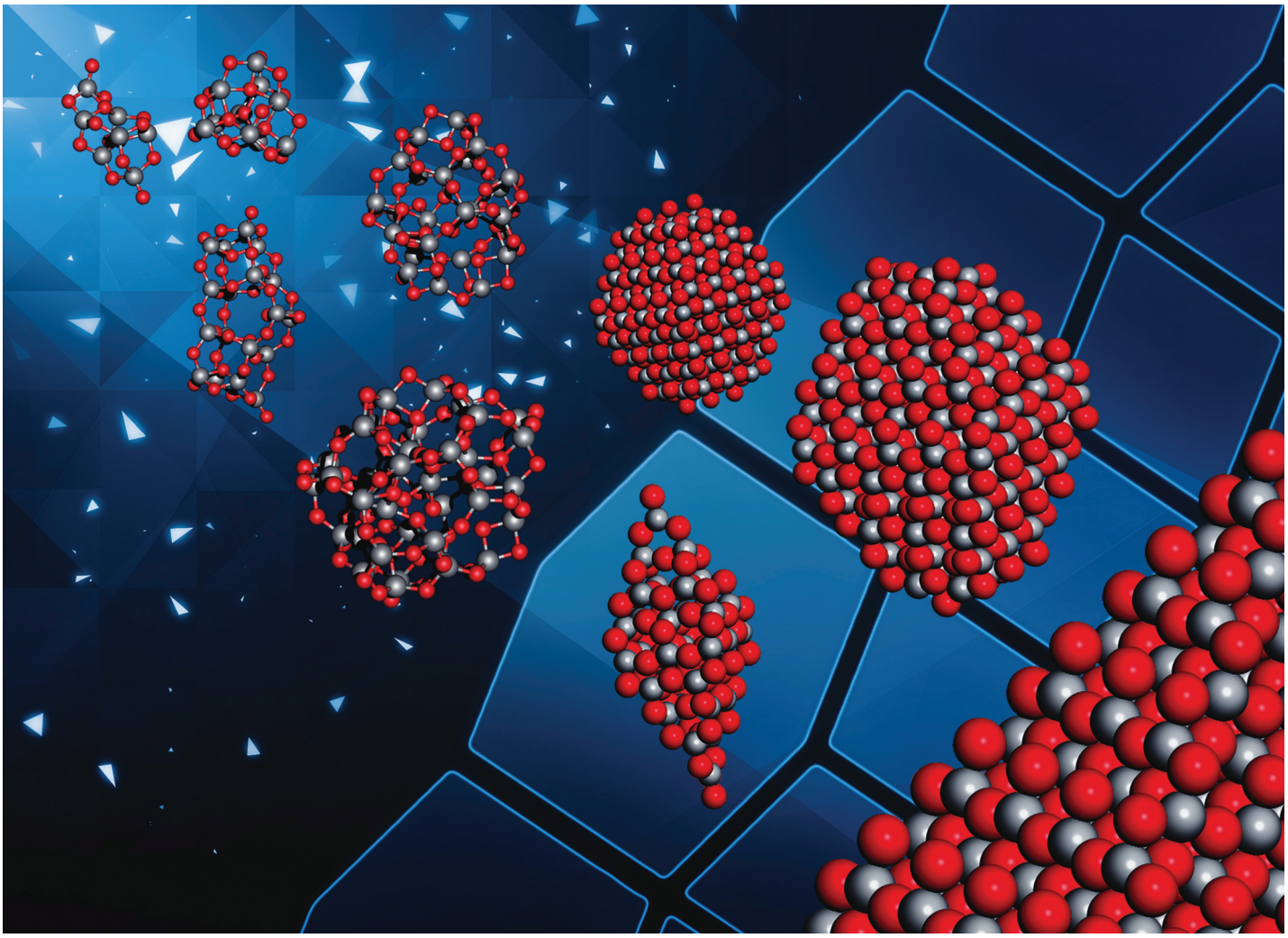

Showcasing research from the group of Stefan Bromley, Nanoclusters and Nanostructured Materials Group, Institute of Computational and Theoretical Chemistry, University of Barcelona, Spain.

Predicting size-dependent emergence of crystallinity in nanomaterials: titania nanoclusters *versus* nanocrystals

Bottom-up and top-down derived nanoparticle structures refined by accurate *ab initio* calculations are used to investigate the size dependent emergence of crystallinity in titania from the monomer upwards. Consistent with available experimental data, we predict to a non-crystalline to crossover size for nanoparticles with 2–3 nm diameter.

As featured in:

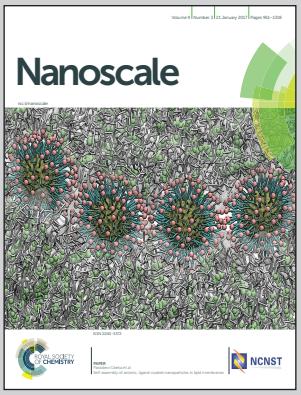

See Stefan T. Bromley *et al.*, *Nanoscale*, 2017, **9**, 1049.

ROYAL SOCIETY OF CHEMISTRY

rsc.li/nanoscale

Registered charity number: 207890

Nanoscale

PAPER

View Article Online
View Journal | View Issue

Cite this: *Nanoscale*, 2017, **9**, 1049

Predicting size-dependent emergence of crystallinity in nanomaterials: titania nanoclusters *versus* nanocrystals†

Oriol Lamiel-Garcia,[a] Andi Cuko,[a,b] Monica Calatayud,[b,c] Francesc Illas[a] and Stefan T. Bromley*[a,d]

Received 22nd July 2016,
Accepted 4th October 2016

DOI: 10.1039/c6nr05788h

www.rsc.org/nanoscale

Bottom-up and top-down derived nanoparticle structures refined by accurate *ab initio* calculations are used to investigate the size dependent emergence of crystallinity in titania from the monomer upwards. Global optimisation and data mining are used to provide a series of $(TiO_2)_N$ global minima candidates in the range N = 1–38, where our approach provides many new low energy structures for N > 10. A range of nanocrystal cuts from the anatase crystal structure are also considered up to a size of over 250 atoms. All nanocrystals considered are predicted to be metastable with respect to non-crystalline nanoclusters, which has implications with respect to the limitations of the cluster approach to modelling large titania nanosystems. Extrapolating both data sets using a generalised expansion of a top-down derived energy expression for nanoparticles, we obtain an estimate of the non-crystalline to crystalline crossover size for titania. Our results compare well with the available experimental results and imply that anatase-like crystallinity emerges in titania nanoparticles of approximately 2–3 nm diameter.

Introduction

Size reduction from the macroscopic to length scales of only a few nanometres can lead to dramatic changes in a material's properties. Further to the effects directly arising from high surface-to-bulk ratios, nano-sized particles often possess distinct atomic and electronic structures with respect to stable bulk crystals. Titania (TiO_2) is a prototypical example of a material displaying an extreme size-dependence of both structure and properties.[1] Under ambient conditions bulk titania is most thermodynamically stable with atomic ordering following the rutile crystal structure. However, upon reduction in size, titania nanoparticles with average diameters less than ~14 nm begin to exhibit the anatase crystal structure.[2] This structural transition has been thermodynamically rationalised by top-down calculations of the size-dependent enthalpies of titania nanoparticles, which highlight the roles of surface energies and surface stresses on nanoparticle stability.[2,3]

Anatase nanocrystals are found to greatly differ from their rutile counterparts in being highly photochemically active and form the basis for many nano-titania based applications (*e.g.* photocatalysts,[4] sunscreens,[5] anti-pollution building materials[6]). Often the key to enhanced photoactivity is to form composite materials containing very small (≤5 nm diameter) stable anatase nanocrystals.[7,8] As with most materials, however, further decreasing the size of anatase nanocrystals will eventually give way to a regime of nanoclusters, which generally do not display a crystalline order, thus losing much of their utility. Evidence from high resolution transmission electron microscopy has shown that isolated anatase nanocrystals can persist down to sizes as small as ~5 nm in diameter.[9] Recent experiments have further shown that the anatase crystal structure is extremely thermally persistent in 4 nm diameter nanoparticles.[10] Although this implies that anatase is still thermodynamically stable, in this latter size range it is unclear whether such nanoparticles retain a facetted nanocrystal morphology. Indirect evidence from modelling suggests that when anatase nanoparticles start to become smaller than ~5 nm, they may begin to exhibit a spherical morphology with an anatase core and an amorphous shell.[11] Although not strictly nanocrystals according to our definition, such core–shell nanoparticles should clearly be regarded as partially crystalline. For even smaller TiO_2 nanoparticles, with average

[a]*Departament de Ciència de Materials i Química Física and Institut de Química Teòrica i Computacional (IQTCUB), Universitat de Barcelona, E-08028 Barcelona, Spain*
[b]*SorbonneUniversités, UPMC Univ Paris 06, CNRS, Laboratoire de Chimie Théorique CC 137, 4, place Jussieu F. 75252, Paris Cedex 05, France*
[c]*InstitutUniversitaire de France, France*
[d]*Institució Catalana de Recerca i Estudis Avançats (ICREA), E-08010 Barcelona, Spain. E-mail: s.bromley@ub.edu*

†Electronic supplementary information (ESI) available. See DOI: 10.1039/c6nr05788h

diameters in the range 2–3 nm, fitting experimental X-ray spectroscopy data using the reverse Monte Carlo refined nanoparticle structures tend to support this feature.[12] With decreasing size, eventually the anatase core is subsumed by the amorphous shell, and the nanoparticles will not exhibit any crystallinity. We refer to the non-crystalline titania species in this ultra-small size regime as nanoclusters.

From a bottom-up perspective, increasing in size from a single TiO_2 monomer, nanoclusters need to attain a certain size before they begin to thermodynamically favour regular atomic ordering characteristic of a bulk crystal. From this perspective, this structural crossover between nanoclusters and nanocrystals can be seen as a size-dependent non-crystalline to crystalline (NC ↔ C) crossover. Herein, we provide an estimate of the NC ↔ C crossover size regime for TiO_2 using accurate quantum chemically calculated energies of relaxed atomistically detailed nanoclusters and nanocrystals derived from bottom-up and top-down approaches respectively.

In Fig. 1 we represent the generic size dependent energetic stability of both non-crystalline (red line) and nanocrystals (blue line) for an arbitrary material. We note that although herein we will use calculated energies at 0 K to demonstrate our approach, these data could equally well be free energies from experiment and/or theory. The energy difference, $\Delta E_{C-NC}(N)$, gives a measure of the metastability of crystalline particles with respect to non-crystalline clusters at relatively small sizes and *vice versa* at larger sizes. Using the plotted energies the NC ↔ C crossover size would seem to be defined as the size at which $\Delta E_{C-NC}(N)$ becomes zero. In general, however, it is not expected that this crossover will always be defined by a definite single transition size above which nanocrystals are always more energetically stable and below which non-crystalline nanoclusters are always more stable. Size dependent structural preferences are well-known in nanocluster systems (*e.g.* icosahedral shell closing) and it is quite possible that, with increasing size, crystallinity would be first energetically favoured in a set of discrete increasingly sized nanoparticles covering a crossover range (N_1, N_2, ... N_C) before being manifestly prevalent for all $N \geq N_C$. More generally, it is quite likely that for sizes close to but smaller than N_C there will be nanoclusters that exhibit partial crystallinity (*e.g.* a nanoparticle with crystalline cores and an amorphous shell). As such we define the NC size range as those nanoparticles which do not exhibit full crystallinity. In turn, we roughly define a fully crystalline nanocrystal as one which can be cut from a bulk crystal and which maintains its atomic ordering upon structural relaxation and with only minor displacement of atomic positions (*i.e.* no more than a ~20% of a bond length). We further note that the NC ↔ C crossover will not generally be to the most stable bulk crystalline phase of the material but rather to a polymorph which is metastable in the bulk. Depending on the material there will be variable number of subsequent size dependent crossovers between polymorphs until the most stable bulk crystalline phase is reached.

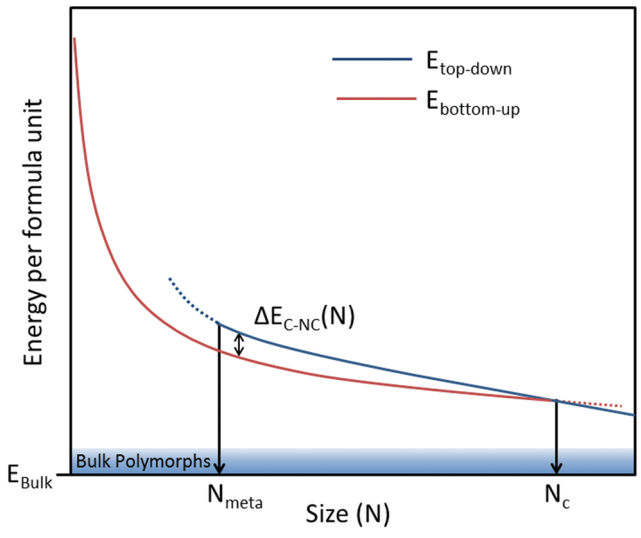

Fig. 1 Schematic representation of size-dependent energetic stability of crystalline (C) and non-crystalline (NC) nanoparticles with respect to their size. The red line indicates the stability of nanoclusters and the blue line that of nanocrystals. $\Delta E_{C-NC}(N)$ denotes the energy difference between a nanocrystal and nanocluster, both having N formula units. The blue shaded region denotes the typical energy range within which metastable bulk polymorphs can exist. N_{meta} and N_C are described in the text.

In Fig. 1 we also note another interesting crossover size, N_{meta}, indicating the smallest size that a nanocrystal can maintain an energetically metastable crystalline structure with respect to a non-crystalline nanocluster of the same size. Related to this concept, there have been important studies of nanosize dependent metastability of one crystal phase over another.[13] The metastability we refer to, however, is, in a converse way, more similar to the metastability that a non-crystalline bulk structure (*e.g.* an amorphous glass) can possess with respect to a crystalline phase. The size region around N_{meta} denotes the limit at which small nanocrystals start to become structurally unstable and spontaneously relax into non-crystalline species. We note that due to the stability of small clusters often being irregularly dependent on size, it is quite possible that close to size N_{meta} there will be a set of different cluster sizes for which the crystalline order is easier to maintain and sizes for which only non-crystalline clusters are structurally stable.

For the vast majority of materials, neither N_C nor N_{meta} crossover sizes have been determined. For highly ionic materials N_C and N_{meta} will be quite similar and small in magnitude. In other words, in such cases the strong near-isotropic electrostatic interactions between the ions drive the system towards crystalline closely packed structures even for very small sizes (*e.g.* $N < 20$ for $(NaCl)_N$,[14] $(MgO)_N$,[15] $(CeO_2)_N$ [16]). For such materials we note that small to moderately sized crystalline nanoparticles appear to be good theoretical models for calculating the properties of large nanocrystals and/or the corresponding bulk crystal.[17–20] For many materials where the tendency to establish highly ordered atomic arrangements is relatively weaker, we may expect that the N_C and N_{meta} transition sizes could be very different. For example, in such a material one may be able to construct relatively small but very

metastable nanocrystals, but where the thermodynamic NC ↔ C transition occurs at significantly larger nanoparticle sizes. Such a situation has been strongly hinted at in the IP-based studies of $(ZnO)_N$ [21] and $(Fe_2O_3)_N$ [22] nanosystems and is found to be the case in our DFT-based study of the $(TiO_2)_N$ nanosystem. In such cases, calculations using such highly metastable nanocrystal models (*i.e.* with sizes close to N_{meta}) as a means to explain experimental data involving considerably larger nanocrystals and/or bulk crystals, should be very carefully assessed.

Using a bottom-up global optimisation approach we show that, in the case of titania, such small bulk-mimicking nanocrystals are significantly metastable with respect to the most energetically stable nanoclusters of a corresponding size. Furthermore, by also considering a set of bulk-derived nanoparticles for various sizes we estimate the lower size limit at which bulk-like nanoparticles actually start to become the most energetically stable titania species. This latter estimate, corresponding to the N_C size for titania, provides a guide to the size of crystalline nanoparticles which can safely be used as natural stable structural models of larger titania nanoparticles used in the experiment. Generally, our work demonstrates how *ab initio* calculations can provide lower bound estimates for N_C. In other words, we show how the intrinsic size regimes for a material's (nano)crystalline stability can be theoretically predicted.

Methodology

In this study we compare two classes of nanotitania species: (i) nanoclusters derived from bottom-up global optimisation, and (ii) nanocrystals derived from cuts from the anatase bulk phase. As the size ranges covered by these two approaches tend to be quite different, and in order to compare their respective energetic stabilities for arbitrary N, general size dependent relationships between energy and size are required for each class. Below we describe how appropriate relationships were derived in each case. The final reported structures of all nanoclusters, nanocrystals, and the bulk anatase crystal, were fully optimised using DFT calculations with no symmetry constraints employing the PBE0 hybrid functional[23] and a Tier 1/Tight basis set of numeric atom-centred orbitals, as implemented in the all-electron code FHI-AIMS.[24] This level of theory has recently been shown to be good for accurately evaluating both relative total energies and trends in the electronic structure of a range of $(TiO_2)_N$ clusters with sizes between N = 4–20.[25]

Top-down derived $(TiO_2)_N$ nanocrystals

Nanoscale titania, due to its technological importance, is intensively studied both theoretically and experimentally. Ideally, from the computational modelling perspective one would like to employ nanoparticles possessing a realistic size and structure in order to probe their properties using efficient yet acceptably accurate descriptions of their electronic structure. Generally, this entails using calculations based on density functional theory (DFT). Titania nanoparticles used in the experiment, however, typically contain many thousands of atoms; a size that is beyond the current capacity of routine computational modelling using DFT. Efforts to model the optical and electronic properties of nanotitania have thus used a variety of models ranging from nanoclusters containing only a few atoms to nanoparticles possessing up to a few hundred TiO_2 units. Often these studies have attempted to find nanoparticles of titania which retain as much as possible the bulk crystalline and electronic structure. The smallest of these nanocrystals correspond closely to the N_{meta} crossover size below which bulk-like crystallinity cannot be maintained. Nanoparticles as small as $(TiO_2)_{15}$ for rutile[26] and $(TiO_2)_{16}$ for anatase[27] have been reported, and even employed as nanocrystal models.[28] According to our definition of a nanocrystal, we rule out the $(TiO_2)_{16}$ anatase cut as a true nanocrystal due to the large change in atomic positions and accompanying changes in the local bonding of the majority of its atoms that occurs upon relaxing its structure, as also noted in other work.[27]

Herein, we employ five nanocrystals all derived from stoichiometric cuts from the bulk anatase crystal phase with between 28–84 TiO_2 units (*i.e.* 84–252 atoms), which retain their atomic structure reasonably well with respect to the original bulk atomic ordering and positions after structural relaxation (see Fig. 2). Anatase nanocrystals are experimentally

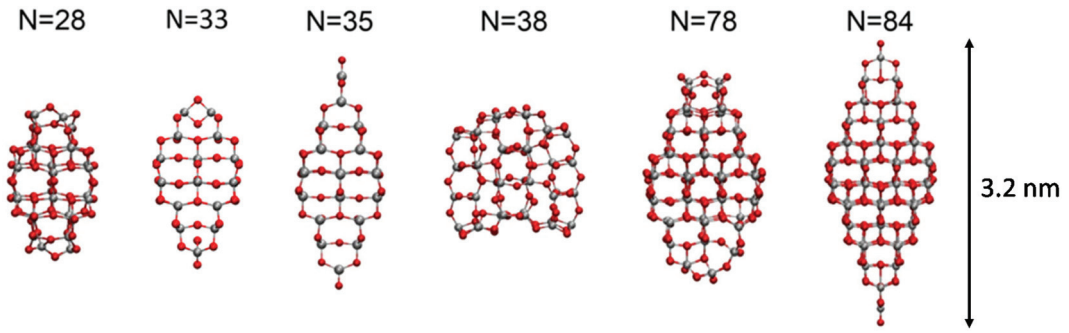

Fig. 2 Atomic structures of the top-down $(TiO_2)_N$ nanocrystals employed. Atom key: O – red, Ti – grey. Note that the scale arrow to the right strictly relates only to the size of the 252 atom $(TiO_2)_{84}$ nanocrystal – the other four nanocrystals have been scaled to show their atomic structure more clearly.

found to exhibit a {101}-faceted bipyramidal shape which typically possess some degree of {001} truncation of the apices. Such a morphology can be rationalised through by cuts of the anatase bulk crystal exposing facets whose size and shape follow their surface energies as described by the Wulff construction.[29] Our nanocrystals with N = 35 and N = 84 were cut from the parent anatase crystal so as to exhibit bipyramidal morphologies, and those with N = 33 and N = 78 units cut to have truncated bipyramidal shapes respectively. The 28 and 38 TiO_2 unit nanocrystals were taken from those studies which used a number of structural principles in order to guide the way in which they were cut from the parent anatase crystal. In particular, the structures of the N = 38 nanocrystal were fabricated according to the requirements that all atoms should have sufficient coordination to support their formal oxidation state (*i.e.* O^{2-} and Ti^{4+} for TiO_2) and that the nanocrystal should have no net dipole moment.[27,30] This procedure results in the N = 38 nanocrystal being fully-coordinated in contrast to the N = 35 and N = 84 bipyramidal nanocrystals which display two apical Ti–O terminations. In the case of the 28 unit nanocrystal a similar, albeit less formal, approach was followed whereby nanocrystals that would be as symmetric as possible in every direction were sought, while still possessing as much anatase-like structure as possible.[31] We note that for this latter $(TiO_2)_{28}$ nanocrystal the original bulk-cut yields four terminal Ti–O groups which persist even after relaxing the structure. Nevertheless, this feature does not appear to detrimentally affect the energetic stability of the nanocrystal compared to similarly sized nanocrystals considered (*i.e.* for sizes N = 33 and N = 35). Conversely, however, we also note that in ref. 31 a N = 38 bulk cut is reported which has two singly coordinated terminal oxygen atoms, which after relaxation form bonds with nearby oxygen atoms (O–O distance of 1.44 Å). This nanoparticle is not used in our study due to this very non-bulk-like feature and the fact that it is highly metastable (>5 eV) relative to the $(TiO_2)_{38}$ bulk cut we employ from ref. 27.

Under the assumption that nanoclusters grow in a perfectly spherical manner one can derive the fraction of surface atoms, $F_{surf}(N)$, to be $kN^{-\alpha}$, where $\alpha = -1/3$ and $k = 4$. Following the derivation for other cluster shapes yields different k values, while α is an unchanged general constant determined by the area-to-volume dimension of $F^{surf}(N)$. Many generic properties, $G(N)$, of simple clusters (*e.g.* total energies, ionisation energies, melting temperatures) can be approximately fitted to a scaling law of the following type:[32]

$$G(N) = G_{bulk} + a_1 N^{-1/3}, \quad (1)$$

where G_{bulk} is a characteristic constant value of the property in question for the chosen bulk phase. For small nanoclusters such fits are worse than those for larger nanoparticles due to the more extreme dependency on properties with small changes in size. This regime of small nanoclusters is often termed the size range where "every atom counts". For large facetted nanocrystals, analysing the most significant size dependent contributions to the total energy yields that it both depends on $F_{surf}(N)$ and $V_{dilate}(N)$, the volume dilation of the nanoparticle induced by surface stress.[3,33] $V_{dilate}(N)$ varies inversely with respect to the radius of the nanocrystal and thus introduces a $bN^{-1/3}$ energy dependence similar to $F_{surf}(N)$. Overall this leads to a general $E(N)$ dependence of the following form for increasingly sized large nanocrystals:[3]

$$\begin{aligned} E(N) &= E_{bulk} + a_1\left(1 - bN^{-1/3}\right)N^{-1/3} \\ &= E_{bulk} + a_1 N^{-1/3} - a_2 N^{-1/3}\cdot N^{-1/3} \\ &= E_{bulk} + a_1 N^{-1/3} - a_2 N^{-2/3}, \end{aligned} \quad (2)$$

where a_1 and a_2 are the constants when the nanocrystals are always of the same shape and crystal structure. We note that for large N, eqn (1) will increasingly become a better approximation to eqn (2) due to the relatively larger magnitude of the exponent of the last term in the latter. More generally, taking eqn (1) as representing the zeroth order dependence on N, we can see eqn (2) as the first three terms of a power series expansion of the form:

$$E(N) = a_0 + a_1 x + a_2 x^2 + a_3 x^3 + \ldots, \quad (3)$$

where $a_0 = E_{bulk}$, $x = N^{-1/3}$ and the a_n values are (possibly N dependent) constants. Eqn (2) has been used to estimate the anatase-to-rutile crossover in titania nanocrystals, with the optimisation of a_1 and a_2 for each polymorph and size considered to obtain the appropriate morphology.[3,34] In this case periodic DFT calculations of bulk titania were used to calculate the surface energies and surface stresses required to evaluate a_1 and a_2.[3] As these top-down calculated values are only strictly valid for infinite slabs, application to faceted nanocrystals was deemed acceptable to the anatase nanocrystals of a minimum size of approximately 450 TiO_2 units (corresponding to a truncated bipyramid with a B/A side length ratio of ~0.3 and side A = 2 nm).[34] Below this size it is more appropriate to perform explicit electronic structure calculations of nanocrystals.[3] In our study we use DFT calculations to directly calculate the fully relaxed structure and energetic stability of $(TiO)_N$ nanoclusters and nanocrystals with sizes $1 < N < 84$ and use these data to extrapolate to nanoparticle sizes with $N \leq 150$. Although quantities calculated for infinite surfaces should not be used in eqn (1) for this size regime, this equation still contains the essential elements to describe the stability of faceted nanocrystals, albeit with more appropriate values of a_1 and a_2.

Bottom-up derived $(TiO_2)_N$ nanoclusters

Numerous previous studies have attempted to find the lowest energy structures of small $(TiO_2)_N$ nanoclusters ($N \leq 20$) without recourse to using bulk crystalline structures.[25,26,35–42] Such a "bottom-up" approach can be attempted by hand using analogy with known nanoclusters of other materials and principles of chemical structure as in ref. 26 and 30. Such intuitive methods, however, are generally not as reliable in finding low energy structures as using global optimisation algorithms to thoroughly search the complex multidimensional potential energy surface (PES) for nanocluster isomer possibilities. The

need for efficient global optimisation tends to increase with nanocluster size as it becomes progressively more difficult to find the lowest energy structures from a bottom-up approach due to the concomitant combinatorial increase in possible atomic configurations.

Here, we employ global optimisation with classical interionic potentials (IPs) to search the PES in a computationally efficient manner, and subsequently refine the resulting low energy cluster structures using unconstrained geometry optimisations at the DFT level of theory. This general IP–DFT strategy has been employed in a number of studies[25,35,39,41,42] with various choices of IP and DFT functionals. We have found that the often-used bulk-parameterised IPs such as those reported by Matsui and Akaogi (MA)[43] are not very size-transferable for evaluating the relative stabilities and structures of small discrete $(TiO_2)_N$ species. We note, for example, that the MA IP tends to predict highly coordinated compact cluster structures to be very energetically stable,[35,42] but which are not found to be particularly low in energy compared to more open structures, when refined using DFT geometry optimizations.[39,41] In an attempt to rectify these shortcomings we have employed two strategies based on the MA IP type.

Firstly, we have taken the original MA IP parameterisation and used this together with another IP which favours the 4-coordination of oxygen ions around each cation. Specifically, we use the interaction parameters of IP by Flikkema and Bromley (FB) which was originally parameterised for $(SiO_2)_N$ nanoclusters.[44] For any particular $(TiO_2)_N$ composition we assign a percentage of the Ti cations and O anions to be treated by the FB IP and the rest by the MA IP. The is purely a formal definition within the overall mixed IP parameterisation and finally all oxygen and all titanium ions are taken to be respectively equivalent after an energy minimisation of a cluster structure. The full set of parameters for this mixed MA–FB IP approach can be found in the ESI.† The FB-treated ions energetically favour the formation of four-coordinated Ti centres largely due to the FB IP possessing a relatively higher degree of O–O repulsion. Thus, when FB-parameterised centres replace the centres originally parametrised by the MA IP (which favour 6-coordinated Ti centres) more open cluster structures are favoured. We found that replacing 30–50% of the original MA-parameterised centres by our FB-parameterised centres was optimal for improving the tendency of the mixed IP to generate low energy $(TiO_2)_N$ cluster structures. We note that this approach was employed previously in ref. 36 to generate candidate global minima for $(TiO_2)_N$ for $N = 8, 10$.

Secondly, we have re-parameterised the original MA IP to reduce its strong tendency to form highly coordinated clusters. Here, the main change was to increase the repulsion between oxygen anions for O–O separations of 1.5–2.5 Å while maintaining very similar Ti–O interaction parameters. We note that the degree of O–O repulsion in this new parameterisation is not as high as in the FB IP (see the ESI† for IP parameters). We found that, as for the mixed IP strategy, this new parameterisation of the MA IP led to low energy cluster structures with relatively less compact structures and fewer highly coordinated Ti centres.

For both the above IP-based approaches we use Monte Carlo basin hopping[45] global optimisation where we typically employ 10 runs each of typically one million steps, each one starting from a different initial structure. For the smallest sizes considered (*i.e.* $N < 15$) we note that the proposed global minima were usually obtained in runs of less than one million steps. During the run, the temperature was automatically adjusted to maintain an average acceptance ratio of new structures of between 65–80%. For the case of the mixed IP approach we also used specific oxygen–oxygen and titanium–titanium swap moves to help ensure that the best configuration of the two oxygen and two titanium types was achieved for any particular cluster structure. The lowest energy 40–50 structures resulting from the 10 runs for each cluster size were then re-optimised using FHI-AIMS with a light Tier 1 basis and the PBE[46] functional. After this refinement, the best 7–8 structures were finally optimised using our reference PBE0/tight Tier 1 settings.

In addition to attempting direct global optimisation of $(TiO_2)_N$ species, we also employed data mining[47] where we took low energy globally optimised structures of $(SiO_2)_N$ [48,49] and $(CeO_2)_N$ [16] and re-optimised them as corresponding $(TiO_2)_N$ nanoclusters. Specifically, we mainly tried columnar-type $(SiO_2)_N$ clusters[49] and tetrahedral $(CeO_2)_N$ fluorite-like cuts.[50] We note, for example, that in the former case low energy structures were found for sizes $N = 12$ and 18, which concurred with the results from our global optimisations. More interestingly, in the latter case, for sizes $N = 10$, 20 and 35, new candidate global minima structures were found as described below.

Results and discussion

For relatively small cluster sizes $(TiO_2)_N$ for $N = 1$–9 we could find no lower energy clusters than those reported previously in the literature indicating that global minima in this size range are reasonably well established. Specifically, our finding for $N = 1$–8 coincide with those reported in both ref. 40 and 41 where global optimisation was performed and, as in the present study, the final structures were optimised with DFT using a hybrid functional. For $N = 9$ and $N = 10$, we concur with the global minima candidate structures found in ref. 41 and 50 respectively. For $(TiO_2)_N$ nanocluster sizes with $N = 11$–14, 16–24, 28, 35 and 38, we report new candidate global minima from our bottom-up global optimisation and data-mining approach (see Fig. 3 and 4). We note that all our reported isomers for these sizes are more energetically stable than any structures we could find in the literature (see the ESI† for a comparison between our results and those reported elsewhere). Herein, we are concerned with the structure and stability of the nanoclusters, and results pertaining to other properties (*e.g.* electronic, vibrational *etc.*) will be reported elsewhere.

In line with the assumptions made in other studies regarding the tendency for higher energetic stability and more bulk-

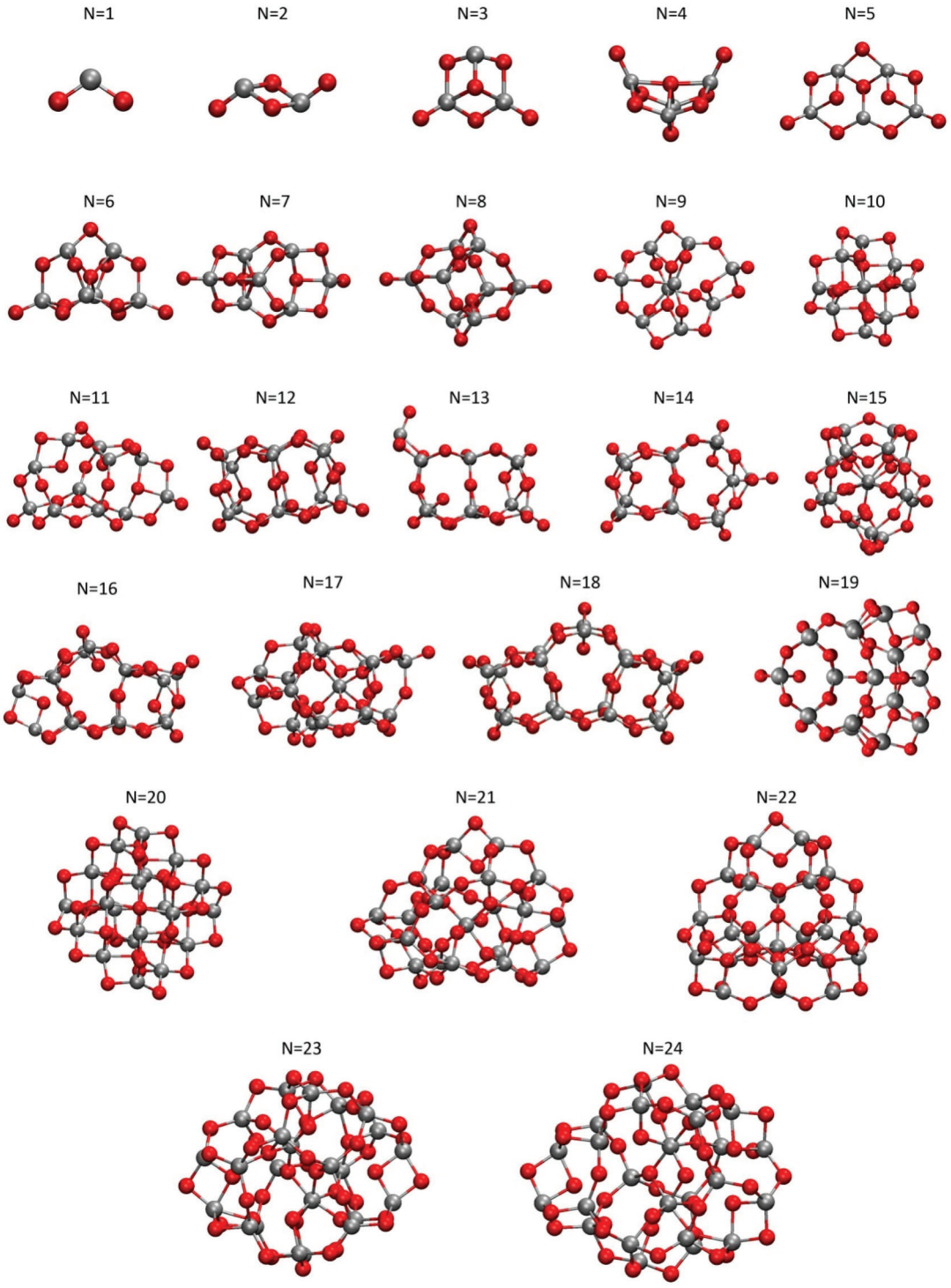

Fig. 3 Structures of the low energy bottom-up derived $(TiO_2)_N$ clusters N = 1–24 employed in this work.

like character being associated with fewer terminal dangling oxygen Ti–O defects,[26,30] our bottom-up generated set of clusters show a clear tendency to exhibit fewer such defects with increasing size. In particular all clusters we find for $N > 18$ are either fully-coordinated (*i.e.* zero terminal defects) or have at most one Ti–O defect. This tendency is also fully in line with the bottom-up studies of $(SiO_2)_N$ clusters where a similar transition to fully-coordinated clusters has been predicted to occur for sizes $N \geq 26$.[51] Generally speaking, we also see a tendency for decreasing structural symmetry in the clusters with increasing size. Although, for example, all $(TiO_2)_N$ global minima in the range N = 1–8 have some symmetry (*i.e.* greater than C_1)

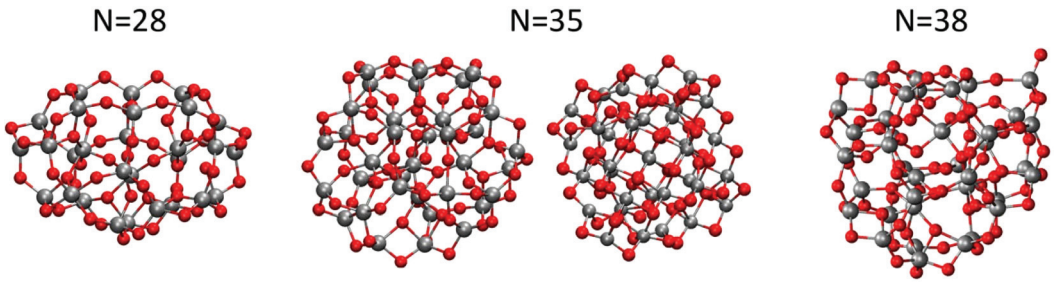

Fig. 4 Structures of low energy bottom-up derived $(TiO_2)_N$ clusters N = 28, 35 (left), 38 found in this work from global optimisation. The N = 35 (right) nanoparticle was obtained from data-mining from a tetrahedral $(CeO_2)_{35}$ nanoparticle in ref. 16 and is calculated to be marginally metastable relative to the $(TiO_2)_{35}$ nanoparticle to its left.

the propensity for our candidate global minima to be symmetric falls away to such an extent that all our lowest energy clusters for $N > 22$ are not symmetric. We note that for the size N = 35, in addition to our lowest energy NC cluster, we also find a highly symmetric and very low energy, yet non-anatase-like, cluster (see Fig. 4) which we discuss below.

Generally, our searches do not find structures which display the anatase crystal structure for N = 1–38. In particular for sizes N = 28, 35 and 38, we find NC clusters which are significantly more stable (by 7.9–9.9 eV total energy) than their correspondingly sized anatase nanocrystal counterparts (shown in Fig. 2). This clearly implies that using metastable anatase nanocrystal structures within this size range to model the behaviour of larger nanocrystals may potentially introduce significant errors, and tests are required to accurately assess the validity and consequences of such modelling approaches.

Estimating the NC ↔ C crossover size regime

Taking the DFT energies of the optimised bulk cut nanocrystals in Fig. 2 we made a fit to eqn (2) to yield a_1 and a_2 for the size range N = 1–150 (see the corresponding data points and blue fit line in Fig. 5). Strictly speaking, as the morphology of our bulk-cut nanocrystals is not always the same, a_1 and a_2 will not be the same for all of them. However, as the considered polymorph (*i.e.* anatase) is always the same and all the considered nanocrystals tend to display similar relaxed surface sites, we fit our eight data points (*i.e.* six bulk cut nanocrystals, and the limits of the infinite anatase crystal and the TiO_2 monomer) with fixed constants for all N values. We also note that by only using the Wulff-type bulk cuts (*i.e.* our bipyramids and truncated bipyramids with N = 33, 35, 78 and 84) we obtain a very similar fit.

For our low energy clusters coming from our bottom-up searches, their structures and morphologies vary immensely with size and thus a fit using eqn (2) is not justified. Instead we assume that although the basic geometric and surface stress energy components of the total energy for regular nanocrystals is captured in eqn (2), a general expansion building on this basis (see eqn (3)) would be more suitable for this diverse set. We have attempted fits using eqn (3) with polynomials from degree 3 to degree 8. We find that for degree 3 and 4 polynomial fits, the resulting extrapolated line does not cross the fit derived for the top-down nanocrystals and simply tends to zero, implying unreasonably, and against experimental evidence, that non-crystalline clusters are always more stable than anatase nanocrystals. For degree 7 and 8 polynomial fits, the extrapolated trend line is non-monotonically decreasing with increasing N, unphysically predicting a decrease in energetic stability with increasing nanoparticle size. Fits with polynomials of degree 5 and 6, however, provide almost exactly the same monotonically decreasing trend line which meets the nanocrystal fit line, which is consistent with the observations. As such, these latter expansions of eqn (3) appear to be the only ones which lead to physical consistent fits of the data. We thus used the degree 5 fit to the nanocluster data which leads to estimate a NC ↔ C crossover size of N = 125 (*i.e.* 375 atoms) as shown in Fig. 5. The fitting parameters used can be found in the ESI† along with the plots of the energetic data with respect to $N^{-1/3}$.

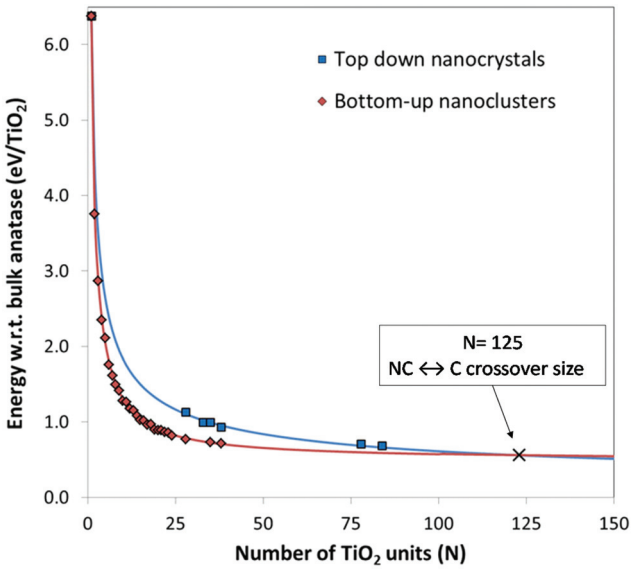

Fig. 5 Energies of bottom-up (red) generated nanoclusters and top-down (blue) generated nanocrystals with corresponding fitting lines. The NC ↔ C crossover size is indicated by a cross at 125 TiO_2 units (*i.e.* 375 atoms).

To provide an idea of the diameter of such an $N = 125$ sized nanoparticle in Fig. 6 we show a spherical semi-crystalline (*i.e.* anatase core and amorphous shell) nanoparticle of 130 TiO_2 units (~2.0 nm diameter) and a facetted anatase bulk cut of 151 TiO_2 units (~2.6 nm diameter). Accordingly, we thus predict the emergence of anatase-like crystallinity in TiO_2 nanoparticle sizes to occur in nanoparticles of approximately 2–3 nm diameter. We note that our prediction, coming purely from a theoretical basis, is fully consistent with the experimental results in ref. 12.

Crystallinity in <2–3 nm diameter non-anatase nanoparticles

Experimentally assessing the degree of crystallinity in very small nanoparticles with diameters <2 nm is clearly complicated by the fact that the concept of long range order is rather ill-defined and thus usual X-ray diffraction (XRD) methods used for larger samples are not applicable. This size regime is also where a bulk electronic structure typically starts to become significantly different from bulk samples also hindering the use of other indirect spectroscopic assessments of bulk-like structures.[52] Theoretically, we can simulate XRD patterns from arbitrarily small nanoparticles but interpreting the results of doing so are rather inconclusive with respect to comparisons with experiment. Here, for example, simulated XRD patterns from seemingly non-crystalline nanoclusters can give rise to broad peaks often taken to be indicative of bulk-like atomic ordering in experimentally measured XRD patterns.[53] To avoid complications of theoretical/experimental comparisons and the formal applicability of XRD for very small nanoparticles, we choose to assess the crystallinity of our nanoparticles through consistently calculating a single alternative measure of the atomic order for both the bulk anatase crystal and our titania nanoparticles. Specifically, we have used the atomic pair distribution function (PDF) which describes the distribution of distances between pairs of atoms in a system (*e.g.* nanoparticle, bulk material). The peaks in the PDF represent the probability to find a neighbourhood particle at the corresponding radial distance from a certain atom. In Fig. 7 we compare the PDFs of a $(TiO_2)_{35}$ top-down bulk cut nanocrystal with that of bulk anatase and the lowest energy $(TiO_2)_{35}$ nanoparticle found from our bottom-up global optimisations. Although clearly not exhibiting the detailed spectra of the perfect bulk anatase crystal, the relaxed top-down $(TiO_2)_{35}$ nanocrystal has a number of well-defined peaks of diminishing size with positions that appear to correspond to those in the bulk anatase crystal. The slight shifting of some peaks to smaller distances in the nanocrystal spectra relative to the bulk anatase spectra is likely due to the surface stress induced compression of the former. Conversely, the more energetically stable bottom-up $(TiO_2)_{35}$ nanocluster has much less well defined spectra with one main fairly broadened peak corresponding to the nearest neighbouring Ti–O bonds. Clearly, although small, the $(TiO_2)_{35}$ nanocrystal can be said to possess some crystallinity, whereas the $(TiO_2)_{35}$ nanocluster is essentially non-crystalline. In this sense, we argue that the blue and red curves, and the point at which they cross in Fig. 5, possess real meaning with respect to a NC ↔ C crossover and thus in assessing the emergence of anatase-like crystallinity with increasing nanoparticle size.

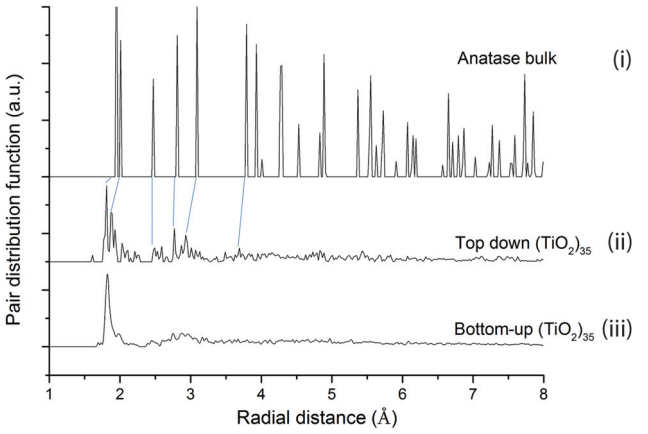

Fig. 7 Pair distribution functions calculated using the Debyer code[54] for: (i) anatase bulk-like nanocrystal, (ii) a top-down $(TiO_2)_{35}$ anatase bulk cut nanocrystal, and (iii) the lowest energy $(TiO_2)_{35}$ nanoparticle from our bottom-up global optimisations. Blue lines indicate tentative correspondence of anatase-like peaks in (i) and (ii).

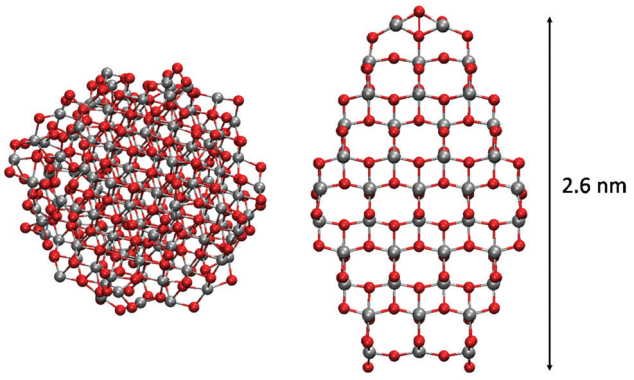

Fig. 6 Nanoparticles with sizes near to the predicted NC ↔ C crossover size. Left: A $(TiO_2)_{130}$ semi-crystalline spherical nanoparticle and right: A $(TiO_2)_{151}$ facetted bulk cut anatase nanocrystal.

Although we have predicted a NC ↔ C crossover which is consistent with experiment, and for which we clearly can define nanocrystals with anatase crystallinity that are metastable to non-crystalline nanoparticles for sizes up to $N = 125$, we also find some very low energy nanoparticles which neither appear to be anatase-like nor totally non-crystalline. Specifically, for $(TiO_2)_N$ sizes $N = 10$, 20 and 35, we obtain very energetically stable nanoclusters from data-mining from tetrahedral nanoclusters reported in ref. 16. For $N = 10$ and $N = 20$ these tetrahedral clusters are actually our best candidate global minima structures. All these nanoclusters are based on cuts from the cubic CeO_2 bulk fluorite crystal structure which has eight-coordinated Ce^{4+} ions and four-coordinated O^{2-} ions. For $(CeO_2)_N$ these bulk-cut-based nanoclusters retain the

as-cut fluorite crystal structure. However, in the case of $(TiO_2)_N$ we find that, upon relaxation, the clusters distort in a such a way as to lower the local atomic coordination of the ions (see the ESI†). This distortion is consistent with the fact that the cubic polymorphs of TiO_2 can only be stabilised at very high temperatures and pressures.[55] Relaxation from a fluorite bulk cut allowing for lowering of coordination would be consistent with a distortion to the columbite crystal structure (*i.e.* the α-PbO_2 structure, also known as the TiO_2 II phase), another known high pressure phase of TiO_2. Experimental X-ray absorption spectroscopy results report evidence for the TiO_2 II phase (*i.e.* columbite) in ~7 nm diameter titania nanoparticles[56] and geologically α-PbO_2-type TiO_2 (*i.e.* columbite) has been found naturally in nanometer sized ultrahigh-pressure inclusions.[57] Indeed, the energetically favoured prevalence for a columbite-like phase at small sizes could be consistent with the high surface stresses in such small nanoparticles which induces an effective high internal pressure. Our comparisons of the structures of the fluorite-cut-derived TiO_2 nanoparticles with the bulk columbite crystal structure, however, do not strongly support the hypothesis that the nanoparticles are simple cuts from the columbite bulk crystal. In fact, although these nanoparticles clearly possess some regular fluorite-derived atomic ordering, they do not appear to be a single phase. From some directions, for example, the clusters appear to exhibit atomic ordering reminiscent of the brookite crystal phase, predicted in some studies to be an intermediate size-dependent stable TiO_2 phase for nanoparticles with diameters between 11–35 nm.[58] The structure of the $Ti_{20}O_{40}$ fluorite-derived nanocluster and its comparison with the original data-mined structure and the brookite crystal can be found in the ESI.†

Conclusions

We present a detailed study of the size dependent energetic stability of nanoscale titania from both a bottom-up and top-down perspective. Using global optimisation and data-mining we report global minima $(TiO_2)_N$ candidates for nanoclusters in the size range N = 1–38 (*i.e.* up to 114 atoms), where in the range N = 11–38, nearly all cluster structures are new and lower in energy than those previously reported. Taking Wulff constructed bulk cuts from the anatase crystal structure and other anatase bulk cuts from the literature, we also track the energetic stability of anatase nanocrystals up to N = 84 (*i.e.* 252 atoms). From direct comparison of the two data sets we can conclude that up to N = 38 anatase nanocrystals are significantly metastable with respect to correspondingly sized non-crystalline nanoclusters. Firstly, this strongly indicates that nanocrystals in this size regime should be employed with caution when used as models of significantly larger nanocrystals and, secondly, that the crossover size at which anatase nanocrystals become more energetically stable than non-crystalline nanoclusters occurs at significantly larger sizes. Using both data sets and fitting using a generalised expansion of a top-down derived energy expression for nanoparticles, we extrapolate the fit to both data sets to predict an approximate NC ↔ C crossover size of N = 125 (*i.e.* 375 atoms). This size corresponds to a nanoparticle diameter of between 2–2.6 nm, depending on nanoparticle morphology, and corresponds well to the observed dominance of amorphous spherical titania nanoparticles of 2–3 nm diameter before facetted anatase nanocrystals tend to take over for larger sizes.[12] We hope that the approach described in this work will inspire similar studies in order to derive estimates of the fundamental NC ↔ C crossover size for a range of other important materials for which nanoscale crystallinity is a key property.

Acknowledgements

Support from Spanish MINECO/FEDER grant CTQ2015-64618-R grant and, in part, by Generalitat de Catalunya grants 2014SGR97, XRQTC is acknowledged. We also acknowledge the NOMAD Center of Excellence project (this project has received funding from the European Union's Horizon 2020 research and innovation programme under grant agreement no. 676580). Access to supercomputer resources was provided through grants from the Red Española de Supercomputación and the COMPHOTOCAT project 2014112608 of the Partnership for Advanced Computing in Europe (PRACE). We also acknowledge funding from H2020 project ITN-EJD-642294 (TCCM: Theoretical Chemistry and Computational Modelling).

References

1 H. Zhang and J. F. Banfield, *Chem. Rev.*, 2014, **114**, 9613–9644.
2 H. Zhang and J. F. Banfield, *J. Mater. Chem.*, 1998, **8**, 2073–2076.
3 A. S. Barnard and P. Zapol, *Phys. Rev. B: Condens. Matter*, 2004, **70**, 235403.
4 X. Chen and A. Selloni, *Chem. Rev.*, 2014, **114**, 9281–9282.
5 M. Kapilashrami, Y. Zhang, Y.-S. Liu, A. Hagfeldt and J. Guo, *Chem. Rev.*, 2014, **114**, 9662–9707.
6 J. Schneider, M. Matsuoka, M. Takeuchi, J. Zhang, Y. Horiuchi, M. Anpo and D. W. Bahnemann, *Chem. Rev.*, 2014, **114**, 9919–9986.
7 W. Dong, Y. Sun, C. W. Lee, W. Hua, X. Lu, Y. Shi, S. Zhang, J. Chen and D. Zhao, *J. Am. Chem. Soc.*, 2007, **129**, 13894–13904.
8 C. Jiang, K. Y. Lee, C. M. A. Parlett, M. K. Bayazit, C. C. Lau, Q. Ruan, S. J. A. Moniz, A. F. Lee and J. Tang, *Appl. Catal., A*, 2016, **521**, 133–139.
9 R. L. Penn and J. F. Banfield, *Geochim. Cosmochim. Acta*, 1999, **63**, 1549–1557.
10 S. Patra, C. Davoisne, H. Bouyanfif, D. Foix and F. Savage, *Sci. Rep.*, 2015, **5**, 10928.
11 J. F. Banfield and H. Zhang, *Mineralogical Society of America*, Washington DC, 2001, vol. 44.

12 H. Zhang, B. Chen, J. F. Banfield and G. A. Waychunas, *Phys. Rev. B: Condens. Matter*, 2008, **74**, 214106–214101.
13 K. Jacobs, J. Wickham and A. P. Alivisatos, *J. Phys. Chem. B*, 2002, **106**, 3759.
14 P. Dugourd, R. R. Hudgins and M. F. Jarrold, *Chem. Phys. Lett.*, 1997, **267**, 186–192.
15 R. Dong, X. Chen, X. Wang and W. Lu, *J. Chem. Phys.*, 2008, **129**, 044705.
16 A. Migani, K. M. Neyman and S. T. Bromley, *Chem. Commun.*, 2012, **48**, 4199–4201.
17 S. T. Bromley, I. Moreira, P. R. de, K. M. Neyman and F. Illas, *Chem. Soc. Rev.*, 2009, **38**, 2657–2670.
18 C. Chizallet, G. Costentin, M. Che, F. Delbecq and P. Sautet, *J. Am. Chem. Soc.*, 2007, **129**, 6442–6452.
19 M. C. C. Wobbe, A. Kerridge and M. A. Zwijnenburg, *Phys. Chem. Chem. Phys.*, 2014, **16**, 22052–22061.
20 C. Loschen, A. Migani, S. T. Bromley, F. Illas and K. M. Neyman, *Phys. Chem. Chem. Phys.*, 2008, **10**, 5730–5738.
21 C. A. C. Richard, S. A. French, A. A. Sokol, A. A. Al-Sunaidi and S. M. Woodley, *J. Comput. Chem.*, 2008, **13**, 2234–2249.
22 A. Erlebach, K. Heinz-Dieter, J. Grabow, F. A. Müller and M. Sierka, *Nanoscale*, 2015, **7**, 2960–2969.
23 C. Adamo and V. Barone, *J. Chem. Phys.*, 1999, **110**, 6158–6169.
24 V. Blum, R. Gehrke, F. Hanke, P. Havu, V. Havu, X. Ren, K. Reuter and M. Scheffler, *Phys. Commun.*, 2009, **180**, 2175–2196.
25 S. Bhattacharya, B. H. Sonin, C. J. Jumonville, L. M. Ghiringhelli and N. Marom, *Phys. Rev. B: Condens. Matter*, 2015, **91**, 241115.
26 Z.-W. Qu and G.-J. Kroes, *J. Phys. Chem. C*, 2007, **111**, 16808–16817.
27 P. Persson, J. C. M. Gebhardt and S. Lunell, *J. Phys. Chem. B*, 2003, **107**, 3336–3339.
28 O. Miroshnichenko, S. Auvinen and M. Alatalo, *Phys. Chem. Chem. Phys.*, 2015, **17**, 5321–5327.
29 G. Wulff, *Z. Kristallogr.*, 1901, **34**, 449–530.
30 P. Persson, R. Bergström and S. Lunell, *J. Phys. Chem. B*, 2000, **104**, 10348.
31 S. Auvinen, M. Alatalo, H. Haario, J.-P. Jalava and R.-J. Lamminmäki, *J. Phys. Chem. C*, 2011, **115**, 8484–8493.
32 R. Johnston, *Masters Series in Physics and Astronomy*, Taylor and Francis, London, 2002.
33 A. S. Barnard and P. Zapol, *J. Chem. Phys.*, 2004, **121**, 4276.
34 A. S. Barnard and L. A. Curtiss, *Nano Lett.*, 2005, **5**, 1261–1266.
35 S. Hamad, C. R. A. Catlow, S. M. Woodley, S. Lago and J. A. Mejias, *J. Phys. Chem. B*, 2005, **109**, 15741–15748.
36 M. Calatayud, L. Maldonado and C. Minot, *J. Phys. Chem. C*, 2008, **112**, 2008.
37 M. Calatayud and C. Minot, *J. Phys. Chem. C*, 2009, **113**, 12186–12194.
38 O. A. Syzgantseva, P. Gonzalez-Navarrete, M. Calatayud, S. Bromley and C. Minot, *J. Phys. Chem. C*, 2011, **115**, 15890–15899.
39 L. Tang, L. Linwei, J. Zhao and R. Qiu, *J. Comput. Chem.*, 2011, **33**, 163.
40 N. Marom, M. Kim and J. R. Chelikowsky, *Phys. Rev. Lett.*, 2012, **108**, 106801.
41 M. Y. Chen and D. A. Dixon, *J. Chem. Theory Comput.*, 2013, **9**, 3189–3200.
42 S. G. Neogi and P. Chaudhury, *J. Comput. Chem.*, 2014, **35**, 51–61.
43 M. Matsui and M. Akaogi, *Mol. Simul.*, 1991, **6**, 239–244.
44 E. Flikkema and S. T. Bromley, *Chem. Phys. Lett.*, 2003, **378**, 622–629.
45 D. J. Wales and J. P. K. Doye, *J. Phys. Chem. A*, 1997, **101**, 5111.
46 J. P. Perdew, K. Burke and M. Ernzerhof, *Phys. Rev. Lett.*, 1996, **77**, 3865–3868.
47 A. Sokol, C. R. A. Catlow, M. Miskufova, S. A. Shevlin, A. A. Al-Sunaidi, A. Walsh and S. M. Woodley, *Phys. Chem. Chem. Phys.*, 2010, **12**, 8438–8445.
48 E. Flikkema and S. T. Bromley, *J. Phys. Chem. B*, 2004, **108**, 9638–9645.
49 S. T. Bromley and E. Flikkema, *Phys. Rev. Lett.*, 2005, **95**, 185505.
50 F. Aguilera-Granja, A. Vega and L. Balbás, *J. Chem. Phys.*, 2016, **144**, 234312.
51 E. Flikkema and S. T. Bromley, *Phys. Rev. B: Condens. Matter*, 2009, **80**, 035402.
52 A. Wood, M. Giersig, M. Hilgendorff, A. Vilas-Campos, L. M. Liz-Marzán and P. Mulvaney, *Aust. J. Chem.*, 2003, **56**, 1051–1057.
53 M. A. Zwijnenburg, *Nanoscale*, 2011, **3**, 3780.
54 Debyer website: https://github.com/wojdyr/debyer. Debyer is a general program for calculating the XRD patterns and pair-distribution functions of nanoparticles.
55 M. Mattensi, J. S. de Almeida, L. Dubrovinsky, N. Dubrovinskaia, B. Johansson and R. Ahuja, *Phys. Rev. B: Condens. Matter*, 2004, **70**, 212101.
56 H. C. Choi, H.-J. Ahn, Y. M. Jung, M. K. Lee, H. J. Shin, S. B. Kim and Y.-E. Sung, *Appl. Spectrosc.*, 2004, **58**, 598.
57 S.-L. Hwang, P. Shen, H.-T. Chu and T.-F. Yui, *Science*, 2000, **288**, 321–324.
58 H. Zhang and J. F. Banfield, *J. Phys. Chem. B*, 2000, **104**, 3481.

Global optimisation of hydroxylated silica clusters: A cascade Monte Carlo Basin Hopping approach

Andi Cuko, Antoni Maciá, Monica Calatayud, Stefan Bromley

Global Optimisation of Hydroxylated Silica Clusters: a Cascade Monte Carlo Basin Hopping Approach

Andi Cuko[1,2], Antoni Maciá[1], Monica Calatayud[2,3], Stefan T. Bromley[1,4*]

[1] *Departament de Química Física and Institut de Química Teòrica i Computacional (IQTCUB), Universitat de Barcelona, E-08028 Barcelona, Spain*

[2] *SorbonneUniversités, UPMC Univ Paris 06, CNRS, Laboratoire de Chimie Théorique CC 137 - 4, place Jussieu F. 75252 PARIS CEDEX 05 - France*

[3] *Institut Universitaire de France, France*

[4] *Institució Catalana de Recerca i Estudis Avançats (ICREA), E-08010 Barcelona, Spain*

* Corresponding author: s.bromley@ub.edu

Abstract

We report on a global optimisation study of hydroxylated silica nanoclusters $(SiO_2)_M{\cdot}(H_2O)_N$ with sizes M = 6, 8, 10 12, and for each size with a variable number of incorporated water molecules (N = 1, 2, 3…). Due to the high structural complexity of these systems and the associated ruggedness of the underlying potential energy landscape, we propose a "cascade" global optimisation approach. Specifically, we use Monte Carlo Basin Hopping (MCBH) where for each step we employ two energy minimisations with: (i) a few-term simple but computationally efficient interatomic potential (IP) which does not distinguish between H-bonded conformational isomers, and then (ii) a more sophisticated IP which accounts for polarisation and H-bonding. Final energies from the MCBH search are then refined with optimisations using density functional theory. The reliability of our approach is first established via comparison with previously reported results for the $(SiO_2)_8{\cdot}(H_2O)_N$ case, and then applied to the M = 6, 10 and 12 systems. For all systems studied our results follow the trend in hydroxylation energy versus N, whereby the energy gain with hydroxylation is found to level off at a point where the average tetrahedral distortion of the SiO_4 centres is minimised. This optimal hydroxylation point is further found to follow an inverse power law with increasing cluster size (M) with an exponent close to -2/3, further confirming work in previous studies for other cluster sizes.

Introduction

Nanosized silica particles are widely used during the preparation of materials (e.g. cement-based materials,[1] coatings,[2] polymers[3]) to significantly enhance their physical and mechanical properties. In addition to their high intrinsic strength (e.g. the Si-O bond 30% being stronger than the C-C bond), the success of silica nanoparticles for such applications is also due them having a relatively high proportion of reactive surface groups which can strongly interact with host materials. Silica is particularly prone to reaction with water, commonly resulting in a surface coverage of hydroxyl (Si-OH) groups.[4] The degree of hydroxylation is found to determine many of the properties of nanosilica. In solution, for example, the pH determines the solubility/hydroxylation of small silicate nanoparticles. Such species are central to the synthesis of technologically important nanoporous silicate materials such as zeolites[5] and occur in (bio)mineral nucleation, growth and dissolution processes.[6] The proportion of hydroxyls on small silica particles can also be deliberately increasing by physico-chemical processing to produce enhanced properties for applications (e.g. epoxidation catalysis[7], mechanically robust antireflective films[8]). The density of surface hydroxyls has further been reported to influence the biocompatibility and toxicity of silica nanoparticles.[9,10]

From a computational perspective the reaction of water with silica surfaces has attracted much attention.[11] For atomic to nanosized hydroxylated silica systems studies have tended to either focus on the detailed thermodynamics of the condensation of small ring- or chain-like $(SiO_2)_M$ $N \leq 6$ oligomers in solution[12,13] using *ab initio* methods, or on larger scale (i.e. with 100s or 1000s of atoms) classical forcefield simulations of hydroxylated nanosilca.[14,15,16] Between these extremes, some recent studies have focussed on attempting to find the most stable structures of hydroxylated silica nanoclusters in the approximate size range of 10-100 atoms.[17,18,19,20] This intermediate size regime is characterised by having non-trivial (i.e. not simply rings or chains) structures which are also not totally amorphous as typically assumed for larger nanoparticles. Hydroxylated silica nanoparticles with such sizes can thus be thought of as species which represent a structurally complex molecular-bulk crossover regime. Such species are likely to be particularly important in understanding nucleation of complex silica solids (e.g. zeolites). Although in such processes, many factors play an important role (e.g. pH, templates)[5] knowing the lowest energy hydroxylated nanosilica species in the absence of such factors provides a baseline to assess how and when they are important. Previous theoretical work in this size regime has specifically investigated hydroxylated silica clusters $(SiO_2)_M{\cdot}(H_2O)_N$ with sizes M = 4, 8, 16, 24, and each with a variable number of incorporated water molecules (N = 1, 2, 3…)[17,18,19,20] Due to their high structural complexity, global optimisation was employed in these studies to find low energy isomers for each stoichiometry. Specifically, a fairly simple set of interatomic potentials was used in conjunction with the Monte Carlo basin hopping (MCBH)[21] approach to first obtain initial cluster structures. Due to approximations in the IP set employed these non-refined structures provide only a poor account of OH···OH hydrogen bonding on the surfaces of the hydroxylated nanoclusters.[19] Optimisations using relatively computationally expensive density functional theory (DFT) calculations on a selection of IP-MCBH-generated structures were used to provide final clusters exhibiting hydrogen bonding.

In this work we report on a MCBH global optimization approach to hydroxylated silica nanosystems employing a cascade local optimization method. First, our method is shown to be reliable by applying it to the previously studied $(SiO_2)_8{\cdot}(H_2O)_N$ system.[18,19] We then, generate global minima candidates for the as yet unreported systems: $(SiO_2)_M{\cdot}(H_2O)_N$, M = 6, 10, 12, each for a

range of *N* values. In previous work it was shown that the hydroxylation reaction energy for silica clusters decreases by addition water molecules until it levels off around an optimal number *N*. This optimal number was found to be cluster size dependent to follow an inverse power law of the form $2M^{-2/3}$. Using our new global minima candidates for $(SiO_2)_M{\cdot}(H_2O)_N$, M = 6, 10, 12 we also further probe the generality of this relation.

Methodology

In this work we apply the MCBH global optimization technique to find low energy global minima candidates for the cluster set $(SiO_2)_M{\cdot}(H_2O)_N$, *M* = 6, 8, 10, 12 for a range of *N*. The general idea behind this technique in based on repeated steps consisting of random structural distortion and a subsequent local optimization. The Metropolis criterion[22] is applied in order to accept or refuse the local optimized structure according to a cost in passing from the initial (before the random distortion) and the final state, and a fictitious temperature. Usually the cost is the energy difference between the two states but in principle it is possible to generate other cost criteria based on system properties. Within a certain (unknown) number of the cyclic repetitions of this procedure is possible to explore the potential energy surface (PES) of the system. At each step, the structure can be locally optimized with both *ab initio* or a classical IP. In the first case, the applicability is limited to relatively small systems due to the high computational expense. This expense not only originates from local optimizations of the system but also from the higher number of steps required to properly sample the PES. Indeed, in principle, the number of energy minima is exponentially proportional to the number of atoms. A typical approach to makes MCBH calculations more computationally amenable is to use IPs for efficient optimisation. Nevertheless, IPs alone, often, cannot be relied upon for an accurate description of a system's properties. Therefore, after an IP-based MCBH run, a certain number of resulting low energy structures can be re-optimized with more accurate methods (e.g. DFT). For some systems, quite accurate IPs have been developed for which parameters have been fitted to experimental and/or *ab initio* data. In principle, the better the IP, the lower the number of structures that require significant further optimization with a more accurate method. However, we note that to have an IP with higher accuracy, you typically require correspondingly more complex functional forms with a higher number of terms. In turn, during a MCBH run, the direct use of such IPs can lead to practical problems in relaxing structures far from the equilibrium geometry (after a random distortion). Here we present a MCBH procedure in which for each step, a cascade structure optimization is performed with two different IPs. The general idea is to first use a robust and efficient IP to pre-optimize a distorted structure and then use more accurate IP for fully relaxing this pre-optimized structure. The Metropolis criterion is than applied after the second optimization. Our cascade-MCBH approach interfaces with the GULP package[23] which offers the possibility of using many IP types. We have implemented this procedure using Atomic Simulation Environment[24] (ASE) modules together.

In the literature, IPs for bare silica (SiO_2) bulk systems, such as TTAM[25] and BKS,[26] have been successfully used. Hassanali and Singer (HS)[27] introduced a IP parameterization for the silica-water interface by adding new three-body terms terms to the BKS IP in order to describe Si-O-H and H-bonds. All these IPs are based on the Buckingham mathematical form as shown in equation (1)

$$V_{ij}(r_{ij}) = \frac{q_i q_j}{4\pi\varepsilon_0 r_{ij}} + A_{ij} exp\left(-\frac{r_{ij}}{B_{ij}}\right) - \frac{C_{ij}}{r_{ij}^6} \quad (1)$$

where i,j ϵ {Si,O}, r_{ij} is the interionic separation, $q_{i,j}$ are the ionic charges and A, B and C are fitted parameters. With respect to nanosilica, Flikkema and Bromley (FB) re-parameterised a Buckingham IP specifically for treating bare silica nanoclusters.[28] Recently, Pedone *et al.*[29] have parameterized a new and more complex Buckingham IP with polarisable ions for hydroxylated silica. This IP also incorporates intra- and inter-bond Morse potentials and a three-body term for hydrogen bonds was shown to provide good structures and vibrational frequencies with respect to experimental and DFT-calculated data on hydroxylated silica surfaces. Recently, a systematic study has showed that this IP is also accurate for the treatment of hydroxylated nanoparticles.[30]

In previous global optimization studies the FB IP and a simplified version of the HS IP (HS_{simp}) has been used for finding low energy clusters where the HS three-body terms were omitted for simplicity and computational efficiency.[17,18] By omitting these terms, the correct description of hydroxyl groups (OH) is lost, therefore, the clusters do not have any H-bond contribution to their stability (see Fig. 1). In this way, isomers stabilized by hydrogen bonds contributions are not easily found only using HS_{simp} in a MCBH run. Such concerns are especially relevant to relatively large clusters and/or a high hydroxylation degree where H-bonding can influence the energetic ordering and structure of low lying minima (each H-bond contributes of about 20 kJ/mol). Thus for silica nanoparticles with increasing size and/or with moderate to high hydroxylation a good description of OH groups and their H-bonding becomes essential in order to avoid missing possible low energy clusters.

In this work we consider hydroxylated silica clusters $(SiO_2)_M{\cdot}(H_2O)_N$ systems with M = 6, 8 10 and 12 each one with different hydroxylation ratio $N{:}M$ ($R_{N/M}$) up to ~65%. As a pre-optimization in the first cascade step we use the FB IP with OH groups described by HS_{simp} IP (IP_1), while for second part of the cascade we use the IP due to Pedone et al. (IP_2)[29]. In general, the mathematical form of a Buckingham IP energy entails that the energy of a pair of atoms tends to -∞ when their distance tends to 0. To avoid such a superposition of atoms caused by random displacements during a MCBH run we added very short range repulsive terms to the Buckingham describing the interaction between unlike charged species in IP_1. In order to more efficiently explore the PES we use a self-correcting temperature technique to keep the accept ratio between 60 and 80%. For each MCBH step atomic displacements are set to a maximum of $\pm$ 0.8 Å for any cartesian coordinate and the energy difference used to discriminate between two different structures is set to 1 kJ/mol. Several runs (at least three) of fifty thousand steps each are performed for all considered systems. The ten most energetically stable isomers resulting from the MCBH global optimization procedure for each system stoichiometry are subsequently refined using DFT. These final optimisations are done employing the FHI-AIMS package[31], using the B3LYP[32] hybrid functional and a tier-1 atomic centred numerical basis set with a light integration grid with. The B3LYP functional has been shown to well describe hydroxylated silica in numerous previous studies.[17,19,33,34]

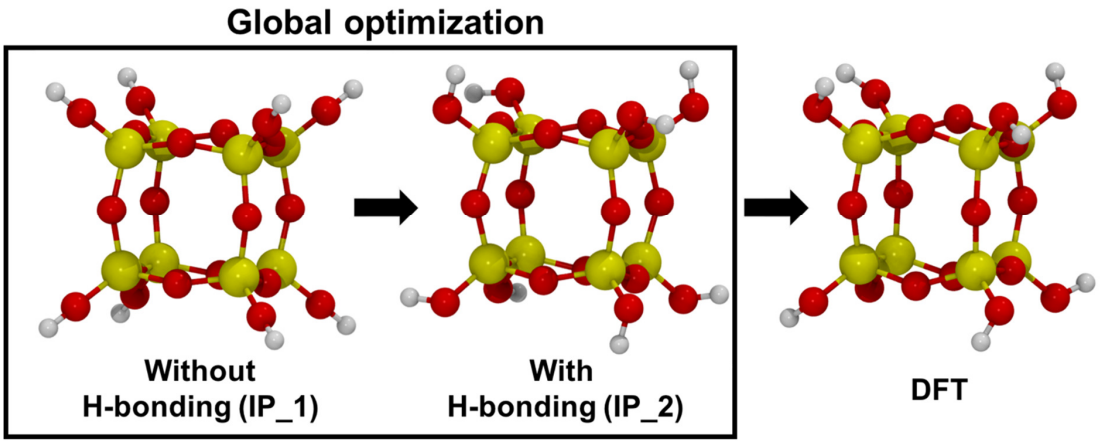

Fig. 1 Structures of a $(SiO_2)_8 \cdot (H_2O)_4$ nanocluster optimized with: IP_1 used in the first cascade step (left), IP_2 used in the second cascade step (middle), and DFT using B3LYP (right). Atom colour key: Si – yellow, Si, O – red, H – grey.

Results and Discussions

We first tested our cascade MCBH methodology on $(SiO_2)_8 \cdot (H_2O)_N$ systems with N = 2-5 incorporated water molecules as previously studied in refs [18] and [19]. Specifically, we consider the three most stable isomers we find for each series with those previously reported. In Fig. 2 we report isomers structures found both from this work and from refs [18] and [19].

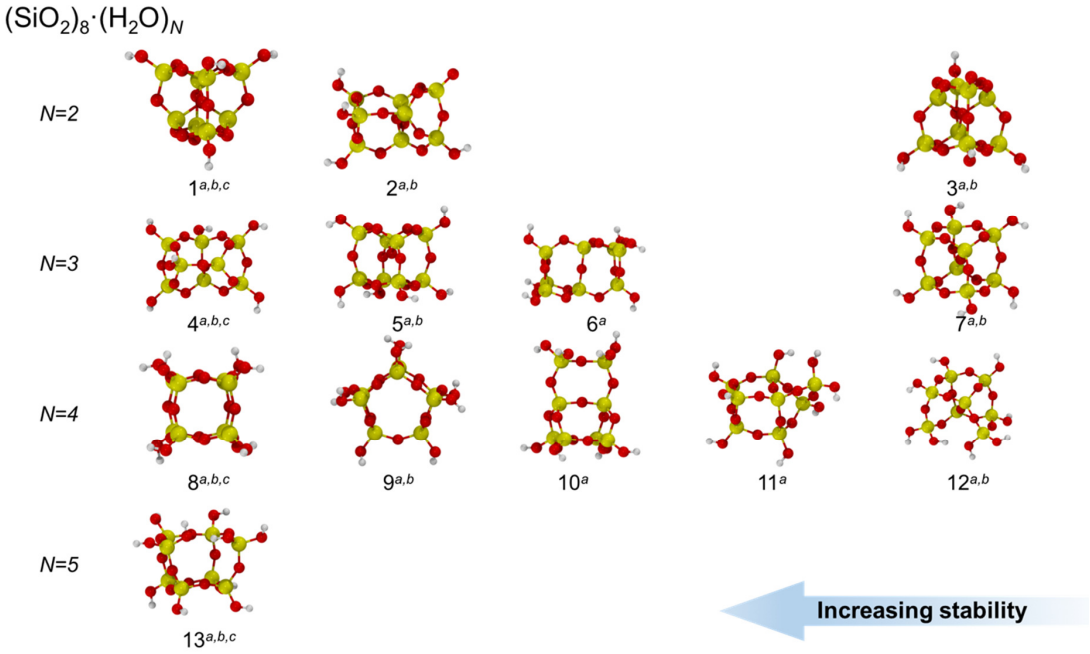

Fig. 2 Structures of $(SiO_2)_8 \cdot (H_2O)_N$ nanoclusters obtained in this work ([a]), ref [19] as ([b]) and in ref [18] as ([c]). Clusters for each N are ordered from left to right according to decreasing energetic stability. In parentheses energy differeneces with respect to the best global minimum candidate (far left of each row) are reported in kj/mol. Atom colour key: Si – yellow, Si, O – red, H – grey.

In our comparison we take all stable conformational isomers related to different H-bonding patterns of the hydroxyls on a single Si-O skeleton with a fixed connectivity to be representations of the same isomer. Typically, the total energy range due to different H-bonding patterns on the same isomer of this size is 1 - 10 kJ/mol. In all cases we report isomers with the lowest energy H-bonded pattern found. We note that although the first part of the cascade does not provide a correct description of H-bonding, in the second part of the cascade several H-bond patterns are sampled which ensures that the conformational space hydroxyl orientations is well explored. This part of the cascade is particularly important for relatively large and highly hydroxylated clusters where H-bonding can contribute a relatively large amount to total energy differences.

In the case of the most energetically stable structures for each N considered (i.e. Fig. 2, isomers 1, 4, 8 and 13) we found the same isomers as in previous works. This result further confirms these candidate structures as global minima. The second most stable isomers for each N (i.e. Fig. 2, isomers 2, 5 and 10) also confirm the corresponding results of refs [18] and [19]. For the third most stable isomers, for two incorporated water molecules (*N* = 2) we also found the previously reported isomer structures. Using the cascade method, however, we were able to find more energetically stable candidates for *N* = 3 (Fig. 2, isomer 6 being 3 kJ/mol lower than cluster 7) and *N* = 4 (isomers 14 and 22 kJ/mol lower than cluster 12). For *N* = 5 we confirm the global minimum candidate isomer structure and other low energy isomers are reported in literature.

After clearly demonstrating the capacity of our cascade MCBH approach for hydroxylated silica clusters for *M* = 8, we applied our method for to the, as yet unreported, systems: $(SiO_2)_M{\cdot}(H_2O)_N$ with *M* = 6, 10, 12, each for a range of N. The obtained new global minima candidate clusters are shown in figure 3. Low numbers of incorporated water (i.e. *N* = 1, 2) do not fully hydroxylate the one-coordinated defective oxygen centres present in anhydrous silica clusters. There are two types of singly-coordinated dangling oxygen defects: (i) oxygen atoms in silanone species (formally: >Si=O, but arguably more accurately: $>Si^{+}\text{-}O^{-}$ [35,36]) having three-coordinated Si-centres, and (ii) non-bridging oxygen (NBO) atoms accompanied with compensating triple coordinated oxygen-sites, also known a compensated NBOs or valence alternation pairs [37,38]. These defective centres are well studied in literature and it is known that they can readily be hydroxylated through reaction with water [4,11]. By increasing the number of incorporated water on an already fully hydroxylated cluster, bridging oxygens (Si-O-Si) are broken and the formation of silanols (Si-OH) occur until there is one -OH group for each Si-centre. Further hydroxylation tends to lead to the formation of geminal silanols (i.e. two OH groups per Si). The hydroxylation reaction (ΔE_{hyx}) energy:

$$\Delta E_{hyx} = E_{(SiO_2)_M(H_2O)_N} - (E_{(SiO_2)_M} + NE_{(H_2O)}) \quad (3)$$

indicates the relative stability of the hydroxylated structures with *N* incorporated water molecules with respect to the equivalent anhydrous silica system. This quantity indicates the tendency of anhydrous silica to be hydroxylated, in particular if ΔE_{hyx} is negative the reaction is energetically favourable. Although strictly speaking a thermodynamically favourable reaction is evaluated by the free energy difference, we neglect the entropic contributions and assume that ΔE_{hyx} a good indicator of reaction favourability.

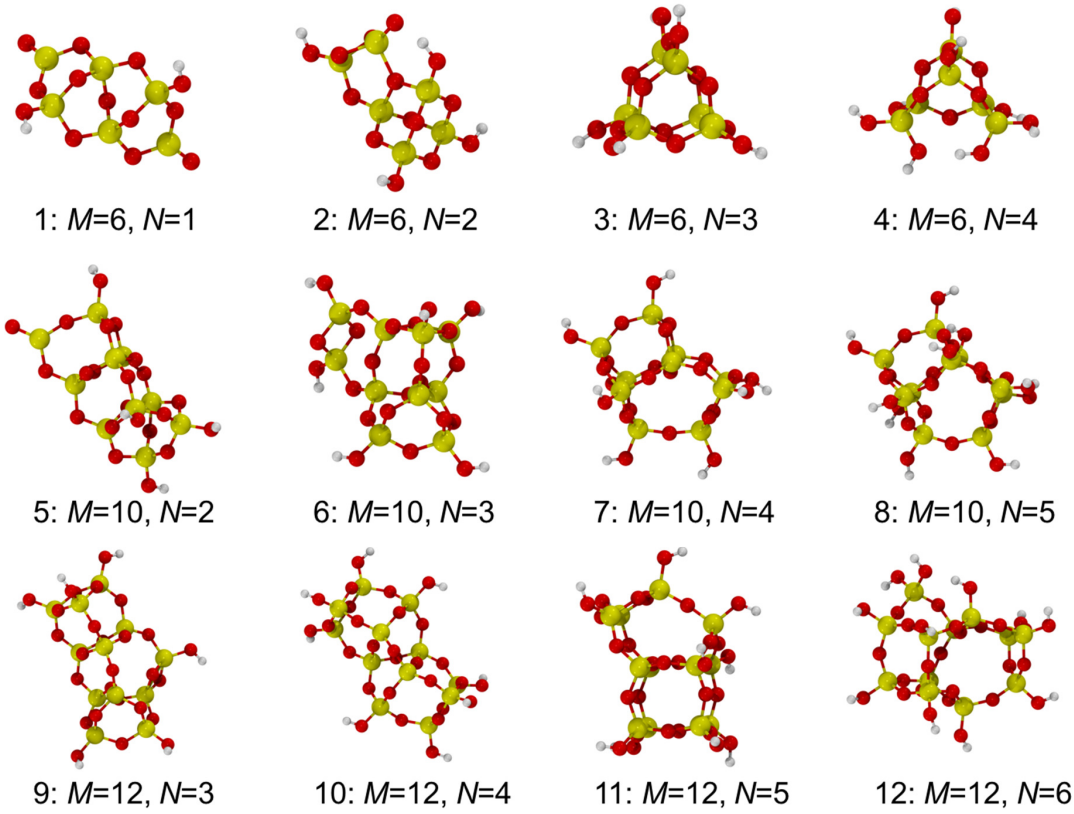

Fig. 3 The most energetically stable $(SiO_2)_M{\cdot}(H_2O)_N$ nanoclusters obtained in this work for M = 6, 10 and 12 silica units, each with a range of incorporated water molecule (N) corresponding to a degree of hydroxylation ($R_{N/M} = N/M$) between 17 - 67%. Atom colour key: Si – yellow, Si, O – red, H – grey.

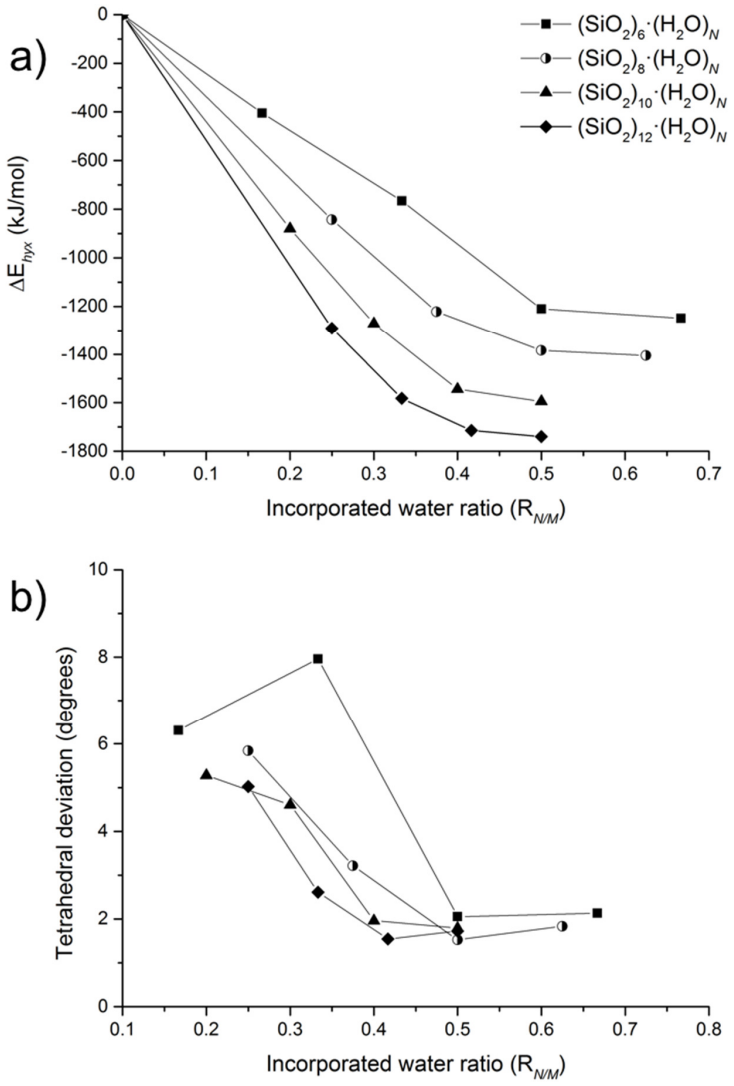

Fig. 4 a) Hydroxylation delta energy (ΔE_{hyx}) in kJ/mol relative to the correspondingly sized global minima $(SiO_2)_M\cdot(H_2O)_N$ clusters for M = 6, 8,10,12 with respect to incorporated water ratio ($R_{N/M}$). b) Deviations from the ideal silicon-centred tetrahedron (SiO_4) in degrees with respect to hydroxylation degree. Symbols for M = 8 shown as half filled circles are also reported in ref [17] and reproduced by us in this work.

In figure 4 we show hydroxylation energies (Fig. 4a) and Si-centred SiO_4 tetrahedral distortions (Fig. 4b) with respect to incorporated water ratio ($R_{N/M}$ = N/M) for the most stable $(SiO_2)_M\cdot(H_2O)_N$ candidates with M = 6, 8, 10, 12. The tetrahedral distortion is taken as the average of the differences between the root mean square of the six O-Si-O angles relative to optimal unstrained value of 109.47 for each SiO_4 centre. Generally, structures made mainly with rings containing more than three -(Si-O)- units are found to have low tetrahedral distortion.[39] Interestingly, several of the structures shown in Fig. 3, can be viewed as being generated from condensation of building blocks of smaller sized isomers. The most common building blocks observed, for instance, are the $(SiO_2)_6\cdot(H_2O)_3$ trigonal prism (Fig. 2: isomer 3), the $(SiO_2)_8\cdot(H_2O)_4$ cubic structure (Fig. 1: isomer 8 -

also known as a double 4-ring or D4R) and the pentagonal $(SiO_2)_8{\cdot}(H_2O)_4$ structure (Fig. 1: isomer 9). As the cluster size increase the most common building block becomes the D4R (e.g. see isomers 9 and 11 in Fig. 3) which only exhibits rings with low tetrahedral distortion. Larger isomers in other work also commonly exhibit the cubic $(SiO_2)_8{\cdot}(H_2O)_4$ D4R unit (e.g. $(SiO_2)_{24}{\cdot}(H_2O)_{12}$ in ref [18] which can be considered as a condensation of D4R units in triangular arrangement).

ΔE_{hyx} is found to be negative and monotonically decreasing with respect to the number of incorporated water molecules showing that the hydroxylation reaction of anhydrous silica is always energetically favoured. We also notice an energetic down shift with respect to *M* for the different *N* series, due to the increasing of the size of the system. The decreasing of ΔE_{hyx} in a series of *N* values for a fixed size *M*, can be split into the contribution by three factors: i) at a low number of incorporated water molecules, the gain in energy is mainly due to hydroxylation of the defective oxygen centres, ii) once a cluster is fully hydroxylated (defective centres are no longer present), ΔE_{hyx} drops because adding further water molecules helps to decrease the tetrahedral distortion of Si-centres (e.g. by hydrolysing small strained rings), iii) at a high number of incorporated water molecules there is a competition between two effects affecting ΔE_{hyx}: the formation of geminal silanols (energetically not favoured effect since O-Si is stronger a bond than O-H), and the formation of hydrogen bonds which is an energetically stabilizing effect. These latter two contributions in phase (iii) seem to be almost equivalent energetically, leading to the drop in ΔE_{hyx} tending to level off. The hydroxylation degree at the transition point between the ii) and the iii) phases can be regarded as the optimal hydroxylation degree ($R_{N/M}^{opt}$). In other words, ($R_{N/M}^{opt}$) is the $R_{N/M}$ value where the hydroxylation reaction energy first levels off to a flatter linear regime due to the minimum tetrahedral distortion being reached with increasing hydroxylation.

$R_{N/M}^{opt}$ was first introduced in ref [18] for systems with *M* = 4, 8, 16, 24. Specifically, $R_{N/M}^{opt}$ was tracked with respect to the number of SiO_2 units (*M*) in order to examine its size dependency. Herein we further add $R_{N/M}^{opt}$ values for the cluster sizes *M* = 6, 10, 12 silica sizes. To extract $R_{N/M}^{opt}$ values for each $(SiO_2)_M$ series we choose the $R_{N/M}$ value that correspond to the cluster with the lowest tetrahedral distortion which is consistent with choice made in ref [18]. The selected $R_{N/M}^{opt}$ values for clusters with *M* = 6, 10, 12 correspond respectively to structures 3, 8, 11 in figure 3. Although the choice of $R_{N/M}^{opt}$ = 0.5 for the set of $(SiO_2)_{10}{\cdot}(H_2O)_N$ clusters is consistent with the $R_{N/M}$ value that lowers the tetrahedral distortion most, we notice that the $R_{N/M}$ value where tetrahedral distortion levels off (i.e. 0.4) would be likewise acceptable.

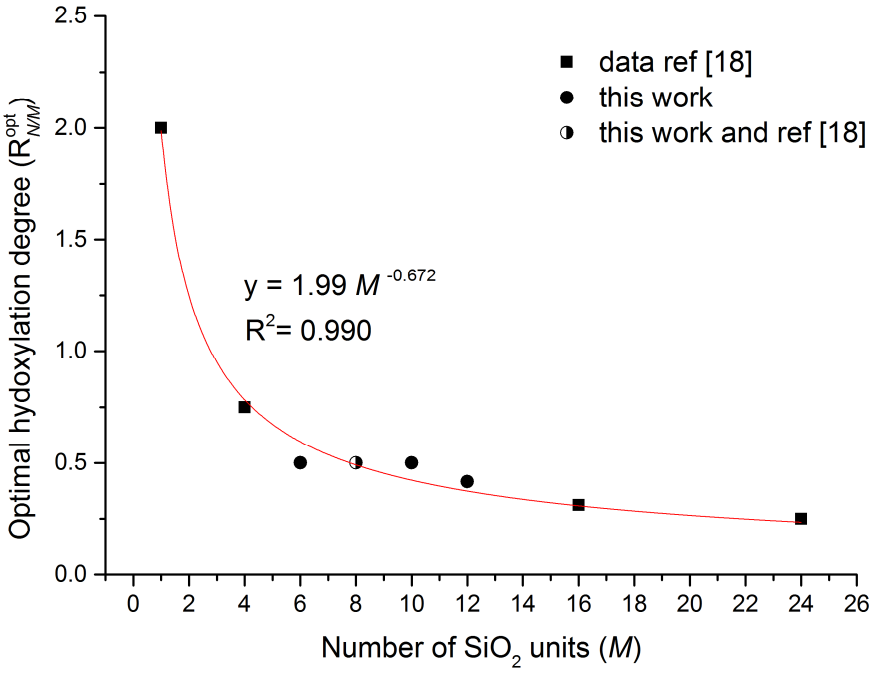

Fig. 5 Data for optimal hydroxylation degree ($R_{N/M}^{opt}$) with respect to cluster size fitted with an inverse power law. Black filled square symbols correspond to data from ref [18].

$R_{N/M}^{opt}$ with respect to the number of SiO_2 units (*M*) is shown in Fig. 5 with data from ref [18] in black filled squares and data from this work in black filled circles. The half-filled circle correspond to the $(SiO_2)_8{\cdot}(H_2O)_N$ set both studied previously and used in this work as test case. The first point of the series (*M* = 1) corresponds orthosilicic acid ($Si(OH)_4$) where $R_{N/M}^{opt} = 2$. $R_{N/M}^{opt}$ is higher for smaller clusters and drop as the size increases and tends to follow an inverse power law. The new data generated in this work (*M* = 6, 10, 12) do not bring to significant changes in the power law equation in ref [18] and confirm the $R_{N/M}^{opt}$ size dependency trend. Interestingly, the exponent of the inverse power law is close to -2/3 while the general size dependency of many properties of a generic nanoparticles scale with a inverse power law but with an exponent of -1/3.[40] Generally, the -1/3 exponent derives from the surface-to-volume ration assuming a spherical nanoparticle shape. For a generic property size dependency, we expect a small deviation in the exponent from -1/3 due non-spherical shape of real structures and possibility due to property fluctuations for their extreme dependency on small changes when systems are relatively small. Nevertheless, the -2/3 exponent in $R_{N/M}^{opt}$ size dependency seems to be affected by some unknown factors for such deviation from -1/3 that we hope to elucidate in future works.

Conclusions

In this work we present a methodology for performing IP-DFT basing hopping global optimization studies on systems such as hydroxylated silica clusters where using an accurate IPs is essential to

correctly describe hydrogen bonds. For the $(SiO_2)_8{\cdot}(H_2O)_N$ test case, the cascade approach finds all previously reported isomers (including global minima candidates) and additionally finds three new low energy isomers. New global minima candidate structures are generated for $(SiO_2)_M{\cdot}(H_2O)_N$ systems with M = 6, 10 and 12, each for a range of N values. The hydroxylation reaction energy trends for these series are consistent with previous works on other cluster sizes. The hydroxylation degree shows a threshold in each case when the hydroxylation-induced structural transformations minimises the tetrahedral distortion around the SiO_4 centres. At this optimal hydroxylation ($R_{N/M}^{opt}$) point the reaction energy starts to level off to a constant value. Confirming previously reported results for other cluster sizes[18], we confirm that the size (M) dependence of $R_{N/M}^{opt}$ follows an inverse power law with an exponent close to -2/3. Generally, the cascade approach we develop enables for the efficient global optimisation of systems which require treatment via complex forcefields.

Acknowledgements

Support from Spanish MINECO/FEDER grant CTQ2015-64618-R grant and, in part, by Generalitat de Catalunya grants 2014SGR97, XRQTC is acknowledged. We also acknowledge the NOMAD Center of Excellence project (this project has received funding from the European Union's Horizon 2020 research and innovation programme under grant agreement No 676580). Access to supercomputer resources was provided through grants from the Red Española de Supercomputación. We acknowledge funding from H2020 project ITN-EJD-642294 (TCCM: Theoretical Chemistry and Computational Modelling). We also thank Ask Hjorth Larsen for technical advice concerning the Atomic Simulation Environment.

References

[1] P. Aggarwal, R. Pratap Singh, Y. Aggarwal, Use of nano-silica in cement based materials — A review, Cogent Engineering 2 (2015) 1078018(1-11).
[2] S. Zhoua, L. Wu, J. Suna, W. Shen, The change of the properties of acrylic-based polyurethane via addition of nano-silica, Progress in Organic Coatings 45 (2002) 33–42.
[3] M. Qu, J. S. Meth, G. S. Blackman, G. M. Cohen, K. G. Sharp, K. J. Van Vliet, Tailoring and probing particle–polymer interactions in PMMA/silica nanocomposites, Soft Matter 7 (2011) 8401-8408.
[4] L. T. Zhuravlev, The surface chemistry of amorphous silica. Zhuravlev model, Colloids and Surfaces A: Physicochemical and Engineering Aspects 173 (2000) 1–38.
[5] C. S. Cundya, P. A. Cox, The hydrothermal synthesis of zeolites: Precursors, intermediates and reaction mechanism, Microporous and Mesoporous Materials 82 (2005) 1–78.
[6] D. J. Belton, O. Deschaume, C. C. Perry, An overview of the fundamentals of the chemistry of silica with relevance to biosilicification and technological advances, FEBS Journal 279 (2012) 1710–1720
[7] P. Chandra, D. S. Doke, S. B. Umbarkar, K. Vank, A. V. Biradar, Silica microspheres containing high density surface hydroxyl groups as efficient epoxidation catalysts, RSC Adv. 5 (2015) 21125-21131.
[8] Y. Wang, M. Y. He and R. Y. Chen, Fabrication of mechanically robust antireflective films using silica nanoparticles with enhanced surface hydroxyl groups, J. Mater. Chem. A 3 (2015) 1609-1618.
[9] A. Marucco, F. Turci, L. O'Neill, H. J. Byrne, B. Fubini, I. Fenoglio, Hydroxyl density affects the interaction of fibrinogen with silica nanoparticles at physiological concentration, Journal of Colloid and Interface Science 419 (2014) 86–94.
[10] H. Zhang, D. R. Dunphy, X. Jiang, H. Meng, B. Sun, D. Tarn, M. Xue, X. Wang, S. Lin, Z. Ji, R. Li, F. L. Garcia, J. Yang, M. L. Kirk, T. Xia, J. I. Zink, A. Nel, C. J. Brinker, Processing Pathway Dependence of Amorphous Silica Nanoparticle Toxicity: Colloidal vs Pyrolytic, J. Am. Chem. Soc. 134 (2012) 15790–15804.

[11] J. Yang, E.G. Wang, Reaction of water on silica surfaces, Current Opinion in Solid State and Materials Science 10 (2006) 33–39.
[12] M. J. Mora-Fonz, C. R. A. Catlow, D. W. Lewis, Oligomerization and Cyclization Processes in the Nucleation of Microporous Silicas, Angew. Chem. Int. Ed. 44 (2005) 3082 –3086.
[13] T. T. Trinh, Antonius P. J. Jansen, R. A. van Santen, Mechanism of Oligomerization Reactions of Silica, J. Phys. Chem. B, 110 (2006) 23099-23106.
[14] D. Makimura, C. Metin, T. Kabashima, T. Matsuoka, Q. P. Nguyen, C. R. Miranda, Combined modeling and experimental studies of hydroxylated silica nanoparticles, J. Mater. Sci. 45 (2010) 5084-5088.
[15] J. Yeon, A.C.T. van Duin, ReaxFF Molecular Dynamics Simulations of Hydroxylation Kinetics for Amorphous and Nano-Silica Structure, and Its Relations with Atomic Strain Energy, J. Phys. Chem. C 120 (2016) 305-3017.
[16] S. Bhattacharya, J. Kieffer, Molecular Dynamics Simulation Study of Growth Regimes during Polycondensation of Silicic Acid: from Silica Nanoparticles to Porous Gels, J. Phys. Chem. C 112 (2008) 1764-1771.
[17] S. T. Bromley, E. Flikkema, Novel structures and energy spectra of hydroxylated $(SiO_2)_8$-based clusters: searching for the magic $(SiO_2)_8O_2H_3$ cluster, J. Chem. Phys., 122, (2005) 114303/1-114303/5.
[18] K.E. Jelfs, E. Flikkema, S.T. Bromley, Hydroxylation of silica nanoclusters $(SiO_2)_M(H_2O)_N$, M = 4, 8, 16, 24: stability and structural trends, Phys. Chem. Chem. Phys. 15 (2013) 20438-20443.
[19] E. Flikkema, K.E. Jelfs, S. T. Bromley, Structure and energetics of hydroxylated silica clusters, $(SiO_2)_M(H_2O)_N$, M = 8, 16 and N= 1 – 4: A global optimisation study, Chem. Phys. Lett. 554 (2012) 117-122.
[20] Evidence for atomic mixing via multiple intermediates during the dynamic interconversion of silicate oligomers in solution, K. E. Jelfs, E. Flikkema, S. T. Bromley, Chem. Comm. 48 (2012) 46-48.
[21] D. J. Wales, J. P. K. Doye, J. Phys. Chem. A 1997, 101, 5111.
[22] N. Metropolis, A.W. Rosenbluth, M.N. Rosenbluth. A.H. Teller and E. Teller, Equation of State Calculations by Fast Computing Machines, J. Chem. Phys. 21 (1953) 1087-1092.
[23] J.D. Gale, GULP: A computer program for the symmetry-adapted simulation of solids, J. Chem. Soc., Faraday Trans. 93 (1997) 629-637.
[24] S. R. Bahn, K. W. Jacobsen, An object-oriented scripting interface to a legacy electronic structure code, Comput. Sci. Eng. 4 (2002) 56-66.
[25] S. Tsuneyuki, M. Tsukada, H. Aoki, Y. Matsui, First-Principles Interatomic Potential of Silica Applied to Molecular Dynamics, Phys. Rev. Lett. 61 (1988) 869-872.
[26] B. van Beest, G. Kramer, R. van Santen, Force fields for silicas and aluminophosphates based on ab initio calculations, Phys. Rev. Lett. 64 (1990) 1955-1958.
[27] A. Hassanali, S. J. Singer, J. Phys. Chem. B 2007, 111, 11181.
[28] E. Flikkema, S.T. Bromley, A new interatomic potential for nanoscale silica, Chem. Phys. Lett. 378 (2003) 622-629.
[29] A. Pedone, G. Malavasi, M.C. Menziani, U. Segre, F. Musso, M. Corno, B. Civalleri, P. Ugliengo, FFSiOH: a New Force Field for Silica Polymorphs and Their Hydroxylated Surfaces Based on Periodic B3LYP Calculations, Chem. Mater. 20 (2008) 2522-2531.
[30] A. Maciá, S. T. Bromley, in preparation.
[31] V. Blum, R. Gehrke, F. Hanke, P. Havu, V. Havu, X. Ren, K. Reuter, M. Scheffler, Phys. Commun., 180 (2009) 2175–2196.
[32] A.D. Becke, Density-functional thermochemistry. III. The role of exact exchange, J. Phys. Chem. 98 (1993) 5648-5652.
[33] M. Delle Piane, M. Corno, A. Pedone, R. Dovesi, P. Ugliengo, Large-Scale B3LYP Simulations of Ibuprofen Adsorbed in MCM-41 Mesoporous Silica as Drug Delivery System, J. Phys. Chem. C 118 (2014) 26737-26749.
[34] A. Rimola, D. Costa, M. Sodupe, J. Lambert, P. Ugliengo, Silica Surface Features and Their Role in the Adsorption of Biomolecules: Computational Modeling and Experiments, Chem. Rev. 113 (2013) 4216-4313.
[35] V.G. Avakyan, V.F. Sidorkin, E.F. Belogolova, S.L. Guselnikov, L.E. Guselnikov, AIM and ELF electronic structure/G2 and G3 π-bond energy relationship for doubly bonded silicon species, H2Si=X (X=E14H2, E15H, E16), Organometallics 25 (2006) 6007–6013.
[36] M. A. Zwijnenburg, A. A. Sokol, C. Sousa, S. T. Bromley, The effect of local environment on photoluminescence: A time-dependent density functional theory study of silanone groups on the surface of silica nanostructures, J. Chem. Phys., 2009, 131, 034705.
[37] S. Hamad and S. T. Bromley, Low reactivity of non-bridging oxygen defects on stoichiometric silica surfaces, Chem. Commun. (2008) 4156-4158.

[38] M. A. Zwijnenburg, F. Illas, S. T. Bromley, Long range coupling between defect centres in inorganic nanostructures: Valence alternation pairs in nanoscale silica, J. Chem. Phys. 137 (2012) 154313
[39] S. T. Bromley, I. de P. R. Moreira, F. Illas, J. C. Wojdeł, Importance of the embedding environment on the strain within small rings in siliceous materials, Phys. Rev. B 73 (2006) 134202.
[40] R.L. Johnston, Atomic and Molecular Clusters, Taylor & Francis, London and New York, 2002.

Dissociative water adsorption on TiO_2 and SiO_2 nanoclusters: dependence on temperature and water vapour pressure

Andi Cuko[1,2], Antoni Macià Escatllar[1], Monica Calatayud[2,*], Stefan T. Bromley[1,3,*]

[1] *Departament de Ciència de Materials i Química Física & Institut de Química Teòrica i Computacional (IQTCUB), Universitat de Barcelona, E-08028 Barcelona, Spain*

[2] *Sorbonne Universités, UPMC Univ Paris 06, CNRS, Laboratoire de Chimie Théorique CC 137 - 4, place Jussieu F. 75252 PARIS CEDEX 05 - France*

[3] *Institució Catalana de Recerca i Estudis Avançats (ICREA), E-08010 Barcelona, Spain*

* Corresponding authors: s.bromley@ub.edu, calatayu@lct.jussieu.fr

Introduction

Nanoparticles of titania (TiO_2) and silica (SiO_2) are two of the most massively produced nanomaterials in the world.[1] Nano-TiO_2 and nano-SiO_2 are both widely used as fillers to improve the properties of materials, whereby the former typically imparts enhanced (photo)electroactive properties and the latter increased resistance and visible light transmittance (e.g. proton conducting electrolytes,[2] photo-resistive rubbers,[3] pollutant-degrading durable mortars[4]). This synergy has also led to a number of mixed-oxide titanosilicate nanomaterials with applications in (photo)catalysis,[5] water remediation,[6] and self-cleaning.[7] In all the above applications, the nano-TiO_2 and nano-SiO_2 components typically, and often deliberately, come into contact with water-containing environments. Understanding and controlling such interactions is thus essential for optimising the performance of these systems. The aqueous chemistry of nano-SiO_2 and nano-TiO_2 is also important for understanding the bottom-up solution syntheses of nanoporous silicates[8] and TiO_2-based nanomaterials[9] and the possible eco-toxicity of these species.[10] Many studies have specifically focussed on the interaction of water with nano-TiO_2 due to the potential these systems for fuel production through photo-dissociative water splitting.[11] A number of recent theoretical studies have used top-down bulk cut nanoparticles containing 10s - 1000s of atoms in order to investigate the electronic properties of nano-TiO_2 photocatalysts[12,13,14,15] and their interactions with water.[16,17,18,19,20,21] Although such calculations can provide important new insights, in most cases the nanoparticles used are still relatively small and idealised model systems as compared to experiments where larger and more complex nanoparticles are typically used. Detailed spectroscopic experiments probing the interaction of water with small oxide (i.e. ~10-30 atoms) systems have tended to focus on hydroxylated silica (e.g. ^{29}Si NMR spectroscopy[22,23,24] and mass spectroscopy[25]). As such there are a number of theoretical studies proposing corresponding structures for small $(SiO_2)_M(H_2O)_N$ species with M=2-4[26,27,28] and their oligomerisation reactions.[27,29,30] Recently, cluster beam experiments reported infrared (IR) photodissociation spectra for gas phase $[(TiO_2)_M(D_2O)_N]^-$ for M=2-4 and N=1-3.[31] Here, direct comparison of the experimental IR spectra with theoretically calculated IR spectra from low energy cluster isomers was used to assign structures to the experimental clusters. Here the assignments were only possible due to cluster structures being available from global optimisation searches.[32] The use of global optimisation provides a means to find stable structures of small nanoclusters that are generally unlike regular cuts from bulk crystals and are very sensitive to size.[33] Herein, following our previous theoretical work on anhydrous SiO_2,[34,35,36] TiO_2[37], and TiO_2-SiO_2[38] nanoclusters and hydroxylated SiO_2[39,40,41] nanoclusters, we use global optimisation to provide detailed bottom-up insights into the structures and stabilities of $(TiO_2)_M(H_2O)_N$ nanoclusters with

sizes from M = 4 - 16 and N/M ratios of ≥ 0.5 (i.e. up to 62 atoms). We compare the obtained structures with the corresponding global minima $(SiO_2)_M(H_2O)_N$ nanoclusters. Further, we calculate how the free energies of both $(TiO_2)_M(H_2O)_N$ and $(SiO_2)_M(H_2O)_N$ nanoclusters depend on size, degree of hydroxylation, temperature and water vapour pressure. In this way we provide an unprecedented detailed comparison between nano-TiO_2 and nano-SiO_2 with respect to how they interact with water, while bridging the gap between very small molecular species and bulk-like nanoparticles for these important hydrated nano-oxide systems.

Methodology

Global optimization of $(TiO_2)_M(H_2O)_N$ systems

In this study we apply Monte Carlo Basin Hopping (MCBH) for exploring the potential energy surface (PES) of hydroxylated $(TiO_2)_M(H_2O)_N$ nanoclusters. This global optimisation methodology consists of repeated steps whereby in each step random structural distortions are applied to a cluster followed by optimisation of the cluster structure to a local energy minimum on the PES. The Metropolis criterion is applied after each step to decide whether or not to accept the new minimum energy structure. This is a probabilistic criterion which depends on the simulation temperature and the energy difference between the present cluster structure and the previously accepted cluster. An accepted cluster is used as initial structure in the following step. In each step, we use interatomic potentials (IPs) for the structural optimisation. The IPs we use are empirical functions that provide a computationally efficient means to evaluate the relationship between structure and energy. Although the IP-MCBH approach is a very effective means to quickly assess many low energy minima on the PES, the IP can only provide a reasonable estimate of energetic stability of any cluster structure. In order to refine the accuracy of our predictions we selected a set of low energy structures from each global optimisation run which were then fully optimised used density functional theory (DFT) based calculations (see details below). We have successfully applied this method in several previous studies, often finding new improved global minima candidates with respect to other reported cluster isomers.[34,35,37,38,39,40]

The choice of the IP plays an important role in determining the accuracy of predicting the structure of low energy clusters. For titania-water systems, although there are a number of empirical IPs available in literature,[42,43,44,45] such IPs are parameterized for bulk titania and were found to be inappropriate for finding low energy nanoclusters in which the coordination of Ti cations ranges from 4 to 6. Therefore in order to have an IP suitable for global optimisation of $(TiO_2)_M(H_2O)_N$

nanoclusters we constructed a new IP. Due to the structural similarities between globally optimized nanoclusters of bare silica and titania,[38] we based our IP on a well-established silica IP for hydroxylated silica systems (FFSiOH).[46] In particular, we have previously shown that FFSiOH is very effective in accurately predicting low energy structures and stabilities of hydroxylated silica nanoclusters.[40,47,48]

In order to provide relevant data to fit our new IP we first select global minima candidates of anhydrous $(TiO_2)_n$ from our previous work[37] with sizes between n = 4 - 14. All the clusters were then manually hydrated by adding molecular water in a dissociative way for low degrees of hydration and via molecularly adsorbed water for highly hydrated clusters. For each cluster we then ran DFT-based *ab initio* molecular dynamics (AIMD) for 3 ps at 300 K employing the PBE functional[49] with a light/tier-1 basis of numerical atom-centred basis functions employing the FHI-AIMS code.[50] In this way we produced a large and varied training set of structures for fitting the parameters of our IP. By adapting the original FFSiOH parameters to reproduce the radial distribution functions of the AIMD runs we produced a new parameterisation which we refer to as FFTiOH. Using this IP in the MCBH runs, we found that it was often difficult to optimise randomly distorted geometries when large core-shell separations occurred. To overcome this issue, we generated a simpler version of FFTiOH where core-shell polarizable ions are removed and the O-H interaction is fitted to a Buckingham potential to mimic as much as possible the original Morse potential. We refer to this modified version as FFTiOH*. To overcome bias of using a single IP in the MCBH global optimisation procedure we also slightly increased the O-O repulsion in FFTiOH* to generate FFTiOH*-mod. The use of FFTiOH*-mod generates slightly more open cluster structures allowing the MCBH searches to explore PES regions not accessible with only FFSTiOH*. The full set of parameters for FFTiOH, FFTiOH* and FFTiOH*-mod are provided in the ESI.

We used the MCBH runs to globally optimise $(TiO_2)_M(H_2O)_N$ clusters with M = 4, 8, 12 and 16 and for each M respectively N = 1 - 4, 1 - 5, 1 - 6 and 1 - 8. A typical MCBH run employed either FFTiOH* or FFTiOH*-mod for 20000-100000 steps depending on the system size. Our MCBH algorithm uses the Atomic Simulation Environment (ASE)[51] for manipulating structures and the GULP[52] code for structural optimisations. During the MCBH procedure the temperature is dynamically adapted to maintain the ratio of accepted steps close to 65%. The MCBH procedure was repeated a number of times for each distinct cluster $(TiO_2)_M(H_2O)_N$ stoichiometry using both FFTiOH* and FFTiOH*-mod to better ensure a thorough search of the respective PES. We note that our MCBH searches were further extended by data mining from hydrated silica nanoclusters from our previous works.[39,40,41]

From each MCBH run a selection of isomers were optimised using progressively more accurate methods. Firstly, the 200-500 lowest energy cluster isomers optimised using FFTiOH* and FFTiOH*-mod during each MCBH run were first post-optimised optimized with FFTiOH. Afterwards, between 50 and 150 (depending on the system size) of the energetically lowest lying structures were fully optimized with DFT based calculations using the PBE functional and a tier1/light numeric atom-centred orbital basis set. Then, all cluster isomers within 0.5 eV of the energetically lowest PBE-optimised structure were further optimized using the PBE0[53] functional and a tier1/tight basis. All DFT based calculations were performed with FHI-AIMS package.[50] Generally, the higher the hydration degree and/or the system size the higher the number of structures were optimized using DFT because of the correspondingly higher density of distinct cluster structures with respect to energy.

Energetics of hydration

As discussed above, both nano-TiO_2 and nano-SiO_2 are prone to incorporate water which we can formally write as

$$(XO_2)_M + (H_2O)_N \rightleftarrows (XO_2)_M \cdot (H_2O)_N \qquad \text{(eq 2.1)}$$

Where X is the cation (i.e. Si, Ti), N and M are respectively the number of in-cluster incorporated waters and the number of formal oxide units. The first measure of stability of water incorporation can be assessed by calculating the energy change for each hydration step, which is known to be system size dependent. Using the lowest energy $(TiO_2)_M(H_2O)_N$ structures for each degree of hydration ($R_{N/M}$ = *N/M*) for any single system size (M) we can calculate the energy change upon hydration with relative to the respective anhydrous bare $(TiO_2)_M$ cluster via

$$\Delta E_{Hyd} = E_{(XO_2)_M(H_2O)_N} - E_{(XO_2)_M} - NE_{H_2O} \qquad \text{(eq 2.2)}$$

where $E_{(XO_2)_M(H_2O)_N}$ and $E_{(XO_2)_M}$ are the energies of hydrated and anhydrous nanoclusters respectively, and E_{H_2O} is the energy of the water molecule. ΔE_{Hyd} provides the energetic strength of the interactions between water and silica/titania for each size considered. A negative ΔE_{Hyd} indicates thermodynamic favorability of cluster hydration and *vice versa*. However, for a better estimation of thermodynamic (un-)favourability, free energies must be considered. With statistical thermodynamics we can estimate free energies entirely from first principle calculations through the

partition function of the system. The partition function for N non-interacting indistinguishable particles is defined as:

$$Q(N,V,T) = \frac{[q(V,T)]^N}{N!} \quad \text{(eq 2.3)}$$

where $q(V,T)$ is the molecular partition function and *N* is the number of particles in the system.

$$q(V,T) = q_{trans}(V,T)\, q_{rot}(T) q_{vib}(T) q_{sym}(T) q_{elec}(T)\, q_{nuc} \quad \text{(eq 2.4)}$$

From the partition function, we can calculate the free energy as:

$$G(T) = -k_B T ln\big(q(V,T)\big) + pV \simeq F(V,T)^{trans} + F(T)^{rot} + F(T)^{vib} + F(T)^{sym} + E^{DFT}$$

$$F(V,T)^{trans} = -\frac{3}{2} k_B T ln\left(\frac{2\pi m k_B T}{h^2}\right) - k_B T ln(V)$$

$$F(T)^{rot} = -k_B T ln\left[8\pi^2 \left(\frac{2\pi k_B T}{h^2}\right)^{\frac{3}{2}}\right] + \frac{1}{2} k_B T ln\big(I_x I_y I_z\big)$$

$$F(T)^{vib} = \sum_i \frac{h\nu_i}{2} + \sum_i k_B T ln\left[1 - exp\left(-\frac{h\nu_i}{k_B T}\right)\right]$$

$$F(T)^{sym} = k_B T ln(\sigma) \quad \text{(eq 2.5)}$$

where m is the system total mass, $I_{x,y,z}$ are the system inertial moments along the x, y and z axes, ν_i are the harmonic vibrational frequencies and σ is the symmetry number. Frequency rotational contributions are calculated within the harmonic and rigid rotor approximations respectively. All systems are treated as ideal gases. Symmetry contributions should formally be considered in order to avoid over-counting the number of possible states. However, for the hydrated systems the presence of hydroxyl groups usually breaks any symmetry and even for the highest symmetric anhydrous systems effect of symmetry has an almost negligible effect on the cluster free energies.

Considering nanoparticles to be in equilibrium with water vapour, the actual degree of hydration of a system will depend on the experimental temperature and water vapour pressure conditions. In a gas-phase hydration reaction, the free energy of the process is described as:

$$\Delta G_{hyd}(T,P) = G_{(XO_2)_M(H_2O)_N]}(T) - G_{(XO_2)_M}(T) - N\mu_{H_2O}(T,P) \quad \text{(eq 2.6)}$$

where $\mu_{H_2O}(T,P)$ is the water chemical potential in equilibrium with the clusters dependent on temperature T and water vapour partial pressure P. Both clusters free energies and the water

chemical potential can be computed from *ab initio* data by means of statistical thermodynamics as shown in equation 2.5. The water vapour partial pressure dependency arises from $-k_B T ln(V)$ term which can be written, according to the ideal gas law, as $-k_B T ln(k_B T/P)$. The same term, in the cluster case can be omitted because the reference volume cancels out since we consider differences in free energy. All quantities were calculated using DFT based calculations using the PBE0 functional and using tier1/tight numerical basis set. Harmonic frequencies were calculated by the finite difference method using a displacement of 0.0025 Å for each degree of freedom.

Results and Discussion

In the following, we provide a detailed comparison of structures and thermodynamical stability of known and globally optimized hydrated titania and hydrated silica nanoclusters.

Structures of the hydrated nanoclusters

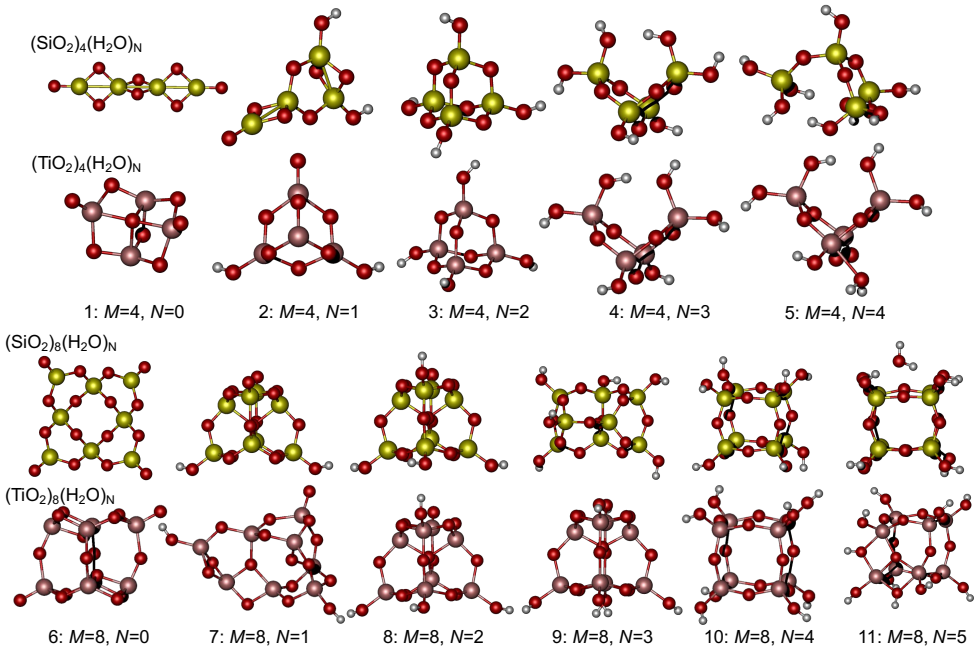

Figure 1. Global optimized $(TiO_2)_M(H_2O)_N$ and $(SiO_2)_M(H_2O)_N$ clusters for M = 4 and 8. Numbers in the cluster labels show M, the number of XO2 units, and N, the number of water molecules incorporated in the cluster. $(SiO_2)_M(H_2O)_N$ clusters are obtained from ref [36,39,40] except the M=8, N=5 which was found in this strudy.

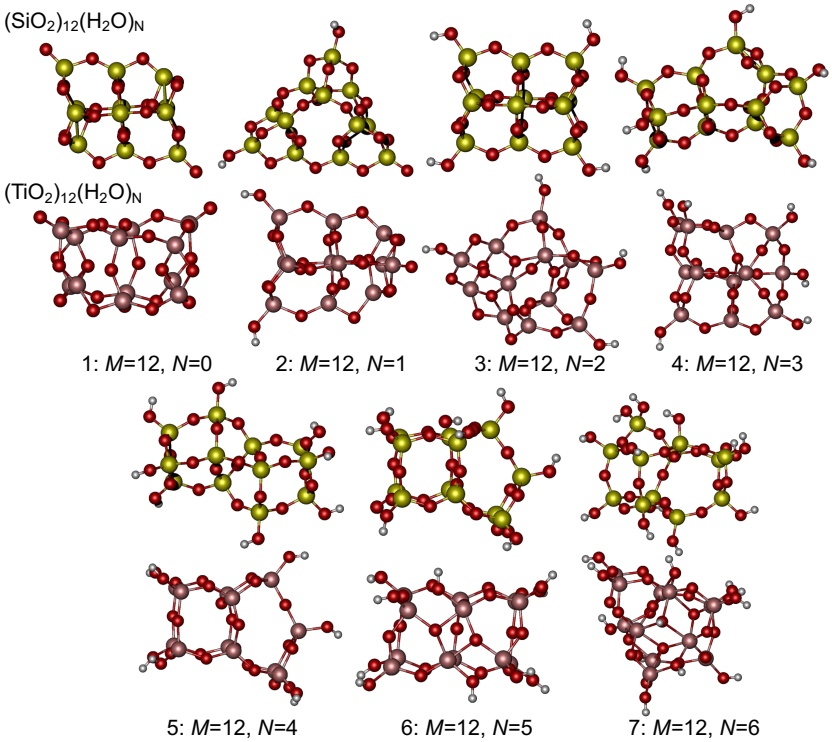

Figure 2. Global optimized $(TiO_2)_M(H_2O)_N$ and $(SiO_2)_M(H_2O)_N$ clusters for M = 12. Numbers in the cluster labels show M, the number of XO2 units, and N, the number of water molecules incorporated in the cluster. $(SiO_2)_M(H_2O)_N$ clusters with N=3-6 are obtained from ref [41] while systems with N=1, 2 are generated applying exactly the same methodology as in ref [41].

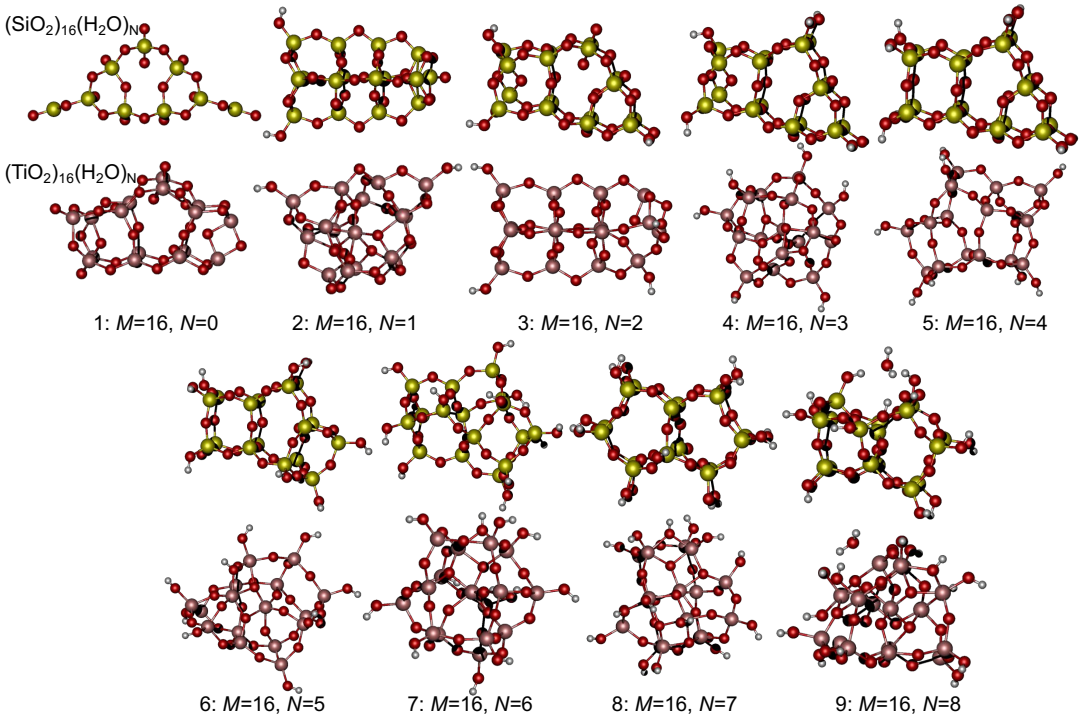

Figure 3. Global optimized $(TiO_2)_M(H_2O)_N$ and $(SiO_2)_M(H_2O)_N$ clusters for M = 16. Numbers in the cluster labels show M, the number of XO2 units, and N, the number of water molecules incorporated in the cluster. $(SiO_2)_M(H_2O)_N$ clusters are obtained from ref [36,39,40].

Both crystalline bulk SiO_2 and TiO_2 have very low solubility in water but both can dissociatively adsorb water on their surfaces. Amorphous phases and nanoclusters more readily absorb dissociated water due to the presence of reactive surface defects such as Non Bridging Oxygens (NBOs), strained rings of different sizes, or terminal O-atoms.[54,55,56,57] Hydration of bare SiO_2 nanoparticles proceeds by saturating the oxygen defective sites first, as they are the most unstable defects. Depending on system size, 1 (for the large particle sizes M=12 and 16) or 2 (for the small particle sizes M=4, M=8) water molecules are enough to fully saturate surface defects on clusters. Further incorporation of water molecules leads to hydroxylation of silicon atoms until each silicon has one hydroxyl group forming cage-like nanoparticles. An even further inclusion of water leads to the formation of geminal silanol groups which tends to open up the cage-like structure. The limit of this behaviour is the complete dissolution of each silicon atom to generate silicic acid ($Si(OH)_4$).

Hydration of titania is similar to silica nanocluster at low hydration degree and small cluster size. As in silica, depending on the system size, 1 or 2 incorporated water molecules are enough to fully hydroxylate the cluster. With further hydration titania also generates cage-like structures, in some cases even identical to silica (i.e. M=4, N=2 and M=8, N=4). For relatively high hydration degrees, titania and silica systems are no longer similar. Titania is able to over coordinate (i.e. Ti atoms can be 4-, 5- and 6-coordinated) and therefore adsorb molecular water without breaking its -Ti-O- network. This is due to the d orbitals in titanium centers which can participate in a dative bond with waters lone pairs (i.e. M=4, N=4). Indeed, highly hydroxylated titania systems, especially those with M=16, become more compact and bulk-like with 6-coordinated Ti atoms in the center of the particle. Further addition of water causes the hydroxylation of intra-network NBOs (i.e. titania systems with M=16 and N<5) still without disruption on the Ti-O network. As an example to show such flexibility of TiO_2 nanoclusters in Fig 4 we report few isomers for M=4, 8 and N=4 systems. Here for systems M=4 the structure prefers to be in an open cage with one water molecule adsorbed (Fig 4: 1) rather than in close cage with two water molecules adsorbed (Fig 4: 2). In the case of M=8 systems, contrary to silica counterpart, the TiO_2 nanocluster with N=4 prefers to maintain the cube like structure and adsorbing water in a dissociative (Fig 4: 3) way rather than in a molecular way (Fig 4: 4) by over 0.1 eV. The opening of the cube-like structure which in SiO_2 systems is preferred, here has an energetic cost of 0.4 eV in total energy.

For M=4, the first two water additions heal the terminal oxygens. Both $(TiO_2)_4(H_2O)_2$ and $(SiO_2)_4(H_2O)_2$ structures are topologically the same, containing the 6-member ring. The 6-member ring contains some strain on it in SiO_2, and therefore the water addition causes the opening of the structure. With N=3, the structure still contains this 6-member ring, and a further addition also causes the opening of this ring, creating a very extended structure. The $(TiO_2)_4(H_2O)_3$ structure shares the same geometry than its silica counterpart, but the following addition of water does not actually cause a further opening of the structure. Instead, water adsorbs in a non-dissociative way upon a Ti center maintaining the same structural geometry as in $(TiO_2)_4(H_2O)_3$. This behaviour is seen in the other particles sizes as well, where an over-addition of water will cause the breaking of bonds on the SiO_2 structure, while in TiO_2 water is unable to break Ti-O bonds, therefore either it will attach OH^- groups to titania, or shared among them, and H^+ to bridging oxygens without causing bond breaking or adsorb in a non-dissociative way forming a dative bond with Ti centers.

Some structures are shared between titania and silica. The particles $(XO_2)_4(H_2O)_2$, $(XO_2)_4(H_2O)_3$, $(XO_2)_8(H_2O)_2$, $(XO_2)_8(H_2O)_4$ are basically the same for both systems. It seems to be the case as well that for bigger sizes particles with different degree of hydration have a very close structure, such as $(TiO_2)_{12}(H_2O)_4$ and $(SiO_2)_{12}(H_2O)_5$, and $(TiO_2)_{12}(H_2O)_2$ with $(SiO_2)_{12}(H_2O)_1$.

Cage Strain

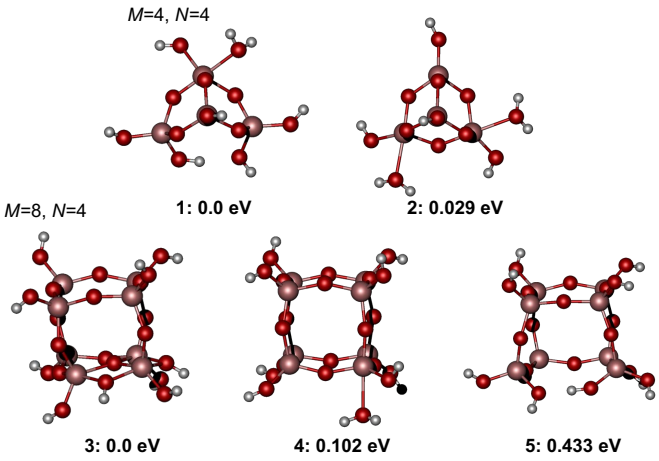

Figure 4. Structural $(TiO_2)_M(H_2O)_N$ isomers for M = 4, 8 and N=4. Numbers in the cluster labels show the relative total energy (eV) at PBE0 tight/tier-1 level of theory. Structure 2 was also reported in ref Dixon.

Hydration free energies

Hydration free energy (ΔG_{hyd}) indicates the thermodynamic tendency of anhydrous nanocluster to be hydrated at specific temperature and pressure conditions (eq. 2.6). In Fig 5 we plot the ΔG_{hyd} of silica (solid lines) and titania (dashed lines) with respect to incorporated water ratio ($R_{N/M}$) at several temperatures (0, 300, 600, 900 K). All hydration energies are normalized by number of oxide units (i.e. M). In the 0 K case each term of eq. 2.6 is approximated by only DFT energies and to distinguish this quantity from free energies we indicate it as ΔE_{hyd}. In all other cases, ΔG_{hyd} is calculated under the assumption that the system is in equilibrium with water vapour at a partial pressure of 1 Pa.

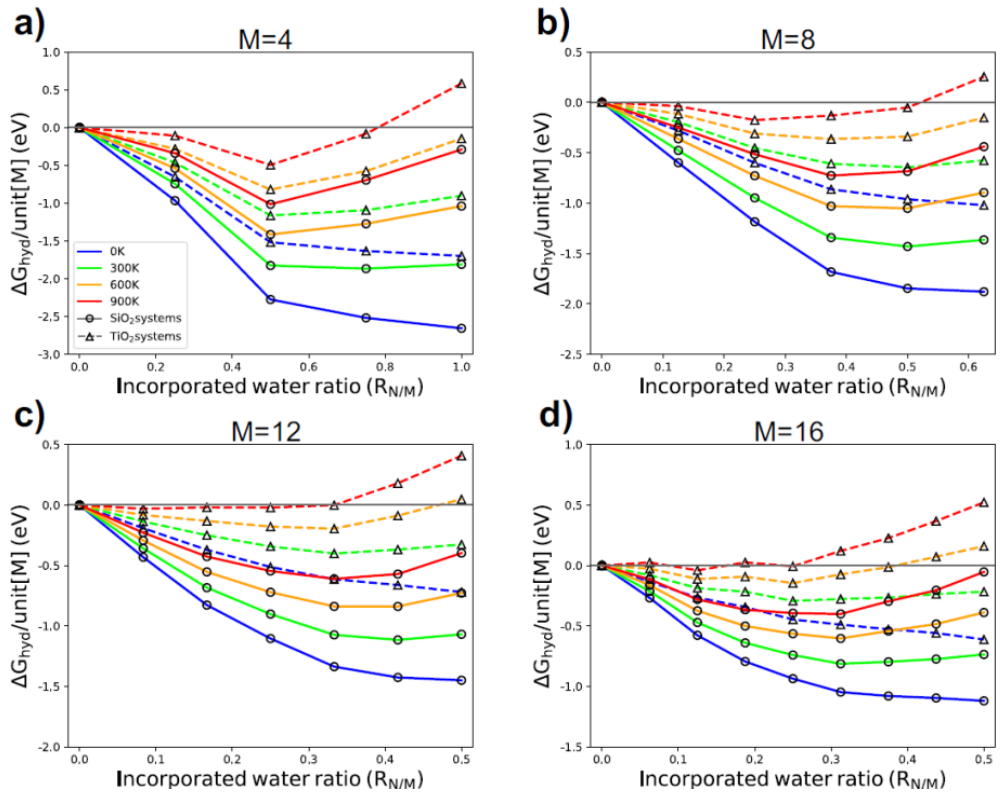

Figure 5. Hydration energies free energies of silica and titania nanoclusters for nanocluster sizes for: a) M=4, b) M=8, c) M=12, d) M=16. Hydration free energies are reported at different temperatures while keeping the water partial pressure at 1 Pa which is sufficiently low to consider water as an ideal gas even at ambient conditions.

As we can see from Fig. 5, the hydration reaction is a more exothermic process on silica nanoclusters than on the correspondingly sized titania nanoclusters. As the system size (M) increases the magnitude of hydration energies decrease. At 0 K, for both titania and silica systems, at all sizes, the hydration energy decreases indicating a higher electronic stability of hydrated systems with respect

to anhydrous ones. The energetic gain can be divided in two regions. At first, the slope is rather large and the energy gain seems constant with a decrease of -0.4 eV for each 0.1% increase of water content for SiO_2, and a decrease of -0.2 eV per 0.1% increase of water content for TiO_2. At a certain degree of hydroxylation that depends on the size and system, there is a change in the energetic gain that seems to reach a saturation value for all cases except for M=4. In this saturation region, the difference in hydration energy between systems stabilizes, and varies with respect to size from 1eV for M=4 to 0.6 eV for M=16. When including thermal contributions to the hydration free energy, ΔG_{hyd} initially decreases with increasing water incorporation until reaching a minimum point where ΔG_{hyd} will start to increase again. The minima coincides with the point where a change of slope happens in the 0K energy diagram. The effect of temperature in the diagrams consist on an increase of the slopes (e.g, lower hydration energy) for both regions. Indeed, at 900K for most of titania systems the ΔG_{hyd} is nearly zero or positive showing that hydration is thermodynamically unfavourable. This is caused mostly by the vibrational contributions to entropy and enthalpy of highly hydrated systems and the higher the hydration degree the higher the impact of these contributions. The minimum of ΔG_{hyd} as the system size increases tend to move towards smaller values of $R_{N/M}$. This indicates that as the system becomes larger, its tendency to be hydrated decreases, or in other words, it tends to be more hydrophobic. Moreover, it is interesting to notice that the silica and titania ΔG_{hyd} minima for small sizes (i.e. M=4, 8) corresponds to the same incorporation of water ratio ($R_{N/M}$), but, for bigger sizes (i.e. M=12, M=16), $R_{N/M}$ is shifted towards smaller values for titania systems. This indicates that already at this subnanometric size scale titania tends to be more hydrophobic than silica.

Band gap dependence

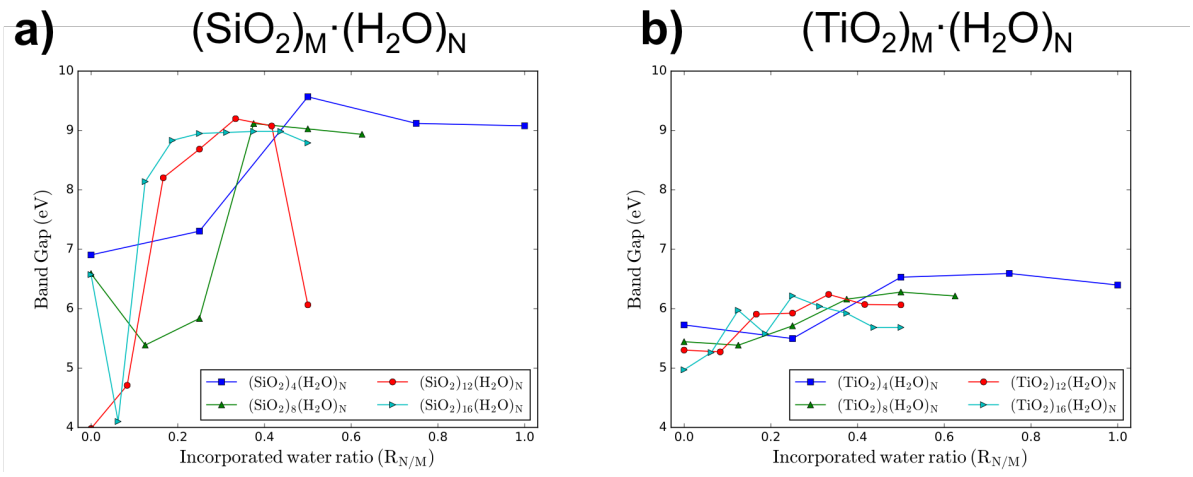

Figure 6. Band gap of silica (a) and titania (b) systems with respect to the incorporated water ratio.

In Fig. 6 we plot the vertical band gap of silica (Fig. 6a) and titania (Fig. 6b) systems with respect to the $R_{N/M}$. While it is known that the DFT calculations employing the hybrid PBE0 functional tend to overestimate band gaps, our discussion is only related to trend and not on absolute values of the band gap. Generally, silica systems show a much higher variability in their band gap with the degree of hydration than titania. Indeed, as example case, in $(SiO_2)_{12}$ systems, the band gap ranges from 4 eV at 0% of hydration to around 9 eV at 33% of hydration while for titania systems at the same size the band gap varies from a minimum of 5.3 eV at 8% of hydration to a maximum of 6.2 eV at 33% of hydration. In silica systems, clusters band gap is extremely sensitive to the type of oxygen defective sites. For instance, for bare nanoparticles with M=4, 8 and 16 and N=0 which have defective oxygen atoms in silanone species have band gaps between 6.5 and 7 eV while for $(SiO_2)_{12}$ which has NBO defective sites the band gap is much lower (i.e. 4 eV). Moreover, systems with defective oxygen atoms in silanone species which by hydration of one water molecule become NBO defective sites (i.e. M=8, 16) lower their band gap while in all the other cases the band gap increases with the hydration of one water molecule. As the hydration increases, the band gap generally increases as well until a maximum value is reached around 35% and 40% of hydration depending on the system size (50% for the M=4 system). Further increase of hydration keeps the band-gap almost constant with the only exception of $(SiO_2)_{12}(H_2O)_6$ in which drops down by 3 eV probably due to the presence of geminal hydroxyl groups. This effect however, is not seen in $(SiO_2)_8(H_2O)_5$ systems.

In titania systems there are only NBO defective site, however there is much greater variety of titanium cation coordination (i.e. 4-, 5- and 6-coordinated Ti centres) and therefore the band gap behaviour with increasing water inclusion ratio is less nicely rationalizable than in silica case, albeit the magnitude of the changes are much smaller. Overall, titania band gap evolution shows some similarities with silica systems: (i) there is a maximum value of the band gap as hydration increases and (ii) after the maximum the band gap remains rather constant (i.e. M=4 and 8). However, in some cases there is a slight decline (i.e. M=12 and 16) in the band gap. We notice that the band gap correlates with electronic state frustration of the system. The higher the band gap the more electronically stable the system should be, and adsorption can influence restoring a large band-gap Therefore, hydration contributes to stabilize the electronic state of both silica and titania nanoparticles but in silica systems this effect is greatly magnified showing that silica is better stabilized than titania by hydration.

Ab initio thermodynamics of hydrated nanoparticles

According to equation 2.6 (ΔG(T, P)) it is possible to define the hydration reaction of clusters as function of temperature (T) and partial pressure of water vapour (P). Since the most thermodynamically stable nanocluster at specific conditions of T and P is the one that minimizes the free energy of hydration, we can plot hydration phase diagrams where each region represents the most thermodynamically stable nanoclusters with specific amount of incorporated water at a certain T and P range. All necessary energy values can be derived from ab initio calculations but it is worth reporting all approximations involved. The main approximations used are related with the partition function formulation under the frame of classical statistical thermodynamics. The partition function formulation is based on the idea that the number of quantum mechanical states accessible to the systems in specific temperature T must be much larger than the number of particles on the system. As temperature approaches 0K this conditions is no longer true thus the system follows Fermi-Dirac statistic instead of the classical Boltzmann one. For instance, for the N_2 molecule at boiling point (~77K), conditions for which the system is not considered as ideal gas, it still obeys Boltzmann statistics.[58] Conversely, at high temperature harmonic-oscillator approximation might no longer be valid due to induced anharmonicities. From this perspective, we consider as reasonable a T range between 100 and 1000 K as considered from other authors for similar purposes.[59] Moreover, in our case we consider water as an ideal gas for a wide range of temperatures but actually this depends on the water partial pressure. Water vapour is in equilibrium with its condensed state at ~3kPa at 300K. In order to consider water as ideal gas, however, we should consider a much lower partial pressure. In the phase diagrams reported in Fig. 7, the water partial pressure that we consider does not overcome the $1x10^5$ Pa (e.g. ~1 atm). At this pressure we can consider water as ideal gas from ~450-500 K and higher. The saturation water pressure at 273K (0ºC) is about 0.6 kPa. In order to treat water as ideal gas in these conditions we should roughly consider either temperatures higher that 400K or pressures lower than 1Pa. Although considering water as an ideal gaz at relatively low temperatures and high pressures is conceptually wrong, these conditions represent a small part of the phase diagrams reported in figure 6 and therefore approximations remain valid for the large part of diagrams.

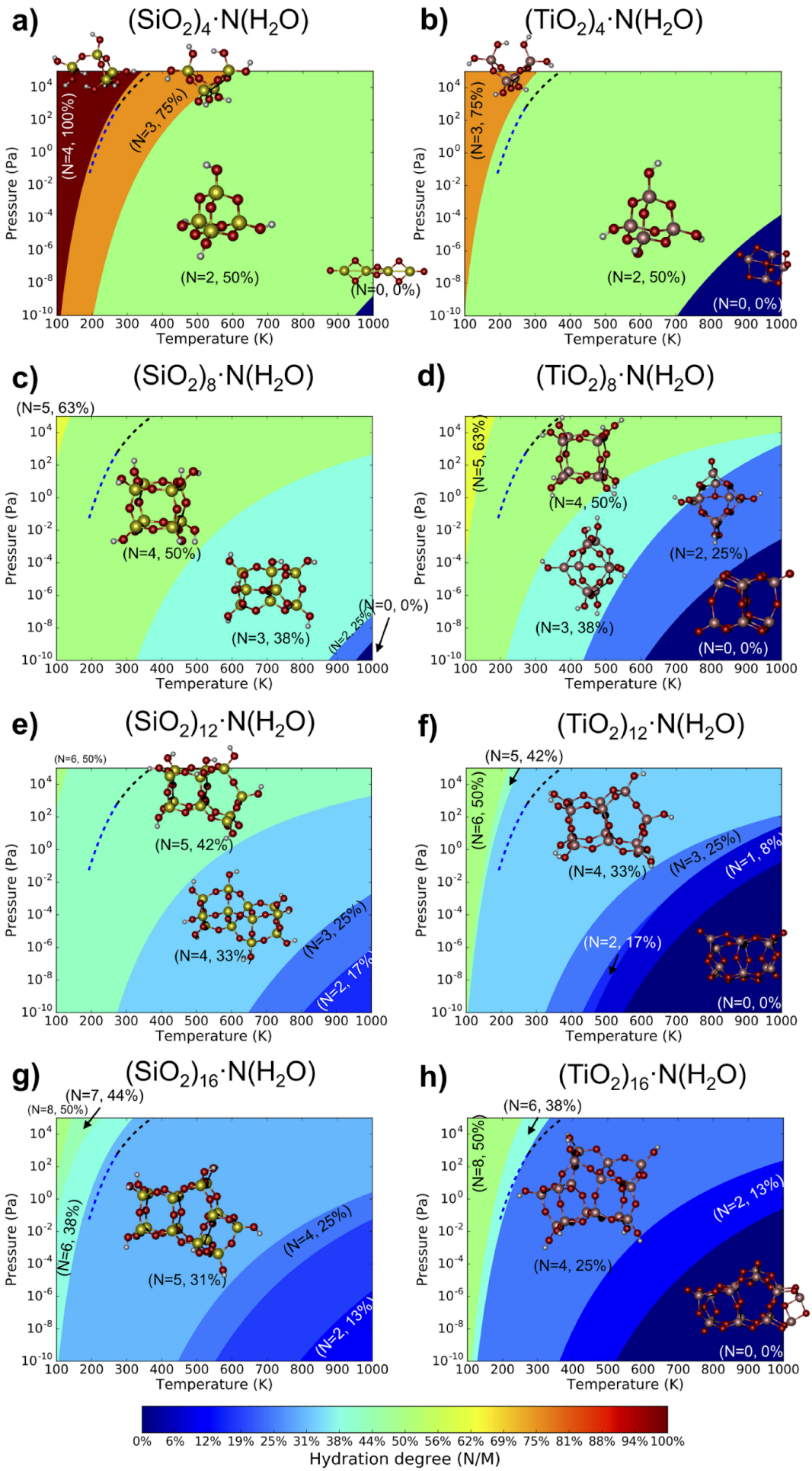
a) $(SiO_2)_4 \cdot N(H_2O)$
(N=4, 100%)
(N=3, 75%)
(N=2, 50%)
(N=0, 0%)
b) $(TiO_2)_4 \cdot N(H_2O)$
(N=3, 75%)
(N=2, 50%)
(N=0, 0%)
c) $(SiO_2)_8 \cdot N(H_2O)$
(N=5, 63%)
(N=4, 50%)
(N=3, 38%)
(N=2, 25%)
(N=0, 0%)
d) $(TiO_2)_8 \cdot N(H_2O)$
(N=5, 63%)
(N=4, 50%)
(N=2, 25%)
(N=3, 38%)
(N=0, 0%)
e) $(SiO_2)_{12} \cdot N(H_2O)$
(N=6, 50%)
(N=5, 42%)
(N=4, 33%)
(N=3, 25%)
(N=2, 17%)
f) $(TiO_2)_{12} \cdot N(H_2O)$
(N=5, 42%)
(N=6, 50%)
(N=4, 33%)
(N=3, 25%)
(N=1, 8%)
(N=2, 17%)
(N=0, 0%)
g) $(SiO_2)_{16} \cdot N(H_2O)$
(N=7, 44%)
(N=8, 50%)
(N=6, 38%)
(N=5, 31%)
(N=4, 25%)
(N=2, 13%)
h) $(TiO_2)_{16} \cdot N(H_2O)$
(N=6, 38%)
(N=8, 50%)
(N=4, 25%)
(N=2, 13%)
(N=0, 0%)
Pressure (Pa)
Temperature (K)
0% 6% 12% 19% 25% 31% 38% 44% 50% 56% 62% 69% 75% 81% 88% 94% 100%
Hydration degree (N/M)

Figure 7. P-T phase diagrams for silica (left side) and titania nanoparticles (right side). Temperature range goes from 100 to 1000 K and P (H_2O partial pressure) range from $1x10^{-10}$ to $1x10^{5}$ Pa (from ~$1x10^{-15}$ to ~1 atm). Blue and black dashed line indicate the equilibrium vapour pressure with respectively ice and liquid water. Colours of P-T phase diagram regions are determined by hydration degree intervals in all the graphs. The cooler the colour (towards dark blue) the lower the hydroxylation degree, the warmer the colour (towards dark red) the higher the hydroxylation degree. From top to bottom graphs are arranged from smallest $(XO_2)_4(H_2O)_N$ to biggest $(XO_2)_{16}(H_2O)_N$ where X=Si, Ti.

In Fig. 7 we plot phase diagrams for both titania and silica systems in thermodynamic equilibrium with water vapor. As discussed before, the pressure and temperature ranges have been chosen in order to consider water as an ideal gas in most of the conditions represented in the graph. Each region of the graph represents the most thermodynamically stable hydrated cluster at the particular conditions of T and P_{H2O} according to equation 2.6. Region colours in phase diagrams are chosen in order to be specific for each hydration degree (i.e. the 50% hydrated structures have same colour in all graphs). As from a first view to phase diagrams, silica and titania, which can have very different properties at macroscopic scale (amorphous silica can be hydrophilic and hydrophobic, while TiO_2 is always hydrophobic), show similar hydration behaviour at nanoscale, especially at the smallest size M=4, and becomes less pronounced as the system size increases. For the systems with M=4 most of the phase diagrams are dominated by the same isomer for both hydrated titania and silica (i.e. M=4; N=2 with 50% of hydration degree.). However, the most stable structure at ambient temperature conditions for silica corresponds to the 75% hydrated system. At relatively higher P_{H2O} and lower T silica becomes 100% hydrated while titania very hardly reaches that degree of hydration. For M=8, silica phase diagram (Fig 7c) is dominated by two structures (i.e. N=3,4) while titania phase diagram (Fig 7d) is dominated by four structures(i.e. N=0,2,3,4). M=8, N=4 is again the same isomer for both systems but for silica the P-T stability region is wider. At ambient conditions (T=300 and 1-1k Pa water partial pressure (the equilibrium vapour partial pressure with its condensed state at 300K is 4.2 kPa)), this last structure is thermodynamically favourable for both systems. At temperatures below 900K silica is stable by just losing one water molecule to form the M=8 N=3 structure. Titania instead shows a higher variety of hydration degree at high temperature, with structures going from N=3 to N=2 and at the end N=0 as temperature increases. Two important features must be highlighted from the plot: (i) systems with N=1 do not appear in the T-P range considered in both titania and silica and (ii) at very low temperatures titania has a larger degree of hydration than silica. This second feature is not exclusive for M=8, but rather appears in all phase diagrams. It must be

noted though that the region falls outside the correct description of water vapour. A possible explanation is that TiO_2 is able to adsorb water molecules more easily than SiO_2 (SiO_2 needs formation of hydroxyls, TiO_2 protonates bridging oxygens). For M=12, silica phase diagram (Fig 7e) is mainly occupied by two structures as in the case of M=8 but with a lower hydration degree of 42% and 33%, compared to the previous 50% and 38% at M=8. Lower hydrated structures are found at high temperature phases (> ~700K). For titania systems at the same size (Fig 7f) the phase diagram is slightly more complex than silica and has more stable phases. Despite that, only 33% and 0% (respectively N=4 and N=0) hydrated phases seems to play a dominant role. Notice that $(SiO_2)_{12}(H_2O)_5$ and $(TiO_2)_{12}(H_2O)_4$ which both occupy most of the area of the phase diagram and the region nearby ambient conditions have the cube motif (i.e. such us M=8, N=4 structures) incorporated in the cluster. This is an indicator of the stability of such motif not only for silica systems (which is already known) but for titania systems as well. Such structural motif could be used as building block to synthesize more complex materials such as titanosilicates in a controlled way. For M=16, silica systems (Fig 7g) show one dominant phase at 31% of hydration degree (i.e. N=5). Maximum hydration degree reaches 50% for narrow regions in the phase diagram at low temperature as in the case of M=12. As temperature rises, the hydration decreases up to 13%. This trend is similar in the case of titania systems but is shifted towards lower hydration degrees (i.e. from 25% to 0% of hydrated degree). Only the low temperature phases (50% and 38%) show similar stabilities with silica phases, albeit with a larger area of the most hydroxylated case for titania.

As an overview on phase diagrams, for both systems the tendency to be hydrated decreases with size. As the system size increases phase diagram region colours shift towards light blue and blue. However, the shift towards low hydrated systems as their size increase is less pronounced for silica than for titania systems indicating that silica nanoparticles are more hydrophilic. Indeed, at high temperature and low water partial pressure (P_{H2O}) silica is completely anhydrous at much higher temperatures than titania. Regions of P-T diagrams with completely anhydrous silica are even hardly present in the T and P range considered. It is worth noticing that at ambient temperature conditions, even at the presence of traces of humidity, clusters tend to hydrate.

Size dependency of hydration degree

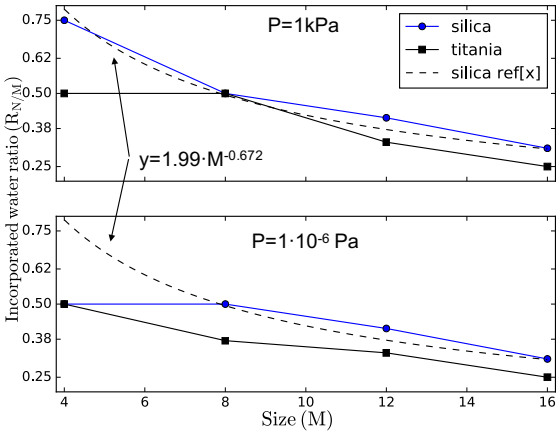

Figure 8. Size dependency of Incorporated water ratio at 300K and two water partial pressure conditions respectively at P=1kPa (top graph) and P=1·10^{-6} Pa (bottom graph). Blue line and markers are relative to silica while black line and markers are referred to titania system. The dashed line is the hydration size dependency of silica systems found in our previous study.

In Fig. 8 we report the size dependency of titania and silica hydration at 300K considering two different water partial pressure conditions: 1kPa and 1·10^{-6} Pa. For both systems the hydration decreases almost linearly with the same slope. However, the titania hydration size dependency curve is slightly shifted towards lower hydrations. This is a further indication that titania tends to be more hydrophobic than silica as the system size increases. The size dependency of hydration degree has been previously studied in our group. In those cases, we showed how optimal hydration degree of silica clusters follows a specific inverse power law trend with increasing system size. The optimal hydration was defined where hydration energy levels off, in other words, when there is no more significant gain in energy when including more water molecules in the cluster. Here we see that this trend, for silica systems is still valid even considering hydration free energies at ambient conditions except for the smallest systems at very low water partial pressure.

Vibration frequencies

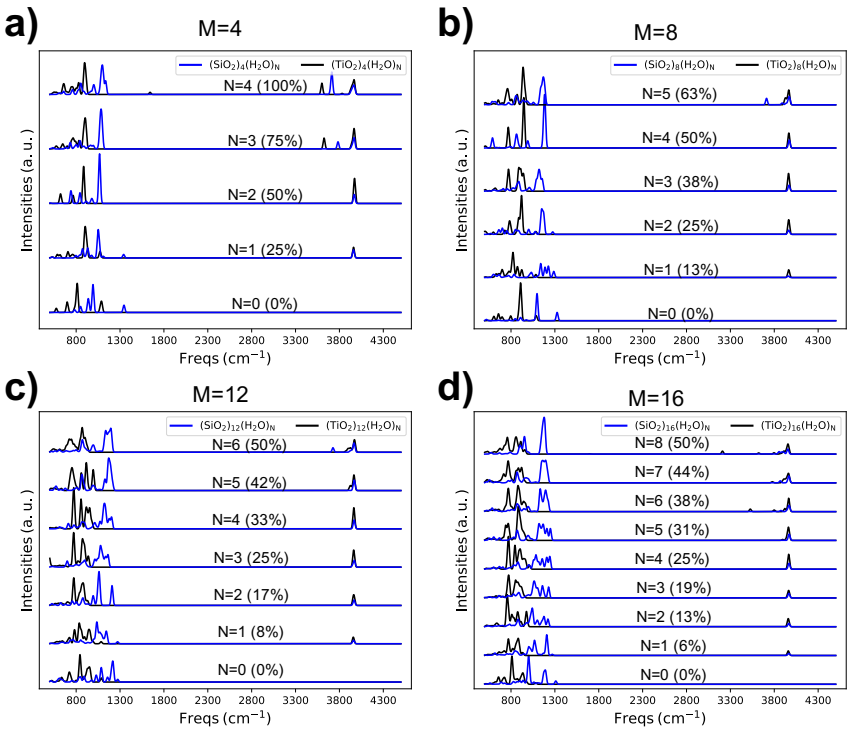

Figure 8. Simulated, infrared harmonic vibrational frequencies of silica (blue line) and titania (black line) line systems at different N incorporated water molecules (hydration degrees in parenthesis). a), b), c), d) represents IR spectra of respectively M=4, 8, 12, 16 system sizes. Each graph is scaled with respect to the most intense peak. Intensities are in arbitrary units.

In Fig. 8 we plot the infrared harmonic vibrational frequencies of all global optimized titania (black line) and silica (blue lines) systems. In all spectra the region of hydroxyl OH stretching (ν_{OH}) around 3900 cm^{-1} is well visible. This peak is persistent with system size and hydration degree and is consistent between titania and silica with the only exception of M=16, N=3 that is slightly red shifted in the silica case with respect to all the other peaks. As the hydration increases there are other stretching modes between 3000 and 3900 cm^{-1} which are originated by OH involved in hydrogen bonds ($\nu_{OH\text{--}O}$). As hydration increases, at fixed systems size M, the ν_{OH} intensifies because of the increasing number of OHs. As the system becomes bigger (increasing M) the OH peaks weakens because the spectra are dominated by the more numerous cation-O vibrational modes. Differences between silica and titania can not be easily spotted in hydroxyl stretching region but rather in the cation-O stretching/bending one. Indeed, between 600 to 1400 cm^{-1} in the spectra there are intense IR peaks mostly dominated by complicated coupling of cation-O stretching and bending modes involving several centres (δν-O-X-O). In silica systems this set of peaks are highly blue shifted (i.e.

mostly with vibrational modes higher than 1000 cm^{-1}) with respect to titania ones (i.e. mostly with vibrational modes lower than 1000 cm^{-1}). Moreover, these δv-O-X-O are slightly blue shifted in the case of silica systems as the hydration degree increases.

Average Coordination Number (ACN)

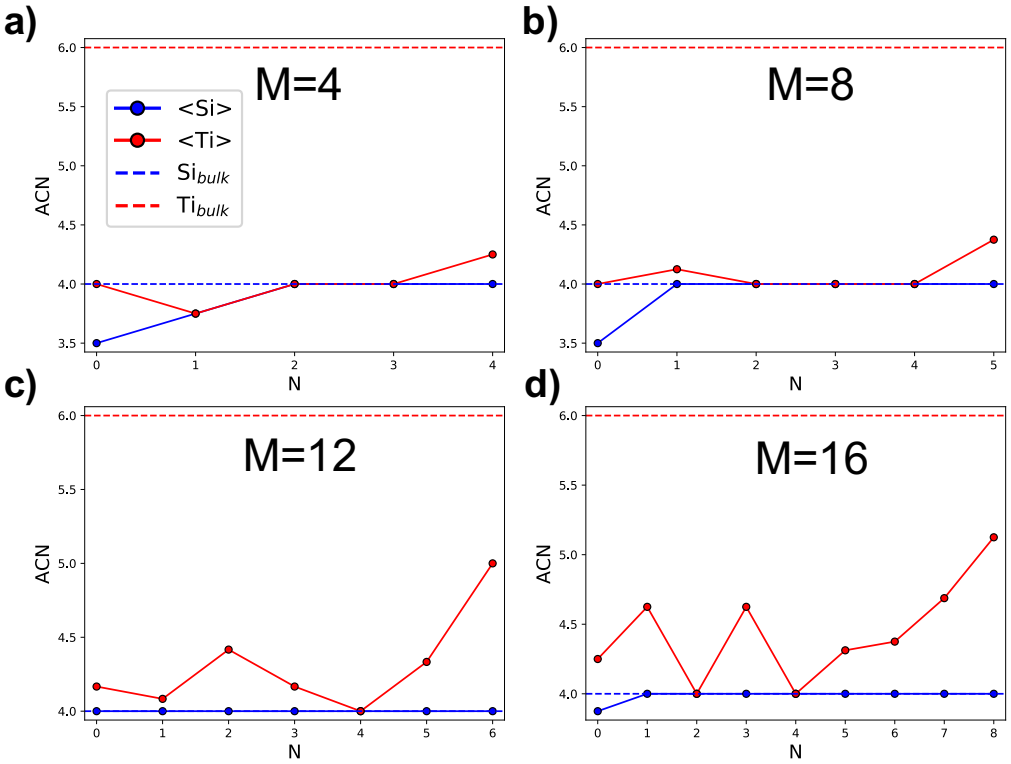

Figure 9. Average Coordination Number (ACN) as a function of N incorporated water molecules for Si and Ti cations. Respective bulk coordination numbers are also reported in dashed lines. The CAN number is defined takin all nearest neighbours within a 2.1 Å cut off in the case of SiO_2 and within a 2.5 Å cut off in the case of TiO_2.

In Fig. 9 we report the cations Average Coordination Number (ACN) in nanoparticles with different sizes (i.e. M) as a function of incorporated water molecules (i.e. N). Distance cutoff values to count a neighbour as a coordinating atom has been chosen according to Cation-O distance distribution in all clusters. All atoms within 2.1 Å from Si cations and within 2.5 Å from Ti cations are counted inside their respective coordination shell. In all the cases Si atoms tends to display at most 4-coordinated anion environment rapidly reaching the bulk value as the number of included water molecules increases. In the case of TiO_2, M=4 and M=8 systems Ti cations tend to display similar coordination environment and by increasing the amount of included water molecules does not change their coordination apart the first one or two waters. This is mainly due to the structural strains these small systems are affected and they release such strains by breaking up after a dissociate water

adsorption. Larger systems, such as M=12 and 16, are found to be more flexible allowing for over coordination of Ti cation caters tending towards the bulk value as the number of included water molecules increase. However, as shown from Fig. 5 and Fig. 7, the hydration reaction free energy for highly hydrated systems (close to $R_{N/M}$~50%) tends to be not favourable therefore such species will not form in realistic equilibrium conditions.

Conclusions

In this work we have investigated structural end energetic properties of the titania and silica nanoclusters hydration by means of accurate ab initio simulations. All structures are generated by employing an IP-based global optimization search which yield to several new global minima candidate isomers for $(TiO_2)_M(H_2O)_N$ with M=4, 8, 12, 16, each for a range of N values. Such isomers can be used to better interpret laser beam experiments of such small systems. Moreover, a new IP for non-bulk hydrated titania was introduced for such study re-parameterized from the well established hydrated nanosilica IP. For such small nanoclusters regime, the hydration energy at 0K is found to be exothermic for a wide range of hydration degree up to -1.0, -2.5 eV / M oxide units for nano-SiO_2 and up to -0.5, -1.5 eV / M oxide units for nano-TiO_2 depending on the system size. We have also calculated hydration free energies which are found to display a moderate temperature dependency. More particularly, some of the titania highly hydrated systems are found to be thermodynamically not stable as the temperature increases. By the ab initio atomistic thermodynamics we could also provide phase diagrams showing the dependence on temperature and water vapour pressure on silica and titania nanoclusters. Such study shows that in ambient conditions, nanoclusters would be hydrated even in traces of water vapour. We also provide a series of structural and electronic properties such as the average cation coordination and the band gap as a function of hydration degrees. The average Ti atoms coordination is found to increase up to 5 with as a result of the structural flexibility of Ti-O network while the average Si atoms coordination reaches rapidly the value of bulk coordination of 4 as the hydration degree increases. Band gaps indicate that the electronic structure is profoundly changed after the hydration of silica nanoclusters while it is less remarkably affected in the case of titania nanoclusters. Our study provides new insight on hydration effects on small titania and silica nanoclusters. We hope to inspire experimental studies, specially from the laser beam community, to address studies on small nanoclusters which can be used as model systems to understand the dissociative water adsorption in macroscopic bulk materials. Such studies could help understating and optimizing the photocatalytic water splitting reaction with oxide materials.

[1] F. Piccinno, F. Gottschalk, S. Seeger, B. Nowack, J. Nanopart. Res. 14, 1109 (2012).
[2] H. Gao H, K. Lian, ACS Appl. Mater. Interfaces. 6, 464 (2014).
[3] H. Yang, Q. Gao, Y. Xie, Q. Chen, C. Ouyang, Y. Xu, X. Ji, J. Appl. Polym. Sci., 132, 42806 (2015).
[4] L. Senff, D. M. Tobaldi, S. Lucas, D. Hotza, V. M. Ferreira, J. A. Labrincha, Composites Part B-Engineering, 44, 40 (2013).
[5] We. Dong, Y. Sun, C. W. Lee, W. Hua, X. Lu, Y. Shi, S. Zhang, J. Chen, and D. Zhao, *J. Am. Chem. Soc.*, 129, 13894 (2007).
[6] P. Wilhelm, D. Stephan, J. Photochem. Photobio. A: Chem., 185 19 (2007).
[7] K. Qi, X. Chen, Y. Liu, J. Xin, C. Mak, and W. Daoud, *J. Mater. Chem.*, **17**, 3504(2007).
[8] C. S. Cundya, P. A. Cox, Microporous and Mesoporous Materials, 82 1 (2005).
[9] M. Cargnello, T. R. Gordon, C. B. Murray, Chem. Rev., 114 9319 (2014).
[10] L. K. Adams, D. Y. Lyon, P. J. J. Alvarez, Water Res. 40, 3527 (2006).
[11] Y. Ma, X. Wang, Y. Jia, X. Chen, H. Han, C. Li, Chem. Rev. 114, 9987 (2014).
[12] K. C. Ko, S. T. Bromley, J. Y. Lee, F. Illas, J. Phys. Chem. Lett. 8, 5593 (2017).
[13] F. Nunzi, S. Agrawal, A. Selloni, F. De Angelis, J. Chem. Theory Comput., 11, 635 (2015).
[14] G. Fazio, L. Ferrighi, C. Di Valentin, J. Phys. Chem. C, 119, 20735 (2015).
[15] O. Lamiel-Garcia, K. C. Ko, J. Y. Lee, S. T. Bromley, F. Illas, J. Chem. Theor. Comput. 13, 1785 (2017).
[16] A. Iacomino, G. Cantele, D. Ninno, I. Marri, S. Ossicini, Phys. Rev. B 78, 075405 (2008).
[17] E. Berardo, M. A. Zwijnenburg, J. Phys. Chem. C, 119, 13384 (2015).
[18] E. G. Brandt, L. Agosta, A. P. Lyubartsev, Nanoscale, 8, 13385 (2016).
[19] K. Shirai, G. Fazio, T. Sugimoto, D. Selli, L. Ferraro, K. Watanabe, M. Haruta, B. Ohtani, H. Kurata, C. Di Valentin, Y. Matsumoto, J. Am. Chem. Soc., 140, 1415 (2018).
[20] D. Cho, K. C. Ko, O. Lamiel-Garcia, K. C. Ko, S. T. Bromley, J. Y. Lee, F. Illas, J. Chem. Theor. Comput. 12, 3751 (2016).
[21] D. Selli, G. Fazio, C. Di Valentin, Catalysts, 7, 357 (2017).
[22] N. Pienack, W. Bensch, Angew. Chem. Int. Ed., 50, 2014 (2011).
[23] C. T. G. Knight, R. J. Balec and S. D. Kinrade, Angew. Chem. Int. Ed., , 46, 8148 (2007).
[24] M. Haouas and F. Taulelle, J. Phys. Chem. B, 110, 3007 (2006).
[25] S. A. Pelster, W. Schrader and F. Schüth, J. Am. Chem. Soc., 128, 4130 (2006).
[26] M. J. Mora-Fonz, C. R. A. Catlow and D. W. Lewis, J. Phys. Chem. C, 2007, 111, 18155.
[27] T. T. Trinh, A. P. Jansen, R. A. van Santen and E. J. Meijer, J. Phys. Chem. C, 2009, 113, 2647.
[28] C. E. White, J. L. Provis, G. J. Kearley, D. P. Riley, J. S. J. van Deventer, Dalton Trans., 2011, 40, 1348.
[29] C. L. Schaffer, K. T. Thomson, J. Phys. Chem. C, 2008, 112, 12653.
[30] T. T. Trinh, X. Rozanska, F. Delbecq, P. Sautet, Phys. Chem. Chem. Phys., 2012, 14, 3369.
[31] M. L. Weichman, S. Debnath, J. T. Kelly, S. Gewinner, W. Schoellkopf, D. M. Neumark, K. R. Asmis, Top. Catal. 61, 92 (2018).
[32] M. Chen, T. P. Straatsma, D. A. Dixon, J. Phys. Chem. A, 119, 11406 (2015).
[33] C. R. A. Catlow, S. T. Bromley, S. Hamad, M. Mora-Fonz, A. A. Sokol, S. M. Woodley, Phys. Chem. Chem. Phys., 12, 786 (2010)
[34] E. Flikkema, S. T. Bromley, J. Phys. Chem. B, 108, 9638 (2004).
[35] S. T. Bromley, E. Flikkema, Phys. Rev. Lett., 95, 185505 (2005).
[36] E. Flikkema, K. E. Jelfs, S. T. Bromley, Chem. Phys. Lett., 554, 117 (2012).
[37] O. Lamiel-Garcia, A. Cuko, M. Calatayud, F. Illas, S. T. Bromley, Nanoscale 9, 1049 (2017).
[38] A. Cuko, M. Calatayud, S. T. Bromley, Nanoscale 10, 832 (2018).
[39] K. E. Jelfs, E. Flikkema, S. T. Bromley, Phys. Chem. Chem. Phys., 15, 20438 (2013).
[40] K. Jelfs, E. Flikkema, S. T. Bromley, Chem. Commun., 48, 46 (2012).
[41] A. Cuko, A. Macia, M. Calatayud, S. T. Bromley, Comput. Theor. Chem. 1102, 38 (2017)
[42] S. Y. Kim, N. Kumar, P. Persson, J. Sofo, A. C. T. Van Duin, and J. D. Kubicki, Langmuir, 29, 7838 (2013).
[43] G. Ricchiardi, A. de Man, and J. Sauer, Phys. Chem. Chem. Phys., 2, 2195 (2000).
[44] A. V. Bandura and J. D. Kubicki, J. Phys. Chem. B, 107, 11072 (2003).
[45] E. Dushanov, K. Kholmurodov, and K. Yasuoka, Nat. Sci., 4, 313 (2012).
[46] A. Pedone, G. Malavasi, M. C. Menziani, U. Segre, F. Musso, M. Corno, P. Ugliengo, Chem. Mater., 20, 2522 (2008).
[47] A. Macià Escatllar, P. Ugliengo, S. T. Bromley, J. Chem. Phys., 146, 224704 (2017).
[48] A. Macià Escatllar, P. Ugliengo, S. T. Bromley, Inorganics, 5, 41 (2017).

[49] J. P. Perdew, K. Burke, and M. Ernzerhof, Phys. Rev. Lett., 77, 3865 (1996).
[50] V. Blum, R. Gehrke, F. Hanke, P. Havu, V. Havu, X. Ren, K. Reuter and M. Scheffler, Phys. Commun., 180, 2175 (2009).
[51] S. R. Bahn, K. W. Jacobsen, Comput. Sci. Eng. 4 56 (2002).
[52] J.D. Gale, J. Chem. Soc., Faraday Trans., 93, 629 (1997).
[53] C. Adamo and V. Barone, J. Chem. Phys., 110, 6158 (1999).
[54] V. G. Avakyan, V. F. Sidorkin, E. F. Belogolova, S. L. Guselnikov, L. E. Gusel'nikov, Organometallics, 25, 6007 (2006).
[55] M. A. Zwijnenburg, A. A. Sokol, C. Sousa, S. T. Bromley, J. Chem. Phys., 131, 34705 (2009).
[56] S. Hamad, S. T. Bromley, Chem. Comm., 0, 4156 (2008).
[57] M. A. Zwijnenburg, F. Illas, S. T. Bromley, J. Chem. Phys., 137, 154313 (2012).
[58] Donald A. McQuarrie and John D. Simon, Physical Chemistry: a Molecular Approach (Sausalito, Calif.: University Science Books, 1997), pp 711-712.
[59] S. Bhattacharya, S. V. Levchenko, L. M. Ghiringhelli, M. Scheffler, New J. Phys., 16, 123016 (2014).